UNIVERSITY OF SOUTHAMPTON

FACULTY OF PHYSICAL SCIENCES AND ENGINEERING
Physics

Exploratory Lattice QCD Studies of Rare Kaon Decays

by

Andrew J. Lawson

Thesis for the degree of Doctor of Philosophy

October 2017

UNIVERSITY OF SOUTHAMPTON

ABSTRACT

FACULTY OF PHYSICAL SCIENCES AND ENGINEERING
Physics

Doctor of Philosophy

EXPLORATORY LATTICE QCD STUDIES OF RARE KAON DECAYS

by Andrew J. Lawson

The rare kaon decays $K \to \pi\ell^+\ell^-$ and $K \to \pi\nu\bar{\nu}$ proceed via flavour changing neutral currents, and are thus heavily suppressed in the Standard Model. This natural suppression makes these decays sensitive to the effects of potential new physics. These decays first arise as second-order electroweak processes, hence we are required to evaluate four-point correlation functions involving two effective operators. The evaluation of such four-point correlation functions presents two key difficulties: the appearance of unphysical terms in Euclidean-space correlators that grow exponentially as the operators are separated, and the presence of ultra-violet divergences as the operators approach each other. I present the results of the first exploratory studies of the calculation of the long-distance contributions to these decays using lattice QCD.

The decays $K \to \pi\ell^+\ell^-$ are completely long-distance dominated; this lattice calculation is thus the first step in providing ab-initio estimates for the amplitudes of these decays. Our simulations are performed using the $24^3 \times 64$ domain wall fermion ensemble of the RBC-UKQCD collaboration, with a pion mass of 430(2) MeV, a kaon mass of 625(2) MeV, and a valence charm mass of 543(13) MeV. In particular we determine the form factor, $V(z)$, of the $K^+(k) \to \pi^+(p)\,\ell^+\ell^-$ decay from the lattice at small values of $z = q^2/M_K^2$ (where $q = k - p$), obtaining $V(z) = 1.37(36),\ 0.68(39),\ 0.96(64)$ for the three values of $z = -0.5594(12),\ -1.0530(34),\ -1.4653(82)$ respectively.

The decays $K^+ \to \pi^+\nu\bar{\nu}$ are short-distance dominated, although the long-distance contributions represent significant sources of uncertainty. The lattice calculation of the decay amplitudes is made particularly difficult by the presence of ultra-violet divergences in the four-point correlators. I present the calculation of the renormalised decay amplitudes, using the $16^3 \times 32$ domain wall fermion ensemble of the RBC-UKQCD collaboration, with a pion mass of 421(1)(7) MeV, a kaon mass of 563(1)(9) MeV, and a valence charm mass of 863(24) MeV. In particular we find the difference between the perturbative and lattice estimates of the charm contribution to these decays to be $\Delta P_c = 0.0040(13)(32)(-45)$.

Contents

List of Figures

List of Tables

Declaration of Authorship

I, Andrew J. Lawson , declare that the thesis entitled *Exploratory Lattice QCD Studies of Rare Kaon Decays* and the work presented in the thesis are both my own, and have been generated by me as the result of my own original research. I confirm that:

- this work was done wholly or mainly while in candidature for a research degree at this University;
- where any part of this thesis has previously been submitted for a degree or any other qualification at this University or any other institution, this has been clearly stated;
- where I have consulted the published work of others, this is always clearly attributed;
- where I have quoted from the work of others, the source is always given. With the exception of such quotations, this thesis is entirely my own work;
- I have acknowledged all main sources of help;
- where the thesis is based on work done by myself jointly with others, I have made clear exactly what was done by others and what I have contributed myself;
- parts of this work have been published as: [2] and [3]

Signed:..

Date:...

Acknowledgements

I would first like to thank my supervisors, Prof. Chris Sachrajda and Dr. Andreas Jüttner, for their support and guidance throughout this project.

Secondly I extend my gratitude to Dr. Antonin Portelli, who provided me with much support and advice, both on computational and theoretical issues surrounding the rare kaon decays $K \to \pi\ell^+\ell^-$. I am also indebted to Xu Feng, whose careful advice was instrumental in developing my understanding of the analysis and renormalisation of $K \to \pi\nu\bar{\nu}$ decays.

I'd also like to thank my colleagues from the RBC-UKQCD collaboration for their useful input. Special thanks go to Prof. Norman Christ for his excellent insights into the rare kaon decay projects and to Prof. Peter Boyle, whose computational efforts underpin large amounts of this work.

I would also like to extend my thanks to my fellow 4007 office members, who have made these last 4 years very memorable. I am grateful to my parents for their constant love and support. Finally, I would like to thank Madi for putting up with me while I worked on strange physics.

Chapter 1

Introduction

The rare kaon decays $K \to \pi \ell^+ \ell^-$ and $K \to \pi \nu \bar{\nu}$ proceed via flavour-changing neutral currents (FCNCs), i.e. $s \to d$ transitions, and hence they first arise only as second-order electroweak processes. This suppression makes these decays ideal for probing for New Physics, by searching for discrepancies between Standard Model predictions of these processes and experimental results. The study of rare kaon decays has thus attracted increasing interest in recent years.

The phenomenology behind each of the rare kaon decays $K \to \pi \ell^+ \ell^-$ and $K \to \pi \nu \bar{\nu}$ is markedly different [4]. The decays $K \to \pi \nu \bar{\nu}$ are known to be short-distance dominated, and hence have traditionally been theoretically cleaner to study than $K \to \pi \ell^+ \ell^-$ decays, which see large contributions from long-distance, hadronic effects. To be more specific, studies of rare kaon decays are usually performed in the context of a low-energy effective theory, where the heavy weak bosons and heavy quarks do not appear as dynamical degrees of freedom. The low-energy (long-distance) hadronic effects are thus separated from the high energy (short-distance) physics; the latter contributions may be computed using perturbation theory.

In $K \to \pi \nu \bar{\nu}$ decays, the presence of a quadratic GIM mechanism [5] enhances the contributions of heavy quark loops; as a result these decays are short-distance dominated. The required hadronic contributions may be obtained from measurements of semileptonic $K^+ \to \pi^0 \ell^+ \nu$ decays. For the decay $K_L \to \pi^0 \nu \bar{\nu}$, the dominant contribution originates from the direct CP-violating amplitude, hence is proportional to the Cabibbo-Kobayashi-Maskawa (CKM) matrix factor $\mathrm{Im}\left(\lambda_q\right)$ (where $\lambda_q = V_{sq}^* V_{qd}$), which significantly suppresses the up and charm contributions. As a result, this decay is entirely dominated by loops involving the top quark, and is thus the theoretically cleanest rare kaon decay channel. A recent theoretical prediction for this branching ratio is [6]

$$\mathrm{Br}\left(K_L \to \pi^0 \nu \bar{\nu}\right) = 3.00(30) \times 10^{-11}, \tag{1.1}$$

where the majority of the error originates from uncertainties in input SM parameters. For the CP-conserving decay $K^+ \to \pi^+ \nu\bar{\nu}$, a recent theoretical prediction for the branching ratio is [6]

$$\mathrm{Br}\left(K^+ \to \pi^+ \nu\bar{\nu}\right) = 9.11(72) \times 10^{-11}. \tag{1.2}$$

The majority of the error again originates from parametric uncertainties in Standard Model parameters; however long-distance contributions of the charm (and up) quarks also represent significant sources of error. It will be important to constrain this source of error as experimental measurements of $\mathrm{Br}\left(K^+ \to \pi^+ \nu\bar{\nu}\right)$ improve. Hence an opportunity for lattice QCD is to provide estimates of the long-distance contributions to these amplitudes, such that the uncertainty from long-distance contributions may be reduced.

On the experimental side, $K^+ \to \pi^+ \nu\bar{\nu}$ is challenging to measure. The current experimental estimate for the branching ratio is [7]

$$\mathrm{Br}(K^+ \to \pi^+ \nu\bar{\nu}) = 1.73^{+1.15}_{-1.05} \times 10^{-10}, \tag{1.3}$$

based on results collected by the experiments E787 [8–11] and E949 [7, 12] at BNL. The new NA62 experiment at CERN [13, 14] is currently aiming to measure approximately 80 $K^+ \to \pi^+ \nu\bar{\nu}$ events over a period of two years, thus reducing the error on the branching ratio to around 10%. Data acquisition began in 2016, and an analysis of 10^{12} kaon decays collected so far is underway [15]. The initial goal of NA62 was to reduce the error on the CKM matrix parameter $|V_{td}|$; however additional physics goals include measuring $\mathrm{Br}\left(K^\pm \to \pi^\pm \ell^+ \ell^-\right)$ to greater accuracy than present, and putting constraints on lepton flavour violating decays such as $K^+ \to \pi^+ \mu^+ e^-$.

The decays $K_L \to \pi^0 \nu\bar{\nu}$ are particularly challenging to measure, given that all particles in the final state are neutral. The E391a experiment at KEK [16] previously set an upper bound for the branching ratio at

$$\mathrm{Br}\left(K_L \to \pi^0 \nu\bar{\nu}\right) \leq 2.6 \times 10^{-8} \,\text{at 90\% confidence level}. \tag{1.4}$$

At present there exists a dedicated experiment at J-PARC (KOTO) [17] to measure the $K_L \to \pi^0 \nu\bar{\nu}$ branching ratio. The KOTO experiment has reported one candidate $K_L \to \pi^0 \nu\bar{\nu}$ event so far based on an analysis of data collected in 2013 [18]. It is worth noting that there is no current plan to measure the decay $K_S \to \pi^0 \nu\bar{\nu}$, which is prohibitively difficult to detect.

On the other hand, the CP-conserving processes $K_S \to \pi^0 \ell^+ \ell^-$ and $K^+ \to \pi^+ \ell^+ \ell^-$, mediated predominantly via a single-photon exchange, are long-distance dominated [2, 19]. The reason for this is that the short-distance top quark contribution is suppressed by the CKM factor $\mathrm{Re}\left(\lambda_t\right)$ and even a potentially large light-quark short-distance contribution is cut off at the charm quark Compton wave length by a logarithmic GIM cancellation [2, 5]. Previous studies of these decays have been performed using chiral perturbation theory [20–23]. $K_L \to \pi^0\ell^+\ell^-$ decays however do have a significant short-distance component proportional to the CP-violating CKM parameter $\mathrm{Im}\left(\lambda_q\right)$. However they also contain an indirect CP-violating contribution due to neutral kaon oscillation [24]. There is significant interference between these two contributions; however it is not possible to determine from experiment whether the inteference is positive or negative. Because of the dominance of long-distance contributions in the decays $K_S \to \pi^0\ell^+\ell^-$ and $K^+ \to \pi^+\ell^+\ell^-$, there are no current estimates for the branching ratios of these processes from first principles. This hence motivates a lattice calculation of these amplitudes [19, 25].

On the experimental side, the branching ratios for $K^+ \to \pi^+\ell^+\ell^-$ processes are known to a high degree of accuracy [26, 27]:

$$\mathrm{Br}\left(K^+ \to \pi^+ e^+ e^-\right) = 3.14(10) \times 10^{-7}, \tag{1.5}$$

$$\mathrm{Br}\left(K^+ \to \pi^+ \mu^+ \mu^-\right) = 9.62(25) \times 10^{-8}, \tag{1.6}$$

which were measured at the CERN NA48/2 experiment. As NA62 increases the statistical precision of these branching ratios, the experiment may become sensitive to lepton flavour universality violation in rare kaon decays [28]. $K_S \to \pi^0\ell^+\ell^-$ decays however are more challenging to measure, although their detection is important for calculating the indirect CP-violating contribution to $K_L \to \pi^0\ell^+\ell^-$ decays via the chain $K_L \to K_1 \to \pi^0\ell^+\ell^-$, where K_1 is the CP-even component of K_L. The branching ratios are currently only known with $\sim 50\%$ errors [29, 30]:

$$\mathrm{Br}\left(K_S \to \pi^0 e^+ e^-\right) = \left(5.8^{+2.9}_{-2.4}\right) \times 10^{-9}, \tag{1.7}$$

$$\mathrm{Br}\left(K_S \to \pi^0 \mu^+ \mu^-\right) = \left(2.9^{+1.5}_{-1.2}\right) \times 10^{-9}. \tag{1.8}$$

Given the difficulty of the experimental measurement, there exists a good opportunity to extract this result instead from lattice QCD simulations. In addition, such a lattice calculation would determine the phase describing the interference between the indirect and direct CP-violating amplitudes, which cannot be determined from experimental measurements of $K_S \to \pi^0\ell^+\ell^-$ branching ratios. Neither NA62 nor KOTO aim to measure this decay, however LHCb are currently exploring the prospect of studying rare K_S decays after the next shutdown and upgrade [31].

In this thesis I will report on our exploratory studies of the rare kaon decays $K \to \pi\ell^+\ell^-$ [2] and $K \to \pi\nu\bar{\nu}$ [3, 32]. The main objective of these studies is to demonstrate the theoretical techniques of Refs. [19, 25, 33], such that the desired rare kaon decay matrix elements may be extracted from lattice QCD simulations. Secondly we can use these exploratory studies to evaluate the feasibility of a physical-point determination of the long-distance contributions to rare kaon decay amplitudes, such that comparisons may ultimately be made with experimental data.

The layout of this thesis is as follows. Chapters 2, 3 and 4 present much of the theoretical background required for this thesis. In chapter 2 we start with an introduction to the Standard Model, where I introduce many of the fundamental concepts required for this thesis. I begin in section 2.1 with a discussion of QCD and the weak interaction, and discuss their symmetries. Following this I introduce Fermi effective theory in section 2.2, which is required to study low-energy processes mediated by the weak interaction. Subsequently in section 2.3 I will introduce chiral perturbation theory, which has been used in previous studies of the long-distance contributions to rare kaon decays. In chapter 3 I provide a review of the current theoretical understanding of rare kaon decays, building on the discussions presented above. I will introduce the effective Hamiltonians required to study each decay at low energies in section 3.1. In section 3.2 I go on to review the current theoretical understanding of these decays, which so far has not included lattice QCD. Chapter 4 then introduces lattice QCD, where I will introduce the concepts behind the discretisation of QCD in section 4.1, as well as details of the numerical simulation in section 4.2. I then move onto an explanation of some of the technical details regarding the construction of correlation functions from our simulation data in section 4.3. I follow this by presenting a generic discussion of the analysis of correlation functions obtained from numerical simulations in section 4.4.

Chapter 5 then introduces the concepts required to study rare kaon decays using lattice QCD. I start in section 5.1 by showing how the operators introduced in chapter 3 translate into correlation functions that may be studied. The analysis of these correlation functions is then introduced in section 5.2. In this section I demonstrate a generic feature of the evaluation of four-point (4pt) correlators in Euclidean spacetime: the presence of intermediate states lighter than the initial particle state give rise to contributions which grow exponentially with the separation of the two operators involved in the 4pt correlator. I hence discuss the exponentially growing contributions that must be removed from our rare kaon decay correlators in order to obtain the desired matrix elements. In section 5.3 I discuss the renormalisation of each individual operator entering the 4pt correlators, as well as the regulation and removal of additional short-distance divergences caused by the contact of the two operators in the 4pt correlators.

At this point the theoretical stage is set, and I move on to a discussion of the results of our rare kaon decay simulations. In chapter 6 I begin with a discussion of our simulations of $K \to \pi\ell^+\ell^-$ amplitudes, which are conceptually simpler as short-distance divergences arising in our lattice simulation cancel automatically via the GIM mechanism. The simulation details and setup are discussed in sections 6.1 and 6.2 respectively. I then move onto a discussion of the numerical results in section 6.3, where I present a detailed analysis of the 4pt correlators. In section 6.4 I present a demonstrative calculation to show how our results might be compared to existing predictions of chiral perturbation theory. I then discuss the future plans for a physical point simulation in section 6.5. In chapter 7 I discuss the results of our $K \to \pi\nu\bar{\nu}$ simulations, where there is a short distance divergence that does not automatically cancel on the lattice. The regulation of this divergence must hence be converted into a continuum scheme. For this we choose the $\overline{\mathrm{MS}}$ scheme, such that we can combine the lattice result with existing results for the short-distance contributions to $K \to \pi\nu\bar{\nu}$ decays to obtain a finite result. The simulation details and setup are discussed in sections 7.1 and 7.2 respectively. The analysis of the lattice results is discussed in detail in section 7.3. In section 7.4 I present the steps required to match the lattice-regulated short-distance divergences in the 4pt correlators to the continuum $\overline{\mathrm{MS}}$ scheme, such that the final answer combining both long-distance lattice results and short-distance perturbative results is finite. Finally in chapter 8 I present my conclusions.

Chapter 2

Standard Model

The Standard Model of particle physics describes three of the four fundamental forces of nature: electromagnetism, and the weak and strong interactions; only gravity is missing. The theory is remarkably robust: barring the detection of neutrino masses, no new physics beyond the Standard Model has been confirmed since its inception. It is clear however that the theory requires extension, as there are many observed phenomena (besides gravity) that it does not explain. For example, the Standard Model does not contain a good dark matter candidate, which would explain the observed velocity distribution in galaxy rotation curves [34]. Additionally the amount of CP-violation in the Standard Model is not enough to satisfy the Sakharov conditions [35], necessary to produce the observed matter-antimatter asymmetry in the universe.

The Standard Model does however appear to be under direct strain in certain areas. There are many ongoing experimental efforts to make precision tests of the Standard Model in the hope of identifying the need for new physics, with the measurement of the anomalous magnetic moment of the muon $(g-2)$ being a particularly well-known example [36]. The current discrepancy between theory and experiment stands at $\sim 3.5\sigma$ [37]. Experiments at Fermilab [38] and J-PARC [39] aim to increase the experimental precision further, and on the theoretical side there are many efforts to reduce the hadronic uncertainties using lattice QCD [40–47].

Tensions also exist in flavour physics: many experimental results for B-meson decays show small deviations from the Standard Model. For example, LHCb has detected 3.5σ discrepancies in $B_s \to \phi\mu^+\mu-$ decays [48]. Further promising deviations have been found by in $B \to D\tau\nu_\tau$ and $B \to D^*\tau\nu_\tau$ decays, where there is a combined discrepancy of $\sim 4\sigma$ between Belle [49], BaBar [50] and LHCb [51] experiments.

In order to support the experimental efforts, it is important to be able to make accurate theoretical predictions using the Standard Model, such that any deviations may be quantified. In this chapter I will hence provide an introduction to the Standard Model, beginning with a cursory overview in section 2.1. This section will introduce standard textbook definitions; books such as Ref. [52] may be consulted for further details. Once the scene is set, I will introduce the details for more specified areas of physics required for this thesis. First I introduce the effective theory used to describe the weak interaction in section 2.2, which is required to analyse weak matrix elements involved in rare kaon decays at low scales $\mathcal{O}(1\,\mathrm{GeV})$ that are within reach of a lattice simulation. Secondly I will introduce chiral perturbation theory in section 2.3, which is a tool to analyse the low-energy dynamics of pseudoscalar mesons. This theory has been previously applied to study the rare kaon decays $K \to \pi\ell^+\ell^-$ that are dominated by low-energy hadronic effects, and to estimate the small long-distance corrections to $K \to \pi\nu\bar{\nu}$ amplitudes.

2.1 Particle Content and Interactions

The gauge group of the Standard Model is $SU(3) \times SU(2) \times U(1)$, with particle content as shown in Table 2.1. The gauge group encodes the fundamental forces of nature that the Standard Model describes. $SU(3)$ describes the strong force, QCD, and $SU(2)\times U(1)$ describes the electroweak interaction, which is broken to the subgroup $U(1)$ below the weak scale; this residual gauge symmetry describes electromagnetism. The spontaneous symmetry breaking of $SU(2)\times U(1) \to U(1)$ is described by the Higgs mechanism, which we will touch on briefly in section 2.1.2.1.

The matter content of the Standard Model is as follows. Firstly we have the fermion sector, of which we define two types: quarks and leptons. The quark sector is made up of three generations of “up-type” quarks (up, charm and top), and three generations of “down-type” quarks (down, strange and bottom). Quarks are the only particles in the Standard Model that interact via $SU(3)$; they additionally interact via the weak force and electromagnetism. The lepton sector is made up of three generations of leptons carrying electromagnetic charge (electron, muon, tau), along with corresponding neutrinos, which do not interact electromagnetically. Secondly we have the gauge sector: the strong interaction is mediated by gluons; the weak interaction by the W and Z bosons, and electromagnetism by the photon. The gluon and photon are massless, as their gauge interactions are unbroken in the Standard Model. Finally we have the scalar (or Higgs) sector, which contains only a single spin-0 particle: the Higgs boson. The W and Z bosons, leptons and quarks all acquire masses at low energies when the Higgs boson acquires a non-zero vacuum expectation value (VEV).

In the following section I will describe the various elements of the Standard Model in more detail which are central to this thesis. I will begin by discussing QCD and its symmetries, which are important preliminaries before we discuss the its discretisation in chapter 4. I will then go on to describe the electroweak interaction in more detail, which is responsible for the decays being studied in this thesis.

Name		$SU(3)$	$SU(2)$	$U(1)$	Spin
Quarks (×3 generations)	Q_i	$\mathbf{3}$	$\mathbf{2}$	$\frac{1}{6}$	$\frac{1}{2}$
	u_i	$\overline{\mathbf{3}}$	$\mathbf{1}$	$-\frac{2}{3}$	$\frac{1}{2}$
	d_i	$\overline{\mathbf{3}}$	$\mathbf{1}$	$-\frac{1}{3}$	$\frac{1}{2}$
Leptons (×3 generations)	L_i	$\mathbf{1}$	$\mathbf{2}$	$-\frac{1}{2}$	$\frac{1}{2}$
	e_i	$\mathbf{1}$	$\mathbf{1}$	1	$\frac{1}{2}$
Gluon	G	$\mathbf{8}$	$\mathbf{1}$	0	1
Electroweak bosons	W	$\mathbf{1}$	$\mathbf{3}$	0	1
	B	$\mathbf{1}$	$\mathbf{1}$	0	1
Higgs	H	$\mathbf{1}$	$\mathbf{2}$	$-\frac{1}{2}$	0

Table 2.1: Matter content of the Standard Model, along with representations and charges under the Standard Model gauge group $SU(3) \times SU(2) \times U(1)$. The index i on the fermion fields runs over the 3 generations.

2.1.1 QCD

QCD is the theory of the $SU(3)$ gauge interaction between quarks and gluons. The Lagrangian of QCD is given by

$$\mathcal{L}_{QCD} = -\frac{1}{4} G^a_{\mu\nu} G^{a\,\mu\nu} + \overline{q}_f \left(i \not{D} - m_f \right) q_f, \tag{2.1}$$

where in addition to Lorentz indices (greek indices), the index f runs over the six flavours of quark, q_f, and the index $a = 1, ..., 8$ runs over colour, i.e. an index for each generator of $SU(3)$. I have suppressed the colour and Dirac indices of the quark fields. The covariant derivative is given by

$$D_\mu = \partial_\mu + ig T^a A^a_\mu, \tag{2.2}$$

where T^a are the generators of the $SU(3)$ algebra and g is the QCD coupling. The gluon field strength tensor, $G^a_{\mu\nu}$, is defined by

$$G^a_{\mu\nu} = \partial_\mu A^a_\nu - \partial_\nu A^a_\mu + ig f^{abc} A^b_\mu A^c_\nu, \tag{2.3}$$

where A^a_μ is the gauge field of the gluon and f^{abc} are the $SU(3)$ structure constants [52].

2.1.1.1 Discrete Symmetries

Besides the $SU(3)$ gauge symmetry, there are global symmetries of QCD, which will be useful for lattice studies. QCD exhibits three discrete symmetries: charge conjugation (C), parity (P) and time-reversal (T). Each of these transformations may be written as unitary operators, transforming a field $\psi \rightarrow U\psi U^{\dagger}$. These symmetries are particularly important for working out the transformation properties of Dirac bilinears. I will hence summarise the effects of these symmetries below [52].

Charge conjugation involves transforming a particle into one with the opposite charge, i.e. its anti-particle. The momentum and spin of the particle are unchanged. The fermion fields transform as

$$\psi\left(x\right) \rightarrow -i\left(\overline{\psi}\left(x\right)\gamma^{0}\gamma^{2}\right)^{T}, \tag{2.4}$$

$$\overline{\psi}\left(x\right) \rightarrow -i\left(\gamma^{0}\gamma^{2}\psi\left(x\right)\right)^{T}. \tag{2.5}$$

Fermions are not eigenstates of charge conjugation (e.g. charge conjugation changes quark flavour); however we may construct Dirac bilinears that are indeed C eigenstates.

A parity transformation encodes a spacial reflection of a particle, i.e. transforming $x \rightarrow x^{P}$, with $x = (x_t, \mathbf{x})$ and $x^{P} = (x_t, -\mathbf{x})$. Parity therefore reverses the momentum of a particle, but does not affect the spin. Under such a transformation, the fermion fields transform as

$$\psi\left(x\right) \rightarrow \eta_{a}\gamma_{0}\psi\left(x_{P}\right), \tag{2.6}$$

$$\overline{\psi}\left(x\right) \rightarrow \eta_{a}^{*}\overline{\psi}\left(x_{P}\right)\gamma_{0}, \tag{2.7}$$

where η_a is a complex phase. Finally we have time-reversal, which is defined somewhat analogously to parity as $x \rightarrow x_T$, with $x_T = (-x_t, \mathbf{x})$. Time-reversal flips both the spin and momentum of a particle. The fermion fields transform as

$$\psi\left(x\right) \rightarrow \gamma_{1}\gamma_{3}\psi\left(x_{T}\right). \tag{2.8}$$

$$\overline{\psi}\left(x\right) \rightarrow -\overline{\psi}\left(x_{T}\right)\gamma_{1}\gamma_{3}. \tag{2.9}$$

Strictly speaking, time-reversal is an antiunitary operator. For the above transformations to hold, T must also act on c-numbers c as $Tc = c^{*}T$. For example, T acts on the time-evolution operator e^{iHt} as $Te^{iHt} = e^{-iHt}T$, effectively changing the sign of t [52].

From the transformations given above we see that the fermion fields are not eigenstates of these symmetries; however Dirac bilinears constructed from these fields are. Table 2.2 gives a summary of the transformation of Dirac bilinears under the transformations C and P. This will become particularly relevant when we consider the creation of QCD bound states. A pion for example is a pseudo-scalar particle, as such we may create a

State	J^{PC}	Γ
Scalar	0^{++}	$\mathbb{1},\ \gamma_0$
Pseudo-scalar	0^{-+}	$\gamma_5,\ \gamma_0\gamma_5$
Vector	1^{--}	$\gamma_i,\ \gamma_0\gamma_i$
Axial-vector	1^{++}	$\gamma_i\gamma_5$
Tensor	1^{+-}	$\gamma_i\gamma_j$

Table 2.2: Quantum numbers of Dirac bilinears of the form $\bar{\psi}\Gamma\psi$.

(positively-charged) pseudo-scalar state using

$$\overline{u}\left(x\right)\gamma_5 d\left(x\right)\left|0\right\rangle, \tag{2.10}$$

where u and d are the up- and down-quark fields respectively. The pion is therefore the lowest energy state that could be created by such an operator. We will revisit this point when we consider the interpolation of meson states in lattice simulations, in section 4.3.

We can also consider combinations of the C, P and T symmetries acting on fields. For example, we can construct a CP transformation by combining both C and P transformations. We remark that it is possible to write an additional term in the QCD Lagrangian that satisfies all the necessary symmetries as discussed in the previous section,

$$\frac{g}{32\pi^2}\theta G^a_{\mu\nu}\widetilde{G}^{a\,\mu\nu}, \tag{2.11}$$

where $\widetilde{G}^a_{\mu\nu}$, the dual field strength tensor, is defined as

$$\widetilde{G}^a_{\mu\nu} = \epsilon_{\mu\nu\rho\sigma}G^{a\,\rho\sigma}. \tag{2.12}$$

It is notable however that this term violates CP symmetry. However, the parameter θ is currently experimentally bound to be $\theta \ll 10^{-9}$ [37]. This is known as the strong CP problem [53, 54]. We do not however include this term in our lattice simulations, and thus we treat QCD to be CP-invariant.

One last important remark regarding these symmetries is that any Lorentz-invariant theory must be invariant under the full CPT symmetry transformation [55]. Hence CP violation is equivalent to T violation. This is an important result for cosmology; without a violation of time reversal it would not be possible to generate a matter-antimatter asymmetry in the universe [35].

2.1.1.2 Chiral Symmetry

Another symmetry that is highly relevant to QCD is chiral symmetry. A QCD-like theory with N_f flavours of massless quarks would have a global $SU\left(N_f\right)_L \times SU\left(N_f\right)_R \times U\left(1\right)_V \times U\left(1\right)_A$ global flavour symmetry group. However this is only true at the Lagrangian level; the $U\left(1\right)_A$ symmetry is anomalous (i.e. the path integral measure is not invariant under this symmetry) [52].

In QCD we observe light pseudoscalar states, but not light scalar states; from this observation we infer that the underlying dynamics of QCD spontaneously break this group down to $SU\left(N_f\right)_V$. In any case chiral symmetry is explicitly broken by quark masses, which mix the right- and left-handed components of Dirac spinors. However, the spontaneous breaking of chiral symmetry at low energies is much stronger than the explicit breaking by the quark masses. Consequently, the three lightest quarks u, d and s have masses small enough such that the QCD Lagrangian exhibits an approximate $SU\left(3\right)_L \times SU\left(3\right)_R$ flavour symmetry. This is the basis of chiral perturbation theory, which we will introduce in section 2.3.

In the case of u and d, we can consider the effect of taking $m_u = m_d$. In this limit there exists an $SU\left(2\right)_V$ flavour symmetry, which we call isospin. For computational reasons (which we will discuss later in section 4.3.2) it is worthwhile to perform lattice QCD simulations in the limit where isospin is a good symmetry; for many quantities the effects of isospin breaking produce effects of $\mathcal{O}\left(1\%\right)$ of isospin-conserving effects, hence may be much smaller than the statistical errors on observables obtained from lattice QCD simulations. In the isospin limit, the up and down quarks form doublets, i.e.

$$q = \begin{pmatrix} u \\ d \end{pmatrix}, \, \overline{q} = \begin{pmatrix} -\overline{d} \\ \overline{u} \end{pmatrix}. \tag{2.13}$$

We assign as isospin quantum number to the individual quarks corresponding to the I_3 component of isospin: $+1/2$ for u and $\overline{d}$, $-1/2$ for $\overline{u}$ and d.

We remark that in the Standard Model, quarks also interact electromagnetically; the different charges between the u and d quarks also leads to isospin-breaking. However, given that the electromagnetic coupling e is much smaller than the strong coupling g in this low energy regime, it too produces only small corrections to the overall QCD matrix elements, and thus up to a good precision we may also neglect electromagnetic effects. However it is important to note that modern lattice simulations are now able to compute QCD matrix elements with sub-percent level errors; for this reason the errors from neglecting isospin-breaking effects are becoming relevant. This is particularly true for quantities such as the anomalous magnetic moment of the muon [36] or the form factors involved in $K^+ \to \pi^0 \ell^+ \nu$ ($K_{\ell 3}$) decays [56, 57]. Some quantities, such as the proton-neutron mass splitting [58], are purely isospin-breaking effects, and thus this is currently a very active area of research in the lattice community [59–61].

2.1.1.3 Conserved Currents

Chiral symmetry is a continuous symmetry of the QCD action, and hence we can define a conserved current and charge in accordance with Noether's theorem [62]. Let us consider the infinitesimal variation of the QCD action under transformations of the form

$$\psi\left(x\right) \rightarrow \psi\left(x\right) + \delta\psi\left(x\right). \tag{2.14}$$

For example, the transformation corresponding to a vector symmetry is defined as

$$\delta\psi\left(x\right) = i\epsilon^{a}\lambda^{a}\psi\left(x\right), \quad \delta\overline{\psi}\left(x\right) = -i\overline{\psi}\left(x\right)\epsilon^{a}\lambda^{a}, \tag{2.15}$$

where $\epsilon^{a} \in \mathbb{R}$ is an infinitesimal parameter, and the matrices λ^{a} correspond to the group associated with the symmetry ($\lambda^{a} = \mathbb{1}$ for $U(1)$, or $\lambda^{a} = T^{a}$ for $SU\left(N_f\right)$). The full vector symmetry holds either for vanishing or degenerate quark masses; hence the $SU\left(2\right)_V$ isospin symmetry exists for $m_u = m_d$. It thus follows from Noether's theorem that we can define conserved currents associated to these symmetries,

$$J^{a}_{\mu}\left(x\right) = \overline{\psi}\left(x\right)\gamma_{\mu}\lambda^{a}\psi\left(x\right), \tag{2.16}$$

satisfying $\partial^{\mu}J^{a}_{\mu} = 0$. This is known as a Ward Identity [63, 64]. Note that the $U(1)_V$ symmetry holds for arbitrary quark masses; the corresponding conserved charge is baryon number.

Let us consider also the axial-vector (or chiral) transformations

$$\delta\psi\left(x\right) = i\epsilon^{a}\lambda^{a}\gamma_5\psi\left(x\right), \quad \delta\overline{\psi}\left(x\right) = i\overline{\psi}\left(x\right)\gamma_5\epsilon^{a}\lambda^{a}. \tag{2.17}$$

In the limit of massless quarks, Eq. (2.17) would be a good symmetry. It thus follows that the quantity $\partial^{\mu}A^{a}_{\mu}$ must be proportional to the quark masses. To show this more explicitly, we consider the variation of the action, S, and operators, $\mathcal{O}$, under this symmetry [65]. The starting point is the path integral, where the expectation value of the operator $\mathcal{O}$ is defined as

$$\langle\mathcal{O}\rangle = \int \mathcal{D}\left[\psi, \bar{\psi}, A\right]\mathcal{O}e^{iS}. \tag{2.18}$$

If we consider the variation of $\langle\mathcal{O}\rangle$ under the transformation Eq. (2.17), we obtain

$$-i\left\langle\delta S\mathcal{O}\right\rangle = \left\langle\delta\mathcal{O}\right\rangle, \tag{2.19}$$

where δS is the variation of the action under the axial transformation, and $\delta\mathcal{O}$ is the variation of $\mathcal{O}$. For the variation of the action we find

$$\delta S = \int d^4x\, \epsilon^a \left[-\partial_\mu A^a_\mu + \{M_q, P^a\} \right]. \tag{2.20}$$

with M_q being the quark mass matrix,

$$A^a_\mu = \overline{\psi}\,(x)\, \gamma^\mu \gamma_5 \lambda^a \psi\,(x) \tag{2.21}$$

being the partially-conserved axial current, and

$$P^a = \overline{\psi}\,(x)\, \gamma_5 \lambda^a \psi\,(x) \tag{2.22}$$

being the pseudoscalar density. This leads to an important result known as the partially conserved axial current (PCAC) relation, which (assuming degenerate quark masses of mass m) may be written as

$$\left\langle \partial^\mu A^a_\mu\,(x)\, \mathcal{O} \right\rangle = 2m \left\langle P^a\,(x)\, \mathcal{O} \right\rangle. \tag{2.23}$$

It is thus clear that in the limit of vanishing quark masses, this current is exactly conserved.

2.1.2 Electroweak Theory

While QCD corresponds to the $SU(3)$ gauge symmetry of the Standard Model, the $SU(2) \times U(1)$ gauge group corresponds to the electroweak interaction. This gauge group is notably broken down to $U(1)$ by the Higgs mechanism [66–68].

The Lagrangian for the electroweak interaction can be summarised as

$$\mathcal{L}_{EW} = \mathcal{L}_{gauge} + \mathcal{L}_{fermion} + \mathcal{L}_{Higgs} + \mathcal{L}_{Yukawa}. \tag{2.24}$$

In this section I will discuss the key features of this Lagrangian in turn. The first term describes the interaction of the gauge bosons themselves, i.e.

$$\mathcal{L}_{gauge} = -\frac{1}{4} W^a_{\mu\nu} W^{a\,\mu\nu} - \frac{1}{4} B_{\mu\nu} B^{\mu\nu}, \tag{2.25}$$

with

$$W^a_{\mu\nu} = \partial_\mu W^a_\nu - \partial_\nu W^a_\mu + \frac{i}{4} g_2 \epsilon^{abc} W^b_\mu W^c_\nu \tag{2.26}$$

being the field strength tensor corresponding to the $SU(2)$ group, and

$$B_{\mu\nu} = \partial_\mu B_\nu - \partial_\nu B_\mu \tag{2.27}$$

being the field strength tensor corresponding to $U(1)$. W_μ^a and g_2 are the gauge fields and coupling constant for $SU(2)$ respectively; similarly B_μ and g_1 (which will appear later) for $U(1)$. The Pauli matrices (σ_a) appearing in Eq. (2.26) are related to the generators of $SU(2)$ by $T^a = \sigma^a/2$. The generator for the $U(1)$ group is Y, the hypercharge. These generators satisfy

$$[T^a, Y] = 0. \tag{2.28}$$

The gauge bosons couple to the fermionic matter of the Standard Model, described by

$$\mathcal{L}_{fermion} = i\overline{Q}_j \not{D} Q_j + i\overline{u}_j \not{D} u_j + i\overline{d}_j \not{D} d_j + i\overline{L}_j \not{D} L_j + i\overline{e}_j \not{D} e_j, \tag{2.29}$$

where the index j runs over the 3 generations of the fermions. The quark contributions have been separated into 3 distinct terms: the first describes left-handed quark doublets

$$Q_i = \begin{pmatrix} u_L \\ d_L \end{pmatrix}, \begin{pmatrix} c_L \\ s_L \end{pmatrix}, \begin{pmatrix} t_L \\ b_L \end{pmatrix}, \tag{2.30}$$

plus singlets for the right-handed up-type and down-type quarks,

$$u_i = u_R, c_R, t_R, \tag{2.31}$$

$$d_i = d_R, s_R, b_R. \tag{2.32}$$

The lepton content is described by left-handed lepton doublets,

$$L_i = \begin{pmatrix} \nu_e \\ e_L \end{pmatrix}, \begin{pmatrix} \nu_\mu \\ \mu \end{pmatrix}, \begin{pmatrix} \nu_\tau \\ \tau \end{pmatrix}, \tag{2.33}$$

and right-handed singlets,

$$e_i = e_R, \mu_R, \tau_R. \tag{2.34}$$

The quantum numbers of these fermions under the $SU(2) \times U(1)$ gauge group are summarised in Table 2.1. The electroweak covariant derivative that appears in Eq. (2.29) is given by

$$D_\mu = \partial_\mu - \frac{i}{2} g_2 \sigma^a W_\mu^a - \frac{i}{2} g_1 Y B_\mu. \tag{2.35}$$

At low energies the $SU(2) \times U(1)$ group is broken down to $U(1)$; it must therefore be possible to construct the generator of $U(1)$, Q, from the components of the larger group.

We thus define

$$eQ = e\left(T_3 + \frac{Y}{2}\right), \tag{2.36}$$

where e is the electromagnetic coupling. The electromagnetic coupling cannot be immediately read off the Lagrangian; however it is possible to see if we perform a change of basis such that

$$\begin{pmatrix} B_\mu \\ W_\mu^3 \end{pmatrix} = \begin{pmatrix} \cos\theta_W & -\sin\theta_W \\ \sin\theta_W & \cos\theta_W \end{pmatrix} \begin{pmatrix} A_\mu \\ Z_\mu \end{pmatrix}. \tag{2.37}$$

We may thus identify A_μ as the massless photon, with a coupling

$$e = g_2 \sin\theta_W = g_1 \cos\theta_W. \tag{2.38}$$

θ_W is known as the Weinberg angle, and the quantity $\sin^2\theta_W$ has been determined experimentally to be 0.23120(15) [37].

2.1.2.1 Electroweak Symmetry Breaking

So far we have included all the necessary interactions in the electroweak Lagrangian, but have not accounted for any mass terms. It is not possible to write down gauge-invariant mass terms for the gauge fields or fermion fields. However, this may be remedied by introducing a new scalar field, H, which may generate the necessary masses via the Higgs mechanism.

The Lagrangian for the Higgs sector is given by

$$\mathcal{L}_{Higgs} = \frac{1}{2}\left(D_\mu H\right)^\dagger D^\mu H - V\left(H\right), \tag{2.39}$$

where the Higgs potential is defined as

$$V\left(H\right) = \lambda\left(H^\dagger H\right)^2 + \mu^2 H^\dagger H. \tag{2.40}$$

The scalar field, H, which we identity as the Higgs field, is an $SU\left(2\right)$ doublet,

$$H = \begin{pmatrix} h^+ \\ h^0 \end{pmatrix}, \tag{2.41}$$

which we would like to acquire a VEV

$$\langle H\rangle = \frac{1}{\sqrt{2}}\begin{pmatrix} 0 \\ v \end{pmatrix}. \tag{2.42}$$

We remark that $SU(2) \times U(1)$ transformations ensure that we can align the VEV in the direction shown, such that the electromagnetic group $U(1)$ with generator Q [Eq. (2.36)] will remain.

The $SU(2) \times U(1)$ group will be broken if we have $\mu^2 < 0$ in Eq. (2.40). The minima of this potential correspond to vacua with

$$v = \sqrt{\frac{-\mu^2}{\lambda}}. \tag{2.43}$$

We can subsequently rewrite our Lagrangian by redefining the Higgs field to be

$$H = h + v. \tag{2.44}$$

Any field that couples to the Higgs will thus gain a mass term associated with the Higgs VEV. For the gauge bosons, these originate from the kinetic term $(D_\mu H)^\dagger D^\mu H$; after spontaneous symmetry breaking the kinetic term may be written as $(D_\mu h)^\dagger D^\mu h$, and we gain the mass terms

$$\mathcal{L}_{Higgs} \supset \frac{g^2 v^2}{4} W^+ W^- + \frac{g^2 v^2}{8} \left(\frac{Z_\mu}{\cos\theta_W} \right)^2, \tag{2.45}$$

where we have defined $W^\pm = (W_1 \pm i W_2)/\sqrt{2}$. We can thus see that we have acquired the masses $M_W = g^2 v^2/4$ and $M_Z = M_W/\cos\theta_W$ for the W and Z fields respectively, while there is one remaining massless gauge field: the photon, A.

2.1.2.2 CKM Matrix

The final component of the electroweak Lagrangian Eq. (2.24) is the Yukawa sector. This sector is composed of couplings between fermions and the Higgs, such that fermions may acquire masses via the Higgs mechanism. The Yukawa Lagrangian is given by

$$\mathcal{L}_{Yukawa} = -y^l_{ij} \overline{L}_i H e_j - y^d_{ij} \overline{Q}_i H d_j - y^u_{ij} \overline{Q}_i \left(i\sigma^2 \right) H^* u_j + h.c., \tag{2.46}$$

where the indices i, j correspond to the three generations of fermions.

After electroweak symmetry breaking, the Yukawa couplings become

$$M_{ij} = \frac{v}{\sqrt{2}} y_{ij}. \tag{2.47}$$

For leptons, the weak eigenstates are the same as the mass eigenstates, and so the matrix M^L_{ij} must be diagonal. However for quarks the weak eigenstate basis is not equivalent to the mass eigenstate basis; to recover the correct mass terms for the quarks we therefore must change basis. We may thus write

$$q^i_{L/R} \to U^{ij}_{L/R} q^j_{L/R}, \tag{2.48}$$

$$M^q_{ij} = U_L m^q_{ij} U^\dagger_R, \tag{2.49}$$

where m^q_{ij} is the diagonal mass matrix for either up-type or down-type quarks,

$$m^q_{ij} = \begin{pmatrix} m_{u/d} & 0 & 0 \\ 0 & m_{c/s} & 0 \\ 0 & 0 & m_{t/b} \end{pmatrix}, \tag{2.50}$$

and U_L, U_R are the matrices corresponding to the change of basis.

We must be consistent with this change of basis across the full Lagrangian; the kinetic terms in Eq. (2.29) are unaffected by this transformation. Furthermore, the terms coupled to the fields Z_μ and A_μ are left invariant. The change is relevant only for the interaction terms between the $W^\pm$ bosons and quarks, i.e.

$$\frac{e}{\sqrt{2}\sin\theta_W} \overline{Q}_i \gamma^\mu W^+_\mu Q_i \to \frac{e}{\sqrt{2}\sin\theta_W} \overline{Q}_i \gamma^\mu W^+_\mu V_{ij} Q_j, \tag{2.51}$$

where

$$V = \left(U^u_L\right)^\dagger U^d_L \equiv \begin{pmatrix} V_{ud} & V_{us} & V_{ub} \\ V_{cd} & V_{cs} & V_{cb} \\ V_{td} & V_{ts} & V_{tb} \end{pmatrix} \tag{2.52}$$

is the Cabibbo-Kobayashi-Maskawa (CKM) matrix [69, 70]. The physical interpretation of this change of basis can hence be understood as follows. The quarks will propagate through space as their mass eigenstates; however the $SU(2)$ quark doublets that experience the weak interaction are superpositions of these mass eigenstates. We therefore find that the weak interaction is capable of changing the flavour of a quark. If neutrinos were massless, there would be no such mixing in the lepton sector: any linear combination of massless eigenstates is still massless, hence the weak and mass bases are equivalent. We now know that this is not true; the discovery of neutrino oscillation [71–73] implies that neutrinos do have masses in nature; the mass eigenstates are again not equivalent to the weak eigenstates. The PMNS matrix [74, 75] describes the mixing within the lepton sector.

We remark that the change of basis involved a unitary transformation, and thus the CKM matrix is also a unitary matrix. A 3×3 unitary matrix has a total of $3^2 = 9$ independent real parameters. We may reduce the number of parameters by absorbing five phases into the quark fields (one might naively expect six, although the sixth phase is an overall phase and does not change the form of the CKM matrix). Thus CKM matrix has four independent parameters, which we decompose into three real angles (θ_{12}, θ_{13}, θ_{23}) and one phase (δ). The PDG parametrisation of the CKM matrix is [76]

$$V_{CKM} = \begin{pmatrix} c_{12}c_{13} & s_{12}c_{13} & s_{13}e^{i\delta} \\ -s_{12}c_{23} - c_{12}s_{23}s_{13}e^{i\delta} & c_{12}c_{23} - s_{12}s_{23}s_{13}e^{i\delta} & s_{23}c_{13} \\ s_{12}s_{23} - c_{12}c_{23}s_{13}e^{i\delta} & -c_{12}s_{23} - s_{12}c_{23}s_{13}e^{i\delta} & c_{23}c_{13} \end{pmatrix}, \tag{2.53}$$

where we have used the notation $s_{ij} \equiv \sin\theta_{ij}$ and $c_{ij} \equiv \cos\theta_{ij}$. The complex phase that appears in this matrix is notable for being the only source of CP-violation in the Standard Model.

2.2 Fermi Effective Theory

The characteristic energy scale of QCD is $\Lambda_{QCD} = \mathcal{O}\left(200\,\mathrm{MeV}\right)$, i.e. the scale at which the theory becomes strongly coupled. At scales sufficiently above Λ_{QCD}, QCD may be treated perturbatively. For contrast, the typical scale of weak interactions is $\mathcal{O}\left(M_W\right)$, which is significantly above Λ_{QCD}. The highest scales in reach of a lattice simulation are typically $\mathcal{O}\left(2\,\mathrm{GeV}\right)$, at such scales it is not possible to resolve such heavy particles. We may thus proceed to "integrate out" these heavy degress of freedom: i.e. formally remove the heavy bosons of the weak interaction and heavy quarks as dynamical degrees of freedom and consider the appropriate low energy effective theory, where light quark interactions mediated by the exchange of heavy particles are described by local operators. The operator product expansion provides us with the theoretical framework to perform this task, which I introduce in this section.

2.2.1 Operator Product Expansion

The idea of the operator product expansion is to factorise out the high-energy (short-distance) and low-energy (long-distance) parts of the theory. Let us consider the example of the four-quark interaction describing a $qs \to qd$ transition [77, 78]. Example diagrams contributing to this transition are shown in Fig. 2.1. We would like to match the full theory of the weak interaction that describes this onto an appropriate effective theory. i.e.

$$A = \int d^4x \sum_i C_i\left(\mu\right) \left\langle Q_i^u\left(\mu\right) - Q_i^c\left(\mu\right)\right\rangle, \tag{2.54}$$

where the local operators Q_i^q ($q = u, c$) involving the active flavours of quarks are weighted by the Wilson coefficients C_i. We have introduced a dependence on the

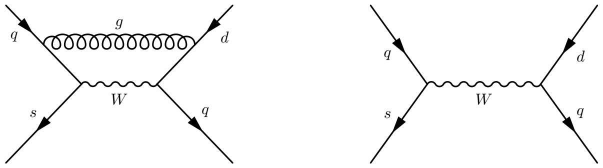

Figure 2.1: Diagrams giving rise to Q_1 and Q_2 (current-current) operators.

renormalisation scale μ, which is the characteristic scale separating the short- and long-distance regimes.

The short-distance behaviour is encoded within the Wilson coefficients, $C_i(\mu)$, which may be computed perturbatively as long as we keep the renormalisation scale μ sufficiently far above Λ_{QCD}. The long-distance behaviour is given by the matrix elements of local operators, $Q_i(\mu)$. We remark that the final amplitude must be independent of μ; this dependence therefore cancels between the Wilson coefficients and the matrix elements in the final result. For the example given here, we have two choices for Q_i which differ only by their colour structure, i.e.

$$Q_1^q = (\bar{s}_i q_j)_{V-A} \left(\bar{q}_j d_i\right)_{V-A}, \tag{2.55}$$

$$Q_2^q = (\bar{s}_i q_i)_{V-A} \left(\bar{q}_j d_j\right)_{V-A}, \tag{2.56}$$

where we have used the notation

$$(\bar{q}q)_{V\pm A} = \bar{q}\gamma_\mu (1 \pm \gamma_5)\, q. \tag{2.57}$$

The indices i, j are colour indices.

2.2.2 Calculation of Wilson Coefficients

The calculation of Wilson coefficients may be performed in perturbation theory at a scale $\mu \gg \Lambda_{QCD}$. The conventional choice of renormalisation scheme for the evaluation of Wilson coefficients is the $\overline{\text{MS}}$ scheme [77–79]. We encounter a problem however if we take $\mu \ll M_W$, as the perturbative calculation introduces terms with large logarithms. For example, while $\alpha_s(\mu)$ may be small, the combination $\alpha_s(\mu)\log\left(M_W^2/\mu^2\right)$ is not and thus the perturbative expansion breaks down. To avoid this, we will make use of renormalisation group improved perturbation theory. The renormalisation group describes the transformation between theories with different choices of renormalisation scale μ. By solving the renormalisation group equations and running from a high scale $\mu_W \simeq M_W$ to a low scale $\mu = \mathcal{O}(1\,\text{GeV})$, we sum the logarithmic terms to all orders in perturbation theory. For example, the leading logarithmic approximation (LLA) sums all terms of the form $\left(\alpha_s(\mu)\log\left(M_W^2/\mu^2\right)\right)^n$, $n \in [0, \infty)$; the next-to-leading logarithmic

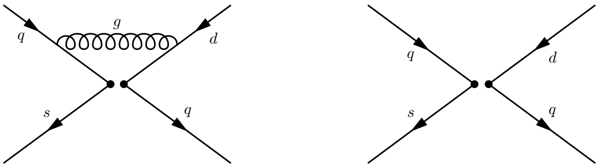

Figure 2.2: Example diagrams contributing to the calculation of Z_{ij}.

approximation (NLLA) extends this to terms of the form $\alpha_s(\mu)\left(\alpha_s(\mu)\log\left(M_W^2/\mu^2\right)\right)^n$, etc.

In the remainder of this section I will detail the evolution of the Wilson coefficients from the scale μ_W down to a scale accessible to lattice simulations. A more comprehensive description of this procedure may be found, for example, in Refs. [77, 78].

2.2.2.1 Operator Renormalisation and Mixing

We begin the calculation by computing the Wilson coefficients $C_i(\mu_W)$, which have been renormalised at a high scale μ_W. The first step is to compute the full Standard Model amplitude to the desired order in perturbation theory, which is achieved by computing diagrams such as in Fig. 2.1. This must be matched onto the amplitude computed in the effective theory (to the same order in perturbation theory), which contains the operators Q_1 and Q_2. This matching reveals an interesting feature of the calculation. When using the renormalised quark states and vertices, the Standard Model amplitude is finite. However in the equivalent calculation in the effective theory with renormalised quark states, where the W propagator has been "pinched" to a point [as in Fig. 2.2], it is divergent. As these divergences do not appear in the full theory, they must be properly regulated and removed. This necessitates an additional renormalisation condition for the operators,

$$\langle Q_i\rangle^b = Z_q^{-2} Z_{ij}\langle Q_j\rangle\,, \tag{2.58}$$

where we have included also the quark renormalisation $q^b = Z_q^{1/2} q$ (the superscript ^{b} indicates the bare, unrenormalised quantity). We remark that Z_{ij} is a matrix, and subsequently the operators Q_i are said to mix under renormalisation. In effect this means that divergences in the matrix element $\langle Q_1\rangle^b$ are regulated by those in the matrix element $\langle Q_2\rangle^b$ and vice versa, such that both renormalised matrix elements are finite. The Wilson coefficients are thus read off by equating the Standard Model amplitude to the effective theory amplitude, i.e. by setting

$$A = C_i Z_q^2 Z_{ij}^{-1}\langle Q_j\rangle^b\,. \tag{2.59}$$

It is also equivalent to consider a picture in which the Wilson coefficients are coupling constants in front of the bare operators within the effective theory. In such a picture it is these "couplings" that must be renormalised to absorb the divergences. The renormalisation condition in such a picture is thus

$$C_i^b = Z_{ij}^c\left(\mu\right) C_j\left(\mu\right). \tag{2.60}$$

These two interpretations are equivalent, and we find that they are related by

$$Z_{ij}^c = Z_{ji}^{-1}. \tag{2.61}$$

2.2.2.2 Renormalisation Group Evolution

At this stage we have the Wilson coefficients renormalised at a scale μ_W; we now must evolve them down to a lower scale μ at which hadronic matrix elements may be computed. The running of the renormalised Wilson coefficients may be obtained by solving the renormalisation group equations

$$\frac{d}{d\ln\mu} C_i\left(\mu\right) = \gamma_{ji}\left(\alpha_s\right) C_j\left(\mu\right), \tag{2.62}$$

where the anomalous dimension, γ, is defined as

$$\gamma_{ij} = Z_{ik}^{-1} \frac{d}{d\ln\mu} Z_{kj}, \tag{2.63}$$

using the renormalisation matrix Z_{ij} defined in Eq. (2.58). This equation may be solved up to some desired order in perturbation theory at a scale $\mu_W \simeq M_W$. We may write the solution in terms of an evolution matrix,

$$C_i\left(\mu\right) = U_{ij}\left(\mu, \mu_W\right) C_j\left(\mu_W\right), \tag{2.64}$$

where $U\left(\mu, \mu_W\right)$ encodes the renormalisation group running from a scale μ_W to a scale μ. The calculation of U thus requires solving

$$U_{ij}\left(\mu, \mu_W\right) = T_g \exp\left[\int_{g(\mu_W)}^{g(\mu)} dg' \, \frac{\gamma_{ij}\left(g'\right)}{\beta\left(g'\right)}\right], \tag{2.65}$$

order by order in perturbation theory, where the g-ordering operator T_g is defined as

$$T_g\, f\left(g_1\right), \ldots, f\left(g_n\right) = \sum_{perm} \Theta\left(g_{i_1} - g_{i_2}\right) \Theta\left(g_{i_2} - g_{i_3}\right) \ldots \Theta\left(g_{i_{n-1}} - g_{i_n}\right) f\left(g_1\right), \ldots, f\left(g_n\right), \tag{2.66}$$

with $\Theta(x-y)$ being the Heaviside step function and the sum runs over all permutations of g_i. The effect is such that in the Eq. (2.65) the coupling constants increase from right to left.

2.2.2.3 Flavour Boundaries

One more complication that arises in this calculation is the fact that we must integrate out heavy quarks as we evolve down to the desired scale. At a scale $\mu < m_b$, the b-quark no longer behaves like an explicit degree of freedom in the theory and thus may be integrated out. There thus exists a threshold at which we must match between a theory with 5 active quark flavours to one with 4 active flavours. At the very least this affects the running of α_s, hence must be taken into account regardless of the process we are computing. Depending upon how low we wish to run, we may also choose to integrate out the charm quark. We should be careful however, as the closer μ is to Λ_{QCD}, the poorer the perturbative description of the physics becomes. In general, the matching matrix M between a f and $f-1$ flavour theory is computed by imposing the condition

$$C_i^f\left(\mu_m\right)Q_i^f\left(\mu_m\right) = C_i^{f-1}Q_i^{f-1}\left(\mu_m\right) \tag{2.67}$$

at the matching scale μ_m.

2.3 Chiral Perturbation Theory

At low scales, the quarks and gluons of QCD are no longer useful degrees of freedom to consider; rather they form bound states: mesons and baryons. It is natural therefore to consider whether it is possible to create a low-energy effective theory of QCD, with hadronic degrees of freedom. In this section I introduce Chiral Perturbation Theory (ChPT), which is a low-energy effective description of the interactions of the pseudoscalar mesons in QCD. Useful reviews may be found in Refs. [80–82]. There are multiple applications of chiral perturbation theory for QCD; one useful feature is that it is possible to use ChPT results to extrapolate lattice results from unphysical meson masses to physical ones. Furthermore ChPT itself has some predictive power; the Lagrangian is written in terms of low-energy constants (LECs) that give the strength of the various interactions that one can write down. The LECs may only be determined by comparing ChPT calculations to either experimental or lattice QCD results. However ChPT may still make useful predictions if LECs can be measured from different processes or if it makes useful parametrisations for form factors that can be used as inputs for fits to experimental data. We do not directly use ChPT in this work; however ChPT is relevant to previous studies of long-distance contributions rare kaon decays, which will be discussed in section 3.2.

In section 2.1.1.2 we briefly introduced the concept of chiral symmetry and chiral symmetry breaking in QCD. The key observation is that the small masses of the u, d and s quarks imply that there exists an approximate $SU\left(3\right)_L \times SU\left(3\right)_R$ symmetry of the QCD Lagrangian, which is broken down to $SU\left(3\right)_V$ by QCD dynamics. This spontaneous symmetry breaking must necessarily result in Nambu-Goldstone bosons (NGBs); one for each of the broken symmetry generators of the residual symmetry. For QCD, these NGBs are the octet of the lightest pseudoscalar mesons, which we can write as

$$\phi = \begin{pmatrix} \frac{\pi_0}{\sqrt{2}} + \frac{\eta}{\sqrt{6}} & \pi^+ & K^+ \\ \pi^- & \frac{-\pi_0}{\sqrt{2}} + \frac{\eta}{\sqrt{6}} & K^0 \\ K^- & \overline{K}^0 & \frac{-2\eta}{\sqrt{6}} \end{pmatrix} \sim \begin{pmatrix} \overline{u}u & \overline{d}u & \overline{s}u \\ \overline{u}d & \overline{d}d & \overline{s}d \\ \overline{u}s & \overline{d}s & \overline{s}s \end{pmatrix} . \qquad (2.68)$$

This octet transforms as $\phi \to U\phi U^\dagger$, where $U \in SU\left(3\right)_V$. This symmetry is exact for degenerate quark masses. Furthermore in the limit of vanishing quark masses the meson states would be massless; however in nature the quark masses explicitly break axial vector symmetries, i.e. they explicitly break $SU(3)_L \times SU(3)_R$ as the left- and right-handed quarks transform differently (electromagnetism also breaks the flavour symmetry). The pseudoscalar mesons thus acquire masses, and hence they are referred to as pseudo-Nambu-Goldstone bosons (pNGBs). In reality, the pion has a rather small mass of $\sim 140\,\text{MeV}$, whereas the kaon has a much larger mass of $\sim 500\,\text{MeV}$. Because we have $m_s \gg m_d \simeq m_u$, we expect that $N_f = 3$ ChPT is naturally less accurate than $N_f = 2$ ChPT. Phenomenologically however, $N_f = 3$ ChPT is far more useful, as it has application to a much larger set of meson decays and interactions.

The pseudoscalar mesons in this octet are much lighter than other hadronic states. For example, the ρ meson is the next-heaviest meson, which has a mass of $m_\rho = 770\,\text{MeV}$. This suggests therefore that the characteristic scale of chiral symmetry breaking is on the order of $1\,\text{GeV}$; below this scale we may hence consider an effective theory in which this octet of pseudoscalar mesons are the only degrees of freedom. The Lagrangian of the effective theory is constructed using symmetry arguments; this "bottom-up" approach contrasts with the "top-down" approach of the operator product expansion presented in section 2.2. The effective Lagrangian must be invariant under chiral symmetry; which can be written in terms of the unitary field

$$\Sigma = \exp\left(\frac{2i\phi}{f}\right), \qquad (2.69)$$

where ϕ is the field defined in Eq. (2.68) and f is a dimensionful parameter such that ϕ has the canonical mass dimension of a scalar field, which can be identified as the pion decay constant. In order to write down a Lagrangian in terms of this field, note that we cannot have terms of the form $\Sigma\Sigma^\dagger = \mathbf{1}$. In general, to form a term that is both Lorentz and $SU\left(3\right)$ invariant, we must take the trace of products of derivatives of Σ and $\Sigma^\dagger$, and each term must have an equal number of derivatives of each. Because each term in the Lagrangian involves derivatives of the field, the amplitudes of the interactions they describe must vanish for vanishing external momenta. Hence the strength of the pseudoscalar meson interactions are proportional to the magnitude of the external momenta. We must identity the expansion parameter for the theory as (p/f), and only even powers appear in the expansion.

Before we write down the Lagrangian for ChPT, we must also understand how quark masses are introduced into the theory, given that they are forbidden by chiral symmetry. The general form for the quark mass terms is $\overline{q}Mq$, where M is a matrix with the quark masses m_d, m_u, m_s respectively on the diagonal. Instead of writing a mass term directly into the ChPT Lagrangian, we may introduce a new 'spurion' field χ, which transforms as

$$\chi \to U_L \chi U_R^\dagger, \quad \chi^\dagger \to U_R \chi^\dagger U_L^\dagger \tag{2.70}$$

under a chiral transformation. We thus recover the mass terms by setting $\chi = \chi^\dagger = 2B_0 M$. Here B_0 is some a priori unknown LEC. The Lagrangian of ChPT at leading order, $\mathcal{O}\left(p^2\right)$, is thus

$$\mathcal{L}_{eff}^{(2)} = \frac{1}{4} f^2 \text{Tr}\left(\partial_\mu \Sigma^\dagger \partial^\mu \Sigma\right) + \frac{1}{4} f^2 \text{Tr}\left(\chi^\dagger \Sigma + \Sigma^\dagger \chi\right). \tag{2.71}$$

We remark that this Lagrangian may be used to compute only tree level scattering amplitudes of pseudoscalar mesons. Higher order (loop) corrections enter at $\mathcal{O}\left(p^4\right)$ in the chiral expansion; for a consistent calculation at this order we must also consider the additional terms involving four derivatives that may enter the chiral Lagrangian, which effectively lead to new tree level contributions. We remark that the theory is renormalisable order by order; the additional tree level contributions introduced at $\mathcal{O}\left(p^4\right)$ act as counterterms to remove divergences from the loop corrections constructed from $\mathcal{L}_{eff}^{(2)}$.

In addition to describing hadronic interactions, we must encode weak and electromagnetic interactions into the chiral Lagrangian in order to describe (semi-)leptonic or non-leptonic weak decays involving the transition $s \to d$. Such a Lagrangian is therefore applicable to studies of the rare kaon decays $K \to \pi \ell^+ \ell^-$, which will be discussed in section 3.2.1. To lowest order, the weak contributions can be written as [20]

$$\mathcal{L}_{\Delta S=1}^{(2)} = \frac{G_F}{\sqrt{2}} V_{ud} V_{us}^* G_8 \left(L_\mu L^\mu\right)_{23}, \tag{2.72}$$

where

$$L_\mu = i f^2 \Sigma \partial_\mu \Sigma^\dagger, \tag{2.73}$$

and the subscript $_{23}$ indicates the relevant entry of the $SU(3)$ matrix (i.e. the entry corresponding to an $s \to d$ transition). This term thus describes the left-handed current of the weak interaction. Electromagnetism may be included as in the Standard Model via a $U(1)$ gauge interaction. We must therefore replace derivatives with their covariant counterparts, which generates the additional terms

$$\mathcal{L}_{EM}^{(2)} = -eA_\mu \mathrm{Tr}\left(\hat{Q}V^\mu\right) + e^2 A_\mu A^\mu \frac{1}{2} f^2 \left(1 - |\Sigma_{11}|^2\right), \tag{2.74}$$

where A_μ is the gauge field of the photon and $\hat{Q} = \mathrm{diag}\,(1,0,0)$ is the generator of the $U(1)$ interaction, the subscript $_{11}$ refers to the corresponding entry of the $SU(3)$ matrix, and

$$V_\mu = \frac{1}{2} i f^2 \left[\Sigma, \partial_\mu \Sigma^\dagger\right] \tag{2.75}$$

is the vector current matrix. This Lagrangian is relevant for studies of the hadronic contributions to $K \to \pi \ell^+ \ell^-$, which have been performed using ChPT up to $\mathcal{O}\left(p^4\right)$ [20].

Chapter 3

Phenomenology of Rare Kaon Decays

The rare kaon decays studied in this thesis are $K \to \pi\ell^+\ell^-$ and $K \to \pi\nu\bar{\nu}$. Phenomenologically these decays are interesting as they proceed via a flavour-changing neutral current (FCNC), i.e. a $s \to d$ transition. These decays are thus forbidden at tree level, and first arise only as second-order electroweak processes. The decay amplitudes for rare kaon decays are studied in an effective theory in which the weak bosons have been integrated out. This allows us to factorise the short-distance contributions, which may be treated in perturbation theory, from the long-distance, hadronic contributions. We can write rare kaon decay amplitudes in the general form

$$A = \int d^4x \sum_{A,B} \langle \pi\ell\bar{\ell}|T\left[\mathcal{O}_A^{\Delta S=1}(x)\,\mathcal{O}_B^{\Delta S=0}(0)\right]|K\rangle + \sum_L \langle \pi\ell\bar{\ell}|\mathcal{O}_L^{\Delta S=1}|K\rangle\,, \tag{3.1}$$

where the lepton ℓ will correspond to the decay being studied. The operators $\mathcal{O}$ will be specific to the process in question. We remark that matrix element is made up two distinct pieces: a local matrix element involving only local operators $\mathcal{O}_L$, and a bilocal matrix element involving the two operators $\mathcal{O}_A$ and $\mathcal{O}_B$, of which $\mathcal{O}_A$ must contain a $s \to d$ transition. It should be noted that the local hadronic matrix element relevant to these decays is equivalent to the one involved in $K^+ \to \pi^0\ell^+\nu$ ($K_{\ell 3}$) decays in the isospin-symmetric limit, and is known accurately from experiment and existing lattice results [56, 57]. Hence in cases where the bilocal matrix element does not provide a large contribution, we require only a perturbative calculation to calculate the Wilson coefficient of the local operator. We describe these decays as being short-distance dominated. In contrast, if it is the bilocal matrix element that gives the dominant contribution, then the decay is said to be long-distance dominated.

In this chapter, I will review the theoretical status of rare kaon decays. I will begin in section 3.1 with a discussion of the underlying theory of the effective weak Hamiltonians

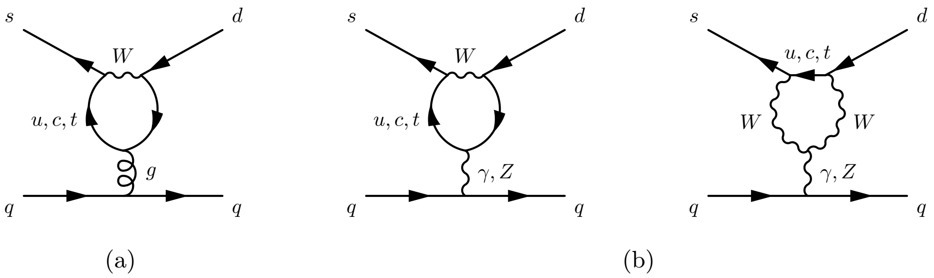

Figure 3.1: Penguin diagrams that give rise to (a) $Q_{3,..,6}$ and (b) $Q_{7,...,10}$.

that are relevant for studying these decays. These Hamiltonians are important for the lattice calculations we perform, and will allow us to write down the rare kaon decay amplitudes in terms of bilocal and local matrix elements. Once this theory has been established, I will move onto a discussion of previous theoretical work on rare kaon decays in section 3.2. This involves work on $K \to \pi\ell^+\ell^-$ decays using ChPT in section 3.2.1, and work on $K \to \pi\nu\bar{\nu}$ decays in section 3.2.3 that primarily involves perturbation theory.

3.1 Effective Hamiltonians for Rare Kaon Decays

In this section I introduce the effective Hamiltonians used to study rare kaon decays. This will give insight into the dominant processes in each of the decays being studied. I will start by introducing the $\Delta S = 1$ Hamiltonian, that is relevant for both $K \to \pi\ell^+\ell^-$ and $K \to \pi\nu\bar{\nu}$. I will then discuss the remainder of the weak Hamiltonians needed to study $K \to \pi\ell^+\ell^-$ decays and $K \to \pi\nu\bar{\nu}$ in turn.

3.1.1 $\Delta S = 1$ Weak Hamiltonian

The first Hamiltonian we will discuss is the $\Delta S = 1$ weak Hamiltonian [77], which describes four-quark interactions with a $s \to d$ transition. The Hamiltonian may be summarised as

$$H_W^{\Delta S=1} = \frac{G_F}{\sqrt{2}} V_{us}^* V_{ud} \left(\sum_{i=1}^{2} C_i(\mu) \left(Q_i^u(\mu) - Q_i^c(\mu) \right) + \sum_{i=3}^{10} C_i(\mu) Q_i(\mu) \right), \tag{3.2}$$

where I have assumed the renormalisation scale $\mu > m_c$ such that there are four active flavours of quark. The operators relevant to $H_W^{\Delta S=1}$ are as follows [77]

$$Q_1^q = (\bar{s}_i q_j)_{V-A}\, (\bar{q}_j d_i)_{V-A} = (\bar{s}d)_{V-A}\, (\bar{q}q)_{V-A}\,, \tag{3.3}$$
$$Q_2^q = (\bar{s}q)_{V-A}\, (\bar{q}d)_{V-A}\,, \tag{3.4}$$
$$Q_3 = (\bar{s}d)_{V-A} \sum_q (\bar{q}q)_{V-A}\,, \tag{3.5}$$
$$Q_4 = (\bar{s}_i d_j)_{V-A} \sum_q (\bar{q}_j q_i)_{V-A} = \sum_q (\bar{s}q)_{V-A}\, (\bar{q}d)_{V-A}\,, \tag{3.6}$$
$$Q_5 = (\bar{s}d)_{V-A} \sum_q (\bar{q}q)_{V+A}\,, \tag{3.7}$$
$$Q_6 = (\bar{s}_i d_j)_{V-A} \sum_q (\bar{q}_j q_i)_{V+A} = -2 \sum_q (\bar{s}q)_R\, (\bar{q}d)_L\,, \tag{3.8}$$
$$Q_7 = (\bar{s}d)_{V-A}\, e_q \sum_q (\bar{q}q)_{V-A}\,, \tag{3.9}$$
$$Q_8 = (\bar{s}_i d_j)_{V-A}\, e_q \sum_q (\bar{q}_j q_i)_{V-A} = e_q \sum_q (\bar{s}q)_{V-A}\, (\bar{q}d)_{V-A}\,, \tag{3.10}$$
$$Q_9 = (\bar{s}d)_{V-A}\, e_q \sum_q (\bar{q}q)_{V+A}\,, \tag{3.11}$$
$$Q_{10} = (\bar{s}_i d_j)_{V-A}\, e_q \sum_q (\bar{q}_j q_i)_{V+A} = -2e_q \sum_q (\bar{s}q)_R\, (\bar{q}d)_L\,. \tag{3.12}$$

Where relevant we have used Fierz identities [83] to group quarks of the same colour indices together in the round brackets. The quark q in the operators $Q_{1,2}^q$ is an up-type quark, i.e. up and charm. Of course in a theory where we evolve to a scale $\mu < m_c$ where the charm no longer appears as an active degree of freedom, the operators $Q_{1,2}^c$ are not present. These operators arise through current-current diagrams as shown in Fig 2.1. For the remaining operators $Q_{1,\ldots,10}$, the sum over q runs over all active quark flavours. $Q_{3,..,6}$ arise through QCD penguins, through diagrams shown in Fig. 3.1(a). $Q_{7,\ldots,10}$ are electromagnetic penguins analogous to $Q_{3,\ldots,6}$, arising through diagrams shown in Fig. 3.1(b). Note we are using the definition from Eq. (2.57) in addition to

$$(\overline{q}q)_L = \overline{q}\,(1-\gamma_5)\,q, \tag{3.13}$$
$$(\overline{q}q)_R = \overline{q}\,(1+\gamma_5)\,q. \tag{3.14}$$

3.1.1.1 Wilson Coefficients

It is helpful to use the unitarity of the CKM matrix,

$$\lambda_u + \lambda_c + \lambda_t = 0; \quad \lambda_q = V_{qd}V_{qs}^*, \tag{3.15}$$

to eliminate λ_c and write the Wilson coefficients as

$$\vec{C}\left(\mu\right)=\vec{z}\left(\mu\right)+\tau\vec{y}\left(\mu\right), \tag{3.16}$$

with [37]

$$\tau=-\frac{\lambda_t}{\lambda_u}\simeq\left(1.5-0.6i\right)\times10^{-3}. \tag{3.17}$$

Hence the up-quark loop contributions are contained within z, top quark-loop contributions within y, and the charm contributions are split between the two. Notably, CP-violating contributions will be proportional to y. The running of the Wilson coefficients down to the 4-flavour theory is described by

$$\vec{v}\left(\mu\right)=U^4\left(\mu,\mu_b\right)M\left(\mu_b\right)U^5\left(\mu_b,\mu_W\right)\vec{v}\left(\mu_W\right), \tag{3.18}$$

where the superscripts indicate the number of active flavours. We may additionally choose to integrate out the charm quark; in such a case we must also consider the running

$$\vec{v}^3\left(\mu\right)=U^3\left(\mu,\mu_c\right)M\left(\mu_c\right)\vec{v}\left(\mu_c\right), \tag{3.19}$$

$$\vec{z}^3\left(\mu\right)=U^3\left(\mu,\mu_c\right)M\left(\mu_c\right)\vec{z}\left(\mu_c\right), \tag{3.20}$$

where we have defined $\vec{v}\left(\mu\right)=\vec{z}\left(\mu\right)+\vec{y}\left(\mu\right)$.

For the time being we will work in the 4-flavour theory, which is the theory we have used for our studies of rare kaon decays to date [2, 3, 32]. In general we find that the operators Q_1^q and Q_2^q provide the largest contributions as the Wilson coefficients for these operators are substantially larger than those of the other operators. The primary reason for the this is that the Wilson coefficients of the operators $Q_{3,\ldots,10}$ are suppressed by the GIM mechanism [5]. This involves a cancellation between the charm and up loop contributions, such that only terms proportional to their masses remain. To understand this fully, we must consider the QCD- and photon-penguins separately to the Z penguin contribution to $C_{3,\ldots,10}$.

For the QCD- and photon-penguins, the calculation of the Wilson coefficients features a logarithmic GIM mechanism [5], i.e. the loop function will depend logarithmically on the quark masses. The heavier quark contributions will therefore not be particularly enhanced with respect to the light quark contributions. For CP-conserving processes, the top quark loop contributions are suppressed by CKM matrix elements. In the contribution from Z-penguins, the presence of a quadratic GIM mechanism (from axial component of the Z boson current) enhances the heavy quark contributions, and particularly the top quark contribution. However these contributions are suppressed because

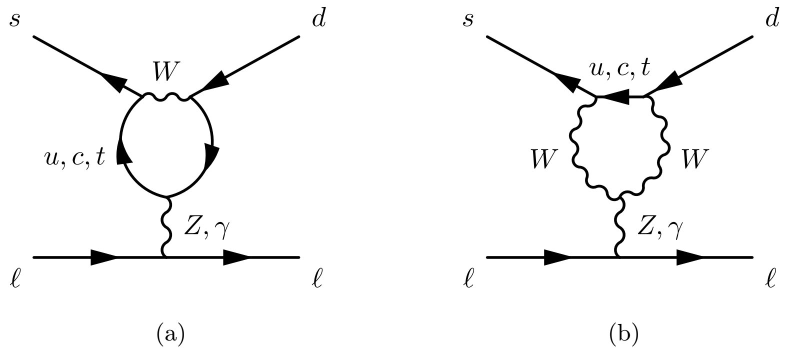

Figure 3.2: Penguin diagrams that gives contributions to the effective $s \to d\ell\bar{\ell}$ vertex in rare kaon decays. When $\ell = \nu$, there is no photon penguin diagram.

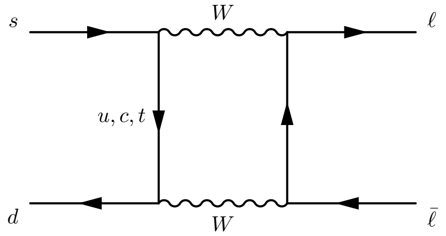

Figure 3.3: Box diagrams that give contributions to the effective $s \to d\ell\bar{\ell}$ vertex.

of the Z boson's weak coupling. In studies of rare kaon decays with four flavours, the operators $Q_{3,\ldots,10}$ hence may be neglected entirely.

In the 3-flavour theory with $\mu < m_c$, the charm contribution is contained only in the Wilson coefficients, not the operators. We expect there may be a small contribution coming from the operators $Q_{3,\ldots,6}$, as the Wilson coefficients do not vanish by the GIM mechanism in this regime. The operators $Q_{7,\ldots,10}$ may still be safely neglected, as they are suppressed by a factor of α/α_s with respect to $Q_{3,\ldots,6}$, which already provide a subleading contribution to the amplitude.

3.1.2 Hamiltonian for $K \to \pi\ell^+\ell^-$

In this section I will discuss how the amplitudes for the decays $K \to \pi\ell^+\ell^-$ may be written in the form of Eq. (3.1), i.e. made up of a bilocal and local matrix element. For the CP-conserving decays $K^+ \to \pi^+\ell^+\ell^-$ and $K_S \to \pi^0\ell^+\ell^-$, the dominant contributions come from the single photon exchange channel. There are additional short-distance contributions from Z-penguins seen in Fig. 3.2 and W-W box diagrams seen in Fig. 3.3, although these are suppressed by the weak coupling and hence may be neglected. These decays will be the target of our lattice calculation, and so I will discuss the construction of the relevant weak Hamiltonian here.

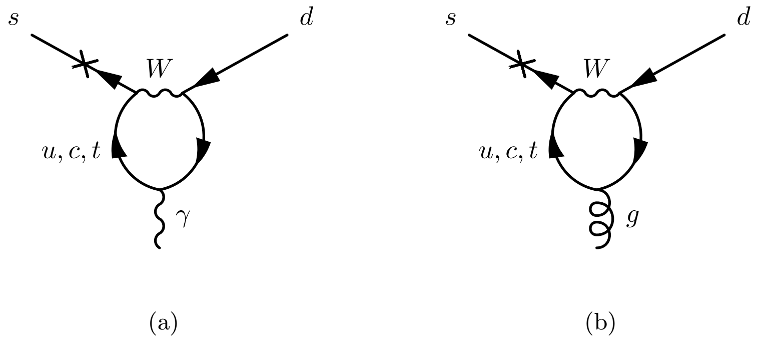

Figure 3.4: Diagrams associated with (a) electromagnetic and (b) chromomagnetic penguin operators respectively. The cross indicates a mass insertion.

The weak Hamiltonian relevant to $K^+, K_S \to \pi\ell^+\ell^-$ amplitudes is given by

$$H_W = H_W^{\Delta S=1} + H_W^{FCNC}, \tag{3.21}$$

where $H_W^{\Delta S=1}$ [Eq. (3.2)] is described in the previous section, and we introduce the short-distance Hamiltonian [77]

$$H_W^{FCNC} = \frac{G_F}{\sqrt{2}} V_{us}^* V_{ud} \left(C_{7V}\left(\mu\right) Q_{7V}\left(\mu\right)\right), \tag{3.22}$$

where

$$Q_{7V} = \left(\bar{s}d\right)_{V-A} \left(\bar{\ell}\ell\right)_V, \tag{3.23}$$

The operator Q_{7V} arises via penguin diagrams shown in Fig. 3.2. The inclusion of this new operator introduces an important feature of the renormalisation-group running of the Wilson coefficient C_{7V}: one must account for the mixing of the bilocal contributions into the local contribution. We must therefore include the operator

$$Q_\gamma = \sum_q e_q \left(\bar{q}q\right)_V \left(\bar{\ell}\ell\right)_V, \tag{3.24}$$

where e_q is the electric charge of a quark q, which is the operator that describes the emission of the photon from a quark. For the Wilson coefficient we have $C_\gamma = 1$, which is a consequence of the Ward-Takahashi identity [63, 64]. We may hence construct a bilocal operator, $\mathcal{B}_\gamma$, using the operators Q_i within $H_W^{\Delta S=1}$,

$$B_\gamma = -i \int d^4x\, T\left[Q_\gamma\left(0\right) Q_i\left(x\right)\right], \tag{3.25}$$

and the corresponding Wilson coefficient is thus given by C_i. The running of the Wilson coefficients C_i is unaffected by the inclusion of Q_{7V}.

We remark that for the QCD-specific component of these amplitudes, it is sufficient to consider the transition $K \to \pi\gamma^*$; we will therefore be interested in the operator

$$Q_{7V}^{\mu} = \bar{s}\gamma^{\mu}\left(1-\gamma_5\right)d, \tag{3.26}$$

such that

$$Q_{7V} = Q_{7V}^{\mu}\left(\bar{\ell}\ell\right)_V. \tag{3.27}$$

It is also worth noting that we could also consider the contribution of the operators [77, 84]

$$Q_{7\gamma} = \frac{e}{8\pi^2}m_s\bar{d}_i\sigma^{\mu\nu}\left(1+\gamma_5\right)s_iF_{\mu\nu}, \tag{3.28}$$

$$Q_{8G} = \frac{g}{8\pi^2}m_s\bar{d}_i\sigma^{\mu\nu}\left(1+\gamma_5\right)T^a_{ij}s_jG^a_{\mu\nu}. \tag{3.29}$$

The operators $Q_{7\gamma}$ and Q_{8G} are electro- and chromo-magnetic operators respectively, which are associated with diagrams such as in Fig. 3.4. These operators are negligible for these decays: the Wilson coefficients are small (owing to GIM suppression), and the contributions are additionally suppressed by the factor of the strange mass. Furthermore, they do not affect the running of the other operators within Eq. (3.21).

To understand the importance of the contributions of each of the operators that make up Eq. (3.21), the arguments are similar to those presented in section 3.1.1.1. The operators Q_1 and Q_2 provide the dominant contributions. In a 4-flavour theory the local operator Q_{7V} may be neglected, as the lighter quark contributions to C_{7V} are GIM suppressed and the top quark contribution is CKM suppressed. Hence in the four flavour theory, the relevant weak Hamiltonian is simply

$$H_W^{4,V} = \frac{G_F}{\sqrt{2}}V_{us}^*V_{ud}\left(\sum_{i=1}^{2} z_i\left(\mu\right)\left(Q_i^u\left(\mu\right) - Q_i^c\left(\mu\right)\right)\right). \tag{3.30}$$

The relevant amplitude corresponding to the $K \to \pi\gamma^*$ transition is hence described by matrix elements of bilocal operators Eq. (3.25).

However a 3-flavour calculation of $K \to \pi\ell^+\ell^-$ is also possible; for such a calculation it would be prudent to also include the operators $Q_{3,\ldots,6}$. The operator Q_{7V} will also be important in the context of the 3-flavour theory. Above the charm scale, we neglect the operator for the reasons given above. Below the charm scale its Wilson coefficient receives significant contributions from the charm quark. This point will be revisited in section 6.5. The weak Hamiltonian that is relevant for a calculation of the contributions to $K \to \pi\ell^+\ell^-$ decays with three active flavours is therefore

$$H_W^{3,V} = \frac{G_F}{\sqrt{2}}V_{us}^*V_{ud}\left(\sum_{i=1}^{2} z_i\left(\mu\right)Q_i^u\left(\mu\right) + \sum_{i=3}^{6}C_i\left(\mu\right)Q_i\left(\mu\right) + C_{7V}\left(\mu\right)Q_{7V}\left(\mu\right)\right). \tag{3.31}$$

Recalling Eq. (3.1), the operators $Q_{1,\ldots,6}$ enter into the bilocal contribution; the remaining operator Q_{7V} gives the local contribution.

3.1.3 Hamiltonian for $K \to \pi\nu\bar{\nu}$

In the discussion in the previous section, I argued that Z-exchange [Fig. 3.2] and box amplitudes [Fig. 3.3] could be neglected for $K \to \pi\ell^+\ell^-$, as the γ-exchange amplitudes gave the dominant contributions. For studies of $K \to \pi\nu\bar{\nu}$ this is not the case, as neutrinos do not couple to the photon. The weak Hamiltonian relevant for a calculation of $K \to \pi\nu\bar{\nu}$ decays with 4 active flavours is [79]

$$H_W = H_W^{\Delta S=1} + H_W^Z + H_W^{WW} + H_W^{\nu}, \tag{3.32}$$

where each component of the Hamiltonian will be introduced in the following section.

Under a renormalisation group analysis, there is no mixing between the box amplitude and Z-exchange, hence the calculation naturally splits into two distinct parts. The analysis of the Z-exchange amplitude is similar to the γ-exchange analysis presented in the previous section. Again we require the operators within $H_W^{\Delta S=1}$; and it is sufficient to consider only Q_1 and Q_2, as the contributions of the remaining operators are negligible. Additionally to construct the bilocal operator we require

$$H_W^Z = \frac{\pi\alpha}{M_W^2 \sin^2\theta_W} C_Z(\mu)\, Q_Z(\mu)\,. \tag{3.33}$$

The Hamiltonian H_W^Z contains the operator describing the coupling of quarks to neutrinos mediated by a Z-exchange,

$$Q_Z = \sum_q \left(I_3^q - 2e_q \sin^2\theta_W\right) Q_V^q - I_3^q Q_A^q, \tag{3.34}$$

where I_3^q is the 3rd component of the weak isospin for the quark q (1/2 and -1/2 for up- and down-type quarks respectively), and

$$Q_V^q = (\bar{q}q)_V\, (\bar{\nu}\nu)_{V-A}\,, \tag{3.35}$$

$$Q_A^q = (\bar{q}q)_A\, (\bar{\nu}\nu)_{V-A}\,. \tag{3.36}$$

Again it may be noted that $C_Z(\mu) = 1$, which follows from the Ward-Takahashi identity and the Adler-Bardeen theorem [79, 85]. Hence we may construct the relevant bilocal operator to be

$$B_Z = -i \int d^4x\, T\left[Q_Z(0)\, Q_i(x)\right], \tag{3.37}$$

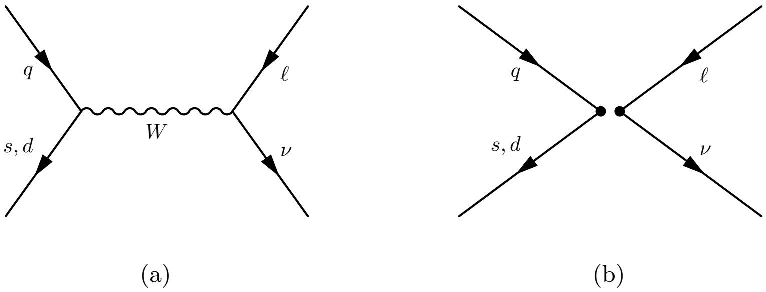

Figure 3.5: (a) Diagrams that give rise to $Q_{\ell q}^{\Delta S=1}$ (s) and $Q_{\ell q}^{\Delta S=0}$ (d), resulting in the local operators shown in (b).

where again the relevant Wilson coefficient is given by C_i. Similar to the γ-exchange amplitude, it should be noted that for the QCD contribution to the Z-exchange amplitude we need consider only the effective $s \to dZ^*$ vertex, hence the relevant operators are

$$Q_V^{q\mu} = \bar{q}\gamma^\mu q, \tag{3.38}$$

$$Q_A^{q\mu} = \bar{q}\gamma^\mu \gamma_5 q. \tag{3.39}$$

For the W-W box contribution to $K \to \pi\nu\bar{\nu}$, the relevant Hamiltonian is

$$H_W^{WW} = \frac{G_F}{\sqrt{2}} \sum_{q=u,c} \sum_{\ell=e,\mu,\tau} \left(V_{qd} Q_{\ell q}^{\Delta S=0} + V_{qs}^* Q_{\ell q}^{\Delta S=1} \right) \tag{3.40}$$

where

$$Q_{\ell q}^{\Delta S=0} = \left(\bar{d}q\right)_{V-A} \left(\bar{\nu}_\ell \ell\right)_{V-A}, \tag{3.41}$$

$$Q_{\ell q}^{\Delta S=1} = \left(\bar{s}q\right)_{V-A} \left(\bar{\nu}_\ell \ell\right)_{V-A}. \tag{3.42}$$

These operators correspond to the diagrams in Fig. 3.5. These operators do not mix and are independent of μ; the Wilson coefficients are hence equal to one. The W-W bilocal operator with an intermediate lepton ℓ is therefore

$$B_{WW,\ell} = -i \int d^4x \, T\left[Q_{\ell q}^{\Delta S=0}(0)\, Q_{\ell q}^{\Delta S=1}(x)\right]. \tag{3.43}$$

Finally, there is the contribution of the local effective Hamiltonian

$$H_W^\nu = \frac{G_F}{\sqrt{2}} \frac{\alpha}{2\pi \sin^2\theta_W} \sum_{\ell=e,\mu,\tau} C_\nu(\mu)\, Q_\nu(\mu), \tag{3.44}$$

where

$$Q_\nu = (\bar{s}d)_{V-A} (\bar{\nu}\nu)_{V-A} \tag{3.45}$$

is the local operator that describes a $s \to d\nu\bar{\nu}$ vertex. The Wilson coefficient $C_\nu(\mu)$ may be decomposed as

$$C_\nu(\mu) = \lambda_c X_c^\ell(x_c) + \lambda_t X_t(x_t), \tag{3.46}$$

$\lambda_q = V_{qs}^* V_{qd}$, $x_q = m_q^2/M_W^2$, and X_q is the loop function associated with the quarks $q = c, t$. The superscript ℓ indicates a dependence on the lepton mass; however this dependence is negligible for the top quark contribution. For the charm quark there is a non-negligible dependence on the tau mass. The loop function X_q depends quadratically upon the mass of the quark, hence X_t makes up the dominant contribution to the decay amplitude.

3.2 Theoretical Progress

In this section I will review the existing theoretical progress on the decays $K \to \pi\ell^+\ell^-$ and $K \to \pi\nu\bar{\nu}$, which has not so far involved a dedicated lattice QCD calculation. I will hence identify the areas where lattice QCD can help to further these existing efforts.

3.2.1 $K_S, K^+ \to \pi\ell^+\ell^-$

For the CP-conserving decays $K^+ \to \pi^+\ell^+\ell^-$ and $K_S \to \pi^0\ell^+\ell^-$, each process is dominated by a single photon exchange transition ($K \to \pi\gamma^*$). Electromagnetic gauge invariance allows us to write down the matrix element in terms of a single invariant form factor, $V(z)$:

$$A = -\frac{G_F\,\alpha}{4\pi} V(z) (p_K + p_\pi)^\mu\, \overline{u}_\ell(p_{\ell^+}) \gamma_\mu \nu_\ell(p_{\ell^-}), \tag{3.47}$$

where p_n, $n = K, \pi, \ell^+, \ell^-$ are the 4-momenta of the particles involved in the decay, $z = q^2/M_K^2$, and $q = p_K - p_\pi$. Previous work on the rare kaon decays $K^+ \to \pi^+\ell^+\ell^-$ and $K_S \to \pi^0\ell^+\ell^-$ has been performed using effective theories such as $SU(3)$ ChPT. One previous ChPT inspired phenomenological analysis of the form factor [21] has led to a parametrization of the form

$$V_i(z) = a_i + b_i z + V_i^{\pi\pi}(z), \tag{3.48}$$

where $V_i^{\pi\pi}(z)$ $((i = +, 0))$ is introduced to account for $\pi\pi \to \gamma^*$ rescattering in $K \to \pi\pi\pi$ decays arising through the diagram show in Fig. 3.6. One opportunity of a lattice

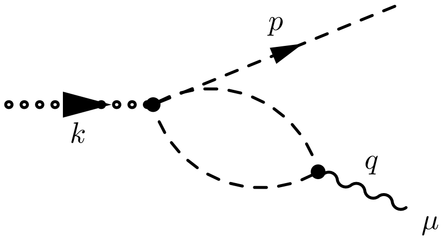

Figure 3.6: The one-loop contribution to the decays $K \to \pi\gamma^*$ arising as $\pi\pi \to \gamma^*$ rescattering in $K \to \pi\pi\pi$ decays.

calculation would be to test the relation Eq. (3.48) by determining the constants a_i and b_i from simulation data. Experimentally the coefficients a_+ and b_+ have been determined from $K^+ \to \pi^+\ell^+\ell^-$ spectra: $a_+ = -0.578(16)$ and $b_+ = -0.779(66)$ from $K^+ \to \pi^+e^+e^-$ data [26] and $a_+ = -0.575(39)$ and $b_+ = -0.813(145)$ from $K^+ \to \pi^+\mu^+\mu^-$ data [27]. For the K_S decay, by assuming vector meson dominance ($a_S/b_S = 1/r_V^2$, $r_V = M_\rho/M_K$) [21] the magnitude of a_0 has been determined to be $|a_0| = 1.06^{+0.26}_{-0.21}$ for the electron [29] and $|a_0| = 1.54^{+0.40}_{-0.32}$ for the muon [30].

The parametrisation of Eq. (3.48) is expected to be a good approximation to the $\mathcal{O}\left(p^6\right)$ ChPT form factor. It is already well known that existing $\mathcal{O}\left(p^4\right)$ ChPT predictions [20] for the parameter b_i do not correctly predict experimental observations [21, 22]. Analysis of this decay in ChPT up to $\mathcal{O}\left(p^4\right)$ gives the following predictions for the coefficients a_i and b_i [21],

$$a_+ = \frac{G_8}{G_F}\left(\frac{1}{3} - w_+\right), \qquad a_0 = -\frac{G_8}{G_F}\left(\frac{1}{3} - w_0\right), \tag{3.49}$$

$$b_+ = -\frac{G_8}{G_F}\frac{1}{60}, \qquad b_0 = \frac{G_8}{G_F}\frac{1}{60}, \tag{3.50}$$

where w_i are defined in terms of $SU(3)$ LECs $N_{14}^r(\mu)$, $N_{15}^r(\mu)$ and L_9^r as

$$w_+ = \frac{64\pi^2}{3}\left(N_{14}^r(\mu) - N_{15}^r(\mu) + 3L_9^r(\mu)\right) + \frac{1}{3}\ln\left(\frac{\mu^2}{M_K M_\pi}\right), \tag{3.51}$$

$$w_0 = \frac{32\pi^2}{3}\left(N_{14}^r(\mu) + N_{15}^r(\mu)\right) + \frac{1}{3}\ln\left(\frac{\mu^2}{M_K^2}\right), \tag{3.52}$$

for some renormalization scale μ. The coefficient b_i depends only on the LEC G_8, which can be determined using information from $K \to \pi\pi$ decay amplitudes [86]. A comparison with the experimental result thus demonstrates that large corrections must be expected at $\mathcal{O}\left(p^6\right)$. Models that go beyond $\mathcal{O}\left(p^4\right)$ ChPT in an attempt to make predictions for b_i have been proposed [22, 23], although such models depend heavily on vector meson masses and thus a comparison with lattice data would be difficult.

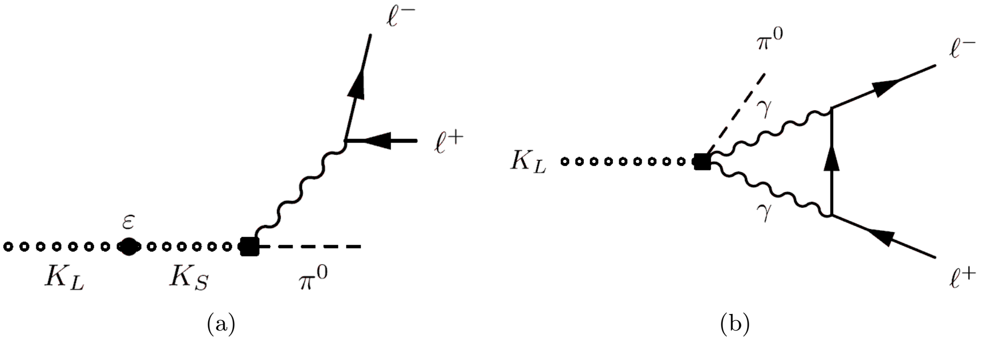

Figure 3.7: The contributions to $K_L \to \pi\ell^+\ell^-$ decays from (a) indirect CP-violation via kaon oscillation and (b) a CP-conserving 2-photon exchange.

3.2.2 $K_L \to \pi^0\ell^+\ell^-$

The decays $K_L \to \pi^0\ell^+\ell^-$ contain a large direct CP-violating contribution proportional to the CKM parameter $\mathrm{Im}\,(\lambda_t)$, hence are predominantly short distance dominated. To describe the short-distance contribution, the relevant weak Hamiltonian is

$$H_W = \frac{G_F}{\sqrt{2}} V_{us}^* V_{ud} \left(\sum_{i=1}^{6,7V} C_i\,(\mu)\, Q_i\,(\mu) + \tau y_{7A}\,(M_W)\, Q_{7A}\,(M_W) \right), \tag{3.53}$$

where we have introduced the new operator

$$Q_{7A} = (\bar{s}d)_{V-A}\,\left(\bar{\ell}\ell\right)_A, \tag{3.54}$$

which arises through Z-penguin diagrams such as those seen in Fig. 3.2, and box diagrams shown in Fig. 3.3. These diagrams of course also involve the operator Q_{7V} owing to the $V-A$ structure of the weak interaction. Note how it is emphasised that we only need to consider the top contribution to the operator Q_{7A}. Furthermore, Q_{7A} does not mix with the other operators and its Wilson coefficient is μ-independent [77].

Additionally, there exists an indirect CP-violating contribution arising from kaon oscillation [4], which may be written as

$$A\left(K_L \to \pi^0\ell^+\ell^-\right) \supset \epsilon A\left(K_S \to \pi^0\ell^+\ell^-\right), \tag{3.55}$$

where ϵ is the indirect CP-violating parameter for the kaon system. This contribution is also shown diagramatically in Fig. 3.7(a). There also exists a significant CP-conserving contribution from $K_L \to \pi^0\gamma\gamma$ through $\gamma\gamma \to \ell^+\ell^-$ scattering, as shown in Fig. 3.7(b).

The CP-violating contributions to $K_L \to \pi^0\ell^+\ell^-$ may be summarised as [24, 87, 88]

$$\mathrm{Br}\left(K_L \to \pi^0 e^+ e^-\right)_{CPV} = \left[15.6\,|a_0|^2 \pm 6.2\,|a_0|\left(\frac{\mathrm{Im}\,(\lambda_t)}{10^{-4}}\right) + 2.4\left(\frac{\mathrm{Im}\,(\lambda_t)}{10^{-4}}\right)\right] \times 10^{-12}, \tag{3.56}$$

$$\mathrm{Br}\left(K_L \to \pi^0 \mu^+ \mu^-\right)_{CPV} = \left[3.7\,|a_0|^2 \pm 1.6\,|a_0|\left(\frac{\mathrm{Im}\,(\lambda_t)}{10^{-4}}\right) + 1.0\left(\frac{\mathrm{Im}\,(\lambda_t)}{10^{-4}}\right)\right] \times 10^{-12}, \tag{3.57}$$

where the term $|a_0|$ originates from Eq. (3.48). Assuming a positive interference, we find [4]

$$\mathrm{Br}\left(K_L \to \pi^0 e^+ e^-\right)_{CPV} = 3.1\,(0.9) \times 10^{-11}, \tag{3.58}$$

$$\mathrm{Br}\left(K_L \to \pi^0 \mu^+ \mu^-\right)_{CPV} = 1.4\,(0.5) \times 10^{-11}. \tag{3.59}$$

Lattice QCD may hence play a role in calculating the long-distance contributions to the amplitude $A\left(K_S \to \pi^0\ell^+\ell^-\right)$, which (as discussed above) is dominated by long-distance processes. Furthermore, a lattice calculation would also be able to determine the sign of the interference between these two contributions, given that it cannot be extracted from experimental data.

3.2.3 $K^+ \to \pi^+\nu\bar{\nu}$

$K \to \pi\nu\bar{\nu}$ decays are some of the theoretically cleanest FCNC processes, because of presence of the quadratic GIM mechanism, which helps to enhance the top quark contributions. The full body of theoretical work involves using short-distance Wilson coefficients calculated in perturbation theory [79, 89–91], and using ChPT to estimate the long-distance corrections [92].

Previous theoretical work on this decay is based mostly in perturbation theory, where the charm is integrated out and the majority of the hadronic contributions can be described by the local short-distance Hamiltonian Eq. (3.44). In practice, the Wilson coefficients that make up Eq. (3.32) are evolved down to a scale $\mu = \mathcal{O}(m_c)$ using renormalisation group techniques; then an OPE is performed to integrate out the charm quark. In effect, this amounts to writing the matrix element of the bilocal operators in terms of the tree-level local matrix element (denoted by the superscript $^{(0)}$) using

$$\int d^4x \left\langle T\left[Q_A Q_B\right]\right\rangle(\mu) = r_{AB}(\mu)\left\langle Q_\nu\right\rangle^{(0)}, \tag{3.60}$$

where the two operators Q_A and Q_B appearing in the bilocal operator are those specific to either the Z-exchange amplitude [Eq. (3.37)] or the W-W box amplitude [Eq. (3.43)], and have corresponding Wilson coefficients C_A and C_B. The overall bilocal contribution to the amplitude may therefore be written as

$$C_A(\mu)\, C_B(\mu)\, r_{AB}(\mu)\, \langle Q_\nu \rangle (\mu)\,. \tag{3.61}$$

It should be noted that the bilocal operator contribution involving up quarks is neglected in this treatment. The quantities r_{AB} have been computed to NNLO [79].

It is useful to introduce the phenomenological parameter

$$P_c^{SD}(X) = \frac{1}{\lambda^4}\left(\frac{2}{3}X_c^e(x_c) + \frac{1}{3}X_c^\tau(x_c)\right), \tag{3.62}$$

where $\lambda = |V_{us}|$, which is the short-distance charm quark contribution. This piece has been calculated in RG-improved perturbation theory to NNLO [6, 79, 90]. Additionally ChPT has been used to estimate the correction [92]

$$\delta P_{c,u} = 0.04(2), \tag{3.63}$$

which describes the long-distance contributions involving charm and up quark loops not accounted for in Eq. (3.44). The full charm quark contribution is thus

$$P_c = P_c^{SD} + \delta P_{c,u}. \tag{3.64}$$

With the parameter P_c we may write the full contribution to the branching ratio

$$\mathrm{Br}(K \to \pi\nu\bar{\nu}) = \kappa_+ \left[\left(\frac{\mathrm{Im}(\lambda_t)}{\lambda^5}X_t(x_t)\right)^2 + \left(\frac{\mathrm{Re}(\lambda_t)}{\lambda^5}X_t(x_t) + \frac{\mathrm{Re}(\lambda_c)}{\lambda}P_c\right)^2\right], \tag{3.65}$$

where

$$\kappa_+ = r_{\kappa_+}\frac{3\alpha^2\mathrm{Br}\left(K^+ \to \pi^0 e^+ \nu\right)}{2\pi^2 \sin^4\theta_W}\lambda^8, \tag{3.66}$$

and r_{κ_+} encodes the isospin corrections in relating $\mathrm{Br}(K \to \pi\nu\bar{\nu})$ to $\mathrm{Br}\left(K^+ \to \pi^0 e^+ \nu\right)$. We remark that the up quark contribution has been absorbed into P_c and X_t in this definition, and unitarity of the CKM matrix (i.e. $\lambda_u + \lambda_c + \lambda_t = 0$) has been used to eliminate λ_u.

A very recent theoretical prediction for this branching ratio at NNLO is [6]

$$\mathrm{Br}(K \to \pi\nu\bar{\nu}) = 9.11(72) \times 10^{-11}, \tag{3.67}$$

where the majority of the error originates from uncertainties in input SM parameters. It should also be noted that the long distance correction $\delta P_{u,c}$ provides a ~ 6% contribution to the branching ratio; the error on this quantity translates into a 3% uncertainty. This error however has only been roughly estimated [92], and thus a rigorous approach to this part of the calculation (e.g. using lattice QCD) is necessary to properly control this source of error. One advantage of a lattice QCD calculation is that the bilocal charm quark contribution may be computed directly, and so the step given in Eq. (3.60) is not performed. Ultimately this means that a higher renormalisation scale $\mu \gg m_c$ may be used for the perturbative parts of the calculation, the results of which are more reliable at higher scales.

3.2.4 $K_L \to \pi^0 \nu\overline{\nu}$

The decay $K_L \to \pi^0 \nu\overline{\nu}$ is the theoretically cleanest rare kaon decay channel, which is completely dominated by a direct CP-violating amplitude involving top-quark loops. The calculation of the branching ratio for this decay is similar to that discussed in the previous section, and is given by

$$\mathrm{Br}\left(K_L \to \pi^0 \nu\bar{\nu}\right) = \kappa_L \left(\frac{\mathrm{Im}\left(\lambda_t\right)}{\lambda^5} X_t\left(x_t\right)\right)^2, \tag{3.68}$$

where κ_L is similar to κ_+ [Eq. (3.66)] and contains the remaining factors such as $\mathrm{Br}\left(K^+ \to \pi^0 e^+ \nu\right)$, with isospin corrections relevant for the uncharged decay. A very recent estimate of this branching ratio is [6]

$$\mathrm{Br}\left(K_L \to \pi^0 \nu\bar{\nu}\right) = 3.00(30) \times 10^{-11}, \tag{3.69}$$

where again the majority of the error is parametric, and mostly due to the uncertainty of the CKM factor $\mathrm{Im}\left(\lambda_t\right)$.

Chapter 4

Lattice QCD

At low energies QCD is strongly coupled, which means that it is impossible to use perturbative techniques to directly analyse the theory in this regime. Few techniques exist for this task; in this chapter I will introduce the method used in this thesis: lattice QCD. Lattice QCD involves discretising the fermion and gauge fields and simulating their interactions in a finite spacetime box by means of large-scale computer simulations. The ultimate aim of lattice simulations is to calculate correlation functions, from which physical observables may be extracted. In continuum quantum field theory, correlation functions may be computed via path integrals, e.g.

$$\langle 0|\mathcal{O}_1(x_1)\ldots\mathcal{O}_n(x_n)|0\rangle = \frac{1}{Z}\int\mathcal{D}\left[A,\psi,\overline{\psi}\right]\mathcal{O}_1(x_1)\ldots\mathcal{O}_n(x_n)\,e^{iS}, \tag{4.1}$$

where S is the action of the theory and Z is the partition function, defined as

$$Z = \int\mathcal{D}\left[A,\psi,\overline{\psi}\right]e^{iS}. \tag{4.2}$$

To simulate QCD we hence formulate it on a Euclidean lattice, and discretise each step in this procedure.

In this chapter I will introduce the standard numerical techniques that we employ in our simulations of rare kaon decays. A more comprehensive review of lattice QCD may be found in texts such as Refs. [93, 94]. In section 4.1 I will discuss the discretisation of the lattice action, then in section 4.2 I will discuss the numerical methods required to solve the path integral by means of Monte Carlo simulations. Subsequently in section 4.3 I will describe how correlation functions are constructed from simulation data. In section 4.4 I will then introduce techniques to analyse these correlation functions such that physical observables may be extracted from simulations.

4.1 Lattice Formulation of QCD

In this section, I will introduce the formalism required to put QCD on the lattice. To achieve this, we must replace the continuum fields and derivatives by the discrete counterparts, in such a way that the lattice action is still invariant under the necessary gauge transformations.

4.1.1 Discretisation of Spacetime

The first stage of the discretisation procedure is to demote the continuous, infinite spacetime to a finite spacetime lattice, which we usually choose to be of size $L^3 \times T$, where L is the number of sites in each spatial direction and T is the number of sites in the time direction. Typically we take $T \simeq 2L$. This discretisation of spacetime imposes two explicit scales on the theory: an infra-red cutoff related to the size of the lattice, L, and an ultra-violet cutoff related to the lattice spacing, a. In order to accurately simulate QCD, we require

$$\frac{1}{L} \ll \Lambda_{QCD} \ll a^{-1}. \tag{4.3}$$

The first of these conditions is required to suppress finite-volume effects; the second to suppress discretisation errors [94].

4.1.2 Gauge Interactions

Let us now consider the gauge transformation for a fermion field, $\psi\left(x\right)$. In the continuum, the action is invariant under the transformation,

$$\psi\left(x\right) \rightarrow \psi'\left(x\right) = \Omega\left(x\right)\psi\left(x\right), \, \overline{\psi}\left(x\right) \rightarrow \overline{\psi}'\left(x\right) = \overline{\psi}\left(x\right)\Omega^{\dagger}\left(x\right), \tag{4.4}$$

for some $SU\left(3\right)$ gauge transformation $\Omega\left(x\right)$. Furthermore, terms involving the covariant derivative $D_\mu\psi\left(x\right)$ [Eq. (2.2)] must transform in the same way. We require these relations to hold on a discrete lattice also.

On the lattice, we replace the derivative by its finite-difference counterpart, i.e. $\partial_\mu \rightarrow \Delta_\mu$. There are multiple possibilities for the finite-difference derivative; here we will demonstrate the symmetrised difference, which acts on the fermion field as

$$\Delta_\mu\psi\left(x\right) = \frac{\psi\left(x + a\hat{\mu}\right) - \psi\left(x - a\hat{\mu}\right)}{2a}, \tag{4.5}$$

where $\hat{\mu}$ indicates a unit vector in the direction corresponding to μ. This approximates the true numerical derivative up to $\mathcal{O}\left(a^2\right)$. The gauge transformation for the fermion fields remains as before; however now we have the issue that terms of the form $\overline{\psi}(x)\,\psi(x+a\hat{\mu})$ in the action are not gauge invariant, i.e.

$$\overline{\psi}(x)\,\psi(x+a\hat{\mu}) \to \overline{\psi}(x)\,\Omega^{\dagger}(x)\,\Omega(x+a\hat{\mu})\,\psi(x+a\hat{\mu}) \neq \overline{\psi}(x)\,\psi(x+a\hat{\mu})\,. \tag{4.6}$$

To remedy this, we introduce the link variable $U_{\mu}(x)$ [95], which transforms as

$$U_{\mu}(x) \to \Omega(x)\,U_{\mu}(x)\,\Omega^{\dagger}(x+a\hat{\mu})\,. \tag{4.7}$$

The index μ on the link variable $U_{\mu}(x)$ can be interpreted such that the link joins a site x with a site $x+a\hat{\mu}$. We remark that these link variables are $SU(3)$ matrices, as opposed to the Lie Algebra valued fields A_{μ} that we use in the continuum. Indeed the link variables can be related to the continuum gauge field A_{μ}. The continuum counterpart of the link variable is the gauge transporter: the path-ordered integral of the gauge field along some curve connecting two points x and y. The lattice link variables may be related to the gauge fields using

$$U_{\mu}(x) = e^{igaA_{\mu}(x)}, \tag{4.8}$$

which is a valid approximation at $\mathcal{O}(a)$, i.e. for a path connecting adjacent lattice sites where no path-ordering is required. With these link variables, a term such as $\overline{\psi}(x)\,U(x)\,\psi(x+a\hat{\mu})$ will now have the correct transformation properties. We remark that the gauge links are oriented depending upon whether the direction is taken to be forward or backward, and so we have

$$U_{\mu}^{\dagger}(x-a\hat{\mu}) = U_{-\mu}(x)\,, \tag{4.9}$$

where the $-\mu$ index implies that the link joins the site x with the site $x-a\hat{\mu}$.

We can use the link variable $U(x)$ to write down gauge invariant terms that may appear in the lattice action. In general, we can construct a gauge invariant term by connecting two fermion fields with link variables, or by making a closed loop out of link variables (a Wilson loop). We can therefore write down the lattice covariant derivative as

$$D_{\mu}\psi(x) = \frac{U_{\mu}(x)\,\psi(x+a\hat{\mu}) - U_{-\mu}(x)\,\psi(x-a\hat{\mu})}{a}, \tag{4.10}$$

which we can use to construct the fermionic part of the action. The simplest term that may appear in the gauge action is known as the plaquette,

$$P_{\mu\nu}(x) = U_{\mu}(x)\,U_{\nu}(x+a\hat{\mu})\,U_{\mu}^{\dagger}(x+a\hat{\nu})\,U_{\nu}^{\dagger}(x)\,, \tag{4.11}$$

which is the shortest Wilson loop (i.e. a square of side length one); the trace of this quantity is gauge invariant and thus may appear in the action.

The simplest possible gauge action is thus

$$S_{gauge} = \frac{2}{g^2}\sum_x \sum_{\mu<\nu} \mathrm{Re}\left(\mathrm{Tr}\left[1 - P_{\mu\nu}(x)\right]\right) \tag{4.12}$$

$$= \frac{a^4}{2g^2}\sum_x \sum_{\mu<\nu} \mathrm{Tr}\left[G_{\mu\nu}(x)\, G^{\mu\nu}(x)\right] + \mathcal{O}\left(a^2\right), \tag{4.13}$$

where g is the QCD gauge coupling and $G_{\mu\nu}$ is the gluon field strength tensor. This action thus reproduces the continuum Yang-Mills action up to terms of $\mathcal{O}\left(a^2\right)$. More refined choices for the gauge action may result in lattice actions which agree up to higher order discretisation effects, such as the renormalisation-group improved Iwasaki [96, 97] and doubly-blocked Wilson (DBW2) actions [98, 99],

$$S_G = \frac{2}{g^2}\left(\sum_x \mathrm{Re}\left[\sum_{\mu<\nu}\left(1 - 8c_1\right) P^{1\times1}_{\mu\nu} + c_1 \sum_{\mu\neq\nu} P^{1\times2}_{\mu\nu}\right]\right), \tag{4.14}$$

where $P^{1\times1}_{\mu\nu}$ is the plaquette term shown in Eq. (4.11), and $P^{1\times2}_{\mu\nu}$ contains all the rectangular and "L-shaped" loops. The Iwasaki action corresponds to the choice $c_1 = -0.331$; the DBW2 action to $c_1 = -1.4069$.

4.1.3 Naive Fermion Discretisation

Using the definition of the covariant derivative in Eq. (4.10), we could write down the action for a fermion of mass m to be

$$S_{ferm}\left(\psi, \overline{\psi}, U\right) = a^4 \sum_x \overline{\psi}(x)\, D(x,y)\, \psi(y), \tag{4.15}$$

where we have defined the Dirac operator as

$$D(x,y) = \sum_\mu \gamma^\mu \frac{U_\mu(x)\,\delta_{x+a\hat{\mu},y} - U_{-\mu}\delta_{x-a\hat{\mu},y}}{2a} + m\delta_{x,y}. \tag{4.16}$$

However, we will show how this choice leads to the famous fermion doubling problem. To demonstrate this, we will consider the propagator for a free fermion (i.e. we set $U_\mu(x) = 1$). Computing the Fourier transform of the Dirac operator, we find

$$\tilde{D}(p) = m + \frac{i}{a}\sum_\mu \gamma_\mu \sin\left(p^\mu a\right). \tag{4.17}$$

On a finite lattice, the entries of the 4-momentum p^μ are restricted to lie in the first Brillouin zone, i.e. $-\pi/a < p^\mu \leq \pi/a$. The Dirac operator can subsequently be inverted to find

$$\tilde{D}^{-1}(p) = \frac{m - ia^{-1}\sum_{\mu}\gamma_{\mu}\sin(p^{\mu}a)}{m^2 + a^{-2}\sum_{\mu}\sin^2(p^{\mu}a)}. \tag{4.18}$$

Considering the massless limit, we find that the propagator

$$\tilde{D}^{-1}(p)\bigg|_{m=0} = -ia\frac{\sum_{\mu}\gamma_{\mu}\sin(p^{\mu}a)}{\sum_{\mu}\sin^2(p^{\mu}a)} \overset{a\to 0}{\to} -i\frac{\not{p}}{p^2}, \tag{4.19}$$

has the correct continuum limit. The free continuum propagator can be seen to have a pole at $p^{\mu} = (0,0,0,0)$. However, on the lattice there also exist poles at the edges of the Brillouin zone, i.e. where some (or all) entries of p^{μ} are π/a, and the rest zero. This leads to $2^4 = 16$ poles in total; these additional 15 fermions are known as doublers.

4.1.4 Wilson Fermions

One possible solution to the doubling problem is the Wilson action, which involves the addition of an operator to the naive fermion action that vanishes as we take $a \to 0$. The Dirac operator for the Wilson action is

$$D_W(x,y) = \sum_{\mu}\frac{(\gamma^{\mu} - r)U_{\mu}(x)\delta_{x+a\hat{\mu},y} - (\gamma^{\mu} + r)U_{-\mu}(x)\delta_{x-a\hat{\mu},y}}{2a} + \left(m + \frac{4r}{a}\right)\delta_{x,y}, \tag{4.20}$$

which is equivalent to the naive Dirac operator in Eq. (4.16), with the addition of an irrelevant dimension 5 operator (made up of the terms proportional to r).

Once again we may compute the inverse Dirac operator, which for free Wilson fermions is [94]

$$\tilde{D}_W^{-1}(p) = \frac{m + \frac{r}{a}\sum_{\mu}(1 - \cos(p^{\mu}a)) - ia^{-1}\sum_{\mu}\gamma_{\mu}\sin(p^{\mu}a)}{\left(m + \frac{r}{a}\sum_{\mu}(1 - \cos(p^{\mu}a))\right)^2 + a^{-2}\sum_{\mu}\sin(p^{\mu}a)^2}. \tag{4.21}$$

Once again we can analyse this operator in the massless limit, where there exists a pole at $p^{\mu} = (0,0,0,0)$. However, the additional terms

$$\frac{r}{a}\sum_{\mu}(1 - \cos(p^{\mu}a)) \tag{4.22}$$

are large when p^{μ} has some entries equal to π/a; this ensures that the doublers are given a particularly heavy mass (proportional to a^{-1}) and therefore completely decouple from the theory as $a \to 0$. This solution comes at a cost however, for the additional terms added to the action explicitly break chiral symmetry.

4.1.5 Overlap Fermions

The fact that Wilson fermions must break chiral symmetry to avoid doublers is a result of the Nielsen-Ninomiya no-go theorem [100], which states that a lattice action in an even number of dimensions cannot be free of doublers while also maintaining chiral symmetry and locality.

Chiral symmetry in the continuum can be summarised by the fact that the Dirac operator satisfies the anti-commutation relation

$$\{D, \gamma_5\} = 0. \tag{4.23}$$

A lattice version of this relation was subsequently defined by Ginsparg and Wilson [101] to be

$$\{D, \gamma_5\} = aD\gamma_5 D, \tag{4.24}$$

which can be seen to reproduce Eq. (4.23) in the limit $a \to 0$. This relation allows us to define a class of lattice actions that avoid the Nielsen-Ninomiya theorem and provide a working form of chiral symmetry on the lattice, which effectively eliminates the mixing of right- and left-handed fermion modes.

An action that satisfies the Ginsparg-Wilson relation Eq. (4.24) is the overlap fermion action,

$$D_{ov} = \frac{1}{a}\left(1 + \gamma_5 \frac{H}{\sqrt{H^2}}\right), \tag{4.25}$$

where $H = \gamma_5 D_{ker}$ and D_{ker} is a lattice Dirac operator satisfying γ_5-hermiticity, e.g. the Wilson Dirac operator. The second term in this equation is equivalent to the function $\operatorname{sign}[H]$. However, computing this function is numerically very expensive, and instead we use domain wall fermions for the results presented in this thesis, which will be discussed in the next section. The overlap action will however be of use to us; in our simulations of rare kaon decays it is necessary to directly simulate leptons on the lattice, which don't interact via QCD. The lepton propagators will be implemented as free overlap fermions, which we will discuss further in section 7.2.

If we set $D_{ker} = D_W$ we can write the overlap action as [102]

$$D\left(0\right) = \rho\left(1 + \gamma_5 \frac{H}{\sqrt{H^2}}\right) \tag{4.26}$$

$$= \rho\left(\frac{X + \omega}{\omega}\right), \tag{4.27}$$

$$D\left(m\right) = \left(1 - \frac{m}{2\rho}\right) D\left(0\right) + m \tag{4.28}$$

$$= \frac{\left(\rho - m/2\right) X + \left(\rho + m/2\right)\omega}{\omega}, \tag{4.29}$$

where we have introduced the parameter ρ, and we define

$$b\left(p\right) = \frac{1}{a}\left(r\sum_{\mu}\left(1 - \cos\left(ap_\mu\right)\right) - \rho\right), \tag{4.30}$$

$$X\left(p\right) = \frac{1}{a}\left(i\sum_{\mu}\gamma_\mu \sin\left(ap_\mu\right) + r\sum_{\mu}\left(1 - \cos\left(ap_\mu\right)\right) - \rho\right), \tag{4.31}$$

$$\omega\left(p\right) = \frac{1}{a}\sqrt{\sum_{\mu}\sin^2\left(ap_\mu\right) + \left(\sum_{\mu}\left(1 - \cos\left(ap_\mu\right)\right) - \rho\right)^2}. \tag{4.32}$$

The free overlap fermion propagator can hence be computed analytically to be

$$\tilde{D}^{-1}\left(p\right) = \frac{1}{2}\frac{\left(\frac{\rho}{a} - \frac{m}{2}\right)X^\dagger\left(p\right) + \left(\frac{\rho}{a} + \frac{m}{2}\right)\omega\left(p\right)}{\left(\frac{\rho^2}{a^2} + \frac{m^2}{4}\right)\omega\left(p\right) + \left(\frac{\rho^2}{a^2} - \frac{m^2}{4}\right)b\left(p\right)}. \tag{4.33}$$

The poles of this propagator are located at

$$\sum_{\mu}\sin^2\left(ap_\mu\right) = -\frac{\rho^2 a^2 m^2}{\rho^2 + \frac{a^2 m^2}{4}} a^2 b\left(p\right)^2 = -\tilde{m}^2 b\left(p\right)^2. \tag{4.34}$$

Provided that we have $0 < \rho < 2r$, we have $b\left(p\right) > 0$ and there exists a pole only at $p^\mu = (0, 0, 0, 0)$ (in the massless case), hence the doubling problem is solved.

4.1.6 Domain Wall Fermions

Domain wall fermions (DWF) avoid the doubling problem and the no-go theorem by introducing a fifth dimension [103]. In the limit of infinite fifth-dimensional extent, this action satisfies the Ginsparg-Wilson relation. We define the length of the new fifth dimension to be L_s, and introduce a new mass parameter, M_5, that varies in this dimension (analogous to the parameter ρ of the overlap formulation). The gauge links have no fifth-dimensional dependence. There are multiple incarnations of DWF; here I introduce Shamir's formulation [104], which is used for the exploratory numerical studies in this thesis. The action is described by

$$\sum_{x,y}\sum_{s,r}\overline{\Psi}\left(x,s\right)D_{dwf}\left(x,s|y,r\right)\Psi\left(y,r\right), \tag{4.35}$$

where x, y indicates coordinates in the 4D theory and $s, r \in [0, L_s - 1]$ are indices along the fifth dimension. The domain wall Dirac operator is

$$D_{dwf}\left(x,s|y,r\right)=\delta_{s,r}D_W\left(x,y\right)+\delta_{x,y}D^5_{dwf}\left(s,r\right), \tag{4.36}$$

where D_W is the usual Wilson operator Eq. (4.20) with the mass term m replaced by M_5, and D^5_{dwf} is defined by

$$\begin{aligned}D^5_{dwf}\left(s,r\right)=\delta_{s,r}&-\left(1-\delta_{s,L_s-1}\right)P_L\delta_{s+1,r}-\left(1-\delta_{s,0}\right)P_R\delta_{s-1,r}\\&+m\left(P_L\delta_{s,L_s-1}\delta_{0,r}+P_R\delta_{s,0}\delta_{L_s-1,r}\right).\end{aligned} \tag{4.37}$$

P_L and P_R are the left- and right-handed projection operators respectively. It is worth noting that the mass parameter of the 4D fermion, m, which we removed from the Wilson part of the action, now appears in this operator. The mass term M_5 is the height of the domain wall, which separates the points $s = L_s - 1$ and $s = 0$.

The interpretation of the physical 4D theory from this 5D theory is as follows. The physical four-dimensional fermion fields are defined as

$$\psi\left(x\right)=P_R\Psi\left(x,L_s-1\right)+P_L\Psi\left(x,0\right), \tag{4.38}$$

such that the right-handed fermion mode originates from one side of the domain wall, and the left-handed mode originates from the other side. In the limit of an infinite fifth-dimensional extent, these right- and left-handed modes are decoupled and we have chiral symmetry. Of course in the continuum quark masses break chiral symmetry explicitly: this explains the term in Eq. (4.37) involving m, which couples the left- and right-handed parts of the theory across the domain wall and leads to the four-dimensional quark mass. On a finite lattice, the finite fifth-dimensional extent leads to a residual chiral symmetry breaking, which we parametrise via the residual mass, m_{res}. This residual mass manifests as an additive renormalisation to the bare quark mass,

$$m_q = m + m_{res}. \tag{4.39}$$

Provided we can simulate with a large enough fifth-dimensional extent such that m_{res} is small, the domain wall formulation provides us with a working definition of chiral symmetry on the lattice.

4.1.7 Conserved Currents

In section 2.1.1.3 I discussed the conserved currents that arise as a result of continuous global symmetries of the QCD action. It is useful to define discrete versions of these symmetries for the lattice action, along with the corresponding currents. Naively we could consider the current Eq. (2.16), for example, i.e. where the current is a local operator. However, this local (or naive) choice does not satisfy the Ward Identity $\Delta^\mu J^a_\mu = 0$. To derive the conserved current, we must directly consider the variation of the action under the symmetry transformation Eq. (2.15). For the Wilson action, this leads us to the result

$$J^a_{W,\mu}(x) = \frac{1}{2}\Big(\overline{\psi}(x+\hat{\mu})(\mathbb{1}+\gamma_\mu)U^\dagger_\mu(x)\lambda^a\psi(x) - \overline{\psi}(x)(\mathbb{1}-\gamma_\mu)U_\mu(x)\lambda^a\psi(x+\hat{\mu})\Big), \tag{4.40}$$

where the matrices λ^a will correspond to the relevant symmetry group for this transformation. For domain wall fermions, the conserved current will depend on the exact implementation chosen. For example, the conserved current for the Möbius DWF formulation [105] is presented in Ref. [106]. Here I will demonstrate the conserved current for Shamir DWF [104].

The Shamir DWF conserved current is made up of the following components. For $\mu = 1, \ldots, 4$, there are components that are identical to that of Wilson, only with fifth-dimensional fields, i.e.

$$\begin{aligned} j^a_\mu(x,s) = \frac{1}{2}\Big(&\overline{\Psi}(x+\hat{\mu},s)(\mathbb{1}+\gamma_\mu)U^\dagger_\mu(x)\lambda^a\Psi(x,s) - \\ &\overline{\Psi}(x,s)(\mathbb{1}-\gamma_\mu)U_\mu(x)\lambda^a\Psi(x+\hat{\mu},s)\Big), \end{aligned} \tag{4.41}$$

while for the fifth dimension the current is

$$j^a_5(x,s) = \overline{\Psi}(x,s)P_R\lambda^a\Psi(x,s+1) - \overline{\Psi}(x,s+1)P_L\lambda^a\Psi(x,s). \tag{4.42}$$

The full four-dimensional conserved current is given by

$$J^a_{DWF,\mu} = \sum_s j^a_\mu(x,s). \tag{4.43}$$

The partially-conserved axial current (PCAC) is difficult to define for the Wilson action because of the explicit violation of chiral symmetry. A lattice version of the PCAC relation has however been derived in Ref. [107]. The axial current is much simpler to define for the (Shamir) DWF action,

$$A^a_{DWF,\mu} = \sum G_s j^a_\mu, \tag{4.44}$$

with j^a_μ defined as in Eq. (4.41) and

$$G_s = \begin{cases} -1 & s \leq L_s/2 \\ 1 & s > L_s/2 \end{cases}. \tag{4.45}$$

Because of the residual explicit chiral symmetry breaking due to the finite extent of the fifth dimension, the PCAC relation is modified slightly to be

$$\left\langle \partial^\mu A^a_\mu \left(x\right) \right\rangle = 2m \left\langle P^a \left(x\right) \right\rangle + 2 \left\langle P^a_{J_5} \left(x\right) \right\rangle, \tag{4.46}$$

where

$$P^a_{J_5}\left(x\right) = \overline{\Psi}\left(x, L_s/2-1\right) P_R \lambda^a \Psi\left(x, L_s/2-1\right) + \overline{\Psi}\left(x, L_s/2\right) P_L \lambda^a \Psi\left(x, L_s/2\right). \tag{4.47}$$

4.2 Numerical Simulation of Lattice Gauge Theory

In the previous chapter I introduced the discrete formulation of QCD; the next step of the procedure is to discretise the path integral Eq. (4.1), which I introduce in this section.

In order to simulate the path integral numerically, we first perform a Wick rotation into Euclidean space, i.e. we take $x_0 \to x_4 = ix_0$. The partition function therefore takes the form

$$Z = \int \mathcal{D}\left[U, \psi, \overline{\psi}\right] e^{-S\left(U, \psi, \overline{\psi}\right)}. \tag{4.48}$$

This thus gives a hint as to how the simulation of QCD will procede: the quantity e^{-S} can be interpreted as a probabilistic weight of a particular path. In order to evaluate this path integral, we must generate a series of field configurations that have been chosen with this correct weight, take measurements using each field configuration, and sum the results.

4.2.1 Pseudofermion Determinant

The simulation of fermions presents an additional problem, as it is not possible to construct anti-commuting fields on a computer directly with feasible resources. It is however possible to integrate out the fermionic fields,

$$\int \mathcal{D}\left[\psi, \overline{\psi}\right] e^{-\overline{\psi}(x) D(x,y) \psi(y)} \propto \det D\left(x, y\right), \tag{4.49}$$

although this produces a new problem, in that $D\left(x, y\right)$ is a very large matrix and the determinant $\det D$ is prohibitively expensive to compute directly. We therefore introduce new bosonic fields χ such that

$$\det D\left(x,y\right) \propto \int \mathcal{D}\left[\chi,\overline{\chi}\right] e^{-\overline{\chi}(x)D^{-1}(x,y)\chi(y)}. \tag{4.50}$$

These bosonic fields χ are known as pseudofermions [93, 94]. These fields are still expensive to simulate; in order to compute propagators for these fields we must compute entries of $D^{-1}\left(x,y\right)$, which is numerically expensive.

4.2.2 Markov Chain Monte Carlo

In a lattice simulation, we typically simulate with lattices that have $\mathcal{O}\left(10^7\right)$ sites or greater; because of the huge number of degrees of freedom it is thus completely unfeasible to directly compute the partition function Eq. (4.48) by means of a direct integration over the space of all ensembles. Instead we rely on statistical methods to approximate the expectation values of desired observables. The expectation value of an observable in the path integral formulation is

$$\langle \mathcal{O} \rangle = \frac{1}{Z} \int \mathcal{D}\left[U,\chi,\overline{\chi}\right] \mathcal{O}\left(U,\chi,\overline{\chi}\right) e^{-S(U,\chi,\overline{\chi})}. \tag{4.51}$$

To evaluate this expectation value, we wish to generate a sequence of N_{cf} field configurations, P_i, with the appropriate weight such that

$$\langle \mathcal{O} \rangle \approx \frac{1}{N_{cf}} \sum_{i=1}^{N_{cf}} \mathcal{O}\left[P_i\right], \tag{4.52}$$

where $\mathcal{O}\left[P_i\right]$ is the observable $\mathcal{O}$ measured using field configuration P_i. In the limit $N_{cf} \to \infty$ we must recover the exact expectation value we are after. The algorithm used to generate the field ensembles used in this thesis is the Hybrid Monte Carlo algorithm [108].

4.3 Correlation Functions

Now that we know how to to put QCD on the lattice and simulate it, we must be able to construct correlation functions (or correlators), which ultimately will be analysed to extract physical observables. The techniques I introduce in this section will ultimately be applied to construct the correlation functions required for rare kaon decays, which we will meet in chapter 5. Before this however, I will introduce the numerical techniques we will use with some illustrative examples.

4.3.1 Construction of Correlators

To demonstrate the basic construction of correlators, I will begin with the example of a two-point correlation function for a pion [94],

$$\left\langle \phi_\pi\left(y\right)\phi_\pi^\dagger\left(x\right)\right\rangle , \tag{4.53}$$

where $\phi_\pi^\dagger\left(x\right)$, is the creation operator for a pion at a position $x \equiv \left(t_\pi, \mathbf{x}\right)$, and $\phi_\pi\left(y\right)$ is the corresponding annihilation operator situated at a position $y \equiv \left(t, \mathbf{y}\right)$. To be more specific, the interpolator $\phi_\pi^\dagger$ will create any state with the same quantum numbers of the pion (i.e. a pseudoscalar state, see Table 2.2); we will elaborate more on this in section 4.4. For example, to create and annihilate a positively charged pion we have

$$\phi_{\pi^+}^\dagger\left(x\right) = \bar{u}\left(x\right)_a^\alpha\left(\gamma_5\right)^{\alpha\beta} d\left(x\right)_b^\beta , \tag{4.54}$$

$$\phi_{\pi^+}\left(x\right) = \bar{d}\left(x\right)_a^\alpha\left(\gamma_5\right)^{\alpha\beta} u\left(x\right)_b^\beta . \tag{4.55}$$

We have explicitly shown the indices corresponding to spin (greek indices) and colour (roman indices). We can insert these definitions into the correlation function Eq. (4.53) and perform Wick contractions to deduce the diagrams (and more importantly, the constituent propagators) that must be computed. We thus obtain:

$$\begin{aligned}
\left\langle \phi_\pi\left(y\right)\phi_\pi^\dagger\left(x\right)\right\rangle &= \left\langle \bar{d}\left(y\right)_a^\alpha\left(\gamma_5\right)^{\alpha\beta} u\left(y\right)_b^\beta\, \bar{u}\left(x\right)_c^\rho\left(\gamma_5\right)^{\rho\sigma} d\left(x\right)_d^\sigma\right\rangle && (4.56)\\
&= -\left\langle \left[d\left(x\right)\bar{d}\left(y\right)\right]_{da}^{\sigma\alpha}\left(\gamma_5\right)^{\alpha\beta}\left[u\left(y\right)\bar{u}\left(x\right)\right]_{bc}^{\beta\rho}\left(\gamma_5\right)^{\rho\sigma}\right\rangle && (4.57)\\
&= -\left\langle \mathrm{Tr}\left[S_d\left(x,y\right)\gamma_5 S_u\left(y,x\right)\gamma_5\right]\right\rangle . && (4.58)
\end{aligned}$$

In the last line we have used the definition of the propagator,

$$S_q\left(x,y\right)_{ab}^{\alpha\beta} = \left[q\left(x\right)\bar{q}\left(y\right)\right]_{ab}^{\alpha\beta} . \tag{4.59}$$

The diagram corresponding to this correlation function is shown in Fig. 4.1.

At this point it is useful to introduce a property of many lattice actions (including all those presented in this thesis), known as γ_5-hermiticity. Under this property the Dirac operator satisfies

$$D\left(x,y\right) = \gamma_5 D^\dagger\left(y,x\right)\gamma_5. \tag{4.60}$$

This property is also satisfied by the propagator, such that

$$\gamma_5 S^\dagger\left(y,x\right)\gamma_5 = S\left(x,y\right). \tag{4.61}$$

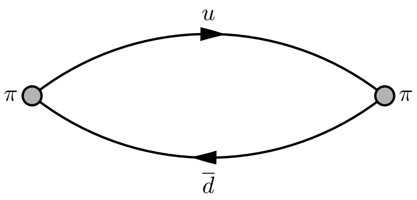

Figure 4.1: Diagram that contributes to the 2pt pion correlation function Eq. (4.58).

Using this, we can thus obtain the backward running propagator in our example from the forward propagator, and thus the correlation function appears as

$$\left\langle \mathrm{Tr}\left[S_u\left(x,y\right)S_d^{\dagger}\left(x,y\right)\right]\right\rangle . \tag{4.62}$$

As noted in section 2.1.1.2, most lattice simulations take place in the isospin limit $m_u = m_d$; in such a case we only need to compute a single propagator to compute the correlation function for the pion. The computation of such a propagator will be discussed in section 4.3.2.

The final step in the procedure is to project out the momentum of the desired hadronic state by means of a Fourier transform. This step is necessary such that the interpolators will couple to specific eigenstates of the Hamiltonian, which we will require for the analysis procedures that we will meet in section 4.4.1. Hence to annihilate a meson with a definite momentum $\mathbf{p}$, we use

$$\tilde{\phi}\left(t,\mathbf{p}\right) = \frac{1}{L^3}\sum_{\mathbf{x}}\phi\left(t,\mathbf{x}\right)e^{-i\mathbf{p}\cdot\mathbf{x}}. \tag{4.63}$$

Note that the Fourier transform is over the spatial components of the lattice. Hence the creation operator is projected to a definite spatial momentum $\mathbf{p}$ on a timeslice t. Applying a momentum projection to our current example, we have

$$C_{\pi^+}^{(2)}\left(\mathbf{p},t,t_\pi\right) = \sum_{\mathbf{x},\mathbf{y}}\left\langle\phi_\pi\left(y\right)\phi_\pi^{\dagger}\left(x\right)\right\rangle e^{-i\mathbf{p}\cdot(\mathbf{y}-\mathbf{x})} \tag{4.64}$$

$$= \left\langle\tilde{\phi}_\pi\left(t,\mathbf{p}\right)\tilde{\phi}_\pi^{\dagger}\left(t_\pi,\mathbf{p}\right)\right\rangle . \tag{4.65}$$

4.3.2 Propagators

The quark propagator is equivalent to the inverse of the Dirac matrix,

$$S\left(x,y\right)_{ab}^{\alpha\beta} = D^{-1}\left(x,y\right)_{ab}^{\alpha\beta} . \tag{4.66}$$

The propagator for a single configuration of a lattice simulation gives the propagation amplitude for each site to every other site, for each spin and colour index. This is therefore a complex square matrix of side length $12N$, where N is the total number of sites in the 4- or 5-dimensional lattice (depending upon the fermion discretisation). Computing the full inverse Dirac matrix is a thus prohibitively expensive task, but it is sufficient to consider only subsets of this large matrix in order to extract the relevant physical information. To stay with our current example [picking up from Eq. (4.62)], we may fix $y = 0$ owing to translational invariance. All we require for the computation therefore is $S\left(x, 0\right)_{ab}^{\alpha\beta}$, which in numerical terms corresponds to the 12 columns of the inverse of the Dirac matrix associated with $y = 0$. A single column of the inverse Dirac matrix may be computed by solving

$$D\left(x, y\right)_{ab}^{\alpha\beta} S\left(y, x_0\right)_{ba_0}^{\beta\alpha_0} = \chi\left(x, x_0\right)_{aa_0}^{\alpha\alpha_0}, \tag{4.67}$$

for S, where χ is the unit vector corresponding to a single site of the lattice x_0 with specific colour and spin indices a_0 and α_0 respectively, i.e.

$$\chi\left(x, x_0\right)_{aa_0}^{\alpha\alpha_0} = \delta\left(x - x_0\right) \delta_{aa_0} \delta^{\alpha\alpha_0}. \tag{4.68}$$

There are many methods of solving such a matrix equation. In most lattice QCD simulations we make use of Krylov subspace methods, such as the conjugate gradient (CG) algorithm, to solve this equation for the propagator, S [93, 94]. The rate of convergence of the CG algorithm is proportional to the square root of the condition number of the Dirac matrix, defined as the ratio between the largest and smallest eigenvalues. This poses a problem in lattice QCD simulations when one wishes to simulate with lighter quark masses: smaller quark masses lead to higher condition numbers. Solving light quark propagators thus generally poses the largest computational burden in lattice simulations; hence this motivates the choice of simulating in the isospin limit with $m_u = m_d$, which we touched on in section 2.1.1.2.

The source χ [Eq. (4.68)] is known as a point source; i.e. we obtain a propagator from a single point to all other lattice sites. Other propagators may be obtained by using different types of sources. In the rest of this section we will introduce the sources we use in our rare kaon decay simulations, which are required to compute the propagators that we will need to construct the diagrams we will meet in section 5.1.

4.3.2.1 Source Smearing

In order to optimise the signal for our correlation functions, it is necessary to optimise the interpolating fields we use for the mesons. In section 4.3 we noted that the meson interpolators do not simply create/annihilate the ground state, but rather a tower of states with the quantum numbers of the interpolating operator. By using more complicated sources, we may obtain a better overlap of the interpolating operator with the ground state mesons that we require. For example, we may use a source with a spatial distribution that more accurately models the wavefunction of the state we wish to interpolate. One advantage of this is that we may obtain a better statistical precision for correlators with no extra computational expense. A better overlap with the ground state will also be useful for the analysis of our correlation functions in section 4.4.

In our studies of rare kaon decays we make use of wall sources [94], which are effectively the sum of all point sources corresponding to a particular timeslice, i.e.

$$\chi_W\left(y,x,\mathbf{p}\right)^{\beta\alpha_0}_{ba_0} = \sum_{\mathbf{x}} \delta(y_0 - x_0)\delta_{ba_0}\delta^{\beta\alpha_0}e^{i\mathbf{p}\cdot\mathbf{x}}. \tag{4.69}$$

Note that it is necessary to specify the momentum of the source before the inversion. Wall sources are advantageous to our studies, as they have a good overlap with the ground state mesons we wish to interpolate.

We remark however that this choice of source is not gauge-invariant, and thus it is necessary to gauge fix the $SU(3)$ field configuration used to compute such propagators (see section 4.3.3). It is also possible to smear the propagator at the sink; for example a wall sink is achieved by performing summing the propagator over space, such that it becomes a function of time only. This may be performed after the inversion, however.

4.3.2.2 Sequential Sources

More complicated correlation functions may be studied to extract matrix elements of physical processes, such as rare kaon decays. Such correlation functions include the insertion of one or more operators between the meson interpolators. As a demonstration, let us extend our present example by inserting a vector current between the two operators. The resulting correlator describes a photon being emitted by a pion, and we will see in chapter 5 that this is relevant for producing Z- and γ-exchange diagrams in rare kaon decays. The corresponding correlation function is

$$C^{\mu}_{J,\pi}\left(t_\pi, t_J, t, \mathbf{p}_1, \mathbf{p}_2\right) = \sum_{\mathbf{z}} \left\langle \tilde{\phi}_\pi\left(t,\mathbf{p}_2\right) J^{\mu}\left(t_J,\mathbf{z}\right) \tilde{\phi}^{\dagger}_{P}\left(t_\pi,\mathbf{p}_1\right)\right\rangle e^{-i\mathbf{q}\cdot\mathbf{z}}, \tag{4.70}$$

with $q = p_1 - p_2$, and J_μ is the local [Eq. (2.16)] or conserved [action dependent, see section 4.1.7] vector current. The Wick contractions for this correlation function are shown in Fig. 4.2. One method of inserting the vector current (either conserved or local) in a simulation is to employ the sequential source method [109].

Moreover, in our calculation we choose to insert the conserved vector current in the sequential propagator [2]. This insertion of the conserved current is complicated somewhat for the 5D DWF action. While the physical fermion fields exist in four-dimensional

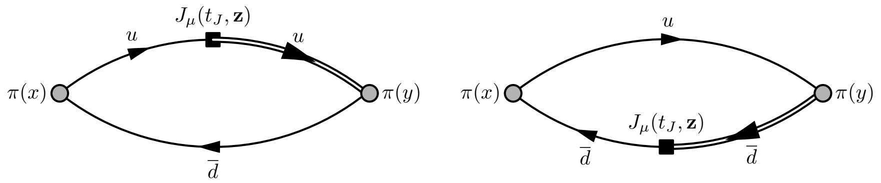

(a) (b)

Figure 4.2: Diagrams that result from Wick contractions of the 3pt correlation function with a current insertion Eq. (4.70). The double line shows the propagator that may be obtained as a result of a sequential inversion.

spacetime, the conserved domain wall current we must consider exists in five-dimensional spacetime. Before we discuss the sequential propagator we first introduce propagators from the 4D surface field ψ [Eq. (4.38)] into the five-dimensional bulk and vice versa, i.e.

$$S_{SB}\left(x,s;y\right)=\left\langle\Phi\left(x,s\right)\overline{\psi}\left(y\right)\right\rangle, \tag{4.71}$$

$$S_{BS}\left(x;y,s\right)=\left\langle\psi\left(x\right)\overline{\Phi}\left(y,s\right)\right\rangle. \tag{4.72}$$

The current that we wish to insert is defined by Eq. (4.41). Putting this together, we must calculate the propagator

$$\Sigma_\mu\left(y_0,y;x_0,x\right)=\sum_{\mathbf{z},s}e^{i\mathbf{q}\cdot\mathbf{z}}S_{BS}(y_0,\mathbf{y};t_J,\mathbf{z},s)K_\mu\left(t_J,\mathbf{z},s\right)S_{SB}(t_J,\mathbf{z},s;x_0,\mathbf{x}), \tag{4.73}$$

where K_μ is the kernel of the conserved current that follows from Eq. (4.41). This propagator corresponds, for example, to the up quark propagator shown in Fig. 4.2(a). We may obtain the 5D sequential propagator from an additional inversion by solving

$$\sum_{y,r}D\left(t_J,\mathbf{z},s;y_0,\mathbf{y},r\right)\Sigma^5_\mu\left(y_0,\mathbf{y},r;x_0,\mathbf{x}\right)=e^{i\mathbf{q}\cdot\mathbf{z}}K_\mu\left(t_J,\mathbf{z},s\right)S_{SB}(t_J,\mathbf{z},s;x_0,\mathbf{x}), \tag{4.74}$$

for Σ^5_μ where D is the five-dimensional Dirac operator, and $\mathbf{q}$ is the momentum transferred through the current. We remark that although this fixes the momentum transfer and the timeslice at which we position the conserved current, we obtain a propagator where the conserved current has been summed across all spatial components of the lattice. Finally the desired 4D sequential propagator is obtained by projecting the result of the inversion (Σ^5_μ) to the four-dimensional surface field using Eq. (4.38).

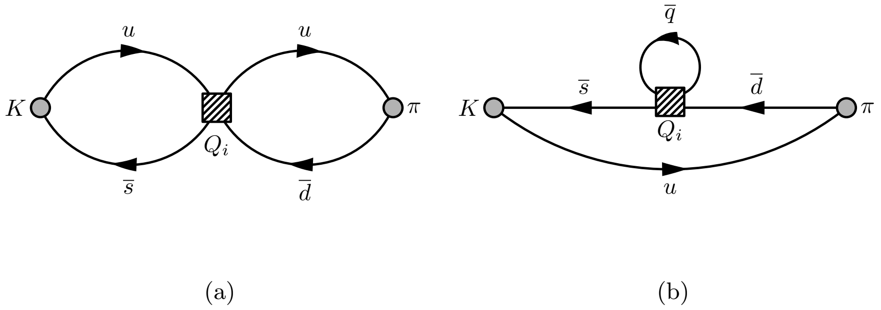

Figure 4.3: Diagrams that result from Wick contractions of the 3pt correlation function with a 4-quark weak operator (Q_i) insertion Eq. (4.77).

Lastly we comment on the γ_5 hermiticity properties of this propagator. In general we find that for a sequential propagator with an operator insertion $\mathcal{O}$, we have

$$\Sigma_{\mathcal{O}}\left(x,y\right)=\gamma_5\Sigma^{\dagger}_{\mathcal{O}^{\dagger}}\left(y,x\right)\gamma_5. \tag{4.75}$$

For the example of the vector current, we simply have

$$\Sigma_{\mu}\left(x,y\right)=-\gamma_5\Sigma^{\dagger}_{\mu}\left(y,x\right)\gamma_5. \tag{4.76}$$

4.3.2.3 Random Volume Sources

The rare kaon decays studied in this thesis are mediated by the weak interaction, the relevant correlation functions may be constructed by inserting the operators $Q_i\left(t_H,\mathbf{x}\right)$ that make up Eq. (3.2) between the relevant pion/kaon interpolators, i.e.

$$C_H\left(t_\pi,t,t_J,\mathbf{p}\right)=\sum_{\mathbf{x}}\left\langle\tilde{\phi}_\pi\left(t_\pi,\mathbf{p}\right)Q_i\left(t_H,\mathbf{x}\right)\tilde{\phi}^{\dagger}_K\left(t_K,\mathbf{p}\right)\right\rangle. \tag{4.77}$$

We can perform Wick contractions using these operators to obtain the diagrams that we must compute in a lattice simulation, which are shown in Fig. 4.3. In 4.3(b) example we see the appearance of a loop; here I will discuss how such a propagator is computed.

The loop propagator we wish to compute is $S(x,x)^{\alpha\alpha}_{aa}$, i.e. the diagonal elements of the inverse Dirac operator. This propagator is defined via

$$\begin{aligned}S(x,x)^{\alpha\alpha}_{aa}=&D^{-1}(x,x)^{\alpha\alpha}_{aa}\\=&\sum_{y,\beta,b}D^{-1}(x,y)^{\alpha\beta}_{ab}\delta(y-x)\delta^{\alpha\beta}\delta_{ab}\\=&\sum_{y,\beta,b}\left\langle D^{-1}(x,y)^{\alpha\beta}_{ab}\eta(y)\eta^{*}(x)\delta^{\alpha\beta}\delta_{ab}\right\rangle_{\eta},\end{aligned} \tag{4.78}$$

where $\eta(x)$ are vectors of random complex numbers that satisfy the constraints [110]

$$|\eta(x)|^2 = 1, \quad \langle \eta(x) \rangle_\eta = 0, \quad \langle \eta(y)\eta^*(x) \rangle_\eta = \delta(y-x). \tag{4.79}$$

We have used the notation $\langle \cdots \rangle_\eta$ to indicate the stochastic average over a large number of noise vectors to distinguish it from the usual gauge average. To satisfy Eq. (4.78) we take $\eta(x)$ to be constant across all spin and color indices corresponding to a single site. The random volume source used for the inversion step is hence

$$\chi_\eta \left(x\right)^{\alpha\beta}_{ab} = \eta\left(x\right)\delta^{\alpha\beta}\delta_{ab}. \tag{4.80}$$

The result of the inversion is multiplied element-wise by $\eta^*(x)$ to obtain the propagator. We use complex $\mathbb{Z}_2$ noise to generate the vectors $\eta(x)$ [111, 112].

4.3.3 Gauge Fixing

There are many aspects of lattice QCD calculations that are necessary to perform at fixed gauge [113], such as calculations with wall sources or computing renormalisation constants non-perturbatively (see section 5.3.1). For our lattice evaluation of rare kaon decay matrix elements we use Coulomb gauge, and for our non-perturbative renormalisation calculations we use Landau gauge.

The Coulomb gauge-fixing condition is to set $\nabla \cdot \mathbf{A} = 0$, which on the lattice is achieved by finding an extremal value of the functional

$$W\left[U\right] = -a^2 \sum_x \sum_{\mu=1}^{3} \mathrm{Tr}\left[U_\mu\left(x\right) + U_\mu^\dagger\left(x\right)\right]. \tag{4.81}$$

This can be achieved by numerically finding a gauge transformation [Eq. (4.7)] that shifts the chosen gauge configuration to one which minimises the function

$$F\left[U,\Omega\right] = -a^2 \sum_x \sum_{\mu=1}^{3} \mathrm{Tr}\left[\Omega\left(x\right)U_\mu\left(x\right)\Omega^\dagger\left(x+\hat{\mu}\right) + \Omega\left(x+\hat{\mu}\right)U_\mu^\dagger\left(x\right)\Omega^\dagger\left(x\right)\right]. \tag{4.82}$$

Landau gauge is closely related to Coulomb gauge and is defined by the condition $\partial_\mu A^\mu = 0$. It is thus equivalent to finding an extremal value of the functional

$$W\left[U\right] = -a^2 \sum_x \sum_{\mu=1}^{4} \mathrm{Tr}\left[U_\mu\left(x\right) + U_\mu^\dagger\left(x\right)\right]. \tag{4.83}$$

4.3.4 Twisted Boundary Conditions

One problem of simulating on a discrete lattice is the quantisation of 3-momentum, which is constrained to take values

$$\mathbf{p} = \frac{2\pi}{L}\left(n_1, n_2, n_3\right), \tag{4.84}$$

with $n_i \in \{0, 1, \ldots, L-1\}$, where L is the spatial extent of the lattice (assumed to be the same in each direction).

A method of circumventing this constraint is to employ twisted boundary conditions [114] for a quark field, q. The standard quark boundary condition we use is defined to be a periodic boundary in the spatial directions, and antiperiodic in time. To define twisted boundary conditions, we generalised the quark field boundary condition to

$$q\left(x_i + L\right) = e^{i\theta_i^q} q\left(x_i\right), \tag{4.85}$$

where we have introduced the quantity θ_i^q as the twist angle in the direction i for the quark field q. Periodic boundary conditions therefore correspond to the choice $\theta_i = 0$, and antiperiodic to $\theta_i = \pi$. With twisted boundary conditions, the momentum of the quark is now

$$p_i = \frac{\theta_i}{L} + 2\pi n_i/L. \tag{4.86}$$

4.4 Extraction of Observables

Once we have computed the propagators, we may contract them together to produce correlation functions, which we can analyse to extract physical observables from the theory. In this section I will describe the analysis procedures we use on our simulation data, in order to extract desired physical quantities along with the corresponding statistical errors [93, 94].

4.4.1 Analysis of Correlation Functions

Let us go back to the example of the two-point correlation function for a pion,

$$C_\pi^{(2)}\left(\mathbf{p}\right) = \left\langle \tilde{\phi}_\pi\left(t, \mathbf{p}\right) \tilde{\phi}_\pi^\dagger\left(t_\pi, \mathbf{p}\right)\right\rangle, \tag{4.87}$$

where $\tilde{\phi}_\pi^\dagger\left(t_\pi, \mathbf{p}\right)$ is the creation operator for a pion with momentum $\mathbf{p}$ at a time t_π, and $\tilde{\phi}_\pi\left(t, \mathbf{p}\right)$ is the corresponding annihilation operator situated at a time t. Between the operators we insert a complete set of states,

$$C_{\pi}^{(2)}\left(t,\mathbf{p}\right)=\sum_{n,m}\left\langle m\left|\tilde{\phi}_{\pi}\left(t,\mathbf{p}\right)\right|n\right\rangle\left\langle n\left|\tilde{\phi}_{\pi}^{\dagger}\left(t_{\pi},\mathbf{p}\right)\right|m\right\rangle. \tag{4.88}$$

We remark that in an infinite volume we would identify the state m as the vacuum state; however because we use a finite lattice with periodic boundary conditions, these so-called "round-the-world" effects must be accounted for. For the moment we will however take m to be the vacuum, leaving us only with a sum over n.

The next step of this analysis is to pull out the time dependence of the operators using the standard Heisenberg picture definition

$$\mathcal{O}\left(t\right)=U^{\dagger}\left(t\right)\mathcal{O}\left(0\right)U\left(t\right), \tag{4.89}$$

where the time-evolution operator is

$$U\left(t\right)=e^{-\hat{H}t}, \tag{4.90}$$

with $\hat{H}$ being the Hamiltonian operator of the system. This operator has the effect of picking out the energy eigenvalue of the state it acts on; we therefore have

$$\begin{aligned}C_{\pi}^{(2)}\left(t,\mathbf{p}\right)&=\left\langle\tilde{\phi}_{\pi}\left(t,\mathbf{p}\right)\tilde{\phi}_{\pi}^{\dagger}\left(t_{\pi},\mathbf{p}\right)\right\rangle && (4.91)\\&=\sum_{n}\frac{1}{2E_{n}\left(\mathbf{p}\right)}\left\langle 0\left|\tilde{\phi}_{\pi}\left(t,\mathbf{p}\right)\right|n\right\rangle\left\langle n\left|\tilde{\phi}_{\pi}^{\dagger}\left(t_{\pi},\mathbf{p}\right)\right|0\right\rangle && (4.92)\\&=\sum_{n}\frac{1}{2E_{n}\left(\mathbf{p}\right)}\left\langle 0\left|e^{\hat{H}(t-T)}\tilde{\phi}_{\pi}\left(\mathbf{p}\right)e^{-\hat{H}t}\right|n\right\rangle\left\langle n\left|e^{\hat{H}t_{\pi}}\tilde{\phi}_{\pi}^{\dagger}\left(\mathbf{p}\right)e^{-\hat{H}t_{\pi}}\right|0\right\rangle && (4.93)\\&=\sum_{n}\frac{1}{2E_{n}\left(\mathbf{p}\right)}e^{-E_{n}(\mathbf{p})(t-t_{\pi})}\left\langle 0\left|\tilde{\phi}_{\pi}\left(\mathbf{p}\right)\right|n\right\rangle\left\langle n\left|\tilde{\phi}_{\pi}^{\dagger}\left(\mathbf{p}\right)\right|0\right\rangle. && (4.94)\end{aligned}$$

We remark that the factor of $1/2E_n$ is a conventional choice of normalisation, and T is the time extent of the lattice. This exponentially decreasing behaviour in time implies that for $t \gg t_\pi$, the ground state behaviour (i.e. the state with the smallest value for E_n) will dominate the behaviour of the correlator. For this correlator this state corresponds to the pion, hence

$$C_{\pi}^{(2)}\left(t,\mathbf{p}\right)\overset{t\gg t_{\pi}}{\to}\frac{1}{2E_{\pi}\left(\mathbf{p}\right)}e^{-E_{n}(\mathbf{p})(t-t_{\pi})}\left|\left\langle 0\left|\tilde{\phi}_{\pi}\left(\mathbf{p}\right)\right|n\right\rangle\right|^{2}. \tag{4.95}$$

This correlator can therefore be fit to this relation in a desired window to extract the parameters $E_\pi(\mathbf{p})$ and $N_\pi(\mathbf{p}) = |\langle 0|\tilde{\phi}_\pi(\mathbf{p})|n\rangle|$. We remark that an optimal choice of interpolating operator can increase the size of this window in which the ground state dominates. Hence N_π will generally depend upon the type of smearing used at the source and sink, which need not necessarily be the same for both. For a point source/sink however it may be noted that N_π would be independent of the momentum of the meson.

At this point we return to the problem of a periodic lattice. With such a lattice the solution Eq. (4.95) breaks down around $|t-t_\pi| \simeq T/2$. To see this, consider also the solution where the state n corresponds to the vacuum, i.e.

$$C_\pi^{(2)}(t,\mathbf{p}) = \sum_m \frac{1}{2E_m(\mathbf{p})} e^{-E_m(\mathbf{p})(T-t+t_\pi)} \left\langle m \middle| \tilde{\phi}_\pi(t,\mathbf{p}) \middle| 0 \right\rangle \left\langle 0 \middle| \tilde{\phi}_\pi^\dagger(t_\pi,\mathbf{p}) \middle| m \right\rangle . \tag{4.96}$$

$$\to \frac{1}{2E_\pi(\mathbf{p})} e^{-E_n(\mathbf{p})(T-t+t_\pi)} \left|N_\pi(\mathbf{p})\right|^2 . \tag{4.97}$$

The lightest state is once again a pion, but propagating in the opposite direction. Combining the two therefore we see that the ground state solution is

$$C_\pi^{(2)}(t,\mathbf{p}) \overset{|t-t_\pi|\gg 0}{=} \frac{\left|N_\pi(\mathbf{p})\right|^2}{2E_\pi(\mathbf{p})} \left(e^{-E_n(\mathbf{p})(t-t_\pi)} + e^{-E_n(\mathbf{p})(T-t+t_\pi)} \right) \tag{4.98}$$

$$= \frac{\left|N_\pi(\mathbf{p})\right|^2}{E_\pi(\mathbf{p})} e^{-E_\pi(\mathbf{p})T/2} \cosh\left(E_\pi(\mathbf{p}) \left[t - t_\pi - \frac{T}{2} \right] \right), \tag{4.99}$$

When we are in the first half of the lattice, we should see therefore that the forward propagating solution dominates; in the second half the backward propagating solution dominates; towards the centre however it is important to consider the overlap of the two.

4.4.1.1 Effective Mass Plots

Once the correlator Eq. (4.87) has been computed on the lattice, we may extract the parameters by fitting to the ansatz given in Eq. (4.99). To do this, we must fit to the expected relation in the region where only the ground state dominates. Effective mass plots are one way of determining where this region is [94].

The basic definition of the effective mass, m_{eff}, is

$$m_{eff}\left(t+\frac{1}{2}\right) = \ln \frac{C(t)}{C(t+1)}, \tag{4.100}$$

where $C(t)$ is the correlator we measure in the simulation. When the correlator is dominated by the behaviour of a single exponential decay ($\propto e^{-m_{eff}t}$), this ratio effectively gives the energy of the ground state. In this region of ground state dominance therefore we expect to see a plateau in the effective mass plot. For two-point functions where we know the exact form of the backward propagating state, we may use the more accurate definition

$$\frac{C(t)}{C(t+1)} = \frac{\cosh\left(m_{eff}\left(T/2-t\right)\right)}{\cosh\left(m_{eff}\left(T/2-t+1\right)\right)}. \tag{4.101}$$

Here we must solve for the effective mass numerically on each timeslice. An example effective mass plot is seen in Fig. 4.4 for a kaon 2pt correlation function. Because the 2pt function is symmetric, it is possible to increase the statistical precision of the fit by

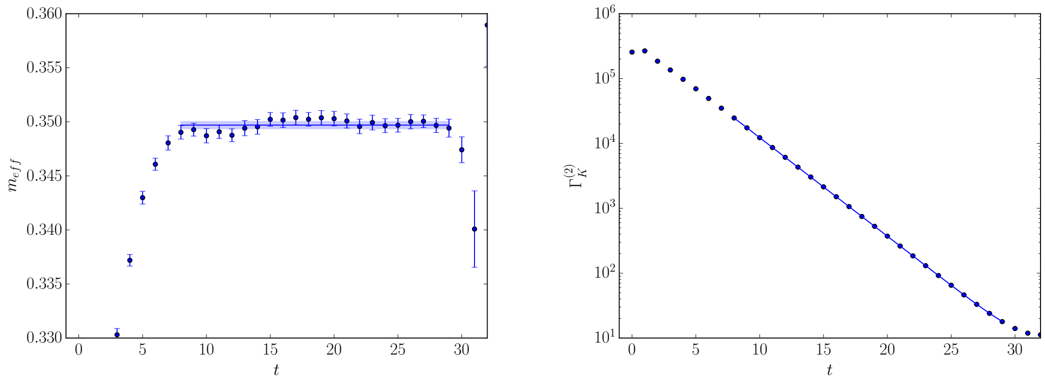

(a) (b)

Figure 4.4: Kaon correlator, fit to the ansatz Eq. (4.99). (a) shows the effective mass plot used to determine the region where the ground state dominates, highlighted by the horizontal line; (b) shows the fit to the folded correlator. Errors have been computed using bootstrap resampling.

"folding" the data (i.e. average pairs of points for which the cosh fit ansatz is equivalent), and fitting the remaining data to the ansatz.

4.4.1.2 3pt Correlators

In our analysis of rare kaon decays, we must also consider the matrix elements of operators, with mesonic initial and final states. This necessitates the analysis of three-point (3pt) correlation functions, e.g. Eqs. (4.70) and (4.77). Later we will also consider the analysis of the 4pt functions corresponding to rare kaon decays in chapter 5.

The analysis of 3pt function is more involved than the 2pt case, but the techniques are analogous. Our starting expression for the 3pt function is

$$C^{(3)}\left(t_i, t_f, t_{\mathcal{O}}, \mathbf{k}, \mathbf{p}\right) = \sum_{\mathbf{x}} \left\langle \tilde{\phi}_f\left(t_f, \mathbf{p}\right) \mathcal{O}\left(t_{\mathcal{O}}, \mathbf{x}\right) \tilde{\phi}_i^\dagger\left(t_i, \mathbf{k}\right)\right\rangle e^{-i(\mathbf{k}-\mathbf{p})\cdot\mathbf{x}}, \tag{4.102}$$

where $\mathcal{O}$ is an operator inserted at a time $t_{\mathcal{O}}$. We proceed again by inserting complete sets of states between the operators and using the time-evolution operator to extract the time dependence. We will however neglect the round-the-world effects, as they are not symmetric as in the 2pt case and hence do not involve the same states; including them thus adds additional (and often unnecessary) parameters to the fit. We thus end up with

$$\begin{aligned} C^{(3)} = \sum_{n,m} \frac{1}{4E_n\left(\mathbf{k}\right)E_m\left(\mathbf{p}\right)} \left\langle 0 \left| \tilde{\phi}_f \right| m, \mathbf{p} \right\rangle \left\langle m, \mathbf{p} \left| \mathcal{O} \right| n, \mathbf{k} \right\rangle \left\langle n, \mathbf{k} \left| \tilde{\phi}_i^\dagger \right| 0 \right\rangle \times \\ e^{-E_m(\mathbf{p})t_f} e^{-t_{\mathcal{O}}(E_n(\mathbf{k})-E_m(\mathbf{p}))} e^{t_i E_n(\mathbf{k})} \\ \rightarrow \frac{N_f\left(\mathbf{p}\right)N_i\left(\mathbf{k}\right)}{4E_i\left(\mathbf{k}\right)E_f\left(\mathbf{p}\right)} e^{-E_f(\mathbf{p})t_f} e^{-t_{\mathcal{O}}\left(E_i(\mathbf{k})-E_f(\mathbf{p})\right)} e^{t_i E_i(\mathbf{k})} \end{aligned} \tag{4.103}$$

In the analysis of 2pt functions we fixed the source timeslice t_i of the meson and varied the sink timeslice t_f; for 3pt functions we again fix the source but we now have the option of fixing the position of the operator at $t_{\mathcal{O}}$ and varying the sink timeslice, or fixing the sink and varying the position of the operator. The form of Eq. (4.103) is valid for both approaches. An effective mass plot of the form given by Eq. (4.100) may be used to determine the region in which the above exponential behaviour dominates, i.e. where it is free from significant excited state or round-the-world effects.

4.4.2 Fitting

Once we have identified the region we wish to fit to, we use a fitting algorithm to extract the desired parameters. This involves minimising

$$\chi^2 = \left(x_i\left(t\right) - y_i\left(t\right)\right)^T w\left(x_i\left(t\right), x_j\left(t'\right)\right)\left(x_j\left(t'\right) - y_j\left(t'\right)\right), \tag{4.104}$$

where $x_i\left(t\right)$ represents a correlator measured on timeslice t, $y_i\left(t\right)$ is the model we are fitting the correlator to (which depends upon the fit parameters), and $w\left(x_i\left(t\right), x_j\left(t'\right)\right)$ is a matrix of weights, defined to be the inverse of the covariance matrix $\mathrm{Cov}^{-1}\left(x_i\left(t\right), x_j\left(t'\right)\right)$. The indices i, j run over all the correlators that are being fit to simultaneously, each with its own corresponding fit function, and t, t' lie within the fit range $[t_{min}, t_{max}]$. The estimator for the covariance matrix itself is given by

$$\widehat{\mathrm{Cov}}\left(x_i\left(t\right), x_j\left(t'\right)\right) = \left\langle\left(x_i\left(t\right) - \left\langle x_i\left(t\right)\right\rangle\right)\left(x_j\left(t'\right) - \left\langle x_j\left(t'\right)\right\rangle\right)\right\rangle, \tag{4.105}$$

where $\langle \dots \rangle$ denotes the gauge average. This is the general procedure for correlated fits; we remark that in some situations the off-diagonal elements of the covariance matrix are not well determined owing to large statistical fluctuations, particularly if the Monte Carlo data set is quite small. In such a case we can reduce to an uncorrelated fit, where we use only the diagonal of the covariance matrix to compute the weights $w\left(x_i\left(t\right), x_j\left(t'\right)\right)$.

4.4.3 Statistical Analysis

All correlation functions we compute on the lattice must be computed over an ensemble of gauge configurations such that we may obtain a Monte Carlo estimate of the path integral. All quantities therefore have a statistical error associated with them; the most common procedures for computing this error are to use either jackknife or bootstrap resampling. The analysis described above must therefore be performed on each set of the resampled data; these results may then be used to compute errors on the quantities obtained from fits.

To begin, we define the set of values that we compute on each of N_{cf} field configurations,

$$\left\{X_1, X_2, \ldots, X_{N_{cf}}\right\}, \tag{4.106}$$

where each X_i is a quantity evaluated on configuration i of the Markov chain. Using the sample of measurements on each configuration, we can estimate the mean and standard deviation of the full distribution of the quantity X over the full ensemble. The unbiased estimators for the mean, $\langle X \rangle$, and the variance, σ_X^2, are defined respectively as

$$\hat{X} = \frac{1}{N_{cf}} \sum_{i=1}^{N_{cf}} X_i, \quad \hat{\sigma}_X^2 = \frac{1}{N_{cf}-1} \sum_{i=1}^{N_{cf}} \left(X_i - \hat{X}\right)^2. \tag{4.107}$$

It should be noted that we can only estimate the mean of the full distribution using a subset of configurations; the estimate we obtain may differ depending upon the exact set of N_{cf} paths we use to estimate it. We can define the variance of the estimator itself as

$$\sigma_{\hat{X}}^2 = \left\langle \left(\hat{X} - \langle X \rangle\right)^2 \right\rangle \tag{4.108}$$

$$= \frac{1}{N_{cf}} \left\langle X^2 \right\rangle - \langle X \rangle^2 + \frac{1}{N_{cf}^2} \sum_{i \neq j} \left\langle X_i X_j \right\rangle. \tag{4.109}$$

We refer to this quantity as the standard error of the mean. If successive X_i are uncorrelated, we thus find that

$$\sigma_{\hat{X}}^2 = \frac{\hat{\sigma}_X^2}{N_{cf}}. \tag{4.110}$$

In practice, once we have measured correlators on N_{cf} field configurations, we perform fits on these data to derive further quantities. Naively, we could perform an analysis on a series of sub-blocks of the N_{cf} correlators, and use the results from each sub-block to compute the error on the mean. However, this method does not produce reliable estimates of the standard error of the mean on small data sets. For this reason, we use resampling methods to estimate the errors [93, 94].

4.4.3.1 Jackknife Resampling

Suppose that we use the full sample of N_{cf} correlators to extract an estimate for a quantity θ, e.g. using a fit. We denote the full sample result as $\hat{\theta}$. Jackknife resampling then proceeds by taking the original sequence of N_{cf} measurements of correlators X_i and creating N_{cf} samples, defined as

$$S_i = \left\{X_1, \ldots, X_{i-1}, X_{i+1}, \ldots, X_{N_{cf}}\right\}, \tag{4.111}$$

as in sample S_i is made up of all measurements except the one taken on configuration i. We can use each jackknife sample to extract a quantity θ_i. We can thus determine the quantities

$$\tilde{\theta} = \frac{1}{N_{cf}} \sum_{i=1}^{N_{cf}} \theta_i, \quad \sigma_{\tilde{\theta}}^2 = \frac{N_{cf} - 1}{N_{cf}} \sum_{i=1}^{N_{cf}} \left(\theta_i - \hat{\theta}\right)^2 . \tag{4.112}$$

The standard error on the mean is given by the square root of the variance, which we quote as the error on the final result. The central value is quoted as the unbiased estimate of the mean, which is given by

$$\hat{\theta} - (N_{cf} - 1)\left(\tilde{\theta} - \hat{\theta}\right) . \tag{4.113}$$

4.4.3.2 Bootstrap Resampling

In general, it is possible to create $N_{cf}^{N_{cf}}$ resampled sets of data of length N_{cf} from the original set of measured correlators; i.e. each correlator in the list for a single resampling may be chosen to be any of the correlators from the original set. In practice it is unfeasible to extract the observable θ from every single possible resampled set of correlators. The bootstrap resampling method proceeds by choosing N_{boot} sets of resampled correlators, where in a single sample S_i each correlator is selected randomly from the full set of correlators. We would expect therefore that a bootstrap sample would contain repeated copies of some correlators, and no copies of some from the original set. Using these correlators we can extract the measurements θ_i on each bootstrap sample S_i, and we estimate

$$\tilde{\theta} = \frac{1}{N_{boot}} \sum_{i=1}^{N_{boot}} \theta_i, \quad \sigma_{\tilde{\theta}}^2 = \frac{1}{N_{boot}} \sum_{i=1}^{N_{boot}} \left(\theta_i - \tilde{\theta}\right)^2 . \tag{4.114}$$

The central value is quoted as $\tilde{\theta}$ with the error $\sigma_{\tilde{\theta}}$. All results presented in this thesis use the bootstrap resampling method.

Chapter 5

Rare Kaon Decays on the Lattice

In our lattice studies of rare kaon decays, we aim to compute the long-distance bilocal hadronic matrix elements that appear in Eq. (3.1). The exact form of the bilocal matrix elements that we compute will depend upon the decay in question, and the relevant matrix elements have been introduced for $K \to \pi \ell^+ \ell^-$ in section 3.1.2 and for $K \to \pi \nu \bar{\nu}$ in section 3.1.3. For the decay $K \to \pi \ell^+ \ell^-$ we need consider only the single photon exchange amplitude, $K \to \pi \gamma^*$. For the decays $K \to \pi \nu \bar{\nu}$ we must consider a Z-exchange amplitude (which is largely analogous to the photon exchange), and a W-W box amplitude. These all involve computing four point (4pt) correlation functions on the lattice, which we will discuss in this chapter.

I will begin this chapter with a discussion of the correlators we will be analysing in section 5.1, where bilocal operators are inserted between our initial and final hadronic states. We can subsequently generate the Wick contractions that correspond to the 4pt correlators. In section 5.2 I will show how in a Euclidean formulation, the 4pt correlation functions are contaminated by unphysical contributions that grow exponentially with the time separation of the two operators. I will also discuss the methods of removal of these growing exponentials. Finally, in order to make contact with continuum physics the operators must be appropriately renormalised; this will be discussed in section 5.3.

5.1 Operators and Contractions

5.1.1 Z and γ Exchange

For the Z and γ exchange amplitudes, the expression for the long-distance amplitudes we wish to compute are given by [19, 33]

$$A_\mu^{i,j}\left(q^2\right) = \int d^4x \left\langle \pi^i\left(p_\pi\right) \right| T\left[J_\mu^j\left(0\right) H_W\left(x\right)\right] \left| K^i\left(p_K\right) \right\rangle , \tag{5.1}$$

where $q = p_K - p_\pi$, $i = +, 0$, and $j = \gamma, Z$ implies we are using the current relevant to the γ- or Z- exchange respectively. Strictly speaking we are computing either the $K \to \pi\gamma^*$ or $K \to \pi Z^*$ amplitudes; the final-state leptons need not be included on the lattice for this matrix element. The four-flavour effective weak Hamiltonian relevant to the transitions $s \to d\ell^+\ell^-$ and $s \to d\nu\bar{\nu}$, where Wilson coefficients and operator matrix elements are calculated using a renormalisation scale μ with $M_W \gg \mu > m_c$, is discussed in section 3.1 and is given by Eq. (3.30). The Hamiltonian that we require for our lattice simulations is given by

$$H_W = \sum_{i=1}^{2} C_i \left(Q_i^u - Q_i^c\right), \tag{5.2}$$

which is equivalent to Eq. (3.30) except that we have omitted the constant prefactor $G_F V_{us}^* V_{ud}/\sqrt{2}$ that we do not include in the quoted lattice results for our matrix elements. Our ultimate goal is to extract the QCD form factors for these decays, which do not depend on these factors.

We will now define the exact forms of the current correponding to the the Z- or γ-exchange diagrams [19, 33]. We will begin with the γ exchange, where we define

$$J_\mu^\gamma = \sum_{q=u,d,s,c} Q_{em}^q J_\mu^{q,V}, \tag{5.3}$$

where $J_\mu^{q,V}$ is the local [Eq. (2.16)] or conserved [action dependent, see section 4.1.7] vector current for the quark q, and Q_{em}^q is its electric charge (2/3 and -1/3 for up- and down-type quarks respectively). For Z-exchange diagrams we have

$$J_\mu^Z = \sum_{q=u,d,s,c} I_3^q \left(J_\mu^{q,V} - J_\mu^{q,A}\right) - 2Q_{em}^q \sin^2\left(\theta_W\right) J_\mu^{q,V}, \tag{5.4}$$

where I_3^q is the 3rd component of the weak isospin for the quark q (1/2 and -1/2 for up- and down-type quarks respectively) and $J^{q,A}$ is the local [Eq. (2.21)] or conserved axial current (also action dependent).

For the γ-exchange diagrams, we may make use of electromagnetic gauge invariance to write down the matrix element in terms of a single invariant form factor,

$$A_\mu^{i,\gamma}\left(q^2\right) \equiv -i\, G_F \frac{V^i\left(z\right)}{\left(4\pi\right)^2} \left(q^2 \left(p_K + p_\pi\right)_\mu - \left(M_K^2 - M_\pi^2\right) q_\mu\right), \tag{5.5}$$

where non-perturbative QCD effects are contained in the form factor $V^i\left(z\right)$, $z = q^2/M_K^2$. We have used the notation of Ref. [4] for $V^i\left(z\right)$ here to facilitate our later comparisons with phenomenological results. For the Euclidean amplitude we use the convention $p^\mu = (iE, \mathbf{p})$. It should be noted that in the case $\mathbf{p}_K = \mathbf{p}_\pi = \mathbf{0}$ the matrix element can be seen to vanish, hence it is important to introduce momentum for the initial/final state in our lattice calculation [2, 19].

For the Z-exchange diagrams, we write the form factor in the more general form [33]

$$A_\mu^{Z,j}\left(p_K,p_\pi\right)=i\frac{G_F}{\sqrt{2}}V_{us}^*V_{ud}\left(F_+^{Z,j}\left(q^2\right)\left(p_K+p_\pi\right)_\mu+F_-^{Z,j}\left(q^2\right)q_\mu\right), \tag{5.6}$$

where we have separated the amplitude into the vector and axial components ($j=V,A$). For the vector component the Ward Identity implies

$$\left(M_K^2-M_\pi^2\right)F_+^{Z,V}\left(q^2\right)=q^2F_-^{Z,V}\left(q^2\right), \tag{5.7}$$

hence we may reduce Eq. (5.6) to a form similar to Eq. (5.5), where there is only one independent form factor. The form factor $F_-^Z\left(q^2\right)$ is not phenomenologically relevant however: when the neutrinos are included in the calculation we see that the spinor product $\bar{u}\left(p_\nu\right)\not{q}\left(1-\gamma_5\right)v\left(p_{\bar{\nu}}\right)$ vanishes (assuming massless neutrinos) [33]. This fact allows us to write the full long-distance Z-exchange contribution to $K\rightarrow\pi\nu\bar{\nu}$ as

$$A_Z=i\frac{G_F}{\sqrt{2}}V_{us}^*V_{ud}\sum_{\ell=e,\mu,\tau}F_Z\left(q^2\right)\left[\bar{u}\left(p_{\nu_\ell}\right)\not{p}_K\left(1-\gamma_5\right)v\left(p_{\bar{\nu}_\ell}\right)\right], \tag{5.8}$$

where I have defined

$$F_Z\left(q^2\right)=2\left(F_+^{Z,V}\left(q^2\right)-F_+^{Z,A}\left(q^2\right)\right), \tag{5.9}$$

and the subscript ℓ here denotes the flavour of the neutrinos. It must be noted that to extract the form factor F_+ with an axial current, results with different Lorentz indices must be combined. This necessitates the introduction of momentum in either the initial or final state such that the matrix element for at least one spatial Lorentz index is non-vanishing. In the case $\mathbf{p}_K=\mathbf{p}_\pi=\mathbf{0}$, we can however make use of the scalar form factor, defined by

$$F_0\left(q^2\right)=\frac{A_0}{M_K+M_\pi}, \tag{5.10}$$

which is related to F_+ and F_- through

$$F_0\left(q^2\right)=F_+\left(q^2\right)+\frac{q^2}{M_K^2-M_\pi^2}F_-\left(q^2\right), \tag{5.11}$$

which can be seen by comparison with Eq. (5.6) and considering the quantity $q^\mu A_\mu$.

If we insert the weak Hamiltonian Eq. (5.2) and the current into Eq. (5.1), we can perform all Wick contractions to produce the diagrams that must be computed [2, 19] (20 for a single type of current for a single kinematic). It is convenient to start by performing the Wick contractions for the insertion of only the operators within H_W to

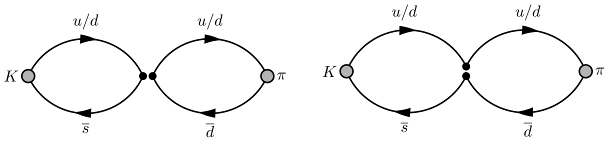

W C

(Wing) (Connected)

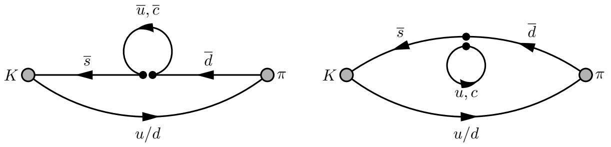

S E

(Saucer) (Eye)

Figure 5.1: The four diagram topologies obtained after performing the Wick contractions of the charged pion and kaon interpolating operators with the H_W operator. The light quark flavour indicated by u/d is u for charged mesons and d for neutral mesons.

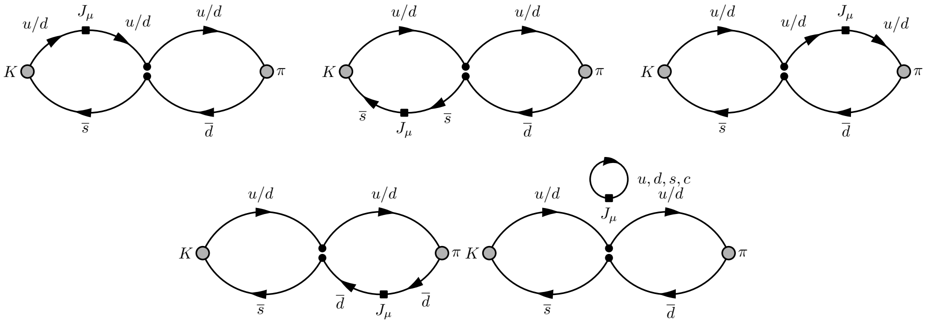

Figure 5.2: The five possible current insertions for the C class of diagrams. The light quark flavour indicated by u/d is u for the charged decays and d for the neutral decay. The fifth diagram shown is a quark-disconnected topology.

obtain the four different classes of diagrams shown in Fig. 5.1. Within each class we have five possible diagrams for each possible insertion of the current. Firstly we may insert the current on any of the propagators in each class. Additionally we may self-contract the current to produce a disconnected diagram, which corresponds to a photon or Z being emitted from a sea quark loop. We illustrate the five insertions for the C class in Fig. 5.2.

We remark that it is also interesting to study the neutral decay $K_S \to \pi^0\ell^+\ell^-$. For this decay we may contract the two quarks within the pion to produce two disconnected diagram topologies shown in Fig. 5.3 [19].

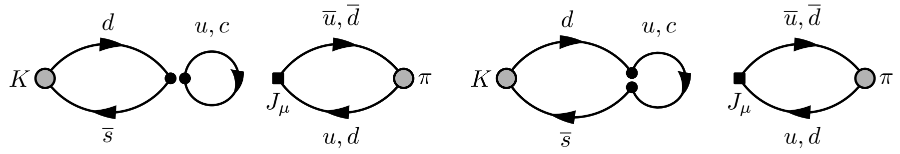

Figure 5.3: The additional two classes of diagrams obtained after performing the Wick contractions of the neutral pion and kaon interpolating operators with the H_W operator.

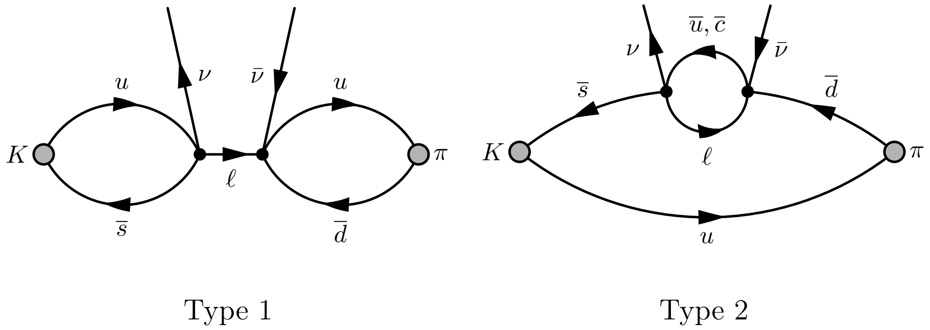

Figure 5.4: The two classes of diagrams the must be computed for W-W exchange amplitudes. The internal lepton propagator will correspond to $\ell = e, \mu, \tau$.

5.1.2 W-W diagrams

The W-W diagram contribution to the $K \to \pi\nu\bar{\nu}$ decay amplitudes can be written as [33]

$$A_{WW} = \frac{G_F}{\sqrt{2}} V_{us}^* V_{ud} \sum_{\ell=e,\mu,\tau} \int d^4x \, \left\langle \pi\nu\bar{\nu} \middle| T \left[Q_{\ell u}^{\Delta S=1} Q_{\ell u}^{\Delta S=0} \right] \middle| K \right\rangle - \{u \to c\}, \qquad (5.12)$$

where the operators $Q_{\ell q}^{\Delta S=0}$ and $Q_{\ell q}^{\Delta S=1}$ are defined in Eqs. (3.41) and (3.42) respectively. With these operators we may perform Wick contractions to give the diagrams that must be computed in our lattice simulation; these are shown in Fig. 5.4 [33]. It should be noted that the two neutrinos are emitted from separate vertices; this non-local structure means that we must directly simulate the internal charged lepton propagator. This can be contrasted with the Z- and γ-exchange diagrams, where the lepton/antilepton pair may be separated entirely from the hadronic matrix element and thus are not simulated. In the following discussion there will hence be an implicit dependence on the lepton flavour. Additionally in the remaining discussion we will omit the prefactor $G_F V_{us}^* V_{ud}/\sqrt{2}$.

In our lattice simulation, we aim to compute the scalar amplitude F_{WW} [33], defined by

$$A_{WW}(p_K, p_\nu, p_{\bar{\nu}}) = i\, F_{WW}(p_K, p_\nu, p_{\bar{\nu}}) \left[\bar{u}(p_\nu) \not{p}_K (1 - \gamma_5) v(p_{\bar{\nu}}) \right], \qquad (5.13)$$

where p_K, p_ν and $p_{\bar{\nu}}$ are the 4-momenta of the kaon, neutrino and anti-neutrino respectively. Multiplying both sides by $\bar{v}(p_{\bar{\nu}}) \not{p}_K (1 - \gamma_5) u(p_\nu)$ and summing over spins, we may project out F_{WW}, i.e.

$$F_{WW} = \frac{-i\,\mathrm{Tr}\left[A_{WW}\cdot\bar{v}\left(p_{\bar{\nu}}\right)\not{p}_K\left(1-\gamma_5\right)u\left(p_\nu\right)\right]}{\mathrm{Tr}\left[\not{p}_K\left(1-\gamma_5\right)\not{p}_{\bar{\nu}}\not{p}_K\left(1-\gamma_5\right)\not{p}_\nu\right]}. \tag{5.14}$$

To understand the origin of Eq. (5.13) in more detail, we write the matrix element Eq. (5.12) in terms of separate hadronic and leptonic factors,

$$A_{WW} = \int d^4x\, H_{\mu\nu}\left[\bar{u}\left(p_\nu\right)\Gamma^{\mu\nu}\nu\left(p_{\bar{\nu}}\right)\right], \tag{5.15}$$

where we define the hadronic factor as

$$H^{\mu\nu}\left(x\right) = \left\langle\pi\left(p\right)\right|T\left[\bar{s}\left(x\right)\gamma_L^\mu u\left(x\right)\bar{u}\left(0\right)\gamma_L^\nu d\left(0\right)\right]\left|K\left(k\right)\right\rangle, \tag{5.16}$$

and the leptonic factor as

$$\Gamma^{\mu\nu}\left(x\right) = \gamma_L^\mu S_\ell\left(x,0\right)\gamma_L^\nu e^{-ip_\nu\cdot x}. \tag{5.17}$$

We can subsequently write the scalar amplitude in the form

$$F_{WW}\left(p_K,p_\nu,p_{\bar{\nu}}\right) = -i\int d^4x\, H_{\mu\nu}c_\rho\mathrm{Tr}\left[\Gamma_{\mu\nu}\gamma_L^\rho\right], \tag{5.18}$$

where the 4-vector c_μ is given by

$$c_\mu = \frac{1}{8}\frac{b_\mu}{b\cdot p_K}, \tag{5.19}$$

with b_μ defined by

$$b_\mu = \frac{1}{4}\mathrm{Tr}\left[\gamma_\mu\not{p}_\nu\not{p}_K\left(1-\gamma_5\right)\not{p}_{\bar{\nu}}\right]. \tag{5.20}$$

The relevant correlation function measured in our lattice simulation gives us

$$F_\rho = \int d^4x\, H_{\mu\nu}\left(x\right)\mathrm{Tr}\left[\Gamma^{\mu\nu}\gamma^\rho\right] = \frac{1}{2}\int d^4x\, H_{\mu\nu}\left(x\right)\mathrm{Tr}\left[\Gamma^{\mu\nu}\gamma_\rho\left(1+\gamma_5\right)\right], \tag{5.21}$$

where the equality holds because $\Gamma_{\mu\nu}$ has a $V-A$ structure. A comparison of Eqs. (5.18) and (5.21) shows us that the scalar amplitude is recovered from $F_{WW} = F_\rho c^\rho$.

5.1.3 Local Operator

In addition to the bilocal contributions, there are short-distance contributions to rare kaon decays, where the hadronic effects are described by a local operator. For the rare kaon decays $K\to\pi\nu\bar{\nu}$ (or the decay $K\to\pi\ell^+\ell^-$ with 3 active flavours), this local operator is additionally required for the renormalisation procedure, to regulate divergences that may arise in the bilocal contribution. This local contribution is not required for our 4-flavour simulations of $K \to \pi\ell^+\ell^-$. This point will be discussed in detail in section 5.3.3.

The local contribution to rare kaon decays may be summarised as [33]

$$A_{loc} = \langle \pi\left(p_\pi\right) | s\gamma^\mu \left(1-\gamma_5\right) d | \, K\left(p_K\right)\rangle \left[\bar{u}_\ell\left(p_\ell\right)\Gamma_\mu v_{\bar{\ell}}\left(p_{\bar{\ell}}\right)\right], \tag{5.22}$$

where $\Gamma_\mu = \gamma_\mu\left(1-\gamma_5\right)$ for $K \to \pi\nu\bar{\nu}$ and $\Gamma_\mu = \gamma_\mu$ for $K \to \pi\ell^+\ell^-$. From a practical perspective we note that the axial current contribution to the matrix element vanishes by parity [33]. Furthermore as our simulations take place in the isospin limit, we may use isospin rotations to write the required matrix element as

$$\frac{1}{\sqrt{2}}\left\langle \pi^+ \left| \bar{s}\gamma_\mu d \right| K^+ \right\rangle = \left\langle \pi^0 \left| \bar{s}\gamma_\mu u \right| K^+ \right\rangle = \mathcal{M}_\mu^{K_{\ell 3}}. \tag{5.23}$$

Hence we may relate the local matrix element to the one involved in semi-leptonic kaon decays $K^+ \to \pi^0\ell^+\nu$ ($K_{\ell 3}$). The $K_{\ell 3}$ matrix element itself may be written in terms of hadronic form factors in a similar manner to Eq. (5.6), i.e.

$$\mathcal{M}_\mu^{K_{\ell 3}} = i\left(f_+\left(q^2\right)\left(p_K+p_\pi\right)_\mu + f_-\left(q^2\right)q_\mu\right), \tag{5.24}$$

with $q = p_K - p_\pi$, and the scalar form factor may similarly be defined as

$$f_0\left(q^2\right) = f_+\left(q^2\right) + \frac{q^2}{M_K - M_\pi} f_-\left(q^2\right). \tag{5.25}$$

5.2 Correlator Analysis

In this section I outline the analysis techniques necessary to extract rare kaon decay amplitudes from the four-point (4pt) correlators measured in our lattice simulation. I begin by discussing the extraction of Euclidean amplitudes in the continuum, followed by a discussion of the additional considerations we must make in discrete spacetime [2].

5.2.1 Continuum Euclidean correlators

One of the key issues in determining the matrix elements of four-point matrix elements in Euclidean space time is the presence of exponentially growing contaminations from intermediate states lighter than the initial state. To see how these terms arise, we consider the example of the "unintegrated" 4pt correlator,

$$\Gamma^{(4)}\left(t\right) = \int d^3\mathbf{x} \; \left\langle f \middle| T\left[\mathcal{O}^{\Delta S=0}\left(0\right)\mathcal{O}^{\Delta S=1}\left(t,\mathbf{x}\right)\right] \middle| K \right\rangle, \tag{5.26}$$

where the final state $\langle f|$ will be $\langle \pi\ell^+\ell^-|$ or $\langle \pi\nu\bar{\nu}|$. The spectral decomposition of this unintegrated 4pt correlator can be written as:

$$\Gamma^{(4)} = \begin{cases} \int_0^\infty dE \, \frac{\rho(E)}{2E} \langle f|\mathcal{O}^{\Delta S=0}|n\rangle \langle n|\mathcal{O}^{\Delta S=1}|K\rangle \, e^{-(E_K-E)t}, & t<0, \\ \int_0^\infty dE \, \frac{\rho_S(E)}{2E} \langle f|\mathcal{O}^{\Delta S=1}|m\rangle \langle m|\mathcal{O}^{\Delta S=0}|K\rangle \, e^{-(E-E_f)t}, & t>0, \end{cases} \tag{5.27}$$

where the functions $\rho(E)$ and $\rho_S(E)$ are the relevant spectral densities which select states with strangeness $S=0$ and $S=1$ respectively. To obtain the matrix element we must perform the remaining integral over t, which can be computed analytically to obtain

$$\begin{aligned} I(T_a,T_b) = &- \int_0^\infty dE \, \frac{\rho(E)}{2E} \frac{\langle f|\mathcal{O}^{\Delta S=0}|n\rangle \langle n|\mathcal{O}^{\Delta S=1}|K\rangle}{E_K-E} \left(1-e^{(E_K-E)T_a}\right) \\ &+ \int_0^\infty dE \, \frac{\rho_S(E)}{2E} \frac{\langle f|\mathcal{O}^{\Delta S=1}|m\rangle \langle m|\mathcal{O}^{\Delta S=0}|K\rangle}{E-E_f} \left(1-e^{-(E-E_f)T_b}\right). \end{aligned} \tag{5.28}$$

The rare kaon decay amplitude we wish to calculate corresponds to the constant terms in the above equation (i.e. those that do not depend on the exponentials in T_a and T_b) [19]. The intermediate states $|m\rangle$ in the second line of Eq. (5.28) must have the flavour quantum numbers of a kaon, i.e. $S=1$, and thus all possible intermediate states will have $E>E_f$; given a sufficiently large T_b this half of the integral should converge to the appropriate value. However the intermediate states $|n\rangle$ in the first line have $S=0$; it is therefore possible to have states with $E<E_K$, which will cause the integral to diverge with increasing T_a. The exponentially growing contributions from these intermediate states do not contribute to the overall decay width and therefore must be removed in order to extract the relevant Minkowski amplitude,

$$A\left(q^2\right) = -i \lim_{T_a,T_b\to\infty} \tilde{I}(T_a,T_b), \tag{5.29}$$

where $\tilde{I}$ indicates the integrated 4pt correlator after subtracting the exponentially growing contributions [19].

The precise identity of these intermediate states will depend upon whether we are considering Z- and γ-exchange diagrams, or W-W diagrams. For the former case where there are no leptonic intermediate states, there are three intermediate states with $E<E_K$: $|\pi\rangle$, $|\pi\pi\rangle$ and $|\pi\pi\pi\rangle$. For the W-W diagrams, the possible intermediate states that possibly provide exponentially growing contributions are $|\ell^+\nu\rangle$, $|\pi\ell^+\nu\rangle$, $|\pi\pi\ell^+\nu\rangle$ and $|\pi\pi\pi\ell^+\nu\rangle$. Of course these states depend also upon the lepton mass, for $\ell=\tau$ no intermediate states produce growing exponentials; for $\ell=\mu$ the states $|\pi\pi\pi\ell^+\nu\rangle$ do not [19, 33].

5.2.2 Lattice implementation

In lattice simulations we compute the correlator in Eq. (5.26) in a finite volume at a finite lattice spacing; for the purposes of the analysis it is useful to translate these continuum, infinite-volume formulas into their discrete, finite-volume counterparts [2]. To make the difference between the two clear, I will not suppress factors of the lattice spacing for the remainder of this section.

The spectral density $\rho\left(E\right)$ in finite volume can be expressed as $\rho\left(E\right)=\sum_n 2E_n\delta\left(E-E_n\right)$ [and similarly for $\rho_S\left(E\right)$]; the phase space integral is hence reduced to a sum over a finite number of states labeled by n. The spatial integrals in Eq. (5.26) are replaced by sums over the spatial extent of the lattice. Similarly the integral over time required to obtain the amplitude is also replaced by a sum.

The replacement of integrals over t by sums in our lattice calculation corresponds to the replacement

$$\int_{-T_a}^{0} dt \rightarrow a\sum_{t=-T_a}^{0}, \quad \int_{0}^{T_b} dt \rightarrow a\sum_{t=0}^{T_b}. \tag{5.30}$$

The sum runs over increments of the lattice spacing, a. We remark that the point at $t=0$ should not be double counted when the two halves of the integral are added together; this is intrinsically related to how the time ordering operator is implemented on the lattice. Because the operators $\mathcal{O}^{\Delta S=0}$ and $\mathcal{O}^{\Delta S=1}$ commute at $t=0$, a proper treatment is to average the two choices of time ordering at this point. In the following analysis the point at $t=0$ is thus weighted by a half; when the two sums are added together the correct result is obtained [2].

We now introduce the compact notation

$$\Delta_n^a = E_K - E_n, \quad \Delta_m^b = E_m - E_f, \tag{5.31}$$

where n and m label the finite volume states contained in the finite volume spectral densities $\rho\left(E\right)$ and $\rho_S\left(E\right)$ respectively, and a and b label which time ordering of the 4pt function the state appears for. The relevant sums corresponding to the integral of Eq. (5.26) can be evaluated as a geometric series, i.e.

$$a\sum_{t=-T_a}^{0} e^{-\Delta_n^a t} = a\frac{1+e^{a\Delta_n^a}\left(1-2e^{\Delta_n^a T_a}\right)}{2\left(1-e^{a\Delta_n^a}\right)}, \tag{5.32}$$

$$a\sum_{t=0}^{T_b} e^{-\Delta_m^b t} = a\frac{1+e^{-a\Delta_m^b}\left(1-2e^{-\Delta_m^b T_b}\right)}{2\left(1-e^{-a\Delta_m^b}\right)}. \tag{5.33}$$

To understand the impact of this analysis, it is instructive to expand the terms in Eq. (5.33) that depend on T_a and T_b. Expanding in powers of the lattice spacing, the unphysical contributions take the form:

$$-a\frac{e^{a\Delta_n^a}}{1-e^{a\Delta_n^a}}e^{\Delta_n^a T_a} = \left(1+\frac{a\Delta_n^a}{2}+\frac{\left(a\Delta_n^a\right)^2}{12}+\mathcal{O}\left(a^3\right)\right)\frac{e^{\Delta_n^a T_a}}{\Delta_n^a}, \tag{5.34}$$

$$-a\frac{e^{-a\Delta_m^b}}{1-e^{-a\Delta_m^b}}e^{-\Delta_m^b T_b} = \left(-1+\frac{a\Delta_m^b}{2}-\frac{\left(a\Delta_m^b\right)^2}{12}+\mathcal{O}\left(a^3\right)\right)\frac{e^{-\Delta_m^b T_b}}{\Delta_m^b}. \tag{5.35}$$

This analysis demonstrates the expectation that the sum reproduces the continuum expectation, up to discretisation effects starting at $\mathcal{O}\left(a\right)$. We remark that we developed this discrete formalism following a preliminary analysis of $K \to \pi\ell^+\ell^-$ simulation data, where we discovered that if we do not account for these effects, the result is an incomplete removal of the exponentially growing behaviour. We stress however that the physical matrix element itself, i.e. the contribution of those terms in Eq. (5.28) without the factors of $e^{\Delta_m^a T_a}$ or $e^{-\Delta_m^b T_b}$, is free of $\mathcal{O}\left(a\right)$ errors as is guaranteed by the prescription of domain wall fermions.

We can thus write the final expression for the integrated lattice correlator,

$$\begin{aligned} I\left(T_a, T_b\right) = a\sum_n \frac{1}{2E_n}\frac{\langle f|\mathcal{O}^{\Delta S=0}|n\rangle\langle n|\mathcal{O}^{\Delta S=1}|K\rangle}{2\left(1-e^{a\Delta_n^a}\right)}\left[1+e^{a\Delta_n^a}\left(1-2e^{\Delta_n^a T_a}\right)\right] + \\ a\sum_m \frac{1}{2E_m}\frac{\langle f|\mathcal{O}^{\Delta S=1}|m\rangle\langle m|\mathcal{O}^{\Delta S=0}|K\rangle}{2\left(1-e^{-a\Delta_m^b}\right)}\left[1+e^{-a\Delta_m^b}\left(1-2e^{-\Delta_m^b T_b}\right)\right]. \end{aligned} \tag{5.36}$$

To extract the matrix element we must therefore remove the exponentially growing contributions as they appear in the above equation. Subsequently to obtain the amplitude the correlator must be integrated within a window large enough such that the remaining exponential dependence on T_a and T_b converges within statistical errors [2].

5.2.3 Removal of Exponentially Growing Intermediate States

Our exploratory simulations use unphysically heavy pions masses; hence we do not see contamination from exponentially growing $|\pi\pi\rangle$ or $|\pi\pi\pi\rangle$ intermediate state contributions. Hence for Z- and γ-exchange diagrams, only the single-pion exponentially growing contribution must be removed in our analysis. For the W-W diagrams, we may have exponentially growing contributions either from $|\ell^+\nu\rangle$ or $\left|\pi^0\ell^+\nu\right\rangle$ intermediate states for $\ell = e, \mu$. I will explain the methods we use to remove these unphysical contributions in the following section.

5.2.3.1 Single Pion Intermediate State

The first possibility of removing the single-pion exponential is to reconstruct its analytical form from Eq. (5.36) [19]. For the Z- and γ-exchange diagram case discussed in the previous section, the final lattice state will be $\langle \pi(\mathbf{p}_\pi)|$ (for clarity I will explicitly include the momenta of the states in the following discussion). The exponential contribution is therefore

$$D_\mu^\pi\left(T_a, \mathbf{p}_K, \mathbf{p}_\pi\right) = a\,\frac{1}{2E_\pi\left(\mathbf{p}_K\right)}\frac{\langle \pi\left(\mathbf{p}_\pi\right)|J^\mu|\pi\left(\mathbf{p}_K\right)\rangle\langle \pi\left(\mathbf{p}_K\right)|H_W|K\left(\mathbf{p}_K\right)\rangle}{1-e^{-a\Delta_\pi^a}}e^{\Delta_\pi^a T_a}. \tag{5.37}$$

The necessary matrix elements and energies can be readily obtained from fits to 2pt and 3pt correlators. We will refer to this method of subtraction as "method 1".

We remark that the single-pion intermediate state is present only for the vector current component of Eq. (5.1). The vector current is parity conserving and subsequently the intermediate states must have odd parity. The axial component of the current required for a Z-exchange is parity violating, and thus the intermediate states must have even parity. Hence the odd-parity $|\pi\rangle$ intermediate state cannot arise with an axial current.

A second method ("method 2") of removing the exponentially growing contribution of the single-pion state is to employ a shift of the weak Hamiltonian by the scalar density, $\bar{s}d$ [115]. We choose a constant c_s such that

$$\left\langle \pi\left(\mathbf{p}_K\right)|H_W'|K\left(\mathbf{p}_K\right)\right\rangle = \langle \pi\left(\mathbf{p}_K\right)|H_W - c_s\bar{s}d|K\left(\mathbf{p}_K\right)\rangle = 0. \tag{5.38}$$

If we replace H_W by H_W' in Eq. (5.36), the contribution of the single-pion intermediate state vanishes. We can show [19] that this shift leaves the total amplitude invariant by writing the scalar density as a total divergence using the chiral Ward identity

$$i\left(m_s - m_d\right)\bar{s}d = \partial_\mu V^\mu_{\bar{s}d}, \tag{5.39}$$

which is exactly satisfied on the lattice.

5.2.3.2 Two and Three Pion Intermediate States

While the two- and three- pion intermediate states do not provide exponentially growing contaminations in our exploratory studies, it is useful to understand how to deal with them in physical simulations. These states will arise in the computation of Z- and γ-exchange amplitudes.

W-W diagram		Z-/γ-exchange	
Decay	Branching Ratio	Decay	Branching Ratio
$K^+ \to e^+\nu_e$	$1.582(7) \times 10^{-5}$	$K^+ \to \pi^+\pi^0$	$2.067(8) \times 10^{-1}$
$K^+ \to \mu^+\nu_\mu$	$6.356(11) \times 10^{-1}$	$K^+ \to \pi^+\pi^+\pi^-$	$5.583(24) \times 10^{-2}$
$K^+ \to \pi^0 e^+\nu_e$	$5.07(4) \times 10^{-2}$	$K^+ \to \pi^+\pi^0\pi^0$	$1.760(23) \times 10^{-2}$
$K^+ \to \pi^0 \mu^+\nu_\mu$	$3.352(33) \times 10^{-2}$	$K_S \to \pi^+\pi^-$	$6.920(5) \times 10^{-1}$
$K^+ \to \pi^+\pi^- e^+\nu_e$	$4.247(24) \times 10^{-5}$	$K_S \to 2\pi^0$	$3.069(5) \times 10^{-1}$
$K^+ \to \pi^0\pi^0 e^+\nu_e$	$2.55(4) \times 10^{-5}$	$K_S \to \pi^+\pi^-\pi^0$	$(3.5)^{+1.1}_{-0.9} \times 10^{-7}$
$K^+ \to \pi^+\pi^- \mu^+\nu_\mu$	$1.4(9) \times 10^{-5}$	$K_S \to 3\pi^0$	$< 2.6 \times 10^{-8}$
$K^+ \to 3\pi^0 e^+\nu_e$	$< 3.5 \times 10^{-6}$		

Table 5.1: Branching ratios and decays widths relevant to rare kaon decays. The decays with (semi-)leptonic final states are relevant for intermediate states in W-W diagrams; those with pure hadronic final states are relevant for intermediate states in Z- and γ-exchange diagrams.

For two-pion intermediate states [19], the relevant matrix elements for their removal are

$$\mathcal{M}_1 = \langle \pi(p_1)\, \pi(p_2) \,| H_W | K(p_K) \rangle \,, \tag{5.40}$$

$$\mathcal{M}_2 = \left\langle \pi(p_\pi) \,| J^i_\mu | \pi(p_1)\, \pi(p_2) \right\rangle \,, \tag{5.41}$$

for $i = V, A$. For the case of the vector current, Eq. (5.41) has the continuum form factor decomposition

$$\epsilon_{\mu\nu\rho\sigma} p_\pi p_1 p_2 F(s,t,u) \,, \tag{5.42}$$

where s, t and u are Mandelstam variables. Because of 4-momentum conservation, p_π is a linear combination of p_1 and p_2, hence upon contraction with the Levi-Civita tensor the quantity vanishes. This effectively encodes the parity conservation of the vector current. On a finite lattice Lorentz symmetry is broken, hence there may be parity-violating contributions from lattice artefacts, e.g. $\propto a^2 \epsilon_{\mu\nu\rho\sigma} p^\nu p^\rho_K \left(p^\sigma_K\right)^3$. Additionally it may be noted that in lattice studies of the $K_L - K_S$ mass difference [1, 115], the $\pi\pi$ intermediate state is also present and provides an on-shell contribution of only a few percent; lattice artefacts may only provide contributions that are a few percent of these. It is reasonable to expect a similar contribution in rare kaon decay amplitudes. Given this suppression we anticipate that within the integration window required to extract the matrix element, these contributions will be negligible [19]. We will be able to validate these expectations in future studies with physical pion masses.

The axial current on the other hand violates parity, and thus the $|\pi\pi\rangle$ intermediate state must be removed if the pions are light enough. To remove these states it is necessary therefore to compute the matrix elements Eqs. (5.40-5.41) such that this state may be removed using techniques analogous to method 1. We remark that we could attempt to use a method analogous to method 2, where we shift the weak Hamiltonian by

$$H_W \to H'_W = H_W + c_p \bar{s}\gamma_5 d. \tag{5.43}$$

However this operator cannot generate an intermediate state with $I = 2$, and hence is unsuitable for removing the $I = 2$ $\pi\pi$ intermediate state.

Three pion on-shell intermediate states are expected to be give very small contributions, as they are strongly phase-space suppressed. An inspection of Table 5.1 demonstrates this significant suppression for $K_S \to 3\pi$ transitions, hence for studies of K_S decays it is expected that this intermediate state will be suppressed enough such that the diverging contribution is completely negligible within the integration window we employ in our lattice simulations. For K^+ decays, the suppression of $K^+ \to 3\pi$ decay widths (as shown in Table 5.1) in comparison to $K^+ \to \pi^+\pi^0$ is less strong; although this is because the $K^+ \to \pi^+\pi^0$ decay itself is suppressed by the $\Delta I = 1/2$ rule [116–118]. In future physical point simulations, it may be necessary to identify and remove this state if we aim for percent-level precision measurements of the matrix elements. Computing the matrix elements to remove this state using method 1 presents a formidable challenge, as the theory of tri-hadron states on the lattice is still in the early stages of understanding [119, 120].

5.2.3.3 Leptonic and Semileptonic Intermediate States

For W-W diagrams, the intermediate states that provide exponentially growing contributions will contain leptons. These are removed using method 1. By comparison with Eq. (5.36), we see that for type 1 diagrams (containing the $|\bar{\ell}\nu\rangle$ intermediate states) we must remove [33]

$$D^{\bar{\ell}\nu}\left(T_a, k, p_\pi, p_\nu, p_{\bar{\nu}}\right) = a \frac{1}{2E_{\bar{\ell}}\left(p_{\bar{\ell}}\right)} \frac{1}{2E_\nu\left(p_\nu\right)} \frac{\mathcal{M}^{\pi\nu\bar{\nu}\to\bar{\ell}\nu}\mathcal{M}^{\bar{\ell}\nu\to K}}{1 - e^{-a\Delta^a_{\bar{\ell}\nu}}} e^{\Delta^a_{\bar{\ell}\nu} T_a}, \tag{5.44}$$

from the full matrix element, where we have defined

$$\mathcal{M}^{\pi\nu\bar{\nu}\to\bar{\ell}\nu} = \left\langle \pi\left(p_\pi\right)\nu\left(p_\nu\right)\bar{\nu}\left(p_{\bar{\nu}}\right)|\mathcal{O}^{\Delta S=0}_{\ell q}|\bar{\ell}\left(p_{\bar{\ell}}\right)\nu\left(p_\nu\right)\right\rangle, \tag{5.45}$$

$$\mathcal{M}^{\bar{\ell}\nu\to K} = \left\langle \bar{\ell}\left(p_{\bar{\ell}}\right)\nu\left(p_\nu\right)|\mathcal{O}^{\Delta S=1}_{\ell q}|K\left(p_K\right)\right\rangle. \tag{5.46}$$

It should be noted from Table 5.1 that $K \to e^+\nu$ decays are heavily helicity suppressed; in practice only the $|\mu^+\nu\rangle$ intermediate state contribution needs to be removed.

Because the leptons do not interact via QCD, we can factorise out the hadronic and leptonic contributions. We interpolate the leptonic states (i.e. a free fermion with 4-momentum p) using [33]

$$\nu(x)\left|\nu(p_\nu)\right\rangle = u(p_\nu)\, e^{ip_\nu\cdot x}\left|0\right\rangle, \tag{5.47}$$

$$\bar\nu(x)\left|\bar\nu(p_{\bar\nu})\right\rangle = \bar v(p_{\bar\nu})\, e^{ip_{\bar\nu}\cdot x}\left|0\right\rangle, \tag{5.48}$$

$$\ell(x)\left|\ell(p_\ell)\right\rangle = u(p_\ell)\, e^{ip_\ell\cdot x}\left|0\right\rangle, \tag{5.49}$$

$$\bar\ell(x)\left|\bar\ell(p_{\bar\ell})\right\rangle = \bar v(p_{\bar\ell})\, e^{ip_{\bar\ell}\cdot x}\left|0\right\rangle, \tag{5.50}$$

where $u(p)$ and $v(p)$ are the conventional positive and negative energy free Dirac spinors respectively. Note that the spinor $u(p)$ is distinct from the up quark operator.

We may thus factorise the matrix elements Eqs. (5.45-5.46) as

$$\left\langle \pi\nu\bar\nu\right|\mathcal{O}_{\ell q}^{\Delta S=0}\left|\bar\ell\nu\right\rangle = Z_V\left\langle\pi\right|\bar u\gamma_\mu(1-\gamma_5)d\left|0\right\rangle\left\langle\nu\bar\nu\right|\bar\nu\gamma^\mu(1-\gamma_5)\ell\left|\bar\ell\nu\right\rangle, \tag{5.51}$$

$$\left\langle\bar\ell\nu\right|\mathcal{O}_{\ell q}^{\Delta S=1}\left|K\right\rangle = \left\langle\bar\ell\nu\right|\bar\nu\gamma_\mu(1-\gamma_5)\ell\left|0\right\rangle Z_V\left\langle 0\right|\bar s\gamma^\mu(1-\gamma_5)u\left|K\right\rangle, \tag{5.52}$$

where we have introduced the renormalisation constant Z_V, which will be discussed in section 5.3. The hadronic matrix elements must be computed in our lattice calculation; on the other hand the leptonic matrix elements may be computed using free field theory. We may rewrite the full exponentially growing contribution in the form

$$D^{\bar\ell\nu}(T_a,k,p_\pi,p_\nu,p_{\bar\nu}) = -f_K f_\pi \bar u(p_\nu)\,\not{p}_K\frac{i\not{p}_{\bar\ell}}{E_{\bar\ell}}\not{p}_\pi(1-\gamma_5)\,v(p_{\bar\nu})\; e^{(E_{\bar\ell}+E_\nu-E_K)T_a}, \tag{5.53}$$

where we have made use of the spinor completeness relation

$$\sum_{spins} u(p)\,\bar u(p) = \not{p}+m, \tag{5.54}$$

(although note we are considering massless neutrinos) and the relations

$$Z_V\left\langle\pi(p_\pi)\right|\bar u\gamma^\mu(1-\gamma_5)d\left|0\right\rangle = -\,f_\pi p_\pi^\mu, \tag{5.55}$$

$$Z_V\left\langle 0\right|\bar s\gamma^\mu(1-\gamma_5)u\left|K(p_K)\right\rangle = f_K p_K^\mu, \tag{5.56}$$

where f_K and f_π are the kaon and pion decay constants respectively.

Now that we have identified the form of the exponentially growing intermediate state in the full matrix element, we must remove it from the scalar amplitude. Recalling the projection we perform using Eq. (5.14), the exact quantity that we must remove in the analysis therefore is [33]

$$\frac{-i\,\mathrm{Tr}\left[D^{\bar\ell\nu}(T_a,p_K,p_\pi,p_\nu,p_{\bar\nu})\cdot\bar v(p_{\bar\nu})\,\not{p}_K(1-\gamma_5)\,u(p_\nu)\right]}{\mathrm{Tr}\left[\not{p}_K(1-\gamma_5)\,\not{p}_{\bar\nu}\not{p}_K(1-\gamma_5)\,\not{p}_\nu\right]}. \tag{5.57}$$

For type 2 diagrams the divergent intermediate states take the form

$$\begin{aligned}D^{\pi^0\bar{\ell}\nu}\left(T_a,p_K,p_\pi,p_\nu,p_{\bar{\nu}}\right)=\int\frac{d^3\mathbf{p}_{\pi^0}}{\left(2\pi\right)^3}&\mathcal{M}_\mu^{\pi^+\to\pi^0}\left(p_\pi,p_{\pi^0}\right)\frac{1}{2E_{\pi^0}}\mathcal{M}_\nu^{\pi^0\to K}\left(p_{\pi^0},p_K\right)\\&\times\bar{u}\left(p_\nu\right)\gamma^\nu\left(1-\gamma_5\right)\frac{i\not{p}_{\bar{\ell}}+m_{\bar{\ell}}}{2E_{\bar{\ell}}}\gamma^\mu\left(1-\gamma_5\right)\nu\left(p_{\bar{\nu}}\right)\\&\times e^{\left(E_{\bar{\ell}}+E_{\pi^0}+E_\nu-E_K\right)T_a},\end{aligned}\tag{5.58}$$

where the required QCD matrix elements are

$$\mathcal{M}_\mu^{\pi^+\to\pi^0}\left(p_\pi,p_{\pi^0}\right)=Z_V\left\langle\pi^+\left(p_\pi\right)|\bar{u}\gamma_\mu\left(1-\gamma_5\right)d|\pi^0\left(p_{\pi^0}\right)\right\rangle,\tag{5.59}$$

$$\mathcal{M}_\nu^{\pi^0\to K}\left(p_{\pi^0},p_K\right)=Z_V\left\langle\pi^0\left(p_{\pi^0}\right)|\bar{s}\gamma_\nu\left(1-\gamma_5\right)u|K^+\left(p_K\right)\right\rangle.\tag{5.60}$$

As noted in section 5.1.3, it is useful to use isospin rotations to write the matrix elements as

$$\left\langle\pi^+\left|\bar{u}\gamma_\mu\left(1-\gamma_5\right)d\right|\pi^0\right\rangle=\sqrt{2}\left\langle\pi^+\left|\bar{d}\gamma_\mu\left(1-\gamma_5\right)d\right|\pi^+\right\rangle,\tag{5.61}$$

$$\left\langle\pi^0\left|\bar{s}\gamma_\mu\left(1-\gamma_5\right)u\right|K^+\right\rangle=\frac{1}{\sqrt{2}}\left\langle\pi^+\left|\bar{s}\gamma_\mu\left(1-\gamma_5\right)d\right|K^+\right\rangle,\tag{5.62}$$

which simplifies the contractions required in a lattice QCD calculation. Additionally, the matrix element for the axial-vector current vanishes by parity; hence only the vector current need be considered [33].

In a lattice calculation there exists a divergent intermediate state for each allowed kinematical configuration of π^0 and ℓ^+ lighter than the intial state, where the momentum is quantised in multiples of $2\pi/L$. In our exploratory simulations there is only one kinematical configuration light enough to produce an exponentially growing contribution, in which the pion is at rest. To remove this exponential, it is sufficient to calculate the matrix elements

$$Z_V\left\langle\pi\left(\mathbf{p}_\pi\right)|\bar{d}\gamma_\mu d|\pi\left(\mathbf{0}\right)\right\rangle=-F_\pi\left(q^2\right)\left(E_\pi\left(\mathbf{p}_\pi\right)+M_\pi\right),\tag{5.63}$$

$$Z_V\left\langle\pi\left(\mathbf{0}\right)|\bar{s}\gamma_\nu d|K\left(\mathbf{0}\right)\right\rangle=-f_0\left(q^2_{max}\right)\left(M_K+M_\pi\right),\tag{5.64}$$

which are written in terms of the pion electromagnetic form factor F_π and the $K_{\ell3}$ form factor f_0, seen previously in Eq. 5.25. These definitions may be used to express the divergent state as [33]

$$\begin{aligned}D^{\pi^0\bar{\ell}\nu}\left(T_a,k,p_\pi,p_\nu,p_{\bar{\nu}}\right)=-f_0\left(q^2_{max}\right)F_\pi\left(q^2\right)\bar{u}\left(p_\nu\right)\left(\not{p}_K+\not{p}_{\pi^0}\right)\frac{i\not{p}_{\bar{\ell}}}{E_{\bar{\ell}}M_\pi}&\\\left(\not{p}_\pi+\not{p}_{\pi^0}\right)\left(1-\gamma_5\right)v\left(p_{\bar{\nu}}\right)e^{\left(E_{\bar{\ell}}+E_\nu-E_K\right)T_a}&.\end{aligned}\tag{5.65}$$

Again it should be noted that in practice we project out the quantity F_{WW} using Eq. 5.14, and thus the same procedure must be used on Eq. 5.65.

In future simulations with physical meson masses, there is also the possibility of exponentially growing states from $|2\pi\ell^+\nu\rangle$ and $|3\pi\ell^+\nu\rangle$ intermediate states. However it can be seen from Table 5.1 that the decays $K\to 2\pi\ell^+\nu$ and $K\to 3\pi\ell^+\nu$ transitions are heavily phase space suppressed; these exponential contributions are likely to be negligible within our integration window [33].

5.2.4 Finite Volume Corrections

At this point it is important to note that multi-particle states such as $\pi\pi$ and $\pi\pi\pi$ will suffer from power-law finite volume corrections in our lattice simulations. These corrections must be applied when these states are on-shell, hence are relevant to the intermediate states that provide exponentially growing contributions [19, 33].

In our exploratory studies we do not have any on-shell multi-hadron states, so there is no finite volume correction necessary for the Z- or γ-exchange diagrams. In future physical simulations the only state for which this will realistically be a problem is $\pi\pi$, if its physical contribution is large enough such that the finite volume correction becomes a significant source of error. However, two-pion finite volume corrections are well-known from the study of $K\to\pi\pi$ decays [121], and additionally in the calculation of the $K_L - K_S$ mass difference, which involves a 4pt correlator with a $\pi\pi$ intermediate state that provides an exponentially growing, unphysical contribution [122, 123]. A similar approach can therefore be used for the calculation of rare kaon decay amplitudes [33].

There is however the issue of finite volume corrections for the W-W diagrams, concerning the $|\ell^+\nu\rangle$ and $\left|\pi^0\ell^+\nu\right\rangle$ intermediate states. For the former there is no finite volume correction, as the neutrino is part of the final state and has fixed momentum; the momentum of the intermediate state lepton is hence also fixed. For $\left|\pi^0\ell^+\nu\right\rangle$ we should however apply a finite volume correction associated with a $\pi^0 - \ell^+$ loop. In our exploratory studies, only the $\left|\pi^0 e^+\nu\right\rangle$ intermediate state is light enough to result in this error.

The finite volume correction for the $\left|\pi^0\ell^+\nu\right\rangle$ may be written in the general form [33]

$$\begin{aligned} F_{WW}^{FV} &= F_{WW}\left(L\right) - F_{WW}\left(\infty\right) \\ &= \left(\frac{1}{L^3}\sum_{\mathbf{k}}\int\frac{dk_0}{2\pi} - \mathcal{P}\int\frac{d^4k}{\left(2\pi\right)^4}\right)\frac{f\left(k_0,\mathbf{k}\right)}{\left(k^2+m_1^2\right)\left(\left(P-k\right)^2+m_2^2\right)}, \end{aligned} \tag{5.66}$$

where $\mathcal{P}$ denotes that the poles in the above expression have been regulated using the principal value prescription. Specifically for $\left|\pi^0\ell^+\nu\right\rangle$, we have $m_1 = m_\pi$, $m_2 = m_\ell$, $P = p_K - p_\nu$, and

$$f\left(k\right) = \frac{\mathrm{Tr}\left[\not{\mathcal{M}}^{\pi^0\to K}\left(1-\gamma_5\right)\left(\not{P}-\not{k}\right)\not{\mathcal{M}}^{\pi^+\to\pi^0}\left(1-\gamma_5\right)\not{p}_{\bar{\nu}}\not{p}_K\left(1-\gamma_5\right)\not{p}_\nu\right]}{\mathrm{Tr}\left[\not{p}_K\left(1-\gamma_5\right)\not{p}_{\bar{\nu}}\not{p}_K\left(1-\gamma_5\right)\not{p}_\nu\right]} \tag{5.67}$$

The techniques for evaluating Eq. (5.66) for $\mathbf{P} \neq \mathbf{0}$ and $m_1 = m_2$ were developed in Ref. [124], where the system is boosted into the centre of mass frame and f is expanded in spherical harmonics. These techniques have been generalised to the case $m_1 \neq m_2$ in Ref. [125], hence may be applied in our studies of rare kaon decays.

5.3 Renormalisation

The renormalisation of the 4pt matrix elements of the form

$$\int d^4x \left\langle f \right| T \left[\mathcal{O}_A \left(x \right) \mathcal{O}_B \left(0 \right) \right] \left| i \right\rangle , \tag{5.68}$$

requires two stages. First, the operators $\mathcal{O}_A$ and $\mathcal{O}_B$ must be renormalised individually. The operators relevant to our calculation are the four-quark operators that make up H_W [Eq. (5.2)], the vector and axial currents $J_\mu^{V,A}$ and the operators [Eqs. (3.41-3.42)] relevant for W-W diagrams. Once these operators are renormalised, we must remove any new UV divergences that arise from the contact of $\mathcal{O}_A$ and $\mathcal{O}_B$. For convenience, I will introduce the compact notation for the bilocal operator,

$$\left\{ \mathcal{O}_A \mathcal{O}_B \right\} = \int d^4x \, T \left[\mathcal{O}_A \left(x \right) \mathcal{O}_B \left(0 \right) \right] . \tag{5.69}$$

The theoretical techniques for the non-perturbative renormalisation of the individual operators are introduced in section 5.3.1. Subsequently the renormalisation of the individual operators needed for this calculation is discussed in section 5.3.2. I will finish with a discussion of the removal of contact divergences in section 5.3.3.

5.3.1 Non-Perturbative Renormalisation

I will begin with a brief overview of momentum subtraction schemes [126]. I will illustrate the procedure by considering the example of the renormalisation of a two-quark Green's function $\langle p_2 | \mathcal{O} | p_1 \rangle$, where $\mathcal{O}$ is some arbitrary two-quark operator. This Green's function is shown diagramatically in Fig. 5.5. The idea of momentum subtraction schemes in general is to set

$$\left. \langle \mathcal{O} \rangle^{\mathrm{RI}} \right|_{p_1^2 = p_2^2 = \mu^2} = Z_{\mathcal{O}} \left(a, \mu_{\mathrm{RI}} \right) Z_\psi^{-1} \left(a, \mu_{\mathrm{RI}} \right) \left. \langle \mathcal{O} \rangle^{\mathrm{lat}} \right|_{p_1^2 = p_2^2 = \mu^2} = \langle \mathcal{O} \rangle^{(0)} , \tag{5.70}$$

where $\langle \mathcal{O} \rangle$ denotes the amputated Green's function, p_i denotes the momentum of the external quark state $|p_i\rangle$, μ_{RI} is the renormalisation scale, and the superscript $^{(0)}$ denotes the tree level value. This thus allows us to match a lattice matrix element to one regulated in our chosen momentum subtraction scheme (labelled lat and RI respectively). Using this condition we can calculate the renormalisation constant, $Z_{\mathcal{O}}$; the quark field

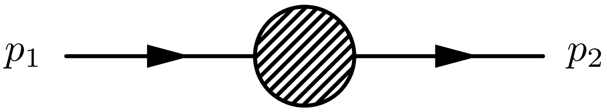

Figure 5.5: Schematic of the momentum flow for the renormalisation condition of a 2pt Green's function using momentum subtraction schemes. For RI-MOM schemes we require $p_1 = p_2$, $p_i^2 = \mu_{\mathrm{RI}}^2$; for RI-SMOM schemes we require $p_1^2 = p_1^2 = (p_1 - p_2)^2 = \mu_{\mathrm{RI}}^2$.

renormalisation Z_ψ may be obtained from a similar calculation, which we discuss below. We remark that the renormalisation condition Eq. (5.70) is gauge dependent, and the conventional choice is to use Landau gauge. To ensure that the non-perturbative determination of $Z_{\mathcal{O}}$ is valid, we must satisfy the conditions

$$\Lambda_{QCD} \ll \mu_{\mathrm{RI}} \ll a^{-1}. \tag{5.71}$$

The upper bound ensures that we avoid discretisation effects, the lower bound avoids unwanted non-perturbative effects. This is particularly necessary for our calculation where there will be a subsequent perturbative matching step, which must take place at a scale sufficiently above Λ_{QCD} to ensure the validity of the use of perturbation theory.

Our exact choice of renormalisation scheme depends upon our choice of kinematical configuration. For example, the regularisation-independent momentum subtraction scheme (RI-MOM) is defined for $p_1 = p_2$, with the renormalisation scale being set by $p_1^2 = p_2^2 = \mu_{\mathrm{RI}}^2$. However this configuration is exceptional (as $q = p_1 - p_2 = 0$), and thus may encounter errors from non-perturbative effects such as Goldstone pole contamination [126]. This can be avoided by employing the regularisation-invariant symmetric momentum subtraction scheme (RI-SMOM) [127, 128]. For this scheme, we wish to consider a non-exceptional momentum configuration, where no partial sum of incoming external momenta vanishes. To ensure the configuration is non-exceptional we impose the condition

$$p_1^2 = p_2^2 = q^2 = \mu_{\mathrm{RI}}^2, \tag{5.72}$$

with $q = p_1 - p_2$. This is the scheme we employ for the non-perturbative renormalisation required in our calculation.

In practice the calculation proceeds by calculating the amputated Green's function

$$\Lambda_{\mathcal{O}}\left(p_1, p_2\right) = S_f^{-1}\left(p_2\right) G_{\mathcal{O}}\left(p_1, p_2\right) S_i^{-1}\left(p_1\right), \tag{5.73}$$

where the subscripts i and f denote the initial and final states respectively, and $q = p_1 - p_2$. To obtain Λ we must compute $G_{\mathcal{O}}$, S_i and S_f, where $G_{\mathcal{O}}$ is defined by

$$\left(G_{\mathcal{O}}\right)_{ab}^{\alpha\beta}\left(p_1, p_2\right) = \sum_{x,y} e^{ip_1 y - ip_2 x} \sum_{z} e^{iqz} \left\langle \psi_f\left(x\right)_a^{\alpha}\, \mathcal{O}\left(z\right)\, \overline{\psi}_i\left(y\right)_b^{\beta} \right\rangle, \tag{5.74}$$

where roman and greek indices correspond to colour and spin respectively, and the quark propagator S is

$$S\left(p\right)_{ab}^{\alpha\beta} = \sum_{x,y} e^{-ip(x-y)} \left\langle \psi\left(x\right)_a^{\alpha}\, \overline{\psi}\left(y\right)_b^{\beta} \right\rangle. \tag{5.75}$$

We remark that $G_{\mathcal{O}}$ and $\Lambda_{\mathcal{O}}$ are tensors in spin and colour; in general it is preferable to work with scalar correlation functions. To achieve this goal, we would like to find a projector $P_{\mathcal{O}}$ that will project out the Dirac structure of the matrix element. To understand this, let us rewrite the renormalisation condition Eq. (5.70) in the form

$$Z_{\mathcal{O}}\left(a, \mu_{\mathrm{RI}}\right) Z_{\psi}^{-1}\left(a, \mu_{\mathrm{RI}}\right) \frac{1}{12} \operatorname{Tr}\left[P_{\mathcal{O}} \Lambda_{\mathcal{O}}^{\mathrm{lat}}\right]\Big|_{p_1^2 = p_2^2 = \mu^2} = 1, \tag{5.76}$$

where the trace runs over both trace and colour. For simple cases the projector may be obtained from the inverse of the tree level result, i.e. $P_{\mathcal{O}} = \left(\Lambda_{\mathcal{O}}^{(0)}\right)^{-1}$. For the example of a bilinear of the form

$$\mathcal{O} = \overline{\psi}_1 \Gamma \psi_2, \tag{5.77}$$

where Γ is the insertion of a gamma matrix (or a product thereof), the required projector for the RI-MOM scheme is simply Γ^{-1}.

The final step is to disentangle the quark and operator renormalisation. One straightfoward method of determining the quark field renormalisation in the RI-SMOM scheme is to consider the Green's function with a conserved vector current insertion, for which we have $Z_{\mathcal{O}} = 1$. Alternatively a local vector current may be used; the required renormalisation constant Z_V for this choice is discussed in the next section. The choice of projector for this method is not unique, which in general may depend upon the external momenta p_1 and p_2. We choose to focus on two choices of projector to determine Z_{ψ}, i.e.

$$Z_{\psi}^{\not{q}} = \frac{1}{12} \frac{q_{\mu}}{q^2} \operatorname{Tr}\left[\not{q} \Lambda_V^{\mu}\right]\big|_{p_1^2 = p_2^2 = \mu^2}, \quad Z_{\psi}^{\gamma_{\mu}} = \frac{1}{48} \operatorname{Tr}\left[\gamma_{\mu} \Lambda_V^{\mu}\right]\big|_{p_1^2 = p_2^2 = \mu^2}, \tag{5.78}$$

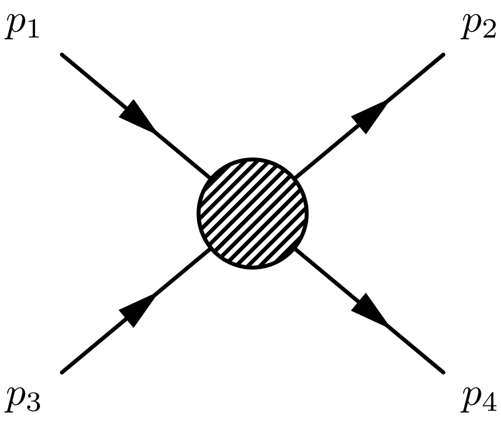

Figure 5.6: Schematic of the momentum flow for the renormalisation condition of a 4pt Green's function using the RI-SMOM scheme. In this scheme the momenta satisfy $p_i^2 = (p_1 - p_2)^2 = (p_3 - p_4)^2 = \mu_{\mathrm{RI}}^2$.

where Λ_V^μ is the amputated Green's function of the conserved vector current. These two choices are labelled by $\not{q}$ and γ_μ respectively.

The above discussion may be generalised to 4pt Green's functions, which is required for the renormalisation of the operators that make up H_W [Eq. (3.30)]. Such a Green's function is shown diagramatically in Fig. 5.6. Again it may be noted that the choice of projectors is again not unique. The exact form of the RI-SMOM scheme used for the renormalisation is thus labelled (a, b), such that a describes the class of projectors used for the H_W operator renormalisation, and b the class of projectors used to calculate Z_ψ [129]. In our studies of rare kaon decays we have made use of the $(\gamma_\mu, \not{q})$ scheme, which corresponds to the choice of

$$P = \frac{\Gamma^\dagger}{\mathrm{Tr}\left[\Gamma^\dagger \Gamma\right]}, \tag{5.79}$$

$$\Gamma = \left(\gamma_\mu \left(1 - \gamma_5\right)\right) \otimes \left(\gamma^\mu \left(1 - \gamma_5\right)\right), \tag{5.80}$$

for the H_W projector.

5.3.2 Local Operator Renormalisation

I will begin the discussion of the renormalisation of individual operators with the currents J_μ that appear in Eq. (5.1). The currents renormalise multiplicatively; we must therefore find the renormalisation constants Z_A or Z_V depending upon the current in question. If we use the conserved current, then no renormalisation is required, i.e. $Z_A = Z_V = 1$. However, if we use the local vector or axial current, then the constants Z_V and Z_A must be determined. However we may note that the effective chiral symmetry of the domain wall action allows us to take $Z_A = Z_V$ (up to $\mathcal{O}\left(a^2\right)$ effects, which we will neglect).

To determine Z_V and Z_A, it is possible to compute matrix elements using the conserved and local vector currents and computing ratios, or use momentum subtraction schemes as described in the previous section. However, with our prescription of domain wall fermions we may also extract them by using definitions of pseudoscalar decay constants [130]. For example, the pion decay constant f_π may be computed using

$$f_\pi = \frac{Z_A \left\langle \pi\left(\mathbf{p}\right) \right| \bar{u}\gamma_0\gamma_5 d \left|0\right\rangle}{E_\pi\left(\mathbf{p}\right)} = \frac{\left(\tilde{m}_u + \tilde{m}_d\right) \left\langle \pi\left(\mathbf{0}\right) \right| \bar{u}\gamma_5 d \left|0\right\rangle}{M_\pi^2} \tag{5.81}$$

where $\tilde{m}_q = m_q + m_{res}$. As m_{res} is already known for the lattices on which we simulate, this allows us to also extract Z_A (and Z_V, as noted in the previous paragraph).

We remark that the renormalisation constants Z_V and Z_A also are required to renormalise the operators $Q_{\ell q}^{\Delta S=0}$ and $Q_{\ell q}^{\Delta S=1}$ from Eqs. (3.41-3.42). The leptons do not experience strong interactions and the renormalisation of the vertex is equivalent to that for a local vector or axial current [33]. As previously noted in section 3.1.3 the Wilson coefficients for the two-quark-two-lepton operators are equal to one; hence there is no additional matching calculation required to combine Wilson coefficient and operator in the same renormalisation scheme.

5.3.2.1 Renormalisation of H_W

The renormalisation of the operators Q_i that make up H_W is a much more involved calculation. The Wilson coefficients C_i are known in the $\overline{\text{MS}}$ scheme at NLO [77]; we thus require Q_i to be renormalised in this scheme also. The renormalisation of the H_W operator is simplified considerably by our prescription of domain wall fermions: the good chiral symmetry prevents the mixing of the operators Q_i (from Eq. (5.2)) with right-handed operators. The renormalisation is thus a two step process. First we renormalise the bare lattice operators non-perturbatively using the RI-SMOM scheme described in section 5.3.1. Subsequently we must perform a matching calculation using continuum perturbation theory to match to the $\overline{\text{MS}}$ scheme [129]. We remark that for this matching calculation to give valid results, we must renormalise the operators at a sufficiently high scale, e.g. $\mu \gtrsim 2\,\text{GeV}$.

The matching procedure can be expressed as the formula [1]

$$H_W = \sum_i C^{\overline{\text{MS}}} \left(1 + \Delta r^{\text{RI}\to\overline{\text{MS}}}\right)_{ij} \left(Z^{\text{lat}\to\text{RI}}\right)_{jk} Q_k^{\text{lat}}, \tag{5.82}$$

where Z^{RI} is the RI-SMOM renormalization matrix for the bare lattice operators, and $\Delta r^{\text{RI}\to\overline{\text{MS}}}$ is the matching matrix [1] for conversion from the RI-SMOM scheme to the

$C_1^{\overline{\text{MS}}}$	-0.2967
$C_2^{\overline{\text{MS}}}$	1.1385
$\Delta r_{11} = \Delta r_{22}$	-6.562×10^{-2}
$\Delta r_{12} = \Delta r_{21}$	7.521×10^{-3}
$Z_{11}^{\text{RI}} = Z_{22}^{\text{RI}}$	0.5916
$Z_{12}^{\text{RI}} = Z_{21}^{\text{RI}}$	-0.05901
C_1^{lat}	-0.2216
C_2^{lat}	0.6439

Table 5.2: Results for the $\overline{\text{MS}}$ Wilson coefficients for H_W [Eq. (5.2)], the $\overline{\text{MS}} \to \text{RI}$ matching, the RI renormalisation matrix and the final lattice Wilson coefficients, all computed using $\mu = \mu_{\text{RI}} = 2.15\,\text{GeV}$ [1].

$\overline{\text{MS}}$ scheme. In the four-flavour theory and considering only the operators Q_1, Q_2 we have

$$\Delta r^{\text{RI}\to\overline{\text{MS}}} = \frac{\alpha_s(\mu)}{4\pi} \begin{pmatrix} -4\ln(2) & -8 + 12\ln(2) \\ -8 + 12\ln(2) & -4\ln(2) \end{pmatrix} \tag{5.83}$$

In our calculation we have used the renormalisation scales $\mu = \mu^{\text{RI}} = 2.15\,\text{GeV}$.

The entries of the matrix $Z^{\text{lat}\to\text{RI}}$ are calculated in the RI-SMOM$(\gamma_\mu, \not{q})$ scheme, as defined in section 5.3.1. Combining all these results, it is possible to determine the final coefficients C_i^{lat} by which we must multiply the bare lattice operators. These results are shown in Table 5.2.

5.3.3 Bilocal Operator Renormalisation

Once we have renormalised the two individual operators that make up the bilocal matrix element, we must remove any new UV divergences that arise as they approach each other [19, 25, 33]. It is possible to see how new divergences arise by examining the diagrams in Figs. 5.2 and 5.4. The relevant subdiagrams associated with the divergences are shown in Fig. 5.7. For example in Fig. 5.7(a), we see that when the current is inserted in the loop of the S or E classes of diagram, we have a subdiagram that resembles the hadronic vacuum polarization, which naïve power counting shows to be quadratically divergent. We remark that for the case of the conserved vector current, electromagnetic gauge invariance reduces this degree of divergence by two (owing to a transversality factor of $q^2 g_{\mu\nu} - q_\mu q_\nu$), leaving at most a logarithmic divergence. This is true despite the fact that the vector current component of the H_W operator is local. If we simulate in the 4-flavour theory we may exploit the GIM mechanism, as the divergence cancels

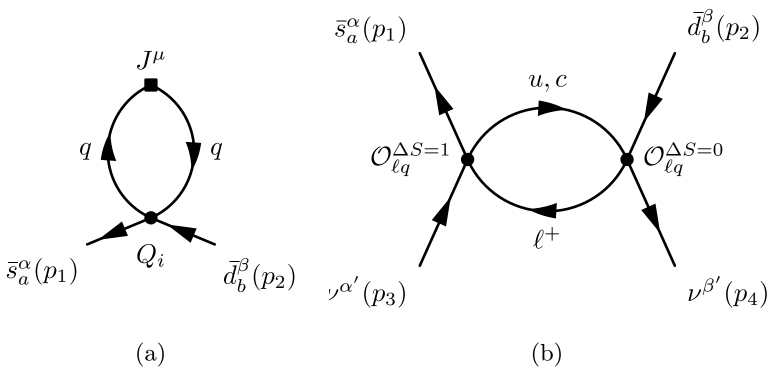

Figure 5.7: Diagrams leading to UV divergencs in (a) Z- and γ-exchange diagrams and (b) W-W diagrams.

between the up and charm quark loops. Hence for 4-flavour studies of $K \to \pi\ell^+\ell^-$, no further bilocal operator renormalisation is necessary.

For the axial current, the diagram in Fig. 5.7(a) is quadratically divergent, as is the diagram in Fig. 5.7(b) for the W-W case. The GIM mechanism however does reduce this divergence from quadratic to logarithmic; however the logarithmic divergence does not cancel completely via GIM. In such cases, the divergence must be removed using a local operator. The purpose of this local operator is hence twofold: it describes the short-distance physics that has been integrated out, and acts as a counterterm to cancel the divergence in the bilocal matrix element. We remark that if we were to use a fermion action without a good prescription of chiral symmetry, a linear divergence would still remain after the GIM cancellation [19, 33]. For this reason, our use of domain wall fermions is important such that the renormalisation procedure is tractable.

5.3.3.1 RI-SMOM Renormalisation

The first stage of the bilocal operator renormalisation is to regulate the divergences in the RI-SMOM scheme. For the renormalisation procedure we consider the 4pt amputated Green's functions of the bilocal operators. Our starting point is the Green's function with the divergence regulated in the lattice scheme; we can convert the regularisation of divergence into the RI-SMOM scheme by introducing a counterterm $X_{AB}\left(\mu_{RI}, a\right)$ to the bilocal operator such that [33]

$$\begin{aligned}\left\{\mathcal{O}_A\mathcal{O}_B\right\}^{\mathrm{RI}}\left(\mu_{\mathrm{RI}}\right) =& Z_A^{\mathrm{RI}}\left(\mu_{\mathrm{RI}}, a\right) Z_B^{\mathrm{RI}}\left(\mu_{\mathrm{RI}}, a\right) \left\{\mathcal{O}_A\mathcal{O}_B\right\}^{lat}(a) \\ &- X_{AB}\left(\mu_{RI}, a\right) Z_L^{\mathrm{RI}}\left(\mu_{\mathrm{RI}}, a\right) \mathcal{O}_L^{lat}(a)\,,\end{aligned} \tag{5.84}$$

where Z_A^{RI} and Z_B^{RI} are the RI-SMOM renormalisation factors for the operators $\mathcal{O}_A$ and $\mathcal{O}_B$ respectively. The counterterm itself may be determined by imposing the renormalisation condition

$$\begin{aligned}\left.\langle\{\mathcal{O}_A\mathcal{O}_B\}\rangle^{\mathrm{RI}}\right|_{p_i^2=\mu_{\mathrm{RI}}^2} =& \frac{Z_A^{\mathrm{RI}}Z_B^{\mathrm{RI}}}{Z_\psi^{\mathrm{RI}}}\left.\langle\{\mathcal{O}_A\mathcal{O}_B\}\rangle^{lat}(a)\right|_{p_i^2=\mu_{\mathrm{RI}}^2} \\ &- X_{AB}(\mu_{\mathrm{RI}},a)\frac{Z_L^{\mathrm{RI}}}{Z_\psi^{\mathrm{RI}}}\left.\langle\mathcal{O}_L\rangle^{lat}(a)\right|_{p_i^2=\mu_{\mathrm{RI}}^2} \\ =& 0,\end{aligned} \tag{5.85}$$

where the $\langle\mathcal{O}\rangle$ is the amputated Green's function of an operator $\mathcal{O}$. The exact form of this condition is arbitrary and thus represents a scheme dependence. The local operator $\mathcal{O}_L$ effectively represents the contributions from bilocal piece where there is arbitrarily high momentum in the loop. We choose the RI-SMOM scale μ_{RI} such that below this scale (i.e. $\mu < \mu_{\mathrm{RI}}$), the loop cannot be resolved and hence appears as an effective local operator.

The RI-SMOM procedure for a 4pt function is similar to that presented for the 2pt function as presented in section 5.3.1. For Z- and γ-exchange diagrams, where the external lepton states are already amputated, we calculate a Green's function of the form Eq. 5.74, but where the operator $\mathcal{O}$ must correspond to the relevant bilocal operator. For the W-W diagrams the calculation is analagous, although we must account for the additional free neutrino propagators that must be included in the lattice calculation; these must therefore be amputated in a similar manner to the quark propagators via Eq. 5.73. The momenta assignments we use for the 4pt-functions are

$$p_1 = (\xi,\xi,0,0)\,,\quad p_2 = (\xi,0,\xi,0)\,,\quad p_3 = (0,-\xi,0,-\xi)\,,\quad p_4 = (0,0,-\xi,-\xi)\,, \tag{5.86}$$

such that $\mu_{\mathrm{RI}}^2 = 2\xi^2$. One can easily verify that this choice satisfies the RI-SMOM condition

$$p_i^2 = q^2 = \mu_{\mathrm{RI}}^2, \tag{5.87}$$

with $q = p_1 - p_2$. The relevant diagrams that must be computed are shown in Fig. 5.7, and the momentum assignments have been highlighted.

In our rare kaon decay simulations, there is only one choice of local operator that mixes with the bilocal operator in each case, which hence may be used to regulate the divergence. For $K \to \pi\ell^+\ell^-$ this operator is Q_{7V} [Eq. (3.23)], for $K \to \pi\nu\bar{\nu}$ is it Q_ν [Eq. (3.45)]; the relevant hadronic contributions in both decays are described by the $K_{\ell 3}$ form factor f_+ [Eq. (5.24)].

5.3.3.2 Matching to $\overline{\mathrm{MS}}$ Scheme

Once we have renormalised the bilocal operator in the RI-SMOM scheme, we need to match it to the $\overline{\mathrm{MS}}$ scheme, in which the Wilson coefficients $C_i(\mu)$ entering the weak Hamiltonian are known. We must therefore relate the bilocal operator regulated in the RI-SMOM scheme to one regulated in the $\overline{\mathrm{MS}}$ scheme. In general, they are related by [33]

$$\begin{aligned}\{\mathcal{O}_A\mathcal{O}_B\}^{\overline{\mathrm{MS}}}(\mu) = {} & Z_A^{\mathrm{RI}\to\overline{\mathrm{MS}}} Z_B^{\mathrm{RI}\to\overline{\mathrm{MS}}}(\mu_{\mathrm{RI}},\mu)\,\{\mathcal{O}_A\mathcal{O}_B\}^{\mathrm{RI}}(\mu_{\mathrm{RI}}) \\ & + Y_{AB}(\mu_{\mathrm{RI}},\mu)\,\mathcal{O}_L^{\mathrm{RI}}(\mu_{\mathrm{RI}})\,. \end{aligned} \tag{5.88}$$

In the first line we thus convert the individual RI-SMOM renormalised operators to the $\overline{\mathrm{MS}}$ renormalised ones using the coefficients $Z_{A,B}^{\mathrm{RI}\to\overline{\mathrm{MS}}}$; in the second line we convert the regulation of the divergence from RI-SMOM to $\overline{\mathrm{MS}}$. We calculate Y_{AB} by imposing the same RI-SMOM condition as on the lattice, i.e. we take

$$\langle\{\mathcal{O}_A\mathcal{O}_B\}\rangle^{\overline{\mathrm{MS}}}(\mu)\Big|_{p_i^2=\mu_{\mathrm{RI}}^2} = \frac{Z_\psi^{\mathrm{RI}}(\mu_{\mathrm{RI}})}{Z_\psi^{\overline{\mathrm{MS}}}(\mu)} Y_{AB}(\mu_{\mathrm{RI}},\mu)\,\langle\mathcal{O}_L\rangle^{(0)}\,, \tag{5.89}$$

where we have imposed Eq. (5.85) to eliminate the RI-SMOM renormalised bilocal contribution, and imposed Eq. (5.70) for the local operator. Note the conversion of the quark field renormalisation Z_ψ to the $\overline{\mathrm{MS}}$ scheme. We therefore obtain $Y_{AB}(\mu_{\mathrm{RI}},\mu)$ via a perturbative calculation to the desired order in perturbation theory, where divergences are regulated using the $\overline{\mathrm{MS}}$ scheme.

This thus defines the bilocal matrix elements in the $\overline{\mathrm{MS}}$ scheme; this matrix element is then multiplied by the relevant Wilson coefficients for the operators $\mathcal{O}_A$ and $\mathcal{O}_B$. We remark however that it is still divergent, i.e. the Wilson coefficients alone do not cancel the renormalisation scale dependence of the bilocal operator. The divergence hence cancels between the bilocal and local parts of the entire calculation, i.e.

$$A = \sum_{A,B} C_A(\mu)\,C_B(\mu)\,\langle f|\,\{\mathcal{O}_A\mathcal{O}_B\}\,|i\rangle^{\overline{\mathrm{MS}}}(\mu) + C_L(\mu)\,\langle f|\mathcal{O}_L|i\rangle\,. \tag{5.90}$$

This demonstrates that the local piece acts both as a counterterm to the divergence within the bilocal matrix element, as well as giving the short-distance contribution of physics above the scale μ [33].

Chapter 6

Results of $K \to \pi\ell^+\ell^-$ Simulations

In this chapter I report on the results of my analysis of the long-distance contributions to $K \to \pi\gamma^*$ matrix elements. Our primary focus is the $K^+ \to \pi^+\gamma^* \to \pi^+\ell^+\ell^-$ decay, although I will also comment briefly on the decay with neutral hadrons. The calculation I present is the first exploratory attempt at a nonperturbative lattice QCD calculation of $K \to \pi\ell^+\ell^-$ amplitudes. The possibility of such a calculation was first introduced in [25], where it was shown that lattice methods can in principle be used to compute such decay amplitudes. These ideas were developed further in [19], where the details of the analysis to extract $K \to \pi\ell^+\ell^-$ matrix elements using renormalised operators were introduced, with full control of ultraviolet divergences. This necessitates the introduction of a charm quark in the calculation, such that logarithmic divergences cancel by the GIM mechanism. The objective of these studies is to demonstrate how the results of [19, 25] can be applied in actual numerical simulations to extract the desired physical information.

The layout of this chapter is as follows. I will introduce the details of our $K \to \pi\ell^+\ell^-$ simulations in section 6.1, before moving onto a more in-depth discussion of the implementation in section 6.2. I will then demonstrate the required analysis to extract the desired matrix elements and form factors in section 6.3. I will then demonstrate how our exploratory results may be used to test previous work based on ChPT in section 6.4. Finally, I will discuss the future plans for a physical point $K \to \pi\ell^+\ell^-$ simulation in section 6.5. The analysis I present in this chapter is my own work. The numerical data were generated jointly by myself and Dr. Antonin Portelli using the codebase UKHadron. The results presented in this chapter have been published in Ref. [2].

6.1 Details of the Simulation

This exploratory study was performed using a $24^3 \times 64$ lattice with an inverse lattice spacing of $1/a = 1.785(5)\,\mathrm{GeV}$ [131, 132], employing Shamir domain wall fermions [104] with Iwasaki gauge action [96]. The ensemble has a residual mass of $am_{res} = 3.08(4) \times 10^{-3}$, a pion mass of 430(2) MeV and a kaon mass of 625(2) MeV. In order to cancel divergences with the GIM mechanism we include a valence charm quark with a bare mass of $am = 0.2$. Using the mass renormalisation factor $Z_m^{\overline{\mathrm{MS}}}(2\,\mathrm{GeV}) = 1.498(34)$ for this lattice [131], this corresponds to an unphysical charm quark of mass $m_c^{\overline{\mathrm{MS}}}(2\,\mathrm{GeV}) = 543(13)\,\mathrm{MeV}$. We use a sample of 128 configurations, each separated by 20 molecular dynamics time units.

6.2 Setup of the calculation

I now move to a detailed explanation of the setup of our calculation. In this section I will introduce the schematic of the relevant 4pt correlator and give an overview of the propagators we choose to use to perform each of the contractions involved in the construction of the correlator. In Sec. 6.2.1 I will give a more technical discussion of the implementation.

In our lattice calculation we aim to measure the "unintegrated" 4pt correlator

$$C_\mu^{(4)}\left(t_K, t_H, t_J, t_\pi, \mathbf{p}_K, \mathbf{p}_\pi\right) = \\ \sum_{\mathbf{x}} \sum_{\mathbf{y}} e^{-i\mathbf{q}\cdot\mathbf{x}} \left\langle \tilde{\phi}_\pi\left(t_\pi, \mathbf{p}_\pi\right) T\left[J_\mu\left(t_J, \mathbf{x}\right) H_W\left(t_H, \mathbf{y}\right)\right] \tilde{\phi}_K^\dagger\left(t_K, \mathbf{p}_K\right)\right\rangle, \quad (6.1)$$

where $\tilde{\phi}_P\left(t, \mathbf{p}_P\right)$ $(P = \pi, K)$ is the annihilation operator for a pseudoscalar meson with spatial momentum $\mathbf{p}_P$ at a time t, and t_P is the source timeslice of the meson. Here we take the electromagnetic current J_μ in Eq. (5.1) to be the conserved lattice vector current. For our choice of action we use the Shamir domain wall conserved current [104]. This choice is made to simplify the renormalisation, as described in section 5.3.3.

We simulate a kaon with momentum $\mathbf{p}_K = 0$ at a time $t_K = 0$ decaying into a pion with momentum $\mathbf{p}_\pi$ at $t_\pi = 28$. We have considered three separate final state pion momenta: $\mathbf{p}_\pi = \frac{2\pi}{L}(1,0,0)$, $\mathbf{p}_\pi = \frac{2\pi}{L}(1,1,0)$ and $\mathbf{p}_\pi = \frac{2\pi}{L}(1,1,1)$, where $L = 24$ is the spatial extent of our lattice. We will thus label each kinematical case by the momentum $\mathbf{p}_\pi$. In all cases the current is situated halfway between the kaon and pion at $t_J = 14$; this position is chosen such that we can integrate over t_H in a window around the current and be far enough away from the positions of the pion/kaon interpolators to avoid the contamination of excited state contributions. We use Coulomb gauge-fixed wall sources in our calculation to give good overlap with the ground state pion and kaon, which allows us to keep the kaon-pion source-sink separation as small as possible to achieve the best possible signal for the amplitude.

The computation of the full set of diagrams corresponding to the rare kaon decay can be accomplished by computing 14 propagators. Four are required to connect the kaon/pion

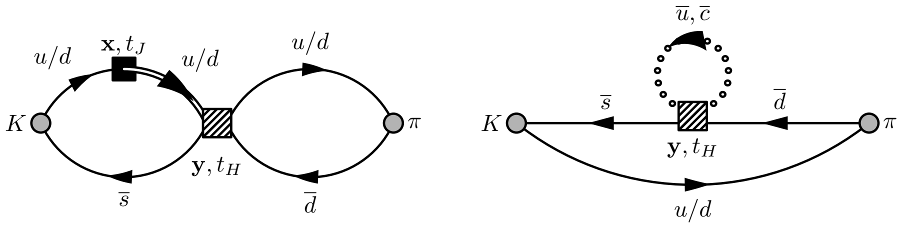

Figure 6.1: Demonstration of how propagators are used to construct diagrams. The position of the H_W operator is indicated by the shaded square, and may be placed at any spacetime position. The insertion of the current is denoted by a black square, fixed on an single time slice and summed over space. The double line represents the part of the propagator computed using a sequential inversion; the dotted line represents the loop propagator, computed using spin-color diluted random volume sources.

sources to the H_W insertion: one strange and one light for the kaon; two light propagators with momenta $\mathbf{0}$ and $\mathbf{p}_\pi$ to produce a pion with momentum $\mathbf{p}_\pi \neq \mathbf{0}$ (this also allows us to make a pion with momentum $\mathbf{0}$). Two more propagators are needed for the loops in the S and E and disconnected diagrams (one light, one charm), and one more for the strange loop in disconnected diagrams. We use each of these seven propagators to calculate a sequential propagator to achieve the current insertion to bring us up to 14. The types of propagators used are shown schematically in Fig. 6.1. Furthermore, to construct all the 2pt and 3pt functions required for our analysis procedure, we also compute one additional strange propagator with momentum $\mathbf{p}_\pi$ such that we can produce a kaon with momentum $\mathbf{p}_\pi$.

6.2.1 Details of the Implementation

The loops in the S and E diagrams require us to compute the propagator from each site to that exact same site for each colour and spin index. This is readily achieved using random spin-colour diluted volume sources, as described in section 4.3.2.3. With this propagator we may insert the operators that make up H_W at any position on the lattice, thus enabling the summation of the position of H_W over the whole lattice.

The insertions of the electromagnetic current are achieved using sequential propagators, which fixes the current insertion to a time t_J. We only consider the element $\mu = 0$ of the current to save computational resources, which is enough to extract the form factor using Eq. (5.5). With the current fixed at a single time the time ordering of the operators is straightforward to implement, which simplifies our analysis procedure. Another advantage is that the current is automatically summed over the entire spatial volume. For our lattice we determine numerically that this spatial sum reduces the statistical error by approximately a factor of 3. The primary disadvantage of this method is that we must perform a new set of inversions if we wish to consider the current at another temporal position, with a different initial (final) state momentum of the kaon (pion) or for a different polarisation.

In our present calculation we omit the disconnected diagrams where the electromagnetic current is self-contracted (see Fig. 5.2). The primary reason for this is practical: we expect the disconnected contribution to be very noisy and thus would require a significantly larger statistical sample to be measured to obtain a signal comparable to the other diagrams (relative to noise). However we also expect the disconnected contribution to be suppressed by a factor of $1/N_c$ and by the approximate $SU(3)$ flavour symmetry. In the continuum we would expect the disconnected contribution to have $\sim 10\%$ of the contribution of the connected part [133]. With our choice of masses the $SU(3)$ suppression is stronger and so the disconnected diagrams are expected to be further suppressed. Nevertheless, our simulation is set up such that the disconnected contribution can be calculated separately to the connected contributions, and can be added at a later stage without having to recalculate any propagators or the connected diagrams that we have already.

For our simulation we choose to use $N_\eta = 14$ random noise sources on each configuration to obtain a reasonable signal for the loop function of the S and E diagrams. While increasing N_η would increase our precision further, we found $N_\eta = 14$ to be a reasonable compromise when also taking into account available computational resources. In addition to this we translate the computation of the 4pt correlator to $N_t = 12$ positions over the time direction of our lattice on a single configuration. Each translation ultilises the same noise propagators generated for the loop diagrams; however we find the signal-to-noise ratio of the S and E diagrams increases by approximately a factor of 3 when we include these additional translations. This is consistent with the increase in statistical precision expected if the translations are statistically independent of each other.

The time positions for the operators in this decay were chosen such that there exists a large enough window to fully integrate over t_H on either side of the current. In such a setup, we found that the closer the position of the current to the pion, the better the signal for the decay. We therefore tested simulating with an additional time position for the current placed closer to the pion such that we may integrate over the region $[t_J - T_a, t_J]$ with an improved precision. We found that this second current insertion would increase the simulation cost by $\sim 50\%$, but reduce the statistical error by a factor of $\sim 25\%$. However the additional cost of these inversions means that the decay can only be translated across eight time positions in the same amount of CPU time as it costs to perform 12 translations with a single current position. We found that the loss of precision from considering fewer translations ultimately cancelled the increase from the second current position.

Description	Source Type	Number of Inversions		
		Light	Strange	Charm
C and W propagators	Gauge-fixed wall	$3N_t$	N_t	0
S and E loops	Random volume	N_η	0	N_η
Current insertions	Sequential	$(3+N_\eta)\,N_t$	N_t	$N_\eta N_t$
Analysis supplements	Gauge-fixed wall	0	N_t	0
Total	-	$N_\eta + N_t\,(6+N_\eta)$	$3N_t$	$N_\eta\,(N_t+1)$
$N_\eta = 14,\ N_t = 12$	-	254	36	182

Table 6.1: Summary of propagators calculated in our simulation for a single choice of pion momentum on a single configuration, and the corresponding number of inversions required. N_η is the number of noise vectors used in the computation of the quark loops; N_t is the number of translations in the time direction across a single configuration at which all the contractions are computed.

On a single configuration we thus require 254 light propagator inversions, 36 strange inversions and 182 charm inversions (including disconnected diagrams would require a further 182 strange inversions). This is summarised in Table 6.1. Because of this large number of light propagators we made use of the HDCG algorithm [134] to accelerate the light-quark inversions. The overhead of deflating the Dirac operator costs the equivalent of two to three conjugate gradient (CG) inversions; however the cost of a light-quark inversion is subsequently reduced by a factor of 4.

6.3 Numerical Results

Ultimately the aim of this calculation is to demonstrate that the matrix element of $K \to \pi\gamma^*$ decays can be determined with controlled systematic errors. In this section I will discuss the numerical results of our simulation, and include a critical discussion of our two primary analysis techniques. Unless otherwise specified, all numerical values will be given in lattice units.

While it is also possible to compute the neutral decay $K_S \to \pi^0\ell^+\ell^-$ using our lattice data, with our current statistics we find that we do not obtain any worthwhile signal for this correlator. The error is dominated by the additional, disconnected contractions shown in Fig. 5.3. These contractions appear much noisier than the other diagrams, and their error is many times larger than the signal from the remaining contractions. The difficulty to extract a signal from our data can also be understood physically: we have only considered photons with small momenta; the structure of the kaon/meson is thus not well enough resolved to obtain a clear signal. When we simulate the decay into a pion with a higher momentum the structure is better resolved, although the correlators with momentum are naturally more noisy. This makes them difficult to analyse with the size of our present statistical sample. For this reason we will focus exclusively on the charged channel.

To obtain the decay amplitude we must consider the "integrated" 4pt correlator,

$$I_\mu\left(T_a, T_b, \mathbf{p}_K, \mathbf{p}_\pi\right) = e^{-(E_\pi(\mathbf{p}_\pi)-E_K(\mathbf{p}_K))t_J} \sum_{t_H=t_J-T_a}^{t_J+T_b} \widehat{C}_\mu^{(4)}\left(t_H, t_J, \mathbf{p}_K, \mathbf{p}_\pi\right), \tag{6.2}$$

in the limit $T_a, T_b \to \infty$ [19]. We define $\widehat{C}_\mu^{(4)}$ as the "reduced" correlator after dividing out the source/sink factors and normalisations which do not contribute to the final amplitude from Eq. (6.1), i.e.

$$\widehat{C}_\mu^{(4)} = \frac{C_\mu^{(4)}}{N_{\pi K}}, \quad N_{\pi K} = \frac{N_\pi N_K^\dagger L^3}{4E_\pi\left(\mathbf{p}_\pi\right) E_K\left(\mathbf{p}_K\right)} e^{-t_\pi E_\pi(\mathbf{p}_\pi)+t_K E_K(\mathbf{p}_K)}, \tag{6.3}$$

with $N_\pi = \langle \pi\left(\mathbf{p}_\pi\right) | \tilde{\phi}_\pi\left(\mathbf{p}_\pi\right) | 0 \rangle$, $N_K^\dagger = \langle 0 | \tilde{\phi}_K^\dagger\left(\mathbf{p}_K\right) | K\left(\mathbf{p}_K\right) \rangle$, and $E_K\left(\mathbf{p}_K\right)$ and $E_\pi\left(\mathbf{p}_\pi\right)$ are the initial state kaon and final state pion energies respectively. These parameters are extracted from fits of the relevant two-point (2pt) correlation functions, which we discuss below. We account for the factor of L^3 (i.e. the spatial volume) as we integrate both $\mathbf{x}$ and $\mathbf{y}$ over all space. The exponential factor outside the integral in Eq. (6.2) effectively translates the decay to $t_J = 0$ (as is allowed by translational invariance), such that our analysis matches up with the discussion presented in section 5.2.

6.3.1 2pt and 3pt Correlators

The first stage of the analysis is to fit the 2pt functions corresponding to the kaon and pion. This is necessary to be able to divide out the source/sink normalisation factors N_P, $P = \pi, K$, that appear in Eq. (6.3), as well as for removing exponentially growing intermediate state contributions. The correlation functions we consider for these states are

$$C_P^{(2)}\left(t_P, t, \mathbf{p}\right) = \left\langle \tilde{\phi}_P\left(t, \mathbf{p}\right) \tilde{\phi}_P\left(t_P, \mathbf{p}\right) \right\rangle. \tag{6.4}$$

The analysis techniques for such correlation functions are presented in section 4.4.1; we thus fit our data to Eq. 4.99. This allows us to extract the wall source/sink factors for each meson, as well as all required meson energies. In our simulations of rare kaon decays we use wall source and sink smearing for the kaon and pion, as explained in section 4.3.2.1. However the sink smearing is applied after the inversion; hence we may also produce a correlator with a point sink. In general we find that we obtain a better signal when using a point sink; this allows us to obtain a better estimate for the energy from these correlators; however the source/sink factors N_P must be obtained using the wall-sinked correlator. For our simulations we consider in total 4 2pt functions for each of

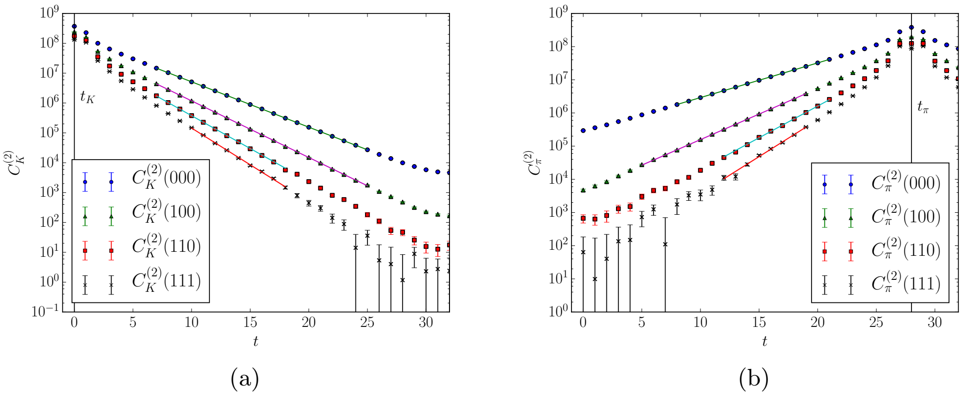

(a) (b)

Figure 6.2: Plots showing fits to (a) kaon and (b) pion (folded) correlators. The source times for each meson are shown by the vertical black lines.

	$\mathbf{p}$			
	$(0,0,0)$	$\frac{2\pi}{L}(1,0,0)$	$\frac{2\pi}{L}(1,1,0)$	$\frac{2\pi}{L}(1,1,1)$
$E_K(\mathbf{p})$	0.34990(39)	0.43663(80)	0.5061(14)	0.5665(36)
$E_\pi(\mathbf{p})$	0.24088(38)	0.3545(14)	0.4402(18)	0.5118(31)
$N_K(\mathbf{p})$	92.69(25)	76.63(34)	65.96(44)	58.6(1.3)
$N_\pi(\mathbf{p})$	87.91(25)	68.97(63)	59.00(51)	52.66(70)
$\mathcal{M}_H(\mathbf{p})$	0.000516(16)	0.00053(18)	0.0032(19)	-0.007(12)
$\mathcal{M}_{\mu=3}^{J,K}(\mathbf{0},\mathbf{p})$	-	0.6733(33)	0.6387(64)	0.635(14)
$\mathcal{M}_{\mu=3}^{J,\pi}(\mathbf{0},\mathbf{p})$	-	0.5158(53)	0.5302(99)	0.590(26)
$c_s(\mathbf{p})$	0.000240(8)	-	-	-

Table 6.2: Table showing fit results to 2pt and 3pt correlators. The double line separates results obtained from 2pt (above) and 3pt (below) correlators.

the kaon and pion, corresponding to the choices of momenta used in our simulations. The results of the fits are shown in Table 6.2; and the corresponding plots of the correlators are shown in Fig. 6.2.

The next stage of the analysis is to extract the matrix elements from 3pt correlators that are necessary for the removal of exponentially growing intermediate state contributions in the 4pt correlator analysis using method 1. The required matrix elements are shown in Eq. (5.37). The 3pt matrix element for the H_W operator is obtained from the correlator

$$C_H(t_K, t_\pi, t_H, \mathbf{p}) = \sum_{\mathbf{x}} \left\langle \tilde{\phi}_\pi(t_\pi, \mathbf{p}) \, H_W(t_H, \mathbf{x}) \, \tilde{\phi}_K(t_K, \mathbf{p}) \right\rangle . \tag{6.5}$$

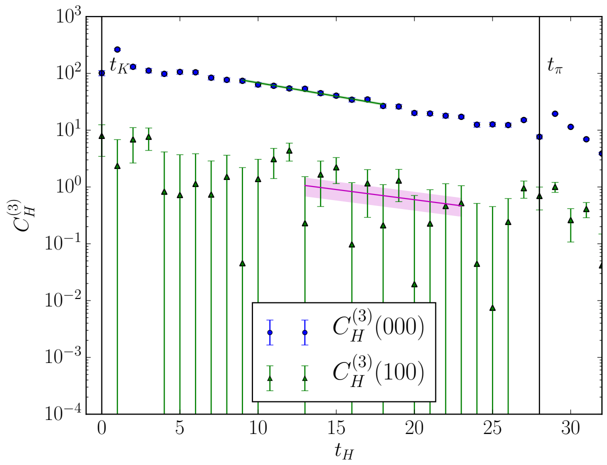

Figure 6.3: Plots of fits to 3pt correlation functions used to extract H_W matrix elements. Results for $\mathbf{p} = (1,1,0)$ and $\mathbf{p} = (1,1,1)$ are not shown as they are too noisy to extract a significant signal.

The asymptotic behaviour of this correlator is given by Eq. (4.103), where the kaon source and pion sink are fixed at t_K and t_π respectively, and we vary the insertion of the H_W operator at t_H. On the other hand, the 3pt matrix element with the vector current insertion is obtained from

$$C^{\mu}_{J,P}\left(t_P, t_J, t, \mathbf{p}_P, \mathbf{p}\right) = \sum_{\mathbf{x}} \left\langle \tilde{\phi}_P\left(t, \mathbf{p}\right) J^{\mu}\left(t_J, \mathbf{x}\right) \tilde{\phi}^{\dagger}_P\left(t_P, \mathbf{p}_P\right) \right\rangle e^{-i\mathbf{q}\cdot\mathbf{x}}, \tag{6.6}$$

for a meson $P = \pi, K$. To obtain the matrix element in this case, the current insertion is fixed at t_J and thus we vary the position of the sink t. In order to remove the exponentially growing state, we only need the 3pt correlator $C^{\mu}_{J,\pi}$ and $C^{(3)}_H\left(\mathbf{p}_K\right)$. However, it is useful for the analysis of the 4pt correlator to also have $C^{\mu}_{J,K}$ and $C^{(3)}_H\left(\mathbf{p}_\pi\right)$. We will discuss this point further in section 6.3.3. The 3pt fit results are given in Table 6.2; with plots showing the fits to $C^{(3)}_H$ in Fig. 6.3 and $C^{\mu}_{J,P}$, $P = \pi, K$ in Fig. 6.4.

Finally, it is also necessary to compute c_s for the removal of exponentially growing contributions using method 2. The parameter is extracted from the ratio of 3pt correlation functions

$$c_s\left(\mathbf{p}_K\right) = \frac{C^{(3)}_H\left(\mathbf{p}_K\right)}{C^{(3)}_{\bar{s}d}\left(\mathbf{p}_K\right)}, \tag{6.7}$$

in the region $t_K \ll t_{\mathcal{O}} \ll t_\pi$, where $t_{\mathcal{O}}$ is the position at which the operator $\mathcal{O} = H_W$ or $\bar{s}d$ is inserted. Equivalently c_s may be extracted from the ratio of similar 4pt functions in the region $t_K \ll t_H \ll t_J$, where we may assume that the 4pt functions are dominated by the exponentially growing contribution of the single-pion intermediate state. In Fig. 6.5 we show the determination of this parameter using Eq. (6.7) and either 3pt or 4pt

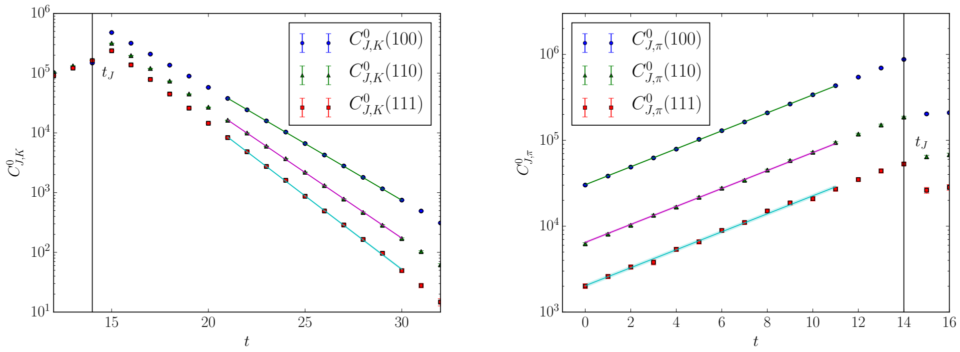

(a) (b)

Figure 6.4: Plots of fits to 3pt (a) kaon and (b) pion correlation functions with a vector current insertion. In each case the initial meson is at rest; the legend indicates the momentum of the final state meson.

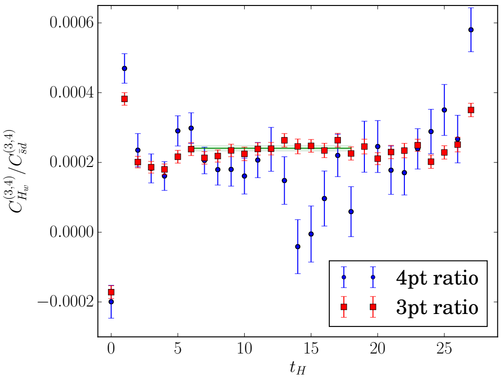

Figure 6.5: Determination of the parameter c_s from a fit to the ratio of 3pt H_W and $\bar{s}d$ correlators. The corresponding ratio of the 4pt correlator (with $\mathbf{p}_\pi = \frac{2\pi}{L}(1,0,0)$) is also shown. The position of the plateau corresponds to $c_s = 0.000240(8)$.

functions. A cleaner signal is obtained from the ratio of 3pt functions, although the ratio of 4pt functions does also agree as expected for $t_K \ll t_H \ll t_J$ (albeit with much larger errors).

6.3.2 4pt correlators

In Fig. 6.6 we show the contributions of each of the diagrams to the 4pt correlator that correspond to the charged rare kaon decay. A comparison of Figs. 6.6(a) and 6.6(b) shows that the dominant contribution to the decay comes from the Q_2 operator, i.e. the W and S diagrams. Furthermore as the loop diagrams S and E are considerably noisier than W and C, it follows that the S diagram will dominate the error on our final result.

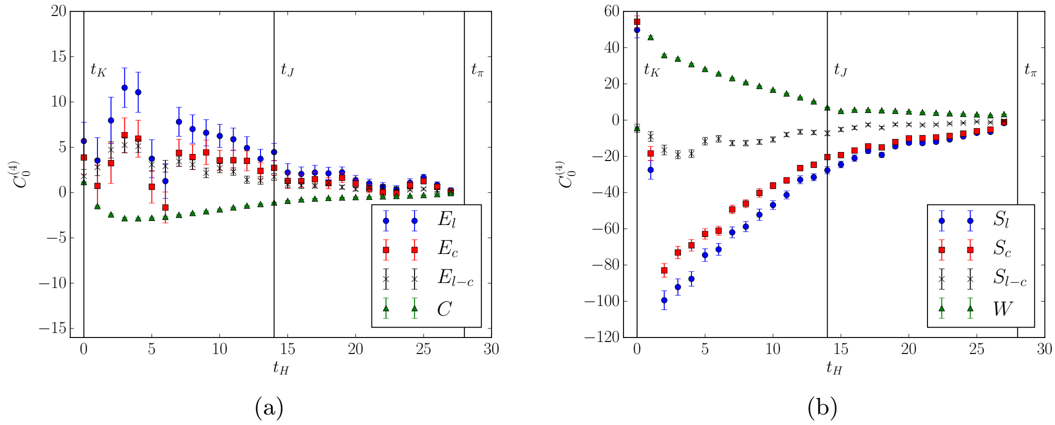

Figure 6.6: The contributions of each of the diagrams to the rare kaon decay corresponding to the weak operators (a) Q_1 and (b) Q_2, both before and after the GIM subtraction, shown for the example kinematic of $\mathbf{p}_K = (0,0,0)$, $\mathbf{p}_\pi = \frac{2\pi}{L}(1,0,0)$. Each diagram has been constructed using the appropriate fractional quark charges (excluding the overall charge factor e), and the correlators have been multiplied by the relevant renormalisation constants and Wilson coefficients for matching to the $\overline{\text{MS}}$ scheme. Time positions of the kaon/pion interpolators and current insertion are indicated.

We remark that each diagram in Fig. 6.6 has already been multiplied by the appropriate renormalisation constants to match to the $\overline{\text{MS}}$ scheme, as defined in Table 5.2. For the scale $\mu = 2.15\,\text{GeV}$, we thus multiply our bare lattice operators Q_1 and Q_2 by the coefficients $C_1^{\text{lat}} = -0.2216$ and $C_2^{\text{lat}} = 0.6439$ respectively. For this analysis we neglect any systematic errors on these Wilson coefficients. However, a full discussion of systematic errors of the renormalisation of the H_W operator has previously been given in the context of $K \to \pi\pi$ decays; see e.g. Refs. [135, 136]. It may be noted that the results for the Wilson coefficients were computed in Ref. [1], where the ensembles used to perform the nonperturbative renormalisation have the same lattice spacing and action, but a smaller volume. The results are also valid for our lattice as the renormalisation procedure depends upon the UV behavior of the theory and thus is insensitive to finite volume effects.

Additionally in Fig. 6.6 we show how the S and E diagrams are obtained by subtracting the charm loop diagram from the up quark loop diagram, i.e. the GIM subtraction. Here we expect the GIM subtraction to be more severe than in the physical case, as we are using a lighter-than-physical charm quark and a heavier-than-physical light quark. With physical masses we should expect the S diagram to have a larger magnitude. In the final correlator the S and W diagrams appear to add destructively; this may have a severe effect on the final result if there is a large degree of cancellation between the contributions of the S and W diagrams to the final matrix element. The combined rare kaon decay 4pt correlators that we analyse are shown in Fig. 6.7. We show these correlators before and

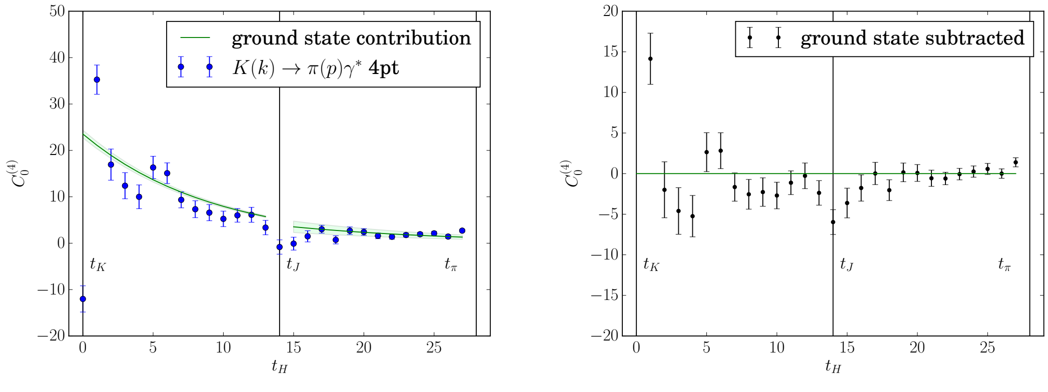

(a) (b)

Figure 6.7: (a) The 4pt rare kaon decay correlator measured in our simulation with $\mathbf{k} = (0, 0, 0)$ and $\mathbf{p} = \frac{2\pi}{L}(1, 0, 0)$. The ground state contribution has been constructed from fits to 2pt and 3pt correlators. (b) The 4pt correlator after removing the ground state contribution (i.e. the single-pion and single kaon intermediate states). Time positions of the kaon/pion interpolators and the current insertion are indicated.

after the removal of unphysical exponential terms that appear as a relic of the Euclidean formulation [19]. The removal of these terms is discussed in the following section.

6.3.3 Removal of single-pion exponential: Method 1

The main difficulty of this analysis is the removal of the exponential term that grows with increasing T_a; however in practice we find that it is necessary to also consider the term that falls exponentially with T_b [as seen in the second line of Eq. (5.36)], as the integral does not converge in the available time extent. This can be attributed to the fact that here the kaon-pion mass difference is rather small; hence the exponent for the exponential decay is small. In practice therefore it is necessary also to remove the single kaon contribution that decays with T_b in a manner similar to the exponentially growing term by reconstructing the state from 2pt/3pt functions. Asymptotically the integrated 4pt correlator can be written in the form:

$$\begin{aligned} I_\mu\left(T_a, T_b, \mathbf{p}_K, \mathbf{p}\right) =& A_\mu\left(\mathbf{p}_K, \mathbf{p}_\pi\right) + c_\mu^1\left(\mathbf{p}_K, \mathbf{p}_\pi\right) e^{\Delta_\pi^a T_a}\left[\frac{\Delta_\pi^a}{1 - e^{-\Delta_\pi^a}}\right] \\ &+ c_\mu^2\left(\mathbf{p}_K, \mathbf{p}_\pi\right) e^{-\Delta_K^b T_b}\left[\frac{\Delta_K^b}{e^{\Delta_K^b} - 1}\right] + \ldots, \end{aligned} \tag{6.8}$$

with $\Delta_\pi^a = E_K\left(\mathbf{p}_K\right) - E_\pi\left(\mathbf{p}_K\right)$ and $\Delta_K^b = E_K\left(\mathbf{p}_\pi\right) - E_\pi\left(\mathbf{p}_\pi\right)$. The terms in the square brackets, which tend towards 1 in the continuum limit, account for the corrections necessary to treat the single meson intermediate states (i.e. the ground state contributions) using a discrete formulation. In terms of particle energies and matrix elements from 3pt functions we can write

$$\begin{aligned} c^1_\mu\left(\mathbf{p}_K,\mathbf{p}_\pi\right) &= \frac{\mathcal{M}^{J,\pi}_\mu\left(\mathbf{p}_K,\mathbf{p}_\pi\right)\mathcal{M}_H\left(\mathbf{p}_K\right)}{2E_\pi\left(\mathbf{p}_K\right)\Delta^a_\pi}, \\ c^2_\mu\left(\mathbf{p}_K,\mathbf{p}_\pi\right) &= -\frac{\mathcal{M}^{J,K}_\mu\left(\mathbf{p}_K,\mathbf{p}_\pi\right)\mathcal{M}_H\left(\mathbf{p}_\pi\right)}{2E_K\left(\mathbf{p}_\pi\right)\Delta^b_K}, \end{aligned} \tag{6.9}$$

where $\mathcal{M}^{J,P}_\mu\left(\mathbf{p}_K,\mathbf{p}_\pi\right) = \langle P,\mathbf{p}_\pi|J_\mu|P,\mathbf{p}_K\rangle$ and $\mathcal{M}_H\left(\mathbf{p}_K\right) = \langle K\left(\mathbf{p}_K\right)|H_W|\pi\left(\mathbf{p}_K\right)\rangle$. Our analysis thus proceeds by removing the terms proportional to c^1_μ and c^2_μ from the 4pt correlator, and fitting the remainder to a constant to obtain A_μ, which is the amplitude in Euclidean space, up to a factor as seen in Eq. (5.29).

It is indeed possible to use Eq. (6.8) to fit the 4pt function directly to remove the ground state contributions. Because the exponents can be obtained much more accurately from 2pt functions, we simply fit the parameters A_μ, c^1_μ and c^2_μ in the region where the ground state contributions dominate. We find that we obtain consistent results when we use this procedure.

The computed values for the coefficients c^1_0 and c^2_0 [obtained using both Eq. (6.9) and the direct 4pt fit] are shown in Table 6.3. We remark that the coefficient c^2_0 becomes significantly less well determined when we increase the momentum of the pion. The reason for this is that the matrix element $\mathcal{M}_H\left(\mathbf{p}\right)$ is difficult to determine precisely when we have $\mathbf{p} \neq \mathbf{0}$. We can thus avoid introducing an unnecessarily large statistical error either by fitting c^2_0 directly from the 4pt correlator or by making well-motivated approximations. The two approximations we have considered are $c^2_0 = -c^1_0$, and $\mathcal{M}_H\left(\mathbf{p}_K\right) = \mathcal{M}_H\left(\mathbf{p}_\pi\right)$. The first approximation holds exactly when $\mathbf{p}_K = \mathbf{p}_\pi$; the second holds exactly in the $SU(3)$ flavour symmetric limit, i.e. when $M_\pi = M_K$. A short proof of each of these statements can be found in Appendix A. A summary of the matrix elements obtained using each of these methods can be found in Table 6.4, and are displayed graphically in Fig. 6.8. We remark that the approximations of c^2_0 need not be exact: they are sufficient if the systematic error on the approximation is significantly smaller than the statistical error on the final signal for the amplitude. Taking correlated differences between the different analysis techniques reveals that the systematic errors on these approximations are substantially less than the statistical errors on the matrix elements.

In Fig. 6.9(a) we display the T_a and in Fig. 6.9(b) the T_b dependence of the integrated 4pt correlator having removed the ground state contributions. In Fig. 6.9(b) we see that after the analytic removal of the single-pion intermediate state, no other exponentially growing states are discernible beyond statistical errors. This suggests that contributions from excited states are adequately suppressed. Fig. 6.9(b) demonstrates the slow exponential decay in T_b which is caused by the small exponent $E_K(\mathbf{p}_\pi) - E_\pi(\mathbf{p}_\pi)$. This appears to be a problem only because our pion and kaon masses are unphysically close; in simulations closer to the physical masses the exponent $E_K(\mathbf{p}_\pi) - E_\pi(\mathbf{p}_\pi)$ will become larger; hence the residual T_b dependence will decay more quickly. Consequently this subtraction may

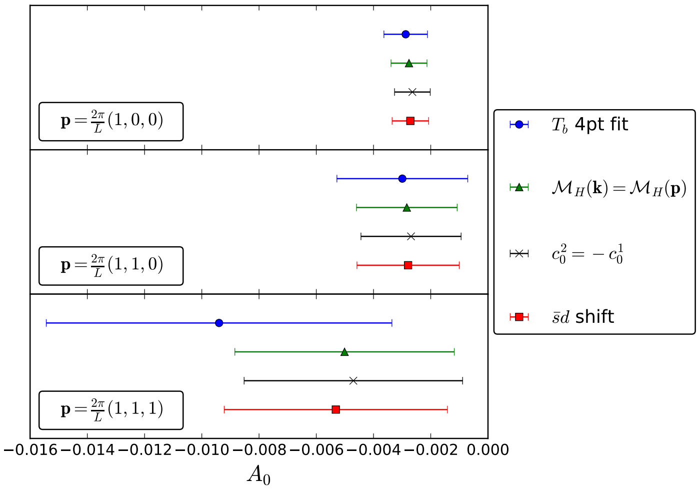

Figure 6.8: Plot of the amplitudes (in lattice units) obtained using each of the different analysis methods.

Coefficient	Description	Kinematic ($\mathbf{p}_\pi$)		
		$\frac{2\pi}{L}(1,0,0)$	$\frac{2\pi}{L}(1,1,0)$	$\frac{2\pi}{L}(1,1,1)$
$c_0^1(\mathbf{p}_K, \mathbf{p}_\pi)$	4pt fit	0.00523(45)	0.0056(13)	0.0050(33)
	2pt/3pt	0.00538(18)	0.00549(20)	0.00611(32)
$c_0^2(\mathbf{p}_K, \mathbf{p}_\pi)$	$\mathcal{M}_H(\mathbf{p}_\pi) = \mathcal{M}_H(\mathbf{p}_K)$	-0.00487(18)	-0.00494(22)	-0.00532(48)
	4pt fit	-0.00464(62)	-0.0046(22)	0.0012(56)
	2pt/3pt	-0.0050(17)	-0.025(20)	0.06(12)
$(c_0^1 + c_0^2)(\mathbf{p}_K, \mathbf{p}_\pi)$	$\mathcal{M}_H(\mathbf{p}_\pi) = \mathcal{M}_H(\mathbf{p}_K)$	0.000516(44)	0.00055(12)	0.00079(38)
	4pt fit	0.00075(61)	0.0009(22)	0.0073(56)
	2pt/3pt	0.0004(17)	-0.020(20)	0.06(12)

Table 6.3: Parameters of Eq. (6.8) (in lattice units) obtained via analytic reconstruction using 2pt and 3pt fit results or fitting the integrated 4pt correlator directly. For c_0^2 the result using the approximation $\mathcal{M}_H(\mathbf{p}_\pi) = \mathcal{M}_H(\mathbf{p}_K)$ is also shown.

become unnecessary in future studies, although in any case it can be removed as we have shown here.

6.3.4 Removal of single-pion exponential: Method 2

The integrated correlators after shifting by the 4pt correlator with H_W replaced by $\bar{s}d$ are shown in Fig. 6.10. We obtain the matrix element by fitting the correlator to a constant in the region where both sides of the integral plateau. We note that the $\bar{s}d$

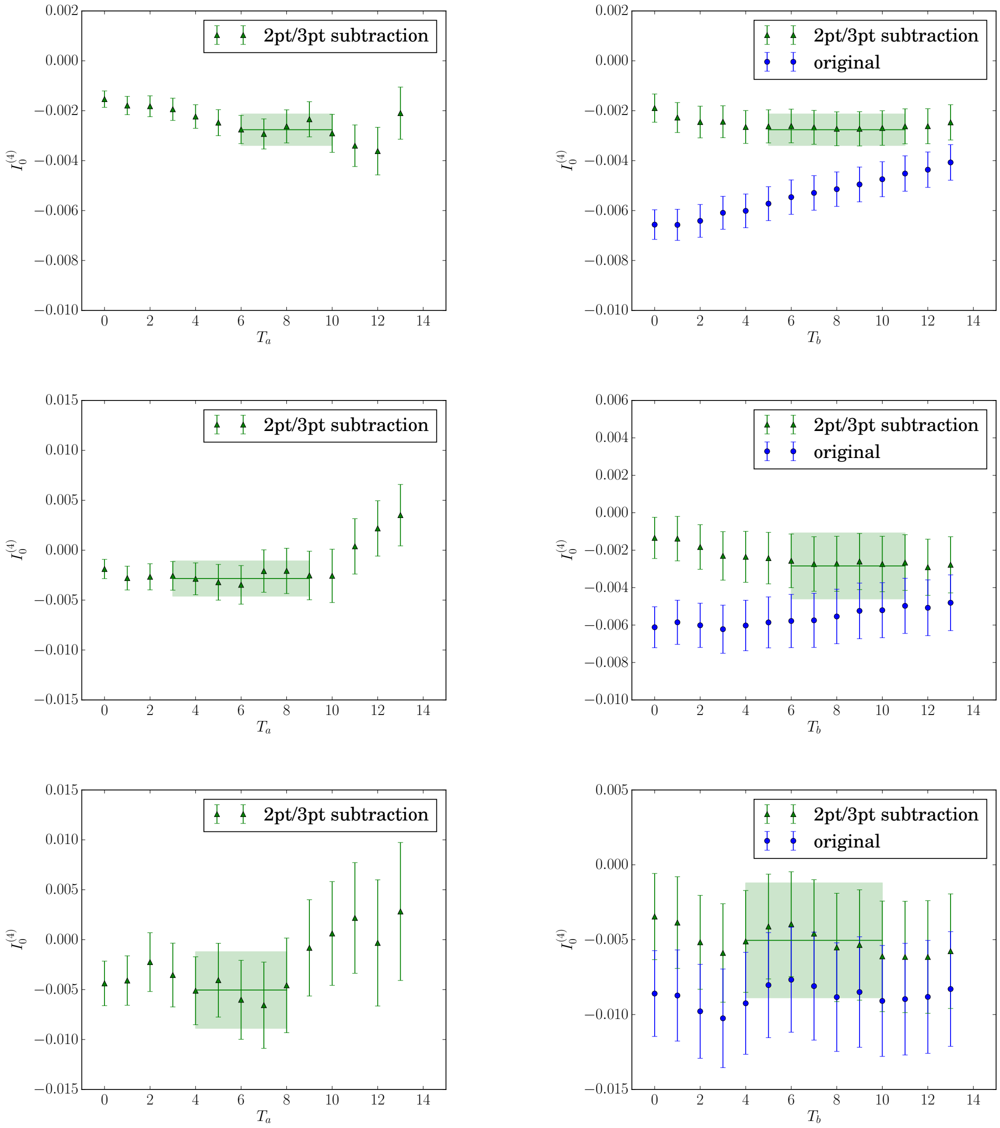

(a) (b)

Figure 6.9: The integrated 4pt correlator, shown for (a) T_b fixed at its lower limit to demonstrate the T_a dependence and (b) T_a fixed at its lower limit to demonstrate the T_b dependence. The kinematics shown are for $\mathbf{p}_\pi = (1,0,0)$, $\mathbf{p}_\pi = (1,1,0)$, $\mathbf{p}_\pi = (1,1,1)$ top to bottom. The single-pion exponential growth has been removed using method 1, with the approximation $\mathcal{M}_H(\mathbf{p}_\pi) = \mathcal{M}_H(\mathbf{p}_K)$. The position of the plateaus corresponds to $A_0 = -0.0028(6)$, $A_0 = -0.0028(18)$, $A_0 = -0.0050(38)$ top to bottom, obtained by fits to the data over the indicated ranges.

Analysis	Kinematic	A_0	$A_0^{C,W}$	$A_0^{S,E}$
method 1 ($\mathcal{M}_H(\mathbf{p}_\pi) = \mathcal{M}_H(\mathbf{p}_K)$)	$\mathbf{p}_\pi = \frac{2\pi}{L}(1,0,0)$	-0.00276(63)	-0.00161(14)	-0.00106(60)
	$\mathbf{p}_\pi = \frac{2\pi}{L}(1,1,0)$	-0.0028(18)	-0.00251(40)	-0.0003(17)
	$\mathbf{p}_\pi = \frac{2\pi}{L}(1,1,1)$	-0.0050(38)	-0.0027(12)	-0.0023(39)
method 1 ($c_0^2 = -c_0^1$)	$\mathbf{p}_\pi = \frac{2\pi}{L}(1,0,0)$	-0.00264(62)	-0.00133(12)	-0.00122(60)
	$\mathbf{p}_\pi = \frac{2\pi}{L}(1,1,0)$	-0.0027(17)	-0.00217(33)	-0.0005(17)
	$\mathbf{p}_\pi = \frac{2\pi}{L}(1,1,1)$	-0.0047(38)	-0.00196(84)	-0.0028(39)
method 1 (4pt fit)	$\mathbf{p}_\pi = \frac{2\pi}{L}(1,0,0)$	-0.00288(76)	-0.00169(17)	-0.00109(73)
	$\mathbf{p}_\pi = \frac{2\pi}{L}(1,1,0)$	-0.0030(23)	-0.00298(52)	-0.0000(22)
	$\mathbf{p}_\pi = \frac{2\pi}{L}(1,1,1)$	-0.0094(60)	-0.0041(13)	-0.0053(61)
method 2	$\mathbf{p}_\pi = \frac{2\pi}{L}(1,0,0)$	-0.00271(64)	-0.00151(16)	-0.00110(58)
	$\mathbf{p}_\pi = \frac{2\pi}{L}(1,1,0)$	-0.0028(18)	-0.00240(48)	-0.0004(17)
	$\mathbf{p}_\pi = \frac{2\pi}{L}(1,1,1)$	-0.0053(39)	-0.0034(12)	-0.0019(38)
$c_s \times \bar{s}d$	$\mathbf{p}_\pi = \frac{2\pi}{L}(1,0,0)$	-0.000010(84)	-0.00002(20)	0.00001(11)
	$\mathbf{p}_\pi = \frac{2\pi}{L}(1,1,0)$	-0.00002(21)	-0.00005(49)	0.00003(28)
	$\mathbf{p}_\pi = \frac{2\pi}{L}(1,1,1)$	0.00032(52)	0.0007(12)	-0.00042(69)

Table 6.4: Summary of matrix elements obtained using various analysis methods. All values are given in lattice units. Results are shown for all classes of diagrams, and also separated into the nonloop and loop contributions.

shift appears to remove the decaying single kaon intermediate state contribution on the T_b side of the integral, in addition to the single-pion exponential term. The reason for this appears to be that c_s is very weakly dependent on the momentum, which can be understood from the fact that it is independent of momentum in the $SU(3)$ symmetric limit (cf. Appendix A).

An important test of this method is to check that the $\bar{s}d$ 4pt correlator gives no contribution to the final amplitude [19]. As a consistency check, we can apply the 'method 1' integration techniques to this correlator in an attempt to verify that the matrix element contribution is consistent with zero. Plots of the integral of this correlator are shown in Fig. 6.11, and the results for each pion momentum are displayed in Fig. 6.12. We remark that the result of these three analyses are generally consistent with zero, as is the difference between the matrix elements obtained using either methods 1 or 2.

6.3.5 Discussion

A summary of the results of our analysis of the 4pt functions for the three choices of pion momenta studied is presented in Table 6.4. A comparison of statistical errors shows that

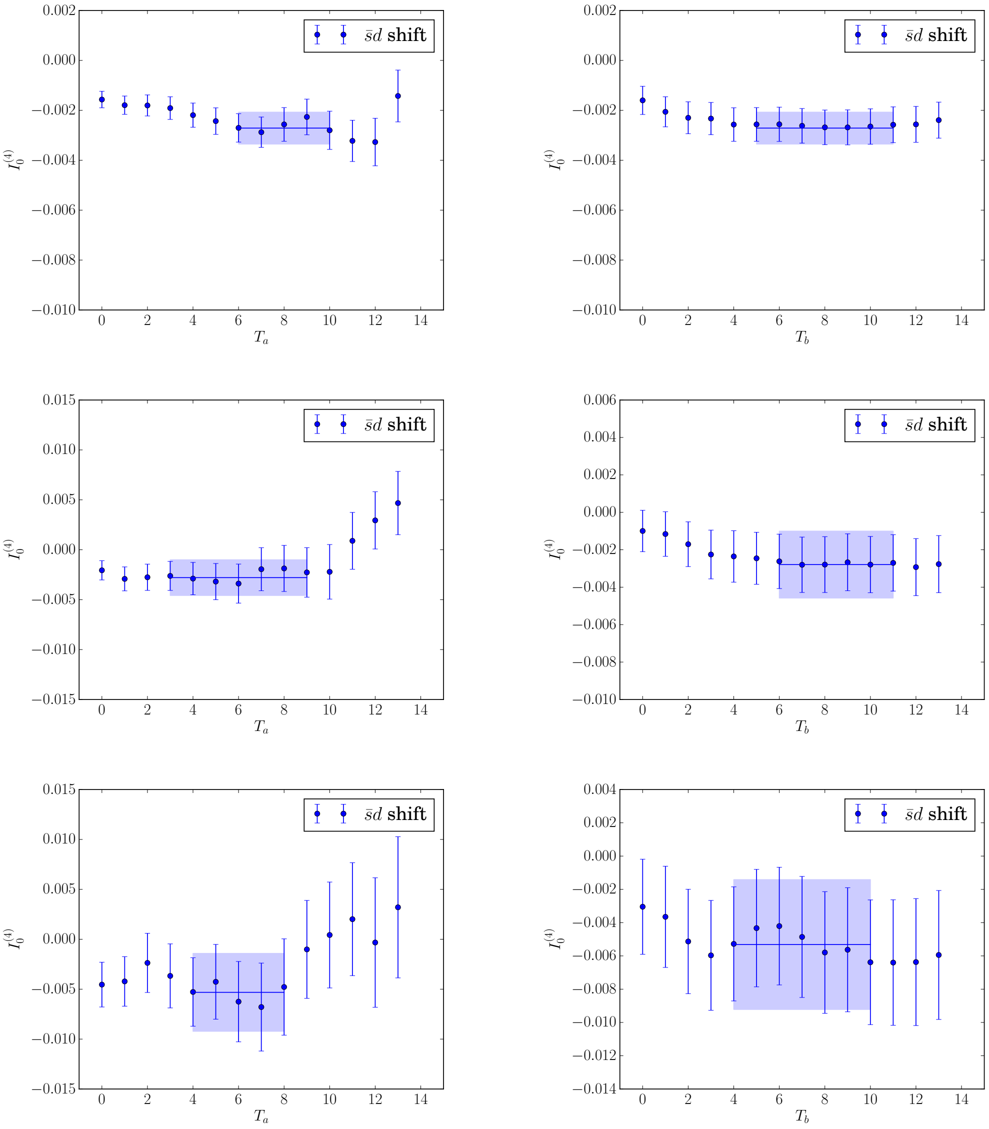

(a) (b)

Figure 6.10: The integrated 4pt correlator, shown for (a) T_b fixed at its lower limit to demonstrate the T_a dependence and (b) T_a fixed at its lower limit to demonstrate the T_b dependence. The kinematics shown are for $\mathbf{p}_\pi = (1,0,0)$, $\mathbf{p}_\pi = (1,1,0)$, $\mathbf{p}_\pi = (1,1,1)$ top to bottom. The single-pion exponential growth has been removed using method 2. The position of the plateaus corresponds to $A_0 = -0.0027(6)$, $A_0 = -0.0028(18)$, $A_0 = -0.0053(39)$ top to bottom, obtained by fits to the data over the indicated ranges.

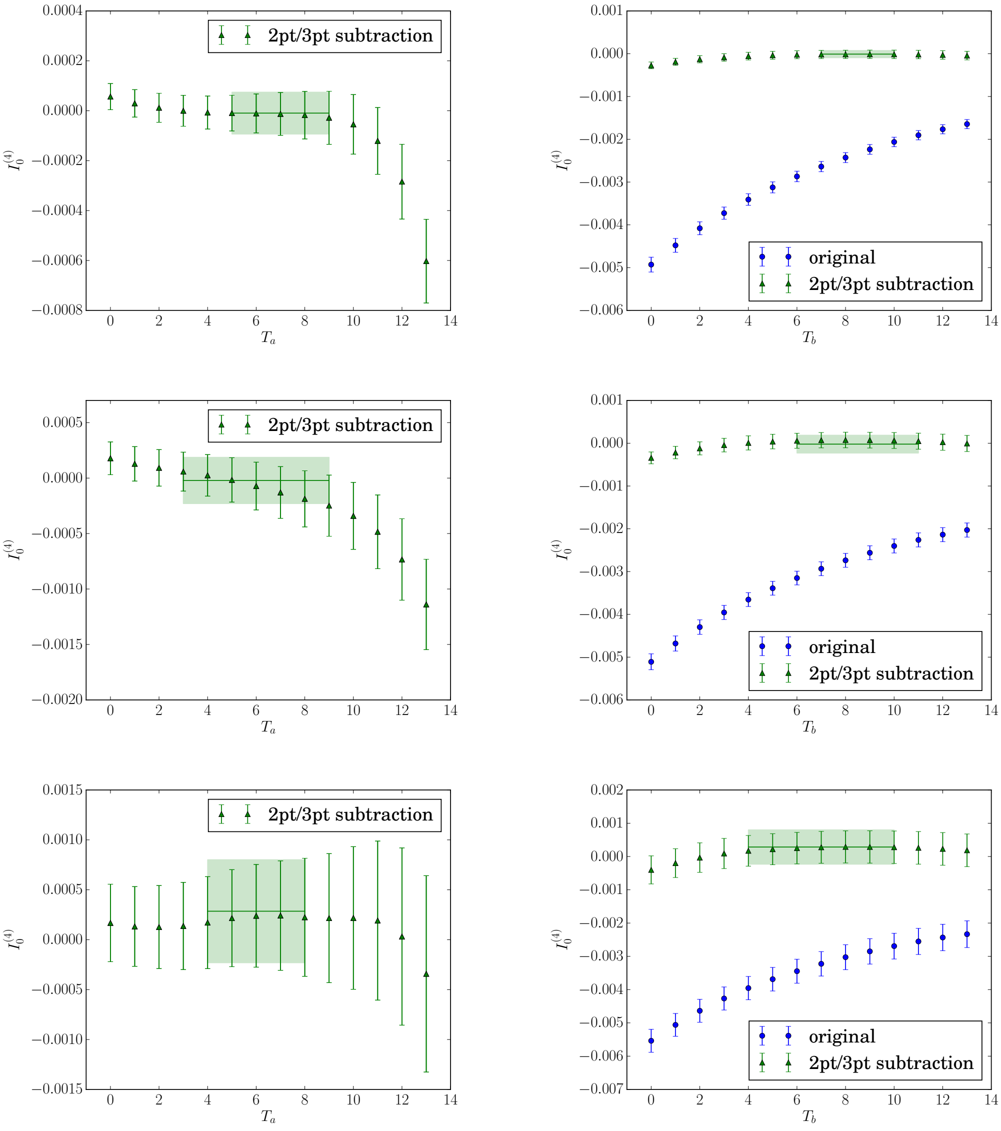

(a) (b)

Figure 6.11: The integrated 4pt correlator, shown for (a) T_b fixed at its lower limit to demonstrate the T_a dependence and (b) T_a fixed at its lower limit to demonstrate the T_b dependence. The kinematics shown are for $\mathbf{p}_\pi = (1,0,0)$, $\mathbf{p}_\pi = (1,1,0)$, $\mathbf{p}_\pi = (1,1,1)$ top to bottom. The single-pion exponential growth has been removed using method 1, with the approximation $\mathcal{M}_{sd}(\mathbf{p}_\pi) = \mathcal{M}_{sd}(\mathbf{p}_K)$. The position of the plateaus corresponds to $A_0^{\bar{s}d} = -0.00001(8)$, $A_0^{\bar{s}d} = -0.00002(21)$, $A_0^{\bar{s}d} = 0.00032(52)$ top to bottom, obtained by fits to the data over the indicated ranges.

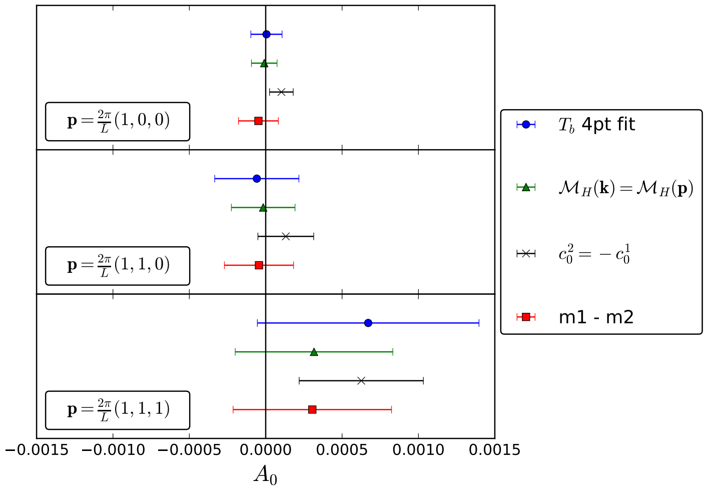

Figure 6.12: Plot of the amplitudes (in lattice units) obtained using each of the different analysis methods for the $C^{(4)}_{\bar{s}d}$ correlator. The expected value of zero is marked explicitly.

$\mathbf{p}_\pi$	$\frac{2\pi}{L}(1,0,0)$	$\frac{2\pi}{L}(1,1,0)$	$\frac{2\pi}{L}(1,1,1)$
z	−0.5594(12)	−1.0530(34)	−1.4653(82)
$V(z)$	1.37(36)	0.68(39)	0.96(64)

Table 6.5: The form factor of the $K(\mathbf{0}) \to \pi(\mathbf{p}_\pi)\gamma^*$ decay computed for the three pion momenta.

both analysis methods 1 and 2 can be used to obtain the matrix element with similar statistical precision. The two methods also show remarkable agreement, suggesting that systematic effects are well controlled by our analysis. The two methods give the best agreement when we use the approximation $\mathcal{M}_H(\mathbf{p}_K) = \mathcal{M}_H(\mathbf{p}_\pi)$ in method 1 when constructing the coefficient c_0^2 of Eq. (6.8). This indicates that this approximation carries a smaller systematic error than the approximation $c_0^1 = c_0^2$ for the choices of masses and pion momenta used in this simulation.

Our cleanest results are obtained when we used method 2 to perform the analysis, which does not use any approximations in the analysis process. Using these results we therefore compute the form factor for the decay using Eq. (5.5). The results for the form factor are presented in Table 6.5.

It is instructive to perform our analysis separately for the loop diagrams S and E, and the nonloop diagrams W and C. While either combination of diagrams does not correspond to entire operators Q_1 and Q_2, it is useful to be able to study the diagrams involving the charm quark separately. The results are also shown in Table 6.4. We remark that we should find that $A_\mu = A_\mu^{C,W} + A_\mu^{S,E}$; it can be seen from the central values in Table 6.4

that this generally holds well for all analysis methods. Small deviations from this relation represent a possible source of systematic error in our analysis procedure, which are introduced by using different choices of fit ranges for the individual diagrams rather than fitting the sum, and thus can be attributed to small excited state contaminations. Such errors however are significantly smaller than our statistical errors. An important observation to make is that even though the contribution of the single-pion intermediate state evidently contributes with opposite sign between the loop and nonloop diagrams (as seen in Fig. 6.6), the four classes of diagrams all contribute constructively to the final matrix element. This is important from the perspective of our unphysical GIM cancellation: if we were to simulate with a heavier (thus more physical) charm quark we would expect the S and E diagrams to have a larger contribution and hence give us a more negative result for the matrix element. However we will leave a numerical test of the charm mass dependence until a future work, as this is not the primary focus of our present study.

Importantly, when simulations are performed with lighter values for M_π and M_K, more states may contribute exponentially growing contributions (from $\pi\pi$ and $\pi\pi\pi$ intermediate states). It is instructive therefore to understand exactly how best to remove the single-pion state from simulations where it gives the only exponentially growing contribution. We have demonstrated the analysis techniques to remove this state cleanly with minimal systematic errors; hence it now remains to extend our simulations to physical masses such that the contributions of additional exponentially growing states can be investigated.

6.4 Form Factor

One opportunity of lattice QCD is to test the previous work on rare kaon decays performed using effective theories such as $SU(3)$ ChPT. Previous theoretical work in ChPT has been summarised in the section 3.2.1. In this section we will demonstrate how we can use our lattice data to test the ansatz Eq. (3.48) for the form factor, which we repeat here for convenience:

$$V_i\left(z\right) = a_i + b_i z + V_i^{\pi\pi}\left(z\right), \tag{6.10}$$

with $z = q^2/M_K^2$, and $V_i^{\pi\pi}\left(z\right)$ $(i = +, 0)$ is introduced to account for $\pi\pi \to \gamma^*$ rescattering in $K \to \pi\pi\pi$ decays.

The form factor is obtain from our lattice data by making use of Eq. (5.5). In Fig. 6.13 we display the dependence of the form factor extracted from lattice data upon $z = q^2/M_K^2$. Although our simulation takes place with highly unphysical masses of the pion and kaon, we are able to make some insights. Since we have only three data points at quite large spacelike momenta, we will not be able to fully explore the ChPT anastz in Eq. (6.10).

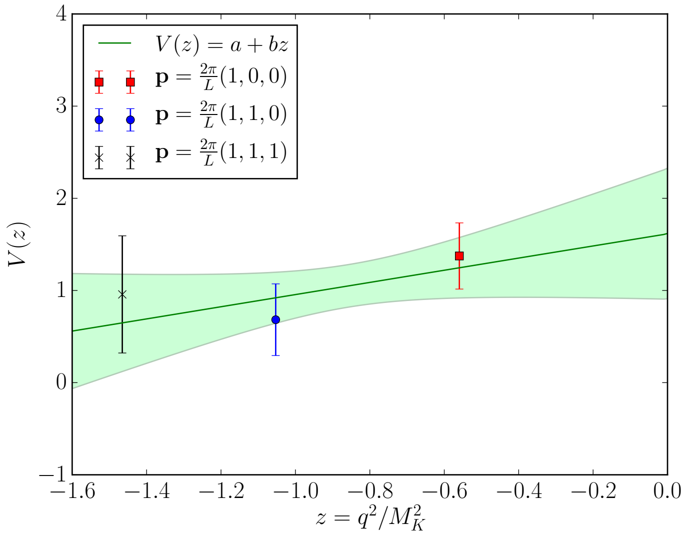

Figure 6.13: Dependence of the form factor for the decay $K^+ \to \pi^+\ell^+\ell^-$ upon $z = q^2/M_K^2$. Our lattice data is fit to a linear ansatz to obtain $a = 1.6(7)$ and $b = 0.7(8)$.

We remark that the contribution of the term $V_i^{\pi\pi}(z)$ is significantly smaller than the linear contribution for physical masses; for our initial calculation we can safely neglect this term. Hence we simply use a linear fit, which does provide a reasonable description of our data with a $\chi^2/\text{d.o.f} = 0.74$. The parameters we obtain, $a_+^{lat} = 1.6(7)$ and $b_+^{lat} = 0.7(8)$, are different from the parameters obtained from phenomenological fits to experimental data, $a_+^{exp} = -0.578(16)$ and $b_+^{exp} = -0.779(66)$. Notably the lattice results are of the opposite signs to the experimental results. It should be remarked that fits to experimental data are unable to determine the signs of a_+ and b_+ definitively; however a ChPT-motivated analysis does show a preference for the negative signs [21]. However such a comparison must be taken with care given the unphysical masses used in our simulation.

6.5 Prospects for Physical Point Calculation

In this section I discuss the future plans for simulations of $K \to \pi\ell^+\ell-$. Our aim is to eventually perform a physical point simulation of these decays with 4 active flavours; we thus must simulate with physical pion and charm masses. However this poses a problem: in order to avoid discretisation errors in the simulation of the charm quark we must use a fine lattice spacing, but we must use a large volume to avoid finite volume effects in the propagation of the pion.

As an intermediate step therefore, I propose a calculation in which we simulate only 3 flavours of quarks, i.e. we integrate out the charm quark. This of course complicates our renormalisation procedure somewhat, as we can no longer rely on the automatic cancellation of logarithmic divergences on the lattice via the GIM mechanism. However, it is possible to use the renormalisation techniques originally developed for $K \to \pi\nu\bar{\nu}$ decays presented in section 5.3.3. Stricty speaking the divergence in the bilocal matrix element involving up-quark loops will still be cancelled by a divergence from the charm quark contribution, however there now exists the extra challenge of converting the divergence regulated by the lattice into a continuum scheme such that it is correctly cancelled by the short-distance charm contribution. In this section therefore I will outline the details of this additional step for the 3-flavour simulation.

6.5.1 Simulation with 3 flavours

As previously discussed in section 3.1.2, the calculation of rare kaon decays with 3 flavours has a small effect upon the choice of operators entering the Weak Hamiltonian. In the 4-flavour theory, where only the operators $Q_1^{u,c}$ and $Q_2^{u,c}$ contribute to H_W [Eq. (3.30)], the up and charm loops provide an equal and opposite divergence, such that their sum is finite. In the 3-flavour theory, the contributions to the matrix element 5.1 made by Q_1^u and Q_2^u only contain the up contribution, hence the matrix elements are logarithmically divergent. In the three-flavour theory, the weak Hamiltonian [Eq. (3.31)] also contains small contributions from the QCD penguin operators $Q_{3,\dots,6}$. The inclusion of these operators produces new Wick contractions: notably with these operators it is possible to generate contractions with u, d or s quarks in the loop. For these operators, it is the strange and down quark loops that are responsible for the divergence. To elaborate for the example of Q_3; the up, down and strange loops will all have an E-type contraction (see Fig. 5.1): the divergences from these three quarks cancel under summation as $Q_u + Q_d + Q_s = 0$. However, the strange and down quarks also have an S-type contraction for this operator (the up quark does not), thus the divergences from these topologies do not cancel.

Additionally, in the 3-flavour theory we must include the local operator Q_{7V}, which is required to both regulate the divergence in the bilocal matrix elements, as well as provide the short-distance charm quark contribution.

On a practical note, it should be remarked that the $Q_{3,\dots,6}$ contractions require the additional calculation of strange quark loops. These have not been included in our exploratory calculation as these propagators were only necessary for disconnected diagrams, which we have neglected. However a complete physical point calculation would necessarily include disconnected diagrams, and hence $Q_{3,\dots,6}$ contractions may also be computed relatively cheaply.

The aim of this calculation is to make use of the software library Grid [137] that is being developed by members of the RBC-UKQCD collaboration. The necessity to perform this simulation is twofold: within UKHadron contractions are inefficient and given the large number of contractions required for rare kaon decays, contraction time makes up approximately 15% of the time in our exploratory simulations. Secondly memory management within UKHadron is inefficient, which limits the number of contractions that can be performed as all propagators are computed and stored in memory before contractions have been performed. Issues such as these inhibit efficient usage of techniques such as all-mode-averaging [138] and low mode deflation [139, 140] that will be necessary to optimise the statistical precision in a physical point simulation. Grid solves these issues, as well as giving other advantages such as being portable to new supercomputing architectures beyond the BlueGene/Q used for the exploratory simulations to date.

Within the framework of Grid I have helped develop the measurement code, implementing all the required rare kaon decay contractions as well as the source/sink smearing and conserved currents necessary to compute the decay amplitudes. Results of all rare kaon contractions in Grid have been tested these against UKHadron to ensure that they produce the same results. The code that I have developed will therefore be used for the production of physical-point data.

6.5.2 3 Flavour Renormalisation

The renormalisation procedure for the 4pt matrix elements obtained in the 3-flavour theory follows the procedure set out in section 5.3.3. Specifically we are required to calculate the terms $X\left(\mu_{\mathrm{RI}}, a\right)$ and $Y\left(\mu_{RI}, \mu\right)$ as seen in Eqs. (5.84) and (5.88). Here I illustrate the speficic procedure required for 3-flavour $K \to \pi\ell^+\ell^-$ decays. The individual operator renormalisation must of course also be taken into account; fortunately the $Z^{\mathrm{RI}\to\overline{\mathrm{MS}}}$ conversion factors are already known for the operators Q_i appearing in H_W, $i = 1, ..., 6$ [Eq. (3.31)].

In order to calculate $X\left(\mu_{\mathrm{RI}}, a\right)$, we break up the calculation for each of the operators Q_i; however the procedure is identical for every single operator. We remark that the role of X is to regulate the logarithmic divergence in the bilocal matrix element; we need therefore only consider diagrams that contribute to this divergence. This involves the diagrams in the S and E classes where the current is inserted in the loop, which we shown in Figs. 6.14(a) and 6.14(b). Similarly the diagram for the local operator is shown in Fig. 6.14(c). We thus recover the counterterm X_i by demanding

$$\Lambda_i^{\mu}\left(\mu_{\mathrm{RI}}\right) - X_i\left(\mu_{\mathrm{RI}}, a\right)\left(\delta^{\mu\nu}q^2 - q^{\mu}q^{\nu}\right)\Lambda_X^{\nu}\left(\mu_{\mathrm{RI}}\right) = 0, \tag{6.11}$$

where Λ_i^{μ} and Λ_X^{ν} are the amputated Green's functions corresponding to the operator Q_i and the local operator Q_{7V}^{ν} respectively. We note that because the matrix element must satisfy the Ward identity, we include the factor $\left(\delta^{\mu\nu}q^2 - q^{\mu}q^{\nu}\right)$ to project out the

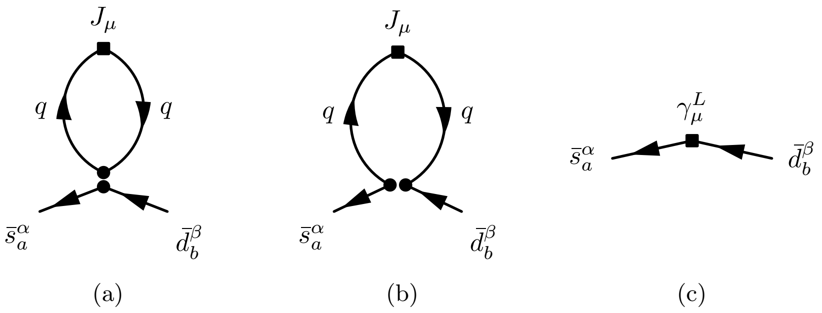

Figure 6.14: Green's functions that must be computed for the renormalisation procedure, corresponding to (a) E and (b) S loop contractions. The exact gamma matrix insertion will depend upon the weak operator Q_i. In (c) we show the Green's function required for calculation of the counterterm.

transverse component. Note we are working in Euclidean space, hence the metric is given by $\delta^{\mu\nu}$.

The calculation of $Y\left(\mu_{RI}, \mu\right)$ is performed for each of the operators Q_i separately. The calculation is done in continuum perturbation theory, using the $\overline{\text{MS}}$ scheme. The answer computed in perturbation theory may be factorised as

$$\left. \langle d| \left\{Q_i, J^\mu\right\} |s\rangle^{\overline{\text{MS}}} \right|_{q^2=\mu_{\text{RI}}^2} = \frac{Z_\psi^{\text{RI}}\left(\mu_{\text{RI}}\right)}{Z_\psi^{\overline{\text{MS}}}\left(\mu\right)} Y_i\left(\mu_{\text{RI}}, \mu\right) \left(\delta^{\mu\nu} q^2 - q^\mu q^\nu\right) \langle d|Q_{7V,\nu}|s\rangle^{(0)}, \quad (6.12)$$

from which we may obtain $Y_i\left(\mu_{\text{RI}}, \mu\right)$ for $i = 1, ..., 6$. The final answer must subsequently be joined up with the local operator, i.e.

$$A^\mu\left(K \to \pi\gamma^*\right) = \sum_i C_i\left(\mu\right) \langle\pi| \left\{Q_i J^\mu\right\} |K\rangle^{\overline{\text{MS}}}\left(\mu\right) + C_{7V}\left(\mu\right) \left\langle\pi|Q_{7V}^\mu|K\right\rangle. \quad (6.13)$$

The Wilson coefficient C_{7V} is known to NLO [77] in the 3-flavour theory. The dependence on the scale μ of the bilocal matrix element hence must cancel with the μ dependence of C_{7V}.

Chapter 7

Results of $K \to \pi\nu\bar{\nu}$ Simulations

In this chapter I report on the calculation of $K \to \pi\nu\bar{\nu}$ rare kaon decay matrix elements. I focus solely on the decay $K^+ \to \pi^+\nu\bar{\nu}$, which is short-distance dominated unlike the decay $K^+ \to \pi^+\ell^-\ell^-$ discussed in the previous chapter. However as experimental measurements of $K^+ \to \pi^+\nu\bar{\nu}$ become more precise it is important to be able to control systematic errors from long-distance hadronic effects. Ultimately the aim of our calculation is to provide a non-perturbative calculation of the quantity P_c [Eq. (3.64)] in the $\overline{\text{MS}}$ scheme, in which the short-distance Wilson coefficients entering the weak Hamiltonian are known. The proposal for such a calculation was originally put forth in Ref. [33], where the details of the analysis to extract $K \to \pi\nu\bar{\nu}$ amplitudes was introduced, with renormalised operators and full control of ultraviolet divergences. The objective of the current study I present here is to demonstrate the application of the techniques of Ref. [33] in a relatively inexpensive, unphysical numerical simulation, which may later be generalised to a simulation at physical masses.

The calculation of $K \to \pi\nu\bar{\nu}$ matrix elements shares many similarities with those of $K \to \pi\ell^+\ell^-$ decays. However the use of an axial current required for the Z-boson exchange makes the renormalisation procedure much more involved. Consequently, the simulation strategy employed for this decay is markedly different for the $K \to \pi\ell^+\ell^-$ decay. I will therefore discuss the details of our $K \to \pi\nu\bar{\nu}$ simulations in sections 7.1 and 7.2, and demonstrate the required analysis to extract the desired matrix elements and form factors in section 7.3. Finally I will discuss the renormalisation procedures necessary to extract the quantity P_c from our simulations in section 7.4, such that a comparison with perturbation theory results may be made. The numerical analysis I present is my own work, with the exception of the non-perturbative renormalisation and calculation of finite-volume corrections, which were peformed by Xu Feng. The numerical data were generated by Xu Feng using the codebase CPS. The results presented in this chapter have been published in Ref. [3] and another paper detailing the analysis is in preparation [32].

7.1 Details of the Simulation

This exploratory study was performed on a similar lattice to our studies of $K \to \pi\ell^+\ell^-$. We used a $16^3 \times 32$ lattice with an inverse lattice spacing of $a^{-1} = 1.729(28)\,\mathrm{GeV}$ [131], employing Shamir domain wall fermions [104] with Iwasaki gauge action [96]. The ensemble has a residual mass of $am_{res} = 3.08(4) \times 10^{-3}$, a pion mass of $421(1)(7)\,\mathrm{MeV}$ and a kaon mass of $563(1)(9)\,\mathrm{MeV}$. The bare charm quark mass used here is $am_c = 0.33$. With the mass renormalization factor $Z_m^{\overline{\mathrm{MS}}}(2\,\mathrm{GeV}) = 1.498(34)$, this corresponds to an unphysical charm quark of mass $m_c^{\overline{\mathrm{MS}}}(2\,\mathrm{GeV}) = 863(24)\,\mathrm{MeV}$. To achieve a high statistical precision we have used a sample of 800 configurations, each separated by 10 molecular dynamics time units.

7.2 Setup of the Calculation

The key difference between the simulations of $K \to \pi\ell^+\ell^-$ and $K \to \pi\nu\bar{\nu}$ decays is that in the former the use of the conserved vector current was advantageous for the renormalisation procedure. This is not true for $K \to \pi\nu\bar{\nu}$, where the axial current plays an important role. Hence an additional nonperturbative renormalisation calculation is required in addition to the calculation of matrix elements. It is more cost effective therefore to use local vector and axial currents.

Because we are not using conserved currents, it is convenient to employ twisted boundary conditions (see section 4.3.4) to insert non-integer values for lattice momenta into our calculation. This may be done to select a momentum configuration in the physically allowed region. It should be noted that with twisted boundary conditions it is not possible to construct a conserved current such that the rare kaon decay matrix elements with a vector current insertion are completely transverse [141], and hence they are not practical to use in simulations of $K \to \pi\ell^+\ell^-$. For the momenta p_K, p_π, p_ν and $p_{\bar{\nu}}$, we may write down the Mandelstam variables

$$s = -\left(p_K - p_\pi\right)^2, \quad t = -\left(p_K - p_\nu\right)^2, \quad u = \left(p_K - p_{\bar{\nu}}\right)^2, \tag{7.1}$$

with $s + t + u = m_K^2 + m_\pi^2$ (note we are working in Euclidean space, hence the negative signs). We can define two independent variables s and $\Delta = u - t$, which must satisfy

$$s \geq 0; \quad \Delta^2 \leq \left(m_K^2 + m_\pi^2 - s\right)^2 - 4m_K^2 m_\pi^2 \tag{7.2}$$

in order to ensure that all external states are on-shell. The region of allowed kinematics are shown by the Dalitz plot in Fig. 7.1. In our lattice simulation we choose to simulate with $\mathbf{p}_K = \mathbf{0}$ and tune the pion momentum $\mathbf{p}_\pi$ such that we satisfy $q^2 = 0$, which

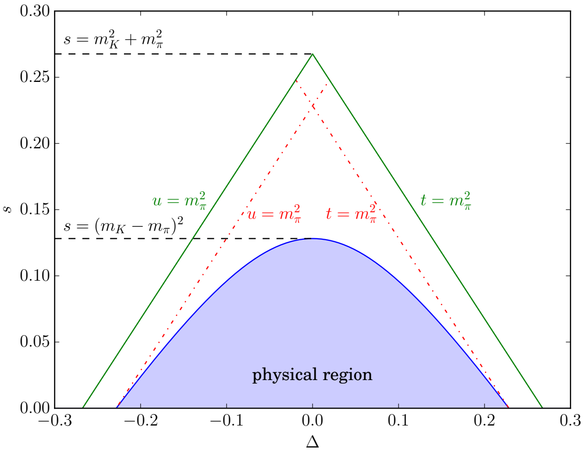

Figure 7.1: Dalitz plot for $K \to \pi\nu\bar{\nu}$ (with physical masses) showing the physical kinematical region.

corresponds to the kinematic $(s, \Delta) = (0, 0)$. Hence we use a pion with momentum

$$\mathbf{p}_\pi = -0.0414\,(1, 1, 1)\,, \tag{7.3}$$

and neutrinos each with $\mathbf{p}_\nu = \mathbf{p}_{\bar{\nu}} = -\mathbf{p}_\pi/2$. Note that the physical kinematical region is very narrow given the heavy pion mass of our simulation; we hence have not explored more of the (Δ, s) phase space as the data would be highly correlated and thus unsuitable for extracting a clear momentum dependence.

Similar to our simulations of $K \to \pi\ell^+\ell^-$, we use Coulomb gauge-fixed wall sources for good overlap with the ground state kaon and pion. However, the construction of the 4pt functions is much different. With a conserved current, it is convenient to use sequential propagators to achieve this insertion in 4pt functions. With local currents, another option is to fix the position of one operator at a single point and use a point source propagator for the internal quark line. The disadvantage to this method is that one loses the spatial summation which is given automatically by the sequential inversion; however this will be somewhat compensated for by the fact that it allows greater flexibility for translating the decay across different timeslices. We remark that a point insertion of a conserved current would involve the calculation of multiple point source propagators from neighbouring spatial sites and is thus not cost effective.

For the W-W diagrams, we additionally require an internal lepton propagator. This is achieved by using a free overlap fermion with infinite time extent [32]. The subtlety of the infinite time extent is required to avoid round-the-world effects for the light leptons e, μ. The propagator itself is obtained from the momentum space propagator $S_\ell\,(p)$ using

$$S_\ell^{(\infty)}\,(t, \mathbf{p}) = \int_{-\pi}^{\pi} \frac{dp_0}{2\pi} S\,(p_0, \mathbf{p})\, e^{-ip_0 t}. \tag{7.4}$$

This integral may be performed analytically using contour integration [142]. On the lattice the propagator we use is defined to be

$$S_\ell^T(t,\mathbf{p}) = \begin{cases} S_\ell^{(\infty)}(t,\mathbf{p}) & -T/2 \le t < T/2, \\ 0 & t \le T/2 \text{ or } t < -T/2, \end{cases} \tag{7.5}$$

i.e. the propagator is constructed by abandoning the periodic boundary conditions in the time direction and restricting the position of the lepton propagator to be in the central portion of our lattice.

7.2.1 Details of the Implementation

The implementation of $K \to \pi\nu\bar{\nu}$ decays shares some similarities with the one used for $K \to \pi\ell^+\ell^-$ decays. For example, we again require four wall source propagators to connect the kaon/pion sources to the H_W insertion. Additionally the loop propagators for the S and E diagram classes (see Fig. 5.1) are computed using spin-colour diluted volume sources (see section 4.3.2.3). This allows us to sum H_W over the whole lattice.

However it is not necessary to insert the current sequentially in the loop propagator for S and E diagrams; instead the loop where the current is inserted may be constructed using point source propagators. We employ time dilution for the calculation of these loop propagators: we place a single random volume wall source on each timeslice. This may be contrasted to using an undiluted random volume wall source, and computing T independent noise vectors. Although the two methods have the same numerical cost, the former reduces the error by a factor of 1.5 with respect to the latter.

The current insertions are achieved by computing point source propagators with momenta $\mathbf{p}_\pi$ and $\mathbf{p}_K$. These propagators are computed on every timeslice. This allows us to insert the current at any time position given fixed values for t_K and t_π. However we also compute the wall source propagators required to interpolate the pion and kaon on every single timeslice. This allows us to translate the decay across all T timeslices of the lattice. Additionally it allows us to vary the source-sink separation of our pion and kaon in addition to inserting the two operators at all combinations of times between the kaon source and pion sink. Furthermore, in order to effectively double the time extent of the lattice, we compute the propagators with both periodic and antiperiodic boundary conditions in the time direction, and use the average of the two. This trick means that we may safely neglect round-the-world effects in the 4pt correlators. Therefore in our calculation we will consider a maximum source-sink separation of 30 timeslices. However for analysis purposes we maintain a distance of at least six timeslices between the operators and the source/sink in order to avoid excited state contamination. We remark that the translation of the decay across the lattice reduces the error by almost a factor of $\sqrt{T}$.

Description	Source Type	Number of Inversions		
		Light	Strange	Charm
C and W Propagators	Gauge-fixed wall	$3T$	T	0
S,E and disconnected loops	Random volume	T	T	T
Internal propagators	Point source	$2T$	$2T$	$2T$
Total	-	$5T$	$4T$	$3T$
$T = 32$, P + AP	-	320	256	192

Table 7.1: Summary of propagators calculated in our simulation on a single configuration, and the corresponding number of inversions required. In the last line I give the total number of inversions including both periodic (P) and anti-periodic (AP) boundary conditions. Free lepton propagators that don't require an inversion are not included here. T is the time extent of the lattice.

Given the large number of light and strange propagators to be calculated, low mode deflation is used to speed up these inversions (with a comparatively small setup cost). This is achieved by using the Lanczos algorithm [143] to compute 100 eigenvectors of the Dirac operator with the smallest eigenvalues. With this technique the CG time is reduced to 16% of the undeflated Dirac operator.

On a single configuration we therefore require 320 light propagator inversions, 256 strange inversions and 192 charm inversions. These are summarised in Table 7.1.

7.3 Numerical Results

The aim of this exploratory calculation is to show that it is possible to extract $K \to \pi\nu\bar{\nu}$ amplitudes from lattice simulations with controlled systematic errors. In this section I present my analysis of the results of $K \to \pi\nu\bar{\nu}$ simulations in order to extract the relevant rare kaon decay matrix elements.

In our studies of $K \to \pi\ell^+\ell^-$ decays, our use of the sequential current meant that it was expensive to consider multiple time positions for the insertion of the current. However the simulation setup for $K \to \pi\nu\bar{\nu}$ allows us to generate data in which both operators in the bilocal matrix element may be translated across the whole lattice. For the analysis therefore it is important that we make best use of all the generated data. In general we observe that the best statistical signal is obtained for correlators where the time between the source and sink is smallest. However, this provides only a narrow window over which to integrate, which doesn't necessarily converge within the available time extent. On the other hand, data with a very large source/sink separation does converge within the integration window, although the statistical signal is poorer.

The analysis approach I employ is to "fix" one of the operators as in the $K \to \pi\ell^+\ell^-$ analysis, and translate its position to $t = 0$ using Eq. (6.2). For a single set of source and sink positions therefore this data may be averaged into a single "effective" 4pt correlator. For example, with $t_K = 0$ and $t_\pi = 18$, we insert both operators in the window $t = 6, ..., 12$. We thus average across seven points where both operators are on the same timeslice, across six points where they are separated by one timeslice, etc. During this averaging procedure it can be verified that there are no significant excited state effects by ensuring all points within each averaging step are consistent within statistical errors. This is done separately for each source/sink position; ultimately one final effective correlator using all available data may be obtained by dividing out the time dependence of the source and sink [i.e. using Eq. (6.3)] and combining the effective correlators from each source/sink separation. The analysis of the resulting 4pt function thus proceeds as described in section 5.2.

7.3.1 2pt and 3pt Correlators

The analysis of the 2pt correlators is similar to the analysis of 2pt correlators in $K \to \pi\ell^+\ell^-$ decays as described in section 6.3.1. In order to remove the time-dependence of and normalisation factors of the source and sink, we require the mass of the kaon, M_K and the energy of the final state pion, $E_\pi(\mathbf{p}_\pi)$. The relevant fits to these correlators with a wall sink and wall source are shown in Fig. 7.2.

In addition, we require the kaon and pion decay constants to remove intermediate states in W-W diagrams, and the renormalisation constant Z_A. These quantities may be obtained from 2pt correlators using Eq. (5.81). We therefore also require the 2pt correlators with wall sources and a point sink or a local axial current sink. The relevant correlators are therefore

$$C(t_P, t) = \left\langle \tilde{\phi}^p_P(t, \mathbf{p})\, \tilde{\phi}^\dagger_P(t, \mathbf{p}) \right\rangle \tag{7.6}$$

where $\tilde{\phi}_P$ is the annihilation operator for a particle P with the superscript p indicating a point sink, and

$$C(t_P, t) = \left\langle \tilde{\phi}^A_P(t, \mathbf{p})\, \tilde{\phi}^\dagger_P(t, \mathbf{p}) \right\rangle \tag{7.7}$$

$$\sim \frac{N^\dagger_P(\mathbf{p})\, N^A_P(\mathbf{p})}{E_P(\mathbf{p})} e^{-E_P(\mathbf{p})T/2} \sinh\left(E_P(\mathbf{p})\left[t - t_P - \frac{T}{2}\right]\right), \tag{7.8}$$

where $\tilde{\phi}^A_P = \bar{q}\gamma_0\gamma_5 u$ is the local axial current operator for a meson P, with $q = d$ for $P = \pi$ and $q = s$ for $P = K$. We have defined the normalisation factors to be $N^A_P(\mathbf{p}) = \langle 0|\tilde{\phi}^A_P|\pi(\mathbf{p})\rangle$ for a local axial current sink and $N^\dagger_P(\mathbf{p}) = \langle \pi(\mathbf{p})|\tilde{\phi}^\dagger_P|0\rangle$ for a wall source. We remark that for the correlator with an axial current sink, the backward propagating state is of opposite sign to the forward one, hence the appearance of a sinh

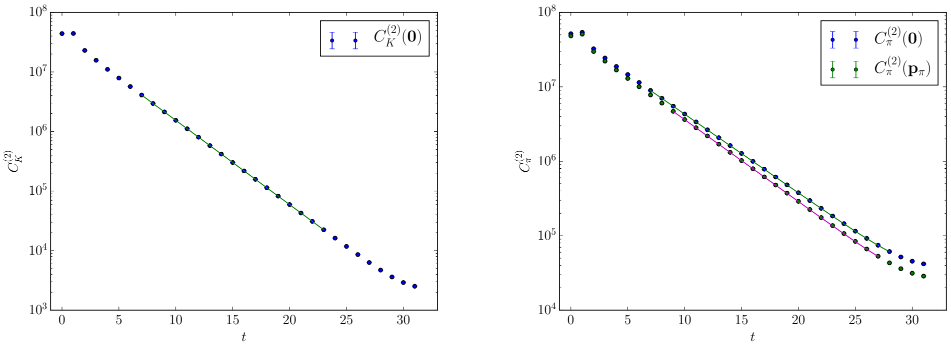

(a) (b)

Figure 7.2: Plots of (a) kaon and (b) pion 2pt correlation functions with wall source and sink smearing.

Particle	$N_P(\mathbf{0})$	$N_P(\mathbf{p}_\pi)$	M_P	$E_P(\mathbf{p}_\pi)$	f_P	$Z_A = Z_V$
pion	76.47(17)	75.22(17)	0.24370(40)	0.25345(40)	0.08897(32)	0.7163(26)
kaon	79.77(18)	-	0.32572(45)	-	0.09769(22)	0.7245(18)

Table 7.2: Table of fit results of 2pt correlation functions involving a pion ($P = \pi$) and kaon ($P = K$), with $\mathbf{p}_\pi = -0.0414(1, 1, 1)$.

function rather than a cosh function. The fits to these correlators are shown in Fig. 7.3. We can subsequently obtain the pseudoscalar meson decay constant using

$$f_P = \frac{(\tilde{m}_1 + \tilde{m}_2)\, N_P^p}{M_P^2}, \tag{7.9}$$

where $\tilde{m}_1$ and $\tilde{m}_2$ are the masses of the two quarks within the meson and $\tilde{m} = m + m_{res}$, where m is the bare quark mass and m_{res} is the DWF residual mass (note $m_{res} = 3.08(4) \times 10^{-3}$ for the ensemble used in this study). The local axial current renormalisation constant Z_A follows from

$$Z_A = \frac{f_P E_P\,(\mathbf{p})}{N_P^A\,(\mathbf{p})}. \tag{7.10}$$

The results of the analysis of 2pt correlators are all summarised in Table 7.2. We remark that we have not however performed a chiral extrapolation of Z_A to the chiral limit; for the remainder of this analysis we will simply use the result from the pion correlator.

For the 3pt correlators, we find that the signal is optimised when analysing correlators with the smallest possible separation between the source and operator, while being free from excited state effects. The dependence on the sink timeslice is then fit to the relation given in Eq. (4.103). The analysis of 3pt functions allows us to obtain parameters

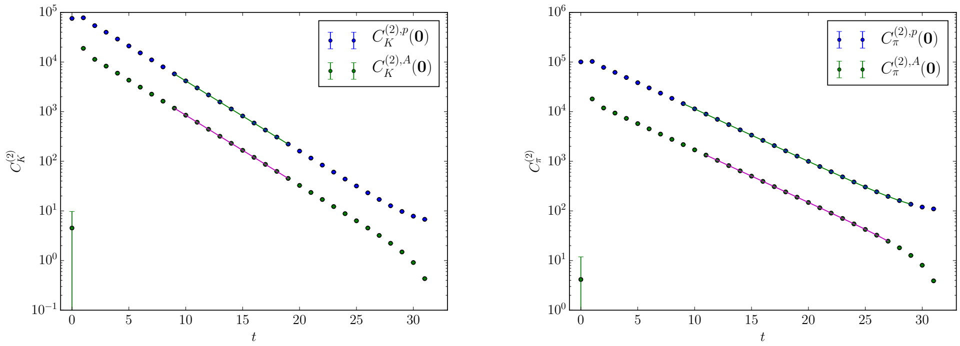

(a) (b)

Figure 7.3: Plots of (a) kaon and (b) pion 2pt correlation functions with a wall source and either a point sink or a local axial current sink.

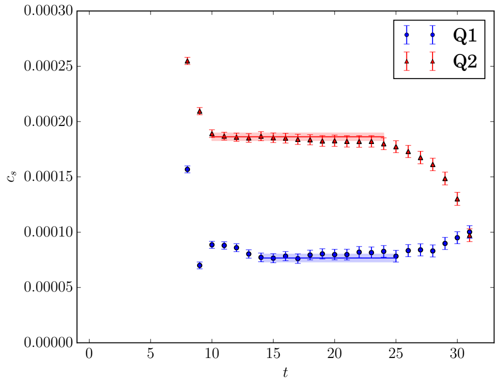

Figure 7.4: Plot of the determination of the parameter c_s for the operators Q_1 and Q_2 that make up H_W. We obtain $c_s^1 = 7.7(3) \times 10^{-5}$ for Q_1 and $c_s^2 = 1.86(3) \times 10^{-4}$ for Q_2.

required for the removal of exponentially growing intermediate states in the 4pt correlator analysis, and also to obtain the local matrix elements required to regulate short-distance divergences in the 4pt correlators.

For Z-exchange diagrams we require the parameter c_s [using Eq. (6.7)] for the removal of the single-pion intermediate state. The analysis is similar to that for $K \to \pi\ell^+\ell^-$, and the extraction of this parameter is shown graphically in Fig. 7.4. For the W-W diagrams we require the matrix elements given by Eqs. (5.63) and (5.64). These matrix elements may be extracted from the correlators

$$C^{\mu}_{P\to\pi}\left(t_P, t_{\mathcal{O}}, t, \mathbf{p}\right) = \sum_{\mathbf{x}} \left\langle \tilde{\phi}_P\left(t, \mathbf{p}\right) \mathcal{O}^{\mu}\left(t_{\mathcal{O}}, \mathbf{x}\right) \tilde{\phi}^{\dagger}_P\left(t_P, \mathbf{0}\right) \right\rangle e^{i\mathbf{p}\cdot\mathbf{x}}, \tag{7.11}$$

where $\mathcal{O}^{\mu} = \bar{s}\gamma^{\mu}d$ for $P = K$ and $\bar{d}\gamma^{\mu}d$ for $P = \pi$. The fits of these correlators to Eq. (4.103) are displayed in Figs. 7.5(a) and 7.6. For the removal of W-W intermediate

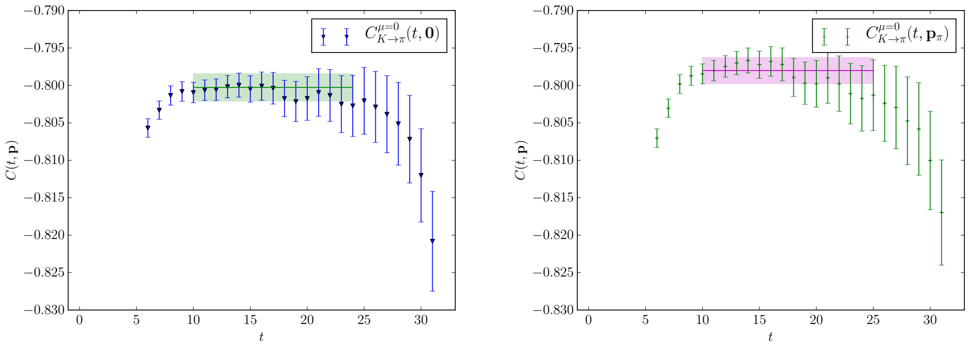

(a)

(b)

Figure 7.5: Plots of fits to $K_{\ell 3}$ correlators (with Lorentz index in time direction, $\mu = 0$), for (a) $q^2 = q^2_{max}$ (initial and final state at rest) and (b) $q^2 = 0$, after dividing out source/sink factors and ground state time dependence. The horizontal lines indicate the best fits and indicate the fit ranges.

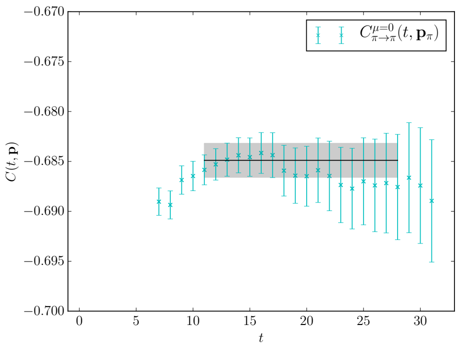

Figure 7.6: Plot of fit to pion correlator with a local vector current insertion (with Lorentz index in time direction, $\mu = 0$), after dividing out source/sink factors and ground state time dependence. The horizontal line indicates the best fit and indicates the fit range.

states we consider only the time component of the currents ($\mu = 0$), as the required matrix element has external states with zero momentum and hence the spatial components of the matrix element vanish. We may subsequently convert the matrix elements into the desired form factors using the relations given in Eqs. (5.63) and (5.64).

Lastly we require matrix elements corresponding to $K_{\ell 3}$ decays; these are the matrix elements necessary for regulating the divergence in the bilocal operators for both Z-exchange and W-W diagrams. From these matrix elements we extract the relevant form factors using Eq. (5.24). In order to extract f_+ we must also calculate the matrix element with $\mu = i$, $i = 1, 2, 3$. The fits to the relevant correlators are shown in Fig 7.7. However, the regulation of the divergence in the Z-exchange diagrams with a vector current insertion requires us to calculate the matrix element with vanishing initial and

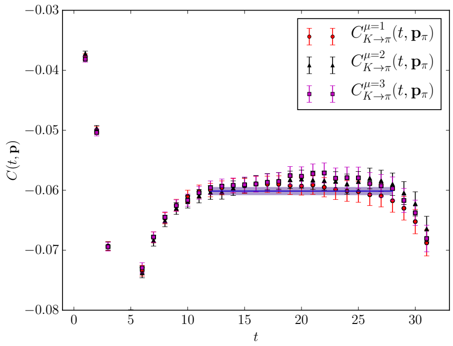

Figure 7.7: Plot of fit to $K_{\ell 3}$ correlators, with spatial Lorentz indices, after dividing out source/sink factors and ground state time dependence. The three spatial directions are fit simultaneously with a single parameter. The horizontal line shows the best fit result and indicates fit range.

Process	$\mathcal{M}^{\mu=0}$	$\mathcal{M}^{\mu=i}$	f_+	f_-	f_0 (F_π)
$K(\mathbf{0}) \to \pi(\mathbf{0})$	$-0.8003(18)$	-	-	-	$-1.0067(36)$
$K(\mathbf{0}) \to \pi(\mathbf{p}_\pi)$	$-0.7980(17)$	$-i \cdot 0.06014(60)$	$0.9929(36)$	$-0.0476(92)$	$0.9929(36)$
$\pi(\mathbf{0}) \to \pi(\mathbf{p}_\pi)$	$-0.6849(17)$	-	-	-	$-0.9868(35)$

Table 7.3: Summary of fit results for 3pt matrix elements (denoted by $\mathcal{M}$) and corresponding form factors required for the analysis of $K \to \pi\nu\bar{\nu}$ decays. In the third row of results the final entry corresponds to the pion electromagnetic form factor, F_π.

final momenta. In this case, we use the scalar form factor f_0 defined in Eq. (5.25). All these fit results are summarised in Table 7.3.

7.3.2 Z-Exchange Analysis

The analysis of the Z-exchange diagrams is separated into the vector and axial current components, because of the different pattern of intermediate states in both cases. In our exploratory studies only the correlator with a vector current contains an unphysical exponentially growing intermediate state (from the single pion); the removal of which is discussed in section 5.2.3.1. I will begin by presenting the analysis for the vector current, followed by the axial current. I will then move onto a discussion of the analysis for the disconnected diagrams.

Matrix Element	μ	Q_1	Q_2	$C_1Q_1 + C_2Q_2$
$\langle \pi(0) \left\| \{J_\mu^V H_W\} \right\| K(0) \rangle$	0	0.00304(12)	0.00109(14)	0.00003(11)
$\langle \pi(p) \left\| \{J_\mu^V H_W\} \right\| K(0) \rangle$	0	0.00287(16)	0.00127(21)	0.00019(16)
	i	$i \cdot 0.000401(65)$	$i \cdot 0.000122(60)$	$i \cdot 0.000008(47)$
$\langle \pi(0) \left\| T[J_\mu^A H_W] \right\| K(0) \rangle$	0	0.07338(42)	$-0.00125(21)$	$-0.01685(18)$
$\langle \pi(p) \left\| T[J_\mu^A H_W] \right\| K(0) \rangle$	0	0.07330(40)	$-0.00148(23)$	$-0.01698(17)$
	i	$i \cdot 0.00605(17)$	$-i \cdot 0.00018(11)$	$-i \cdot 0.00153(11)$
$\langle \pi(0) \left\| T[J_\mu^A H_W] \right\| K(0) \rangle_{disc}$	0	0.001134(84)	$-0.000343(93)$	$-0.000468(69)$

Table 7.4: Summary of fit results for Z-exchange analysis. The double line separates results for the vector current (above) from the results for the axial current (below).

Form Factor	Q_1	Q_2	$C_1Q_1 + C_2Q_2$
$F_0^V(q^2_{max})$	$-0.00382(15)$	$-0.00137(17)$	$-0.00004(13)$
$F_+^V(q^2)$	$-0.00393(22)$	$-0.00163(25)$	$-0.00022(19)$
$F_+^V(q^2) - X_V f_+(q^2)$	$-0.00015(14)$	$-0.00028(15)$	$-0.00018(11)$
$F_0^A(q^2_{max})$	$-0.09231(64)$	0.00158(26)	0.02119(24)
$F_+^A(q^2)$	$-0.09221(63)$	0.00198(34)	0.02160(31)
$F_{0,disc}^A(q^2_{max})$	$-0.00143(11)$	0.00043(12)	0.000589(87)

Table 7.5: Summary of form factors obtained from Z-exchange analysis. The upper case F denotes the Z-exchange form factor, obtained using Eqs. (5.6) and (5.10). The lower case f denotes the $K_{\ell 3}$ form factor, obtained using Eq. (5.24). The double line separates results for the vector current (above) from the results for the axial current (below).

7.3.2.1 Vector Current

The analysis of the vector current proceeds in a similar manner to the analysis presented for $K \to \pi\ell^+\ell^-$ decays in section 6.3.2. We employ "method 2" to remove the exponentially growing contribution from the single-pion intermediate state, i.e. we shift the weak Hamiltonian by the scalar density $\bar{s}d$. The effect of this shift is shown for the unintegrated correlators in Fig. 7.8. Additionally we may note that there is a large peak at the point $t_H - t_J = 0$; this is a signature of the short-distance divergence caused by the contact of the two operators in the 4pt correlator.

The integrated correlators with a vector current insertion are shown in Fig. 7.9 where the final state pion is at rest, and Fig. 7.10, where the final state pion has the momentum $\mathbf{p}_\pi$. We only study the $\mu = 0$ component of the current to extract the desired form

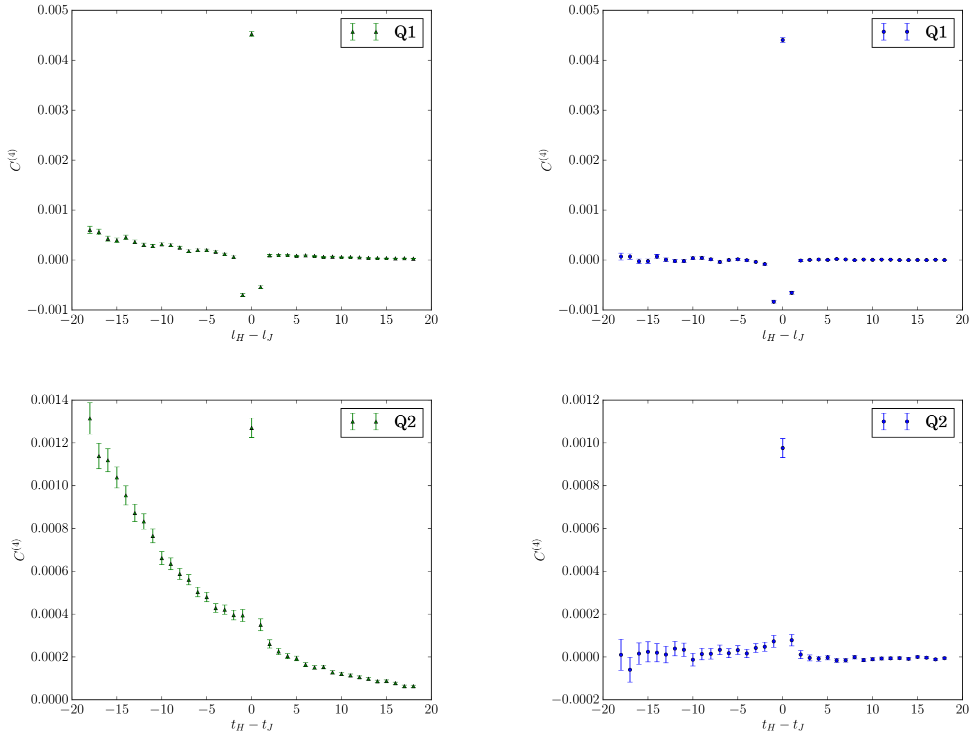

(a) (b)

Figure 7.8: Plots of the unintegrated 4pt correlator for Z-exchange diagrams with a vector current insertion, for each operator that makes up H_W. The correlator is shown (a) before and (b) after shifting by the scalar density $\bar{s}d$ to remove the growing exponential term of the single-pion intermediate state.

factor, as discussed in section 5.1.1. When the pion has non-zero momentum, we may also study the correlators with $\mu = i$; however the best signal is observed for the $\mu = 0$ component. The fit results are summarised in Table 7.4, and the corresponding form factors in Table 7.5.

It should be noted that in the case $\mathbf{p}_K = \mathbf{p}_\pi = \mathbf{0}$, the matrix element vanishes; the non-zero signal we observe is purely the short-distance divergence caused by the contact of the local current and H_W operators (note that we still however must remove the unphysical exponentially growing intermediate state contributions). This explains our choice of fit range very close to the start of the integral; after capturing the short-distance divergence there is no remaining signal, only noise. This known result may be used to calculate the counterterm X_V required to remove the divergence in the matrix element by demanding

$$A^V_\mu\left(\mathbf{0},\mathbf{0}\right) - X_V\left(a\right) A^{K_{\ell 3}}_\mu\left(\mathbf{0},\mathbf{0}\right) = 0. \tag{7.12}$$

The counterterms calculated using this method are summarised in Table 7.6. After the removal of the divergence, there is almost no signal for the vector matrix element; this is

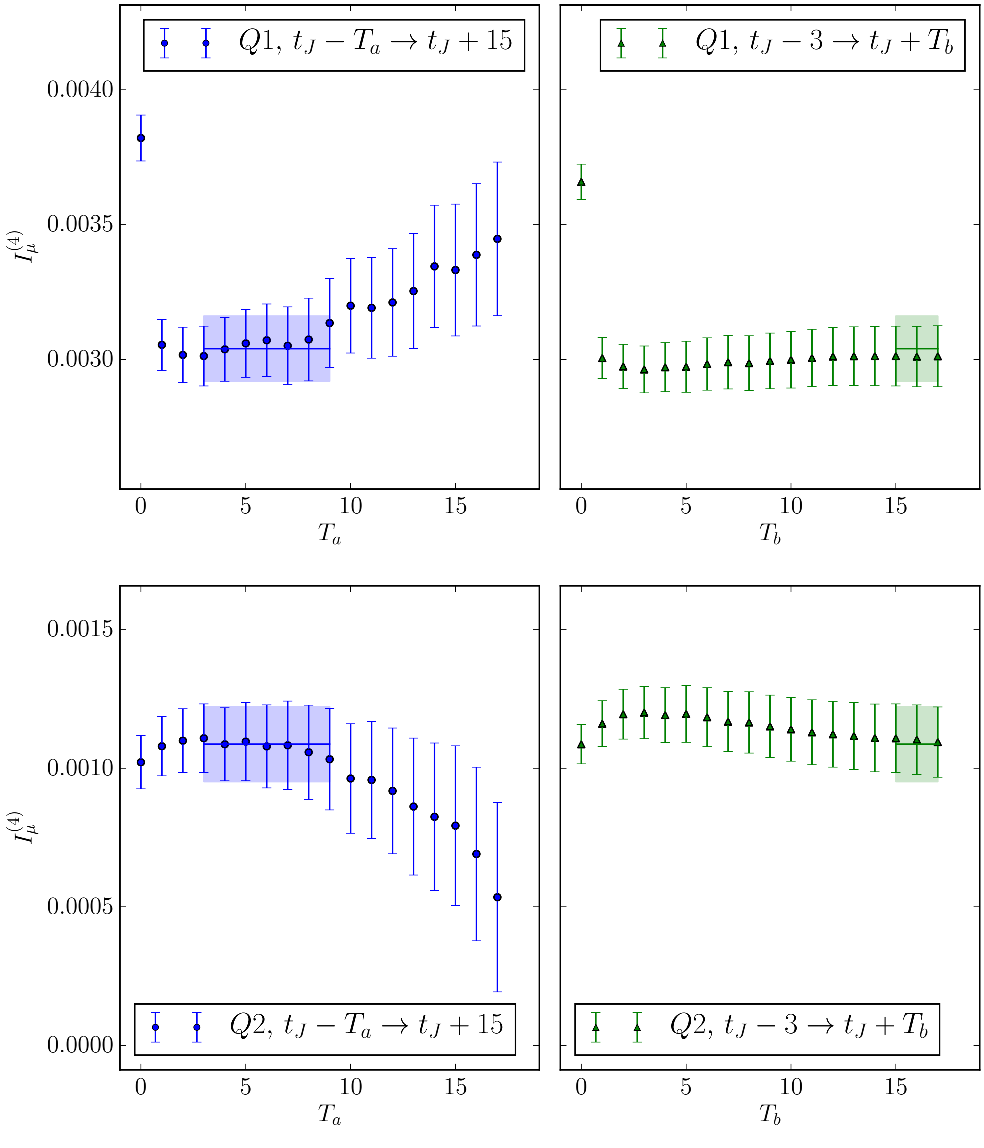

(a) (b)

Figure 7.9: The integrated 4pt correlator for Z-exchange diagrams with a vector current insertion, shown with (a) varying T_a and fixed T_b and (b) vice versa, with $\mathbf{p}_K = \mathbf{p}_\pi = \mathbf{0}$. Results are shown for the operators Q_1 (top) and Q_2 (bottom). The result for the matrix element is indicated by the horizontal band and indicates the fit range used for its extraction.

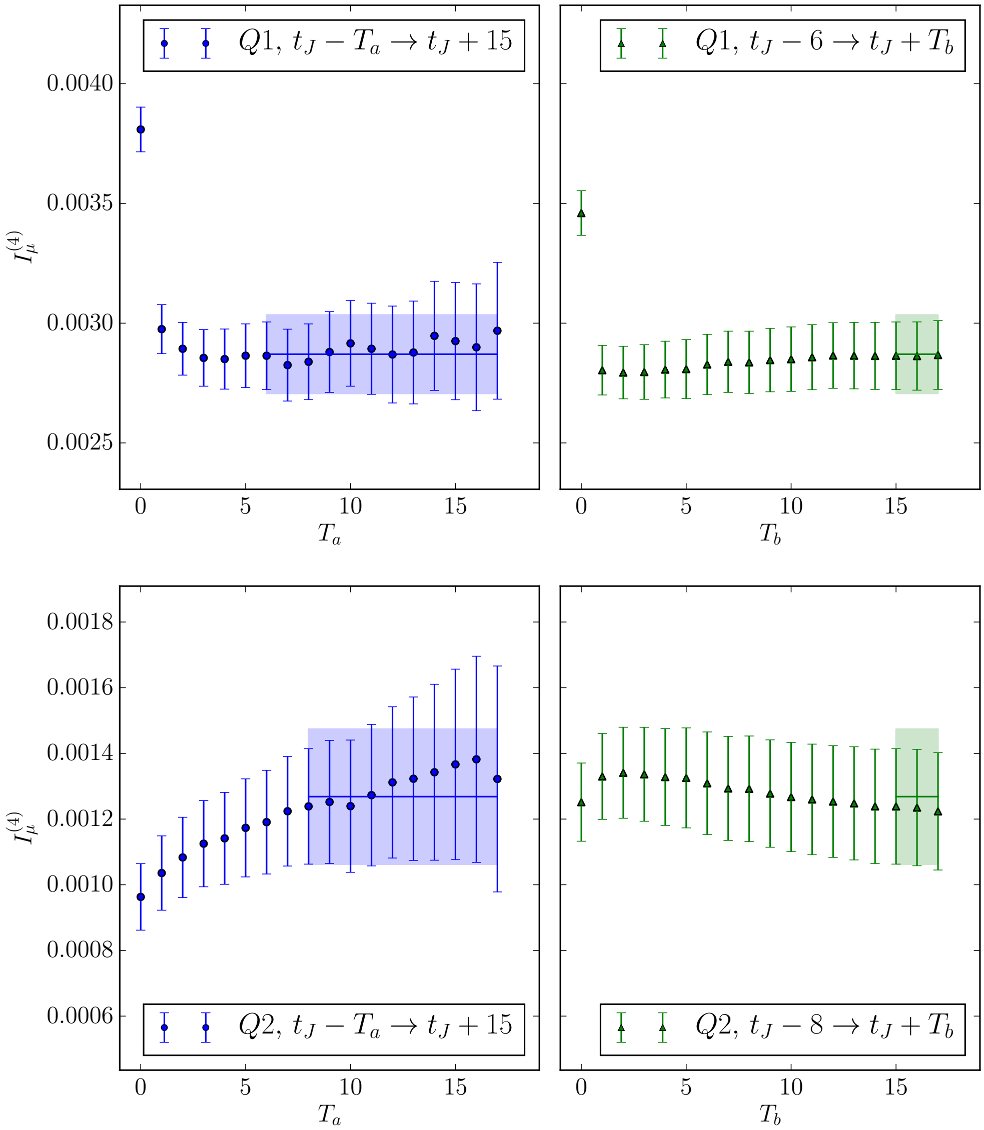

(a) (b)

Figure 7.10: The integrated 4pt correlator for Z-exchange diagrams with a vector current insertion, shown with (a) varying T_a and fixed T_b and (b) vice versa. Results are shown for the operators Q_1 (top) and Q_2 (bottom). The result for the matrix element is indicated by the horizontal band and indicates the fit range used for its extraction.

	Q_1	Q_2	$C_1Q_1 + C_2Q_2$
$X_V\ (a)$	$-0.00380(15)$	$-0.00136(17)$	$-0.00004(13)$

Table 7.6: Counterterms for removing the short-distance divergent in Z-exchange diagrams with a vector current insertion.

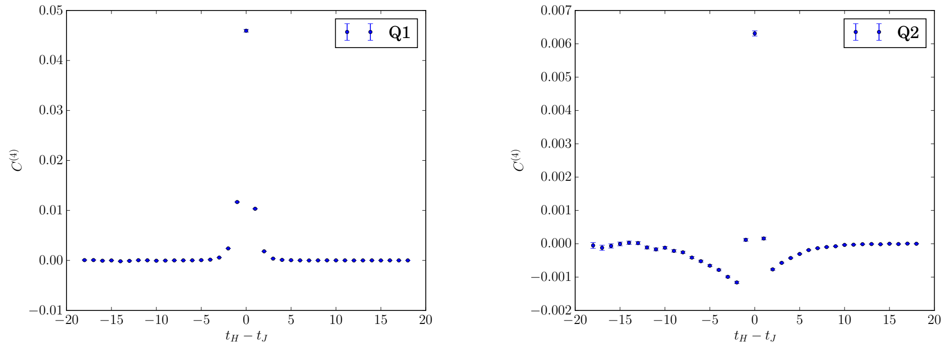

(a) (b)

Figure 7.11: Plots of the unintegrated 4pt correlator for Z-exchange diagrams with an axial current insertion, for each operator (a) Q_1 and (b) Q_2 that makes up H_W.

not unexpected given that we are using a very small final state pion momentum, and are thus not far removed from the point $\mathbf{p}_K = \mathbf{p}_\pi = \mathbf{0}$ at which the matrix element vanishes.

It should be remarked that after the removal of the divergence, the remaining matrix element is UV-finite, and no further matching step is necessary. This method is distinct from the method required to regulate the divergence in the axial current matrix elements in the $\overline{\text{MS}}$ scheme, which will be discussed in section 7.4.

7.3.2.2 Axial Current

The analysis of the axial current is straightforward for our exploratory studies in that the correlators do not contain any exponentially increasing intermediate state contributions. It therefore suffices to integrate our correlators in a large enough window such that the integrals converge. Of course in future simulations at the physical point, we would expect to see an exponential increase for negative values of $t_H - t_J$ from a $\pi\pi$ intermediate state. For this analysis we note that we must consider both the $\mu = 0$ and $\mu = i$ components of the current in order to extract the desired form factors using Eq. (5.6).

The unintegrated correlators are shown in Fig. 7.11; for demonstration we show only the $\mu = 0$ component. It should be noted that for both operators Q_1 and Q_2 these correlators do become consistent with zero at large values of $|t_H - t_J|$; this is a good indicator that our integrals will converge within the available time extent. Additionally we may note the large peak at the point $t_H = t_J$, which is indicative of the short-distance divergence that must be removed.

The integrated correlators are shown in Fig. 7.12 for $\mu = 0$ and Fig. 7.13 for $\mu = i$, where the final state pion has momentum $\mathbf{p}_\pi$. This figure shows the plateaus of the integrated correlator at large values of $|t_H - t_J|$; the matrix element is extracted from a constant fit to this plateau. The results are summarised in Table 7.4, and the corresponding form factors obtained using Eq. (5.6) are given in Table 7.5.

7.3.2.3 Disconnected Diagrams

In figure 7.14 I show the unintegrated correlators for the disconnected topologies of Z-exchange diagrams (e.g. as appearing in Fig. 5.2), with the axial current insertion. It must be noted that the disconnected diagrams have been calculated using $\mathbf{p}_K = \mathbf{p}_\pi = \mathbf{0}$ (i.e. at $q^2 = q^2_{max}$); the disconnected diagram with a vector current insertion thus vanishes. Additionally note that there is no short-distance divergence present in these diagrams from the contact of the two operators. The analysis thus proceeds in a similar manner to the analysis presented above; the fit results to these disconnected diagrams are shown in Table 7.4. We note that although the percentage errors on the disconnected contributions are very large, the absolute errors are only about 20% of the errors on the connected contributions. Although the disconnected diagrams have only been calculated using $\mathbf{p}_K = \mathbf{p}_\pi = \mathbf{0}$ (i.e. at $q^2 = q^2_{max}$), we observe that their overall contribution is only a small percentage of the connected contribution (after renormalisation), and hence it is reasonable to neglect this small systematic error. This suppression of disconnected diagrams is not unexpected; as noted in section 6.2.1 the disconnected diagrams with u, d and s loops sum to zero in the $SU(3)$-symmetric limit, and the remaining charm quark loop contribution is suppressed by its heavy mass.

7.3.3 W-W Analysis

In this section I will present the numerical analysis of the W-W diagrams. This analysis is broken up into two parts corresponding to the "type 1" and "type 2" topologies (shown in Fig. 5.4), because of the different pattern of intermediate states in each case. The theory behind the exponentially growing intermediate states appearing in W-W diagrams is presented in section 5.2.3.3.

7.3.3.1 Type 1 Diagrams

I begin with the presentation of the analysis for type 1 diagrams, where we expect exponentially growing contributions from $|\ell\nu\rangle$ intermediate states, which may only appear

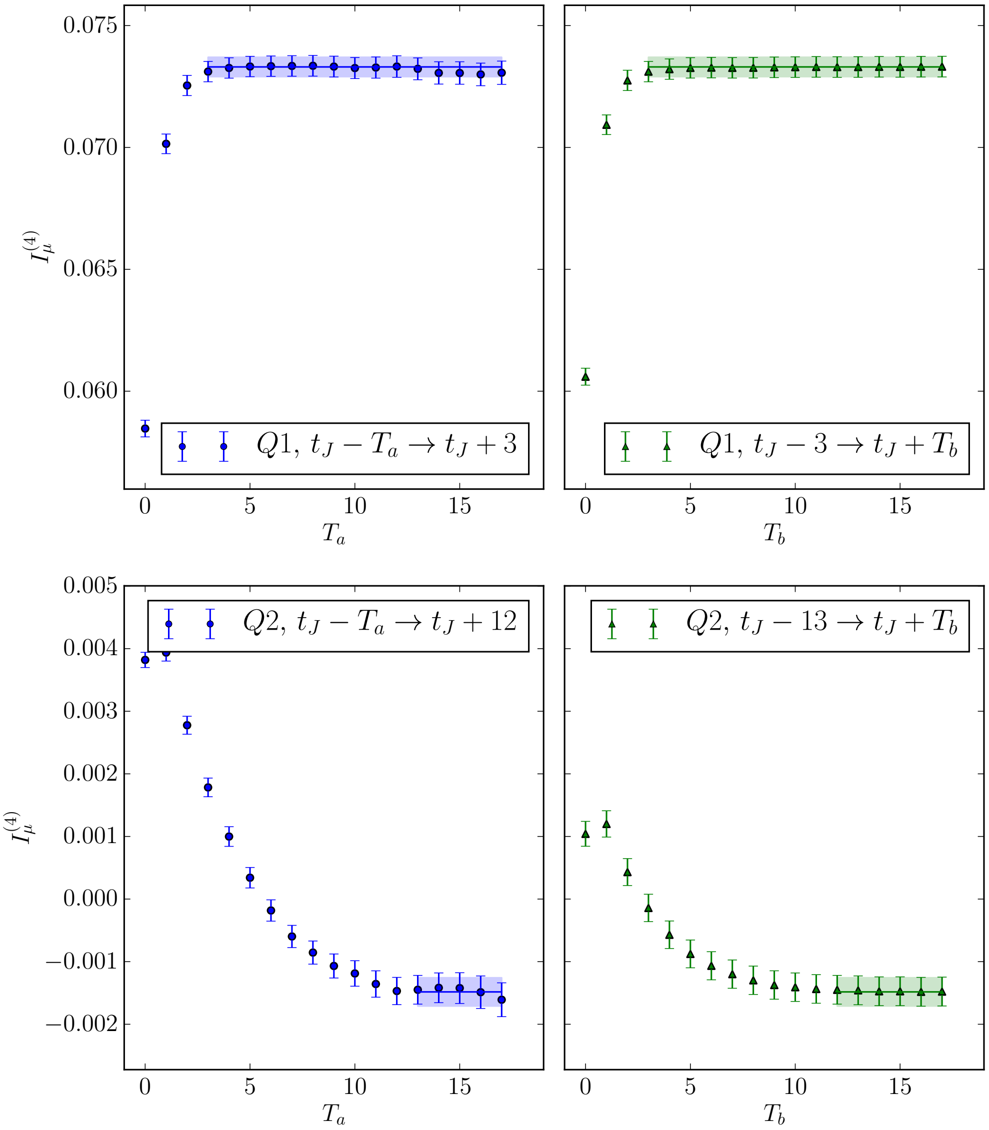

(a) (b)

Figure 7.12: The integrated 4pt correlator for Z-exchange diagrams with an axial current insertion ($\mu = 0$), shown with (a) varying T_a and fixed T_b and (b) vice versa. Results are shown for the operators Q_1 (top) and Q_2 (bottom). The result for the matrix element is indicated by the horizontal band and indicates the fit range used for its extraction.

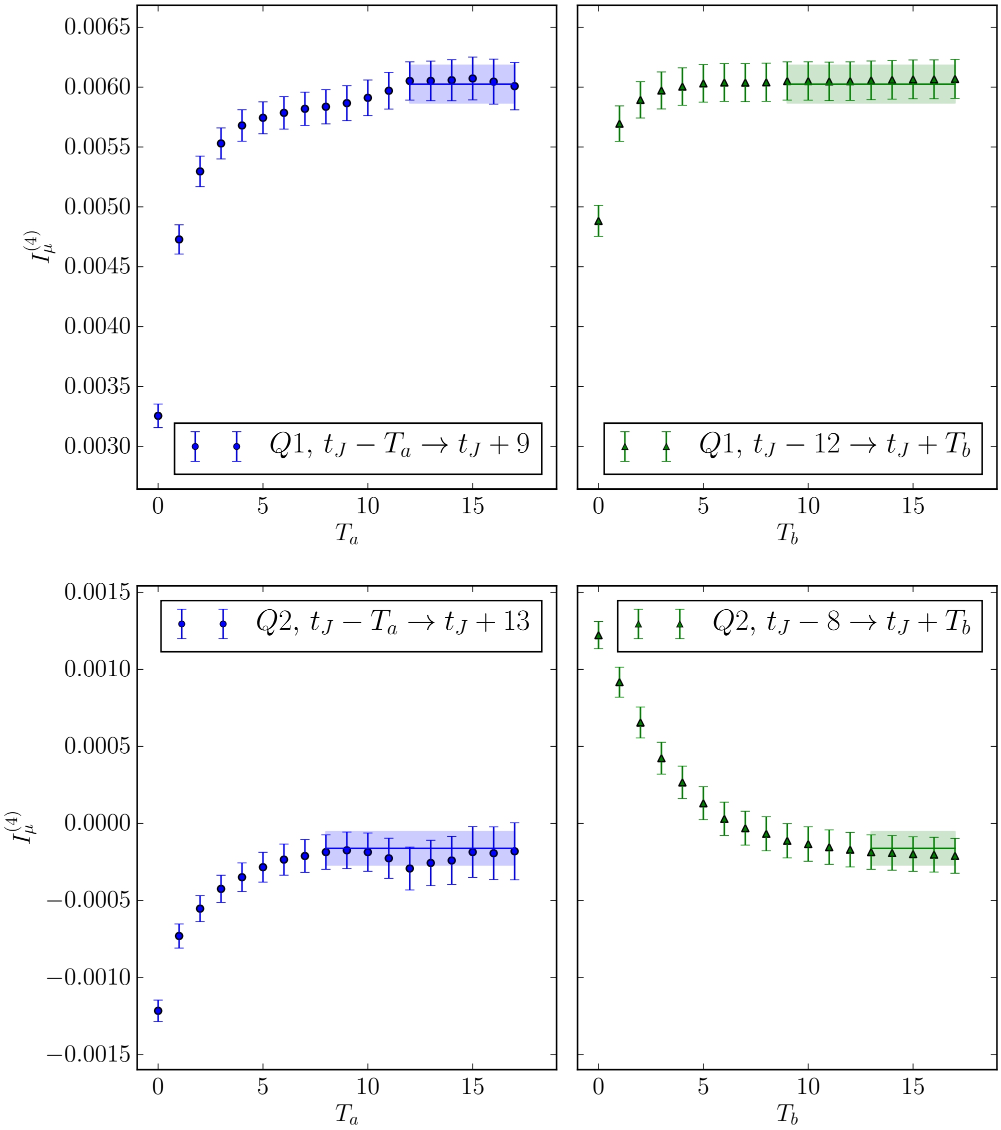

(a) (b)

Figure 7.13: The integrated 4pt correlator for Z-exchange diagrams with an axial current insertion ($\mu = i$), shown with (a) varying T_a and fixed T_b and (b) vice versa. Results are shown for the operators Q_1 (top) and Q_2 (bottom). The result for the matrix element is indicated by the horizontal band and indicates the fit range used for its extraction.

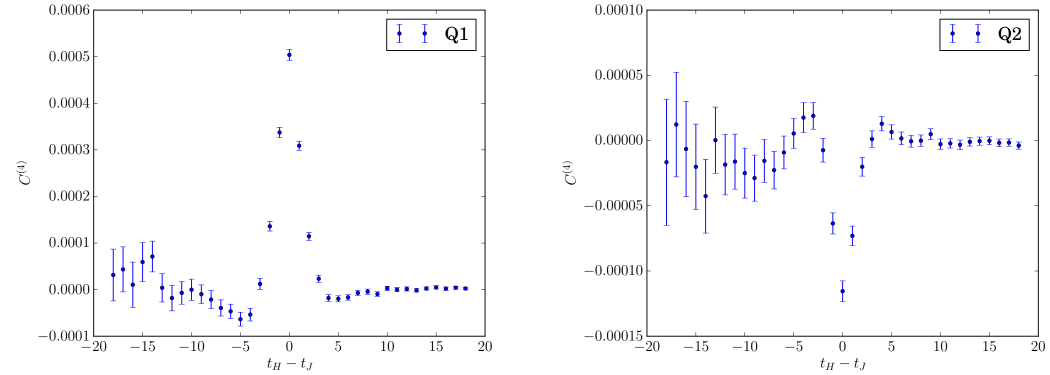

Figure 7.14: Plots of the unintegrated 4pt correlator for quark-disconnected Z-exchange diagrams with an axial current insertion, for each operator that makes up H_W.

for $\ell = e, \mu$. The unintegrated correlators are shown in Fig. 7.15. We see that for the intermediate state muon, there is a clear exponential increase as the operators are separated. This exponentially growing contribution however is absent for the electron intermediate state; this is due to helicity suppression as described in section 5.2.3.3. The muon contribution with the exponentially growing state removed is shown in Fig. 7.16.

In Fig. 7.17 I show the W-W diagram correlators after integrating over the position of $\mathcal{O}^{\Delta S=1}_{\ell\nu}$. For both sides of the integral, at large time separations the integral can be seen to converge. The matrix element is extracted by a constant fit to the region where the integral converges. We remark that when the intermediate lepton is either an electron or muon, the T_a side of the integral converges quickly and then begins to accumulate noise; the best signal is obtained by fitting before this noise dominates. We remark that we can inspect Fig. 7.15 for the electron and Fig. 7.16 for the muon to determine where the unintegrated correlator agrees with zero within statistical errors to be sure that we do not truncate the integral too early.

Fig. 7.17 also shows how the T_b side of the integral converges rather slowly for the intermediate states with an electron or muon; for this reason it is reasonable to question whether or not it converges completely within the available time extent. The lightest intermediate state for $t_{\Delta S=1} > t_{\Delta S=0}$ is $\pi K \ell^+ \nu$, which is responsible for this slow exponential decay. While we do not have the necessary matrix elements to remove this slow exponential decay using method 1, we may perform a direct fit of the 4pt correlator to extract the necessary parameters. Hence we fit the unintegrated correlator to the relation

$$F^{\ell}_{WW}\left(t_{\Delta S=1}, t_{\Delta S=0}\right) = N^{\ell\nu}_{\pi K} \exp\left(-\Delta E^{\ell\nu}_{\pi K}\left(t_{\Delta S=1} - t_{\Delta S=0}\right)\right) \tag{7.13}$$

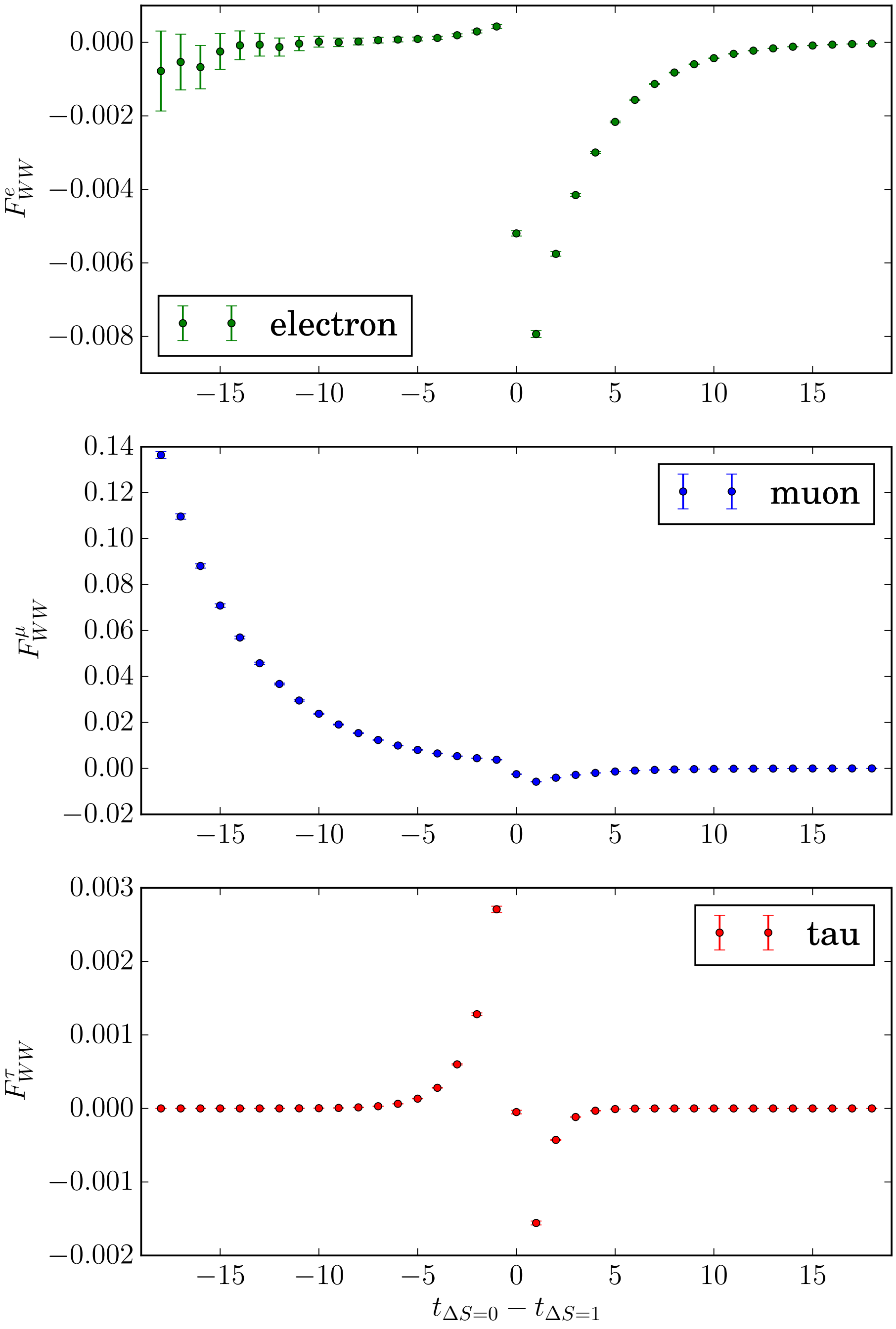

Figure 7.15: Type 1 unintegrated correlators F_{WW} for the three different flavours of intermediate leptons.

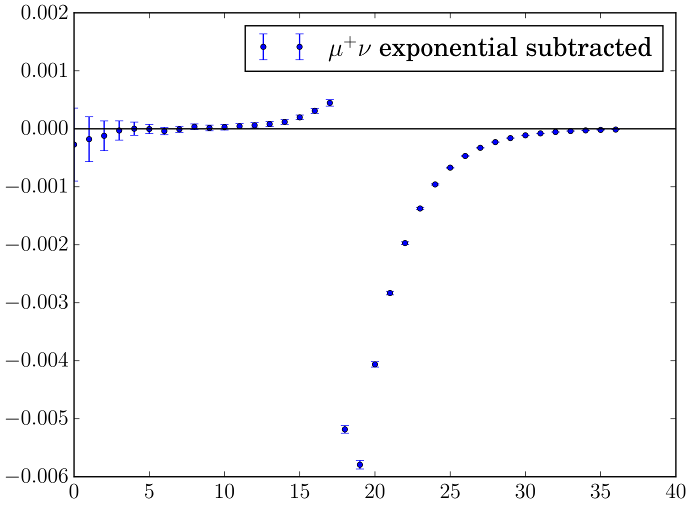

Figure 7.16: Unintegrated 4pt correlator for W-W diagram with intermediate muon, after removing the $\mu^+\nu$ intermediate state. The horizontal black line shows the position of zero.

Lepton	$N^{\ell\nu}_{\pi K}$	$\Delta E^{\ell\nu}_{\pi K}$
electron	-0.05729(12)	0.57944(89)
muon	-0.032674(88)	0.57805(92)

Table 7.7: Fit results [to Eq. (7.13)] for the $K\pi\ell^+\nu$ intermediate states in type 1 W-W diagrams.

in the region $t_{\Delta S=1} \gg t_{\Delta S=0}$. The fit parameters we obtain are displayed in Table 7.7. The contribution we remove from the integrated correlator is

$$I^{\ell}_{WW}\left(t_{\Delta S=1}, t_{\Delta S=0}\right) = \frac{N^{\ell\nu}_{\pi K}}{e^{\Delta E^{\ell\nu}_{\pi K}} - 1} \exp\left(-\Delta E^{\ell\nu}_{\pi K}\left(T_b\right)\right). \tag{7.14}$$

An inspection of Fig. 7.17 shows that the integral does indeed converge to the same answer within the available statistical precision whether or not this state is removed.

7.3.3.2 Type 2 Diagrams

In the analysis of type 2 diagrams we expect there to be exponentially growing contributions from $|\ell\nu\rangle$ intermediate states, $\ell = e, \mu$. The unintegrated correlators are shown in Fig. 7.18. At first glance, it appears that there is no exponentially growing contribution to these correlators. This is because the mass difference $E_K\left(\mathbf{p}_K\right) - E_\pi\left(\mathbf{p}_K\right) - E_\ell\left(-\mathbf{p}_\pi/2\right)$ is very small such that the exponentially growing behaviour is very weak. In Figure 7.19 I show the integrated correlators; for the case of the muon it can be seen that this state

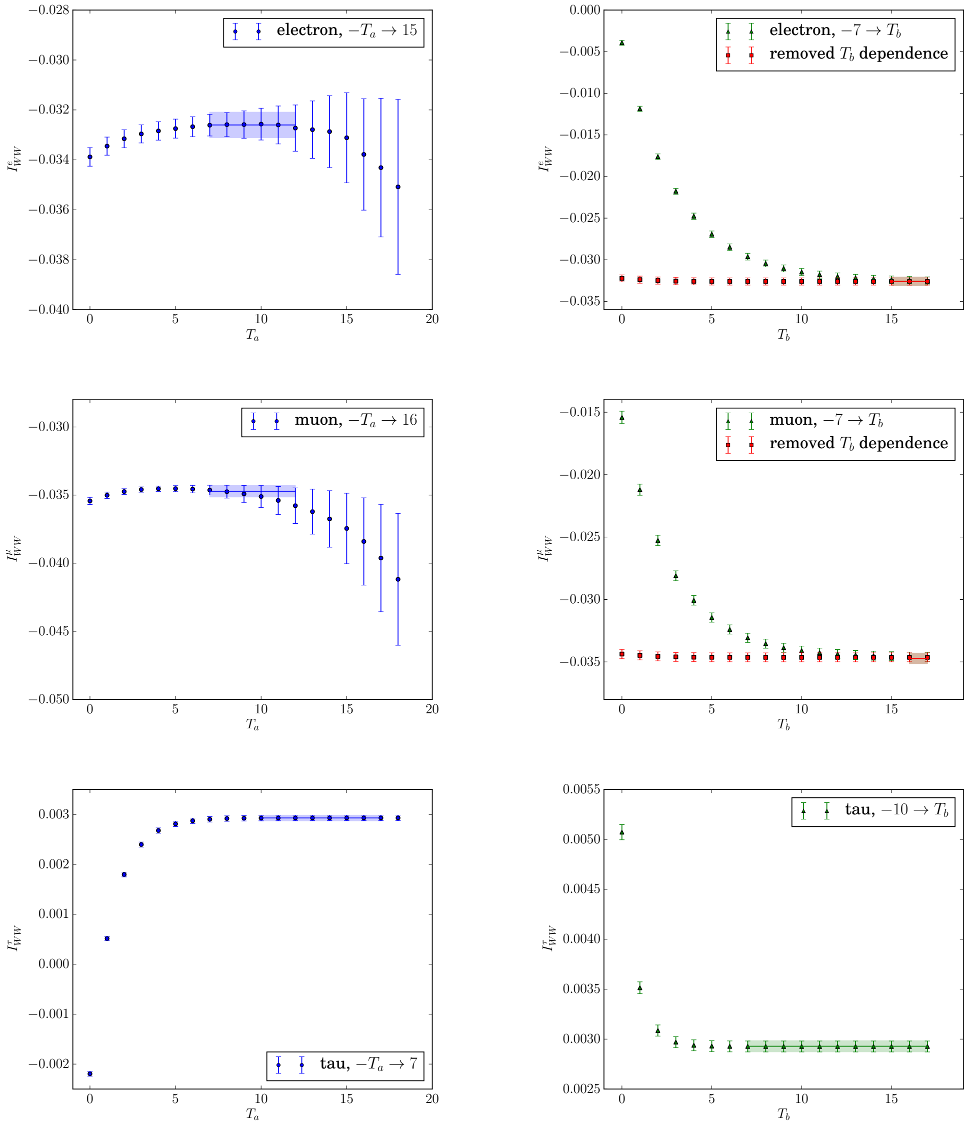

(a) (b)

Figure 7.17: The integrated 4pt correlator for type 1 W-W diagrams, shown for (a) T_b fixed to demonstrate the T_a dependence and (b) vice versa. Integration limits and intermediate lepton flavour are indicated within the legend. For the electron and muon I show the T_b dependence before and after its removal using a direct fit of the 4pt correlator.

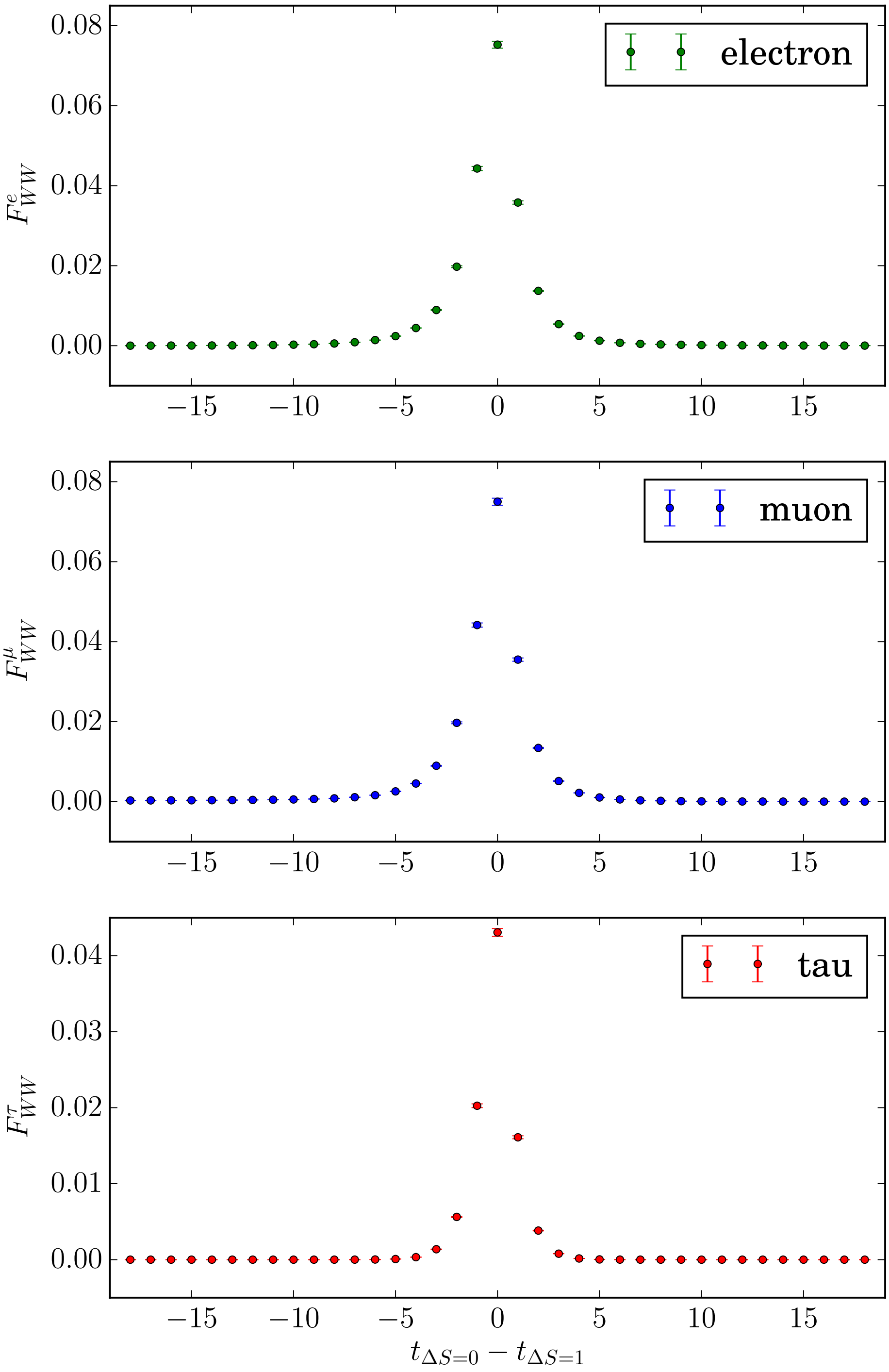

Figure 7.18: Type 2 unintegrated correlators F_{WW} for the three different leptonic intermediate states.

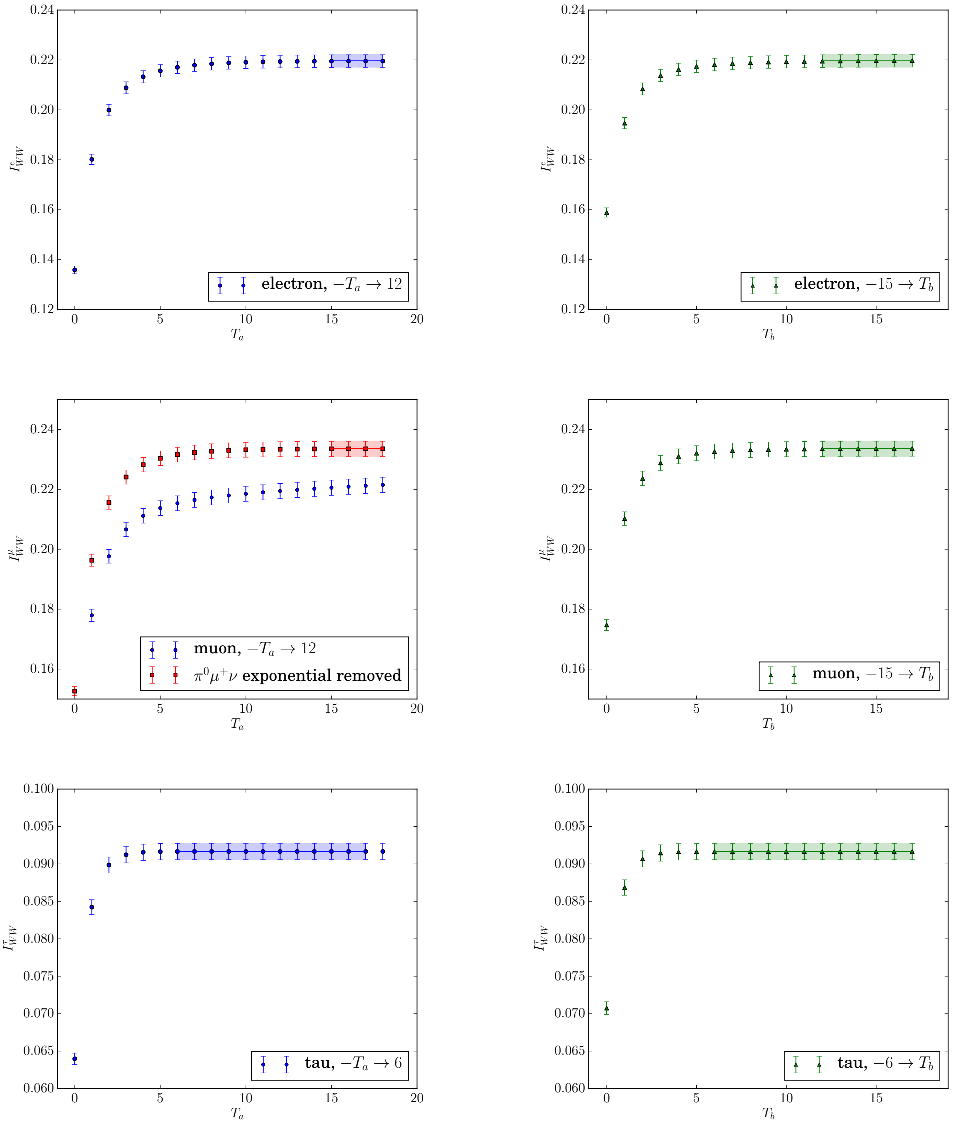

(a) (b)

Figure 7.19: The integrated 4pt correlator for type 2 diagrams, shown for (a) T_b fixed to demonstrate the T_a dependence and (b) vice versa. Integration limits are indicated within the legend. For the muon I show the T_a dependence before and after removing the $\pi^0\ell^+\nu$ intermediate state exponential.

must be removed to avoid a significant systematic effect. For the electron however we find that this state is absent. The reason for this is that the intermediate state pion carries discrete lattice momenta, while the electron carries the twisted momentum. The ground state hence is given by a pion with zero momentum, and thus the electron experiences helicity suppression similar to the type 1 case.

Lepton	Type 1	Type 2
electron	-0.03260(51)	0.2197(25)
muon	-0.03472(42)	0.2336(25)
tau	0.002929(55)	0.0917(11)

Table 7.8: Summary of fit results for W-W analysis. The results are shown before multiplying by the relevant individual operator renormalisation constants.

7.4 Renormalisation

Before we can compare our lattice results to the continuum, we must regulate the short-distance divergences that appear in the bilocal matrix elements as a result of the contact of the two operators involved. For Z-exchange diagrams, these divergences appear in the E (Q_1) and S (Q_2) diagram topologies; for W-W diagrams they appear in the type 2 topology. These divergences do not appear in the final result; rather they will cancel with divergences appearing in the Wilson coefficient of the local matrix element. These Wilson coefficients have previously been computed in the $\overline{\mathrm{MS}}$ scheme, hence our aim is to regulate the divergence in the same scheme.

The total expression for the bilocal matrix element, where divergences have been regulated in the $\overline{\mathrm{MS}}$ scheme, may be summarised as

$$\mathcal{A}^{\overline{\mathrm{MS}}}\left(q^2\right) = \frac{i}{3}\sum_{\ell=e,\mu,\tau}\left(F_Z^{\overline{\mathrm{MS}}}\left(q^2\right) + F_{WW}^{\ell,\overline{\mathrm{MS}}}\left(q^2\right)\right)\left[\bar{u}\left(p_{\nu_\ell}\right)\not{p}_K\left(1-\gamma_5\right)v\left(p_{\bar{\nu}_\ell}\right)\right], \tag{7.15}$$

with

$$F_Z^{\overline{\mathrm{MS}}}\left(q^2\right) = \sum_i F_{Z,i}\left(q^2\right) - 2\left(C_i^{\mathrm{lat}}X_{A,i}\left(a,\mu_{\mathrm{RI}}\right) - C_i^{\overline{\mathrm{MS}}}Y_{A,i}\left(\mu,\mu_{\mathrm{RI}}\right)\right)f_+\left(q^2\right) \tag{7.16}$$

$$F_{WW}^{\ell,\overline{\mathrm{MS}}}\left(q^2\right) = F_{WW}^{\ell}\left(q^2\right) - 2\left(Z_V X_{WW}^{\ell}\left(a,\mu_{\mathrm{RI}}\right) - Y_{WW}^{\ell}\left(\mu,\mu_{\mathrm{RI}}\right)\right)f_+\left(q^2\right), \tag{7.17}$$

where the index i indicates the relevant operator of H_W for Z-exchange diagrams, and the form factors F_Z and F_{WW} are defined in Eqs. (5.9) and (5.14) respectively, and contain lattice-regulated divergences. The factor of 1/3 arises from an average over the 3 lepton flavours. It is implicit in the above equation that the divergence in F_Z^V has been removed using counterterm X_V discussed in section 7.3.2.1. I include the lepton sub/superscripts ℓ here for to show which parts of the calculation depend upon the lepton flavours.

We are interested in a comparison between our lattice results and results using perturbation theory. To aid this comparison, we define the ratio

$$R_{AB}\left(\Delta, s\right) = \frac{F_{AB}\left(\Delta, s\right)}{2f_{+}\left(s\right)}, \tag{7.18}$$

where $f_{+}\left(s\right)$ is the $K_{\ell 3}$ form factor, and the kinematical variables Δ and s were introduced in section 7.2. As in section 5.3.3 I use the labels A and B to denote the operators involved in the bilocal matrix elements; however for clarity I will use Z or WW when referring to the results for Z-exchange and W-W diagrams respectively. These ratios are of course dependent upon the kinematical configuration we choose for our simulation; however we have only considered one kinematical point here and thus are unable to determine the dependence on these variables. In the remaining discussion this dependence will be neglected.

The ratios defined by Eq. (7.18) are related to the quantity P_c that appears in Eq. (3.65) by

$$P_c = \frac{1}{3}\frac{1}{\lambda^4}\sum_{\ell=e,\mu,\tau}\left[\frac{\pi^2}{M_W^2}\left(R_Z\left(\mu\right) + R_{WW}^{\ell}\left(\mu\right)\right) + C_\nu^c\left(\mu\right)\right], \tag{7.19}$$

where C_ν^c is the component of the $\overline{\text{MS}}$ Wilson coefficient of the local operator Q_ν that describes the short-distance charm-quark contribution to $K \to \pi\nu\bar{\nu}$. The normalisations follow from the definitions of the weak Hamiltonians discussed in section 3.1.3. It is also convenient to define the quantity

$$\Delta R_{AB}\left(\mu\right) = R_{AB}\left(\mu\right) - r_{AB}\left(\mu\right), \tag{7.20}$$

where r_{AB} is defined in Eq. (3.60). This quantity thus gives the difference between the non-perturbative and perturbative estimates of the bilocal contribution.

In this rest of this section I present the results of the procedure for the renormalisation of bilocal matrix elements, which is discussed in detail in section 5.3.3. This procedure can be split into 2 parts. First I begin in section 7.4.1 by discussing the calculation of the term $X_{AB}\left(\mu_{\text{RI}}\right)$ required to convert the bare lattice matrix element into one regulated in the RI-SMOM scheme. Secondly I discuss the calculation of the perturbative matching to the $\overline{\text{MS}}$ scheme, $Y_{AB}\left(\mu_{\text{RI}}, \mu\right)$, in section 7.4.2. The overall result is then summarised in section 7.4.3.

7.4.1 RI-SMOM renormalisation

The first step of the renormalisation procedure is to convert the regularisation of the UV-divergences from the lattice scheme to the RI-SMOM scheme. The counterterms are

μ	Z-exchange			W-W		
	Q_1	Q_2	$C_1Q_1 + C_2Q_2$	e	μ	τ
1.00	6.659(39)	1.671(18)	0.382(12)	4.958(140)	5.481(155)	2.866(80)
1.25	6.019(32)	1.516(14)	0.342(9)	4.697(115)	4.690(115)	2.613(6 3)
1.50	5.379(26)	1.365(14)	0.299(10)	3.889(73)	3.878(72)	2.279(42)
1.75	4.723(22)	1.211(12)	0.255(8)	3.304(48)	3.289(47)	2.030(29)
2.00	4.112(20)	1.061(12)	0.217(7)	2.644(36)	2.679(36)	1.756(24)
2.25	3.555(19)	0.932(12)	0.178(8)	2.215(28)	2.213(28)	1.506(19)
2.50	3.045(18)	0.815(12)	0.142(8)	1.821(21)	1.818(21)	1.276(15)
2.75	2.605(17)	0.701(12)	0.119(7)	1.492(17)	1.487(17)	1.074(12)
3.00	2.229(18)	0.601(11)	0.101(7)	1.200(13)	1.203(13)	0.897(10)
3.25	1.897(19)	0.513(11)	0.085(7)	0.969(9)	0.968(9)	0.737(7)
3.50	1.596(21)	0.441(12)	0.066(8)	0.778(7)	0.777(7)	0.602(5)
3.75	1.347(23)	0.377(13)	0.052(9)	0.620(6)	0.618(6)	0.486(5)
4.00	1.130(23)	0.327(12)	0.037(8)	0.483(5)	0.483(5)	0.387(4)

Table 7.9: Counterterms for removing the short-distance divergence in WW diagrams and Z-exchange diagrams with an axial current insertion. The counterterms are calculated separately for each operator Q_i entering H_W for Z-exchange diagrams, and for each internal lepton in W-W diagrams. Results are quoted in units of 10^{-2}.

calculated by imposing the condition

$$Z_A^{\mathrm{RI}} Z_B^{\mathrm{RI}} \left\langle d\nu\bar{\nu}\right| \left\{\mathcal{O}_A \mathcal{O}_B\right\} \left|s\right\rangle^{lat}(a)\Big|_{p_i^2=\mu_{\mathrm{RI}}^2} - X_{AB}\left(\mu_{\mathrm{RI}}, a\right) Z_V \left\langle d\nu\bar{\nu}\right|\mathcal{O}_\nu\left|s\right\rangle^{lat}\Big|_{p_i^2=\mu_{\mathrm{RI}}^2} = 0, \tag{7.21}$$

where the operators $\mathcal{O}_A$ and $\mathcal{O}_B$ are those specific to either Z-exchange or W-W diagrams. I have used to notation for the bilocal operator defined in Eq. (5.69). Note that for the Z-exchange diagrams, this procedure is only necessary for the axial current; the removal of the divergence in the bilocal matrix element with a vector current is discussed in section 7.3.2.1.

The RI-SMOM renormalisation procedure for the 4pt functions is discussed in section 5.3.3.1; here I present the results. To study the RI-SMOM scale dependence of the counterterm X_{AB}, the NPR calculation has been performed at multiple values of μ_{RI}, from $\mu_{\mathrm{RI}} = 1\,\mathrm{GeV}$ to $4\,\mathrm{GeV}$ in steps of $0.25\,\mathrm{GeV}$. These results have been computed by Xu Feng using the codebase CPS. I quote the results of his analysis in Table 7.9. The subsequent RI-SMOM regulated results are shown graphically in Fig. 7.20.

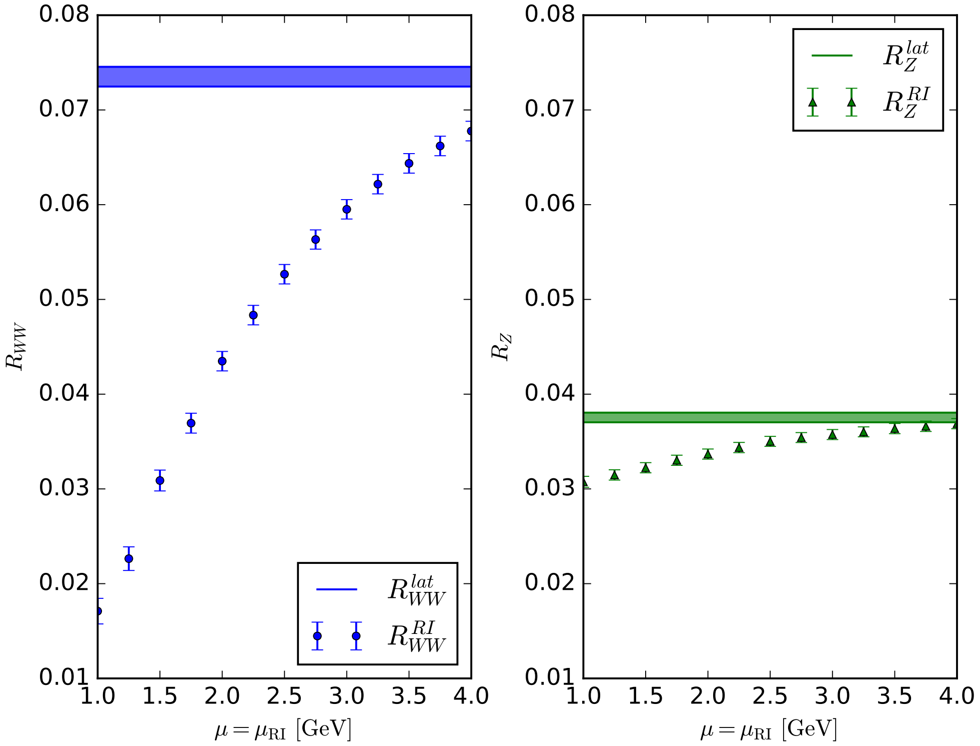

Figure 7.20: Results for the ratio R [Eq. (7.18)], i.e. the form factors obtained from bilocal matrix elements, normalised by the $K_{\ell 3}$ form factor $f_+\left(q^2\right)$, for W-W diagrams (left) and Z-exchange diagrams (right). The horizontal bands shows the results before the regulation of the divergence in the RI-SMOM scheme; the points show the RI-SMOM regulated results. These results additionally include the normalisation factor $\pi^2/\lambda^4 M_W^2$.

Parameter	Value	Parameter	Value
$\sin^2\theta_W\,(M_Z)$	0.23126(5)	$\alpha\,(M_Z)$	0.1185(6)
λ	0.22537(61)	$m_b\,(m_b)$	4.18(3) GeV
$M_Z = \mu_W$	91.1876(21) GeV	μ_b	5.0 GeV
M_W	80.385(15) GeV	$m_c\,(m_c)$	1.080 GeV

Table 7.10: Summary of input parameters and matching scales used for results obtained using RG-improved perturbation theory.

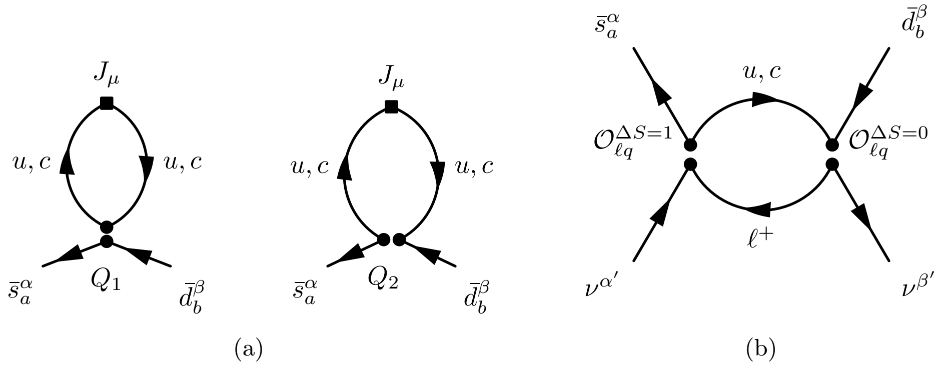

Figure 7.21: Diagrams that must be computed for the perturbative matching of (a) Z-exchange and (b) W-W diagrams.

7.4.2 Perturbative Matching

In order to compute the matching $Y_{AB}(\mu, \mu_{\mathrm{RI}})$, we follow the discussion of 5.3.3.2. The quantity of interest is obtained by imposing the condition

$$\langle d\nu\bar{\nu}| \{\mathcal{O}_A \mathcal{O}_B\} |s\rangle^{\overline{\mathrm{MS}}}(\mu)\Big|_{p_i^2=\mu_{\mathrm{RI}}^2} = \frac{Z_\psi^{\mathrm{RI}}(\mu_{\mathrm{RI}})}{Z_\psi^{\overline{\mathrm{MS}}}(\mu)} Y_{AB}(\mu_{\mathrm{RI}}, \mu) \langle d\nu\bar{\nu}|Q_\nu|s\rangle^{\mathrm{RI}}(\mu_{\mathrm{RI}})\Big|_{p_i^2=\mu_{\mathrm{RI}}^2}, \tag{7.22}$$

On a technical note, we note that this matching procedure is similar to the procedure used to integrate out the charm quark in the perturbative treatment of $K \to \pi\nu\bar{\nu}$ decays, which is discussed in section 3.2.3. Specifically, from a comparison of Eqs. (3.60) and (7.22) we deduce that

$$r_{AB}(\mu) = Y_{AB}(\mu, \mu_{\mathrm{RI}} = 0). \tag{7.23}$$

The quantities r_{AB} for each relevant set of operators has been computed to NNLO in Ref. [79]. Additionally, Ref. [79] contains a detailed description of the NNLO calculation of the H_W Wilson coefficients C_1 and C_2 in the $\overline{\mathrm{MS}}$ scheme.

To evaluate $Y_{AB}(\mu, \mu_{\mathrm{RI}})$ we may thus use existing NNLO perturbative results for part of our calculation and compute

$$Y_{AB}(\mu, \mu_{\mathrm{RI}}) = \Delta Y_{AB}(\mu, \mu_{\mathrm{RI}}) + Y_{AB}(\mu, 0). \tag{7.24}$$

We have therefore computed $\Delta Y_{AB}(\mu, \mu_{\mathrm{RI}})$ to $\mathcal{O}\left(\alpha_s^0\right)$. The expressions for $\Delta Y_{AB}(\mu, \mu_{\mathrm{RI}})$ are given in Appendix B. We remark that we set $\mu = \mu_{\mathrm{RI}}$ in our calculation, this allows $Z_\psi^{\mathrm{RI}}/Z_\psi^{\overline{\mathrm{MS}}} = 1 + \mathcal{O}(\alpha_s)$ [128]. We have taken the running of the charm quark mass into account in these expressions, which at NNLO is given by [79]

$$m_c^2\left(\mu\right) = \kappa_c\left(1 + \left(\frac{\alpha_s\left(\mu\right)}{4\pi}\right)\xi_c^{(1)} + \left(\frac{\alpha_s\left(\mu\right)}{4\pi}\right)^2\xi_c^{(2)}\right)m_c^2\left(m_c\right), \tag{7.25}$$

with $\kappa = \eta_c^{\frac{24}{25}}$, $\eta_c = \alpha_s\left(\mu\right)/\alpha_s\left(m_c\right)$, and

$$\xi_c^{(1)} = \frac{15212}{1875}\left(1 - \eta_c^{-1}\right), \tag{7.26}$$

$$\xi_c^{(2)} = \frac{966966391}{10546875} - \frac{231404944}{3515625}\eta_c^{-1} - \frac{272751559}{10546875}\eta_c^{-2} - \frac{128}{5}\left(1 - \eta_c^{-2}\right)\zeta\left(3\right), \tag{7.27}$$

where ζ is the Riemann zeta function. Using this expression, along with the 3-loop running of $\alpha_s\left(\mu\right)$ [79], we find that the unphysical value of the charm quark mass $m_c\left(\mu = 2\,\text{GeV}\right) = 863\,\text{GeV}$ used in our lattice calculation corresponds to $m_c\left(m_c\right) = 1.080\,\text{GeV}$. We can therefore use this value as an input in our perturbative expressions rather than the physical mass $m_c\left(m_c\right) = 1.275(25)$ [37]. The input parameters and matching scales used for the renormalisation group running analysis are summarised in Table 7.10.

The quantities r_{AB} and ΔY_{AB} are subsequently combined with the relevant Wilson coefficients C_A and C_B (as required by Eqs. (7.16-7.17)), which where necessary are also obtained from a perturbative calculation. The results for each of these quantities (combined with Wilson coefficients) are shown graphically in Fig. 7.22, showing the dependence on the renormalisation scale $\mu = \mu_{\text{RI}}$. We note that a consistent perturbative treatment requires that for each combined quantity $C_A C_B \Delta Y_{AB}$ and $C_A C_B r_{AB}$, the series is truncated at the desired order (i.e. NNLO for r_{AB} and NLO for ΔY_{AB}). Each step of the calculation is thus organised by powers of $\alpha_s\left(\mu\right)$ until the final result is collated. The calculation of ΔY thus makes use of the LO $\overline{\text{MS}}$ running of m_c (only the $\mathcal{O}\left(\alpha_s^0\right)$ term in Eq. (7.25)); we have not however considered the RI-SMOM scale dependence of the charm quark mass. Our calculation serves mainly as a demonstration, which may indeed be improved upon by future perturbative efforts.

7.4.3 Final Result

The overall results for the non-perturbative determination of the bilocal matrix elements, where the divergence is regulated in the $\overline{\text{MS}}$ scheme, are displayed in Fig. 7.23. An interesting feature of the calculation is that the lattice and perturbative results show large discrepancies for the Z-exchange and W-W diagrams individually, but when combined the discrepancy is considerably smaller. The final result we quote is therefore

$$R\left(\Delta, s\right) = 0.1232(13)(32)(-45), \quad \Delta R\left(\Delta, s\right) = 0.0040(13)(32)(-45). \tag{7.28}$$

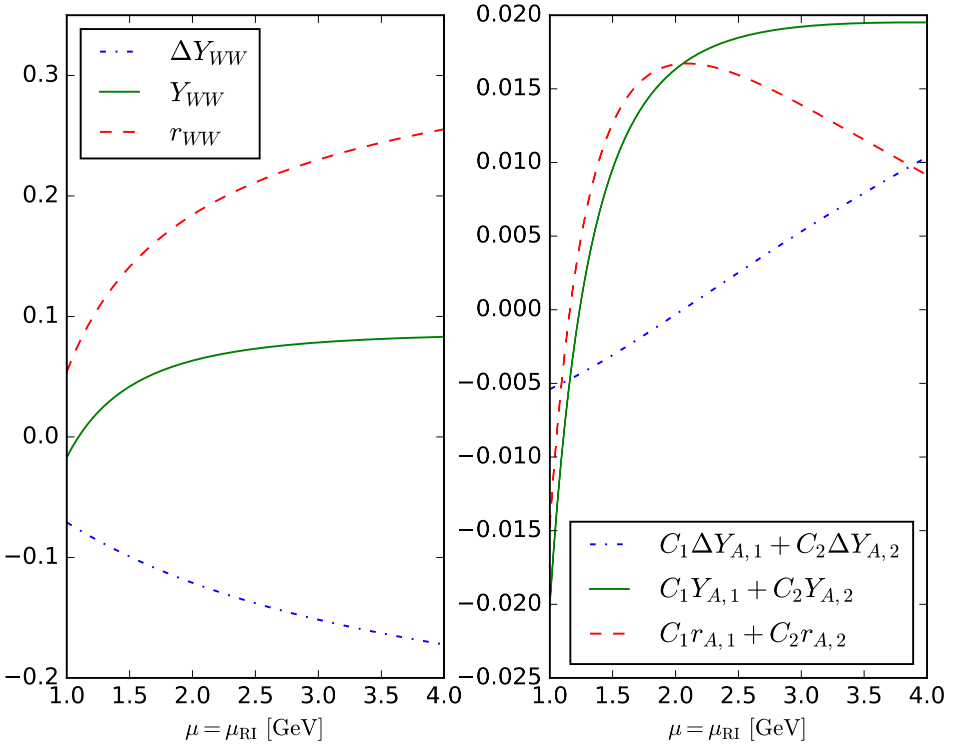

Figure 7.22: Dependence of the quantities $Y_{AB}(\mu, \mu_{\mathrm{RI}})$, $r_{AB}(\mu, \mu_{\mathrm{RI}})$ and $\Delta Y_{AB}(\mu, \mu_{\mathrm{RI}})$ on the renormalisation scale $\mu = \mu_{\mathrm{RI}}$. Results for the W-W diagram are shown on the left, and Z-exchange on the right (matching is only required for the axial current).

The central value quoted corresponds to $\mu = \mu_{\mathrm{RI}} = 2\,\mathrm{GeV}$; the first error is statistical, and the second is an estimate of the error from the residual renormalisation scale dependence by varying $\mu = \mu_{\mathrm{RI}}$ from 1 GeV to 3 GeV. Note that at scales as low as 1 GeV, we would expect that higher order perturbative corrections are significant; however for scales as high as 3 GeV our non-perturbative calculation may suffer from sizeable discretisation errors, given that the condition Eq. (5.71) must be satisfied for reliable results. The third error is a finite volume error, which has been estimated by Xu Feng using the formulae within Ref. [33]. Finally we may also include the local charm quark contributions, such that the full up and charm quark contribution is

$$P_c = 0.2529(13)(32)(-45). \tag{7.29}$$

The results presented above may be used to draw an interesting comparison between the results from the lattice and those calculated in perturbation theory, however a fully quantitative comparison is premature [in particular with the quantity $\delta P_{u,c}$ of Eq. (3.63)], given numerous sources of uncontrolled systematic errors in our calculation. The errors

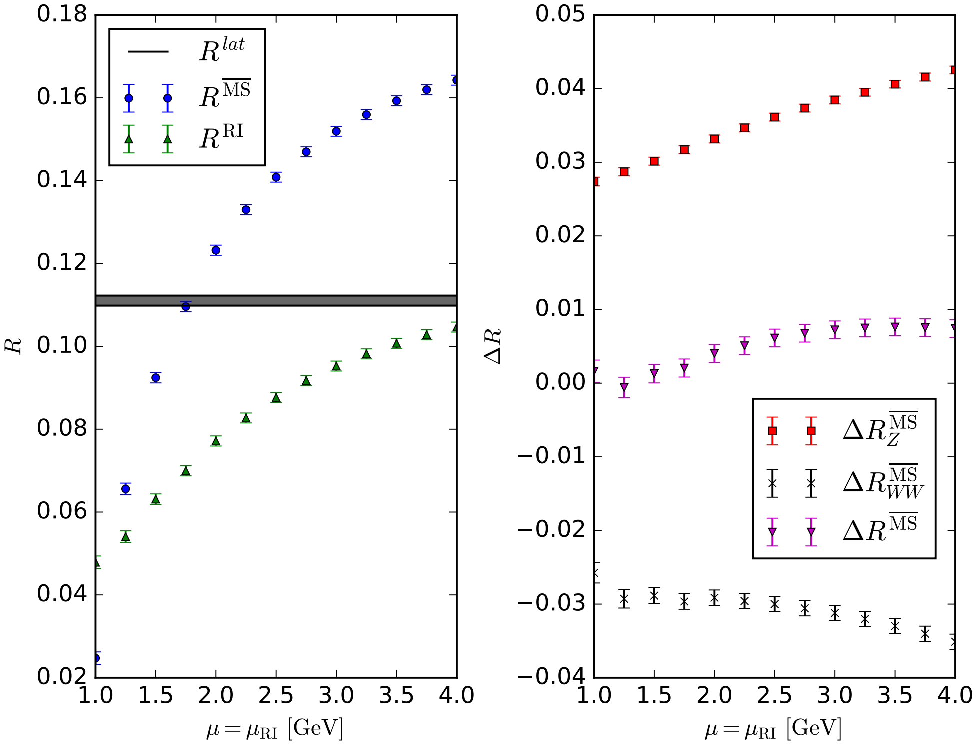

Figure 7.23: Plot summarising the total results for the ratio Eq. (7.18) for $K \to \pi\nu\bar{\nu}$ decays. On the left I show the results regulated on the lattice (horizontal band), in the RI-SMOM scheme (blue circles) and in the $\overline{\text{MS}}$ scheme (green triangles). On the right I show the difference between the results obtained from the lattice and the results obtained using perturbation theory. Note how the discrepancy between the lattice and perturbative results is large for both WW and Z-exchange diagrams, but these discrepancies largely cancel in the total result.

.

from the residual renormalisation scale dependence and non-exponential finite volume corrections have been mentioned above, however we have neglected errors from the momentum dependence of our form factors and from the unphysical masses used in our simulation.

For the momentum dependence, the source of error is twofold. Firstly, there is a small error from the fact that the disconnected contributions have been calculated with both the initial state kaon and final state pion at rest. It is reasonable to neglect this error in the final result $R(\Delta, s)$, where the disconnected contribution is a sub-percent effect. Secondly, we have neglected the dependence of R on the variables s and Δ; in future studies we aim to simulate with multiple kinematical configurations such that the dependence may be properly quantified.

Lastly, it must of course be noted that this study was performed using unphysical masses for the pion and kaon, as well as an unphysically light charm quark. An interesting study for future simulations will be to see whether the unphysical masses have a significant effect on the cancellation of the quantity $\Delta R\,(\Delta, s)$ between the Z-exchange and W-W diagrams shown in Fig. 7.23. However, the simulation of the physical charm mass is an expensive prospect, as it requires a very fine lattice to control discretisation errors, as well as a volume large enough to avoid significant finite volume effects.

Chapter 8

Conclusions

This chapter summarises the findings from chapters 6 and 7.

The main objective of this work it to demonstrate that it is possible to calculate the long-distance contributions to rare kaon decays amplitudes using lattice QCD. One general feature of the calculation of the 4pt correlators involved is the appearance of intermediate states lighter than the initial kaon, which lead to unphysical, exponentially growing contributions. We have shown that for the π intermediate states in γ- and Z-exchange diagrams and $\ell^+\nu$ states in W-W diagrams, it is possible to remove these states with controlled systematic errors. It has been instructive to understand how to remove these states in cases when they are the only exponentially growing contributions in the correlators. The stage is now set for a calculation with physical kaon and pion masses, in particular such that $\pi\pi$ or even $\pi\pi\pi$ intermediates states will contribute, which will allow us to develop the analysis techniques further to handle new exponentially growing contributions.

Although our calculation has been performed with unphysical values for the kaon and pion masses, it is nevertheless interesting to make qualitative comparisons to physical results. As a schematic calculation, we have tested using $\mathcal{O}(p^4)$ ChPT formulas to extrapolate our results to physical pion and kaon masses to compare with experimental data. For both the lattice and experimental results a ChPT-motivated fit ansatz can be used to produce values of $V_+(0)$, which is known at $\mathcal{O}(p^4)$. Our lattice result $[a_+^{lat} = 1.6(7)]$ cannot reasonably be compared to the experimental result $[a_+^{exp} = -0.578(16)]$ at this stage, as our simulations use meson masses that are considerably heavier than their physical values. As we begin to simulate with lighter pion and kaon masses, we will be able to study the mass dependence of a_+ and b_+ and ultimately at the physical point we can make direct comparisons with experiment. It is important to note that the size of the errors on the results of our calculation are an order of magnitude greater than those obtained from fits to experimental results. Hence in a physical study we would require a much greater computational effort to increase the number of gauge samples that are studied, expanding the number of calculations performed on each sample and employing further variance reduction methods such as all-mode averaging [138, 144] and all-to-all propagators [145]. This physical study is currently in preparation and will make use of the codebase Grid. All rare kaon decay contractions necessary for the project have been implemented in Grid and tested against existing results.

For our studies of $K \to \pi\nu\bar{\nu}$ decays, it is again premature to compare our estimates for the long-distance matrix elements to those from perturbation theory, especially as we have used an unphysically light charm quark. For this reason there is no meaningful comparison between the long-distance correction to P_c, given by $\Delta R\,(\Delta, s) = 0.0040(13)(32)(-45)$ to the quantity $\delta P_{u,c} = 0.04(2)$. However we have discovered the interesting feature is that the quantity ΔR experiences large cancellations between the Z-exchange and W-W diagrams, and it will be interesting to see whether this feature persists in a physical calculation. As an intermediate step, simulations using the $32^3 \times 64$ RBC-UKQCD DWF ensemble, with a pion mass of $m_\pi = 170\,\mathrm{MeV}$ are being performed, which will aid in the understanding of the error caused by the unphysical pion mass. The lower pion mass also increases the available (Δ, s) phase space, and hence these simulations will also allow for a study of kinematical dependence the form factors.

For both $K \to \pi\ell^+\ell^-$ and $K \to \pi\nu\bar{\nu}$ decays, one significant barrier that must be overcome for a physical calculation is the inclusion of a physical charm mass. Using the physical charm mass poses substantial computational costs, since we must use both a sufficiently small lattice spacing to avoid lattice artefacts due to the large charm mass, and a sufficiently large volume to avoid finite-volume effects from the pion. For $K \to \pi\ell^+\ell^-$ decays, where the charm contribution does not dominate, it is possible to work in a theory where the charm quark is integrated out. Although this complicates the renormalisation procedure, it is analogous to that presented here for $K \to \pi\nu\bar{\nu}$ decays. Hence future studies of $K \to \pi\ell^+\ell^-$ will take place on RBC-UKQCD's $48^3 \times 96$ DWF ensemble, with a physical pion mass. These studies will begin shortly; given current computational resources, the results from such simulations will be available within two years. Ultimately however we aim to perform simulations of both decays with a physical charm quark, using RBC-UKQCD's $64^3 \times 128$ ensemble with a physical pion mass and an inverse lattice spacing $a^{-1} = 2.38$ GeV. Such a calculation should become possible in the next three to four years when the next generation of computers becomes available.

Appendix A

Approximations

A.1 $c_0^2(\mathbf{k}) = -c_0^1(\mathbf{k})$

In this section we provide a justification for the approximation $c_0^2\left(\mathbf{k},\mathbf{p}\right) = -c_0^1\left(\mathbf{k},\mathbf{p}\right)$ [2]. The basis of this approximation is the identification that the relation holds exactly when $\mathbf{k} = \mathbf{p}$. To show this, we define $c_0^1(\mathbf{k})$ and $c_0^2(\mathbf{k})$ respectively as

$$c_0^1\left(\mathbf{k}\right) = \frac{\mathcal{M}_0^{J,\pi}\left(\mathbf{0}\right)\mathcal{M}_H\left(\mathbf{k}\right)}{2E_\pi\left(\mathbf{k}\right)\left(E_K\left(\mathbf{k}\right) - E_\pi\left(\mathbf{k}\right)\right)},\; c_0^2\left(\mathbf{k}\right) = -\frac{\mathcal{M}_0^{J,K}\left(\mathbf{0}\right)\mathcal{M}_H\left(\mathbf{k}\right)}{2E_K\left(\mathbf{k}\right)\left(E_K\left(\mathbf{k}\right) - E_\pi\left(\mathbf{k}\right)\right)}. \tag{A.1}$$

In general the current matrix element can be decomposed as

$$\mathcal{M}_\mu^{J,P}\left(k,p\right) = \left(k+p\right)_\mu F^P\left(\left(k-p\right)^2\right), \tag{A.2}$$

where F^P is the electromagnetic form factor of the particle P. At the point $k = p$, we find that

$$\mathcal{M}_0^{J,P}\left(k,k\right) = 2E_P\left(\mathbf{k}\right)Q, \tag{A.3}$$

where E_P is the energy of the particle in question, and Q is its charge (in units of the elementary charge). The factor of $2E_P\left(\mathbf{k}\right)$ is canceled by the normalization factor in both $c_0^1(\mathbf{k})$ and $c_0^2(\mathbf{k})$. The remaining factor of

$$\frac{\mathcal{M}_H\left(\mathbf{k}\right)}{E_K\left(\mathbf{k}\right) - E_\pi\left(\mathbf{k}\right)} \tag{A.4}$$

is common to both $c_0^1(\mathbf{k})$ and $c_0^2(\mathbf{k})$; it is thus clear to see that $c_0^2(\mathbf{k}) = -c_0^1(\mathbf{k})$.

A.2 $SU(3)$ symmetric limit

In this section we show that the quantity $\langle \pi (\mathbf{p})| H_W |K (\mathbf{p})\rangle$ is independent of momentum in the $SU(3)$ symmetric limit [2]. Let us consider the matrix element

$$\begin{aligned} \mathcal{M}_H (\mathbf{p}) &= \langle \pi (\mathbf{p})| H_W |K (\mathbf{p})\rangle && \text{(A.5)} \\ &= \langle \pi (\mathbf{k})| B_\pi^{-1} (k, p) H_W B_K (k, p) |K (\mathbf{k})\rangle && \text{(A.6)} \end{aligned}$$

where $B_P (k, p)$ is the boost into the frame where the particle P has momentum $\mathbf{k}$ from the frame where it has momentum $\mathbf{p}$. The Lorentz boost depends on the particle's mass, and so in general the quantity

$$B_\pi^{-1} (k, p) H_W B_K (k, p) \tag{A.7}$$

cannot be trivially decomposed. However when we take the limit $M_K \to M_\pi$, we find that

$$B_\pi^{-1} (k, p) H_W B_\pi (k, p) = H_W . \tag{A.8}$$

The equality holds because the operator H_W is a Lorentz scalar. It holds therefore that in the $SU(3)$ symmetric limit, the matrix element $\langle \pi (\mathbf{p})| H_W |K (\mathbf{p})\rangle$ is independent of momentum. A similar argument is true also for $\langle \pi (\mathbf{p})| \bar{s}d |K (\mathbf{p})\rangle$. As a result the ratio c_s [Eq. (6.7)] is also independent of momentum in this limit.

Appendix B

Perturbative Results

B.1 Expressions for ΔY_{AB}

In this section I give the results for the calculation of amputated Green's functions corresponding to ΔY_{AB} [Eq. (7.24)]. The relevant Feynman diagrams to be computed are shown in Fig. 7.21. These diagrams are evaluated to $\mathcal{O}\left(\alpha_s^0\right)$ [32].

I start with the W-W exchange diagrams, shown in Fig. 7.21. To regulate divergences in the loop integrals, we use dimensional regularisation. Hence we generalise to d dimensions and define $\epsilon = (4-d)$. The amputated Green's function we must compute is

$$\Gamma_{WW}\left(q\right) = \Gamma^{u}_{WW}\left(q\right) - \Gamma^{c}_{WW}\left(q\right) \tag{B.1}$$

$$\Gamma^{q}_{WW}\left(q\right) = \mu^{\epsilon}\int \frac{d^dk}{\left(2\pi\right)^d}\left(\gamma^L_\mu S_q\left(-k\right)\gamma^L_\nu\right)\otimes\left(\gamma^\mu_L S_\ell\left(k+q\right)\gamma^\nu_L\right), \tag{B.2}$$

where q is the momentum transfer, k is the loop momentum, and the propagator for quarks (subscript q) or leptons (subscript ℓ) is given by

$$S_q\left(k\right) = \frac{-i\not{k}+m_q}{k^2+m_q^2}\delta_{ab}, \quad S_\ell\left(k\right) = \frac{-i\not{k}+m_\ell}{k^2+m_\ell^2}, \tag{B.3}$$

where we note the colour structure of the quark propagator (although I otherwise suppress colour indices for notational convenience). We have used the notation $\gamma^L_\mu = \gamma_\mu\left(1-\gamma_5\right)$ (similarly we will use $\gamma^R_\mu = \gamma_\mu\left(1+\gamma_5\right)$). The factor μ^ϵ appears to account for the missing mass dimension when performing the integral in d rather than 4 dimensions; μ hence sets the $\overline{\text{MS}}$ renormalisation scale. We perform the calculation at $\mu = \mu_{\text{RI}}$.

To obtain Y_{WW} from Γ_{WW}, we project out the Dirac structure (the colour structure is trivial) using the projector

$$P_{WW} = \frac{\Gamma^{\dagger}}{\mathrm{Tr}\left[\Gamma^{\dagger}\Gamma\right]}, \tag{B.4}$$

$$\Gamma = \left(\gamma_{\rho}\left(1-\gamma_5\right)\right) \otimes \left(\gamma^{\rho}\left(1-\gamma_5\right)\right); \tag{B.5}$$

and hence we calculate

$$Y_{WW}\left(\mu, \mu_{\mathrm{RI}}\right) = \mu^{\epsilon}\mathrm{Tr}\left[\Gamma_{WW}P_{WW}\right] \tag{B.6}$$

$$= \int \frac{d^d k}{\left(2\pi\right)^d} \frac{\mathrm{Tr}\left[\gamma^L_{\mu} S_q\left(-k\right)\gamma^L_{\nu}\gamma^R_{\rho}\right] \mathrm{Tr}\left[\gamma^{\mu}_L S_{\ell}\left(k+q\right)\gamma^{\nu}_L\gamma^{\rho}_R\right]}{\mathrm{Tr}\left[\gamma^L_{\sigma}\gamma^R_{\delta}\right]\mathrm{Tr}\left[\gamma^{\sigma}_L\gamma^{\delta}_R\right]}. \tag{B.7}$$

At this point the computation may be performed using standard results for one-loop integrals (which may be found within Ref. [52], for example). We remark that the quantity Y_{WW} is logarithmically divergent (even after the GIM cancellation); however the quantity ΔY_{WW} is finite.

The results for ΔY_{WW} may be written as

$$\Delta Y_{WW}\left(\mu_{\mathrm{RI}}\right) = 16\left[\left(I_{WW}\left(0, \mu_{\mathrm{RI}}, m_{\ell}\right) - I_{WW}\left(m_c, m_{\ell}, \mu_{\mathrm{RI}}\right)\right) - \left(I_{WW}\left(0, m_{\ell}, \mu_{\mathrm{RI}}\right) - I_{WW}\left(m_c, m_{\ell}, \mu_{\mathrm{RI}}\right)\right)\right], \tag{B.8}$$

with the integral

$$I_{WW}\left(m_1, m_2, \mu\right) = \frac{1}{16\pi^2}\int_0^1 dx\ \left(2\Delta + x\left(1-x\right)\mu^2\right)\log\Delta, \tag{B.9}$$

and we have introduced the factor Δ, given by

$$\Delta = x\left(1-x\right)\mu^2 + xm_1^2 + \left(1-x\right)m_2^2. \tag{B.10}$$

The integral over x is a result of using a Feynman parametrisation to compute the integral Eq. (B.7).

The Z-exchange diagrams are shown in Fig. 7.21(a). The amputated Green's function may be written as

$$\Gamma^{j}_{Z,1} = -Q_j\mu^{\epsilon}\int\frac{d^d k}{\left(2\pi\right)^d}\mathrm{Tr}\left[\gamma^L_{\mu}S_q\left(k+q\right)\Gamma_{\nu}S_q\left(k\right)\right]\gamma^{\mu}_L\otimes\gamma^{\nu}_L, \tag{B.11}$$

$$\Gamma^{J}_{Z,2} = Q_j\mu^{\epsilon}\int\frac{d^d k}{\left(2\pi\right)^d}\gamma^L_{\mu}S_q\left(k+q\right)\Gamma_{\nu}S_q\left(k\right)\gamma^{\mu}_L\otimes\gamma^{\nu}_L, \tag{B.12}$$

where $j = V, A$. The factors Q_j for each current are $Q_A = -I_3$ and $Q_V = I_3 - 2Q_{em}\sin^2\theta_W$, and the gamma matrix product Γ_j is $\Gamma_A = \gamma_{\nu}\gamma_5$ or $\Gamma_V = \gamma_{\nu}$. However only the axial current is needed for the renormalisation of Z-exchange diagrams. Again we project out the Dirac structure using Eq. (B.4) to obtain

$$\Delta Y^{A}_{Z,2}\left(\mu,\mu_{\mathrm{RI}}\right)=2Q_A\left[\left(I_{Z,A}\left(0,\mu_{\mathrm{RI}}\right)-I_{Z,A}\left(m_c,\mu_{\mathrm{RI}}\right)\right)+I_{Z,A}\left(m_c,0\right)\right], \tag{B.13}$$

$$\Delta Y^{A}_{Z,1}\left(\mu,\mu_{\mathrm{RI}}\right)=N_c\Delta Y^{A}_{Z,2}\left(\mu,\mu_{\mathrm{RI}}\right), \tag{B.14}$$

with

$$I_{Z,A}\left(m,\mu\right)=\frac{1}{16\pi^2}\int_0^1 dx\,\left[3x\left(1-x\right)\mu^2+4m^2\right]\log\left(x\left(1-x\right)\mu^2+m^2\right). \tag{B.15}$$

References

[1] RBC-UKQCD collaboration, N. H. Christ, T. Izubuchi, C. T. Sachrajda, A. Soni and J. Yu, *Long distance contribution to the $K_L - K_S$ mass difference*, *Phys. Rev.* **D88** (2013) 014508, [`1212.5931`].

[2] N. H. Christ, X. Feng, A. Juttner, A. Lawson, A. Portelli and C. T. Sachrajda, *First exploratory calculation of the long-distance contributions to the rare kaon decays $K \to \pi\ell^+\ell^-$*, *Phys. Rev.* **D94** (2016) 114516, [`1608.07585`].

[3] Z. Bai, N. H. Christ, X. Feng, A. Lawson, A. Portelli and C. T. Sachrajda, *Exploratory Lattice QCD Study of the Rare Kaon Decay $K^+ \to \pi^+\nu\bar{\nu}$*, *Phys. Rev. Lett.* **118** (2017) 252001, [`1701.02858`].

[4] V. Cirigliano, G. Ecker, H. Neufeld, A. Pich and J. Portoles, *Kaon Decays in the Standard Model*, *Rev. Mod. Phys.* **84** (2012) 399, [`1107.6001`].

[5] S. L. Glashow, J. Iliopoulos and L. Maiani, *Weak interactions with lepton-hadron symmetry*, *Phys. Rev.* **D2** (1970) 1285–1292.

[6] A. J. Buras, D. Buttazzo, J. Girrbach-Noe and R. Knegjens, *$K^+ \to \pi^+\nu\bar{\nu}$ and $K_L \to \pi^0\nu\bar{\nu}$ in the Standard Model: status and perspectives*, *JHEP* **11** (2015) 033, [`1503.02693`].

[7] E949 collaboration, A. Artamonov et al., *New measurement of the $K^+ \to \pi^+\nu\bar{\nu}$ branching ratio*, *Phys. Rev. Lett.* **101** (2008) 191802, [`0808.2459`].

[8] E787 collaboration, S. Adler et al., *Evidence for the decay K+ —> pi+ neutrino anti-neutrino*, *Phys. Rev. Lett.* **79** (1997) 2204–2207, [`hep-ex/9708031`].

[9] E787 collaboration, S. Adler et al., *Further search for the decay K+ —> pi+ neutrino anti-neutrino*, *Phys. Rev. Lett.* **84** (2000) 3768–3770, [`hep-ex/0002015`].

[10] E787 collaboration, S. Adler et al., *Further evidence for the decay K+ —> pi+ neutrino anti-neutrino*, *Phys. Rev. Lett.* **88** (2002) 041803, [`hep-ex/0111091`].

[11] E787 collaboration, S. S. Adler et al., *Search for the decay K+ —> pi+ nu anti-nu in the momentum region P(pi) less than 195-MeV/c*, *Phys. Lett.* **B537** (2002) 211–216, [`hep-ex/0201037`].

[12] E949 collaboration, V. Anisimovsky et al., *Improved measurement of the K+ —> pi+ nu anti-nu branching ratio*, *Phys. Rev. Lett.* **93** (2004) 031801, [`hep-ex/0403036`].

[13] G. Anelli et al., *Proposal to measure the rare decay* $K^+ \to \pi^+ \nu \bar{\nu}$ *at the CERN SPS, CERN-SPSC-2005-013, CERN-SPSC-P-326* (2005) .

[14] NA62 collaboration, M. Moulson, *Searches for rare and forbidden kaon decays at the NA62 experiment at CERN*, in *Meeting of the APS Division of Particles and Fields (DPF 2013) Santa Cruz, California, USA, August 13-17, 2013*, 2013. `1310.7816`.

[15] NA62 collaboration, F. Gonnella, *The NA62 experiment at CERN*, *J. Phys. Conf. Ser.* **873** (2017) 012015.

[16] E391A collaboration, J. Ahn et al., *Experimental study of the decay K0(L) —> pi0 nu nu-bar*, *Phys. Rev.* **D81** (2010) 072004, [`0911.4789`].

[17] KOTO collaboration, T. Yamanaka, *The J-PARC KOTO experiment*, *PTEP* **2012** (2012) 02B006.

[18] J-PARC KOTO collaboration, J. K. Ahn et al., *A new search for the* $K_L \to \pi^0 \nu \bar{\nu}$ *and* $K_L \to \pi^0 X^0$ *decays*, *PTEP* **2017** (2017) 021C01, [`1609.03637`].

[19] RBC-UKQCD collaboration, N. H. Christ, X. Feng, A. Portelli and C. T. Sachrajda, *Prospects for a lattice computation of rare kaon decay amplitudes:* $K \to \pi \ell^+ \ell^-$ *decays*, *Phys. Rev.* **D92** (2015) 094512, [`1507.03094`].

[20] G. Ecker, A. Pich and E. de Rafael, $K \to \pi \ell^+ \ell^-$ *Decays in the Effective Chiral Lagrangian of the Standard Model*, *Nucl. Phys.* **B291** (1987) 692.

[21] G. D'Ambrosio, G. Ecker, G. Isidori and J. Portoles, *The Decays* $K \to \pi \ell^+ \ell^-$ *beyond leading order in the chiral expansion*, *JHEP* **9808** (1998) 004, [`hep-ph/9808289`].

[22] S. Friot, D. Greynat and E. De Rafael, *Rare kaon decays revisited*, *Phys. Lett.* **B595** (2004) 301–308, [`hep-ph/0404136`].

[23] A. Z. Dubnickova, S. Dubnicka, E. Goudzovski, V. N. Pervushin and M. Secansky, *Kaon decay probe of the weak static interaction*, *Phys. Part. Nucl. Lett.* **5** (2008) 76–84, [`hep-ph/0611175`].

[24] G. Isidori, C. Smith and R. Unterdorfer, *The Rare decay* $K_L \to \pi^0 \mu^+ \mu^-$ *within the SM*, *Eur. Phys. J.* **C36** (2004) 57–66, [`hep-ph/0404127`].

[25] G. Isidori, G. Martinelli and P. Turchetti, *Rare kaon decays on the lattice*, *Phys. Lett.* **B633** (2006) 75–83, [`hep-lat/0506026`].

[26] NA48/2 collaboration, J. Batley et al., *Precise measurement of the $K^{\pm} \to \pi^{\pm}e^{+}e^{-}$ decay*, *Phys. Lett.* **B677** (2009) 246–254, [0903.3130].

[27] NA48/2 collaboration, J. Batley et al., *New measurement of the $K^{\pm} \to \pi^{\pm}\mu^{+}\mu^{-}$ decay*, *Phys. Lett.* **B697** (2011) 107–115, [1011.4817].

[28] A. Crivellin, G. D'Ambrosio, M. Hoferichter and L. C. Tunstall, *Violation of lepton flavor and lepton flavor universality in rare kaon decays*, *Phys. Rev.* **D93** (2016) 074038, [1601.00970].

[29] NA48/1 collaboration, J. Batley et al., *Observation of the rare decay $K_S \to \pi^0 e^+ e^-$*, *Phys. Lett.* **B576** (2003) 43–54, [hep-ex/0309075].

[30] NA48/1 collaboration, J. Batley et al., *Observation of the rare decay $K_S \to \pi^0 \mu^+ \mu^-$*, *Phys. Lett.* **B599** (2004) 197–211, [hep-ex/0409011].

[31] LHCb collaboration, C. Marin Bento, *Recent results and prospects of rare kaon decay measurements at LHCb*, *PoS* **HQL2014** (2014) 024.

[32] Z. Bai, N. H. Christ, X. Feng, A. Lawson, A. Portelli and C. T. Sachrajda, "Exploratory Lattice QCD Study of the Rare Kaon Decay $K^+ \to \pi^+\nu\bar{\nu}$.".

[33] RBC-UKQCD collaboration, N. H. Christ, X. Feng, A. Portelli and C. T. Sachrajda, *Prospects for a lattice computation of rare kaon decay amplitudes II $K \to \pi\nu\bar{\nu}$ decays*, *Phys. Rev.* **D93** (2016) 114517, [1605.04442].

[34] P. J. E. Peebles, *Principles of physical cosmology*. 1994.

[35] A. D. Sakharov, *Violation of CP Invariance, c Asymmetry, and Baryon Asymmetry of the Universe*, *Pisma Zh. Eksp. Teor. Fiz.* **5** (1967) 32–35.

[36] F. Jegerlehner and A. Nyffeler, *The Muon g-2*, *Phys. Rept.* **477** (2009) 1–110, [0902.3360].

[37] Particle Data Group collaboration, C. Patrignani et al., *Review of Particle Physics*, *Chin. Phys.* **C40** (2016) 100001.

[38] W. Gohn, *The muon g-2 experiment at Fermilab*, in *18th International Workshop on Neutrino Factories and Future Neutrino Facilities Search (NuFact16) Quy Nhon, Vietnam, August 21-27, 2016*, 2016. 1611.04964.

[39] J-PARC g-2 collaboration, T. Mibe, *New g-2 experiment at J-PARC*, *Chin. Phys.* **C34** (2010) 745–748.

[40] ETM collaboration, F. Burger, X. Feng, G. Hotzel, K. Jansen, M. Petschlies and D. B. Renner, *Four-Flavour Leading-Order Hadronic Contribution To The Muon Anomalous Magnetic Moment*, *JHEP* **02** (2014) 099, [1308.4327].

[41] T. Blum, P. A. Boyle, T. Izubuchi, L. Jin, A. Jüttner, C. Lehner et al., *Calculation of the hadronic vacuum polarization disconnected contribution to the muon anomalous magnetic moment*, *Phys. Rev. Lett.* **116** (2016) 232002, [1512.09054].

[42] RBC/UKQCD collaboration, T. Blum et al., *Lattice calculation of the leading strange quark-connected contribution to the muon $g2$*, *JHEP* **04** (2016) 063, [1602.01767].

[43] B. Chakraborty, C. T. H. Davies, P. G. de Oliviera, J. Koponen and G. P. Lepage, *The hadronic vacuum polarization contribution to a_μ from full lattice QCD*, 1601.03071.

[44] M. Della Morte, A. Francis, V. Gülpers, G. Herdoíza, G. von Hippel, H. Horch et al., *The hadronic vacuum polarization contribution to the muon $g-2$ from lattice QCD*, 1705.01775.

[45] J. Green, O. Gryniuk, G. von Hippel, H. B. Meyer and V. Pascalutsa, *Lattice QCD calculation of hadronic light-by-light scattering*, *Phys. Rev. Lett.* **115** (2015) 222003, [1507.01577].

[46] N. Asmussen, J. Green, H. B. Meyer and A. Nyffeler, *Position-space approach to hadronic light-by-light scattering in the muon $g-2$ on the lattice*, *PoS* **LATTICE2016** (2016) 164, [1609.08454].

[47] T. Blum, N. Christ, M. Hayakawa, T. Izubuchi, L. Jin, C. Jung et al., *Connected and Leading Disconnected Hadronic Light-by-Light Contribution to the Muon Anomalous Magnetic Moment with a Physical Pion Mass*, *Phys. Rev. Lett.* **118** (2017) 022005, [1610.04603].

[48] LHCb collaboration, R. Aaij et al., *Angular analysis and differential branching fraction of the decay $B_s^0 \to \phi\mu^+\mu^-$*, *JHEP* **09** (2015) 179, [1506.08777].

[49] Belle collaboration, S. Hirose, *Measurement of $\bar{B} \to D^{(*)}\tau^-\bar{\nu}_\tau$ at Belle*, *Nucl. Part. Phys. Proc.* **287-288** (2017) 185–188.

[50] BaBar collaboration, J. P. Lees et al., *Evidence for an excess of $\bar{B} \to D^{(*)}\tau^-\bar{\nu}_\tau$ decays*, *Phys. Rev. Lett.* **109** (2012) 101802, [1205.5442].

[51] LHCb collaboration, R. Aaij et al., *Measurement of the ratio of branching fractions $\mathcal{B}(\bar{B}^0 \to D^{*+}\tau^-\bar{\nu}_\tau)/\mathcal{B}(\bar{B}^0 \to D^{*+}\mu^-\bar{\nu}_\mu)$*, *Phys. Rev. Lett.* **115** (2015) 111803, [1506.08614].

[52] M. E. Peskin and D. V. Schroeder, *An Introduction to quantum field theory*. 1995.

[53] C. G. Callan, Jr., R. F. Dashen and D. J. Gross, *The Structure of the Gauge Theory Vacuum*, *Phys. Lett.* **63B** (1976) 334–340.

[54] R. Jackiw and C. Rebbi, *Vacuum Periodicity in a Yang-Mills Quantum Theory*, *Phys. Rev. Lett.* **37** (1976) 172–175.

[55] J. S. Schwinger, *The Theory of quantized fields. 1.*, *Phys. Rev.* **82** (1951) 914–927.

[56] FlaviaNet Working Group on Kaon Decays collaboration, M. Antonelli et al., *An Evaluation of $|V_{us}|$ and precise tests of the Standard Model from world data on leptonic and semileptonic kaon decays*, *Eur. Phys. J.* **C69** (2010) 399–424, [`1005.2323`].

[57] S. Aoki et al., *Review of lattice results concerning low-energy particle physics*, *Eur. Phys. J.* **C77** (2017) 112, [`1607.00299`].

[58] S. Borsanyi et al., *Ab initio calculation of the neutron-proton mass difference*, *Science* **347** (2015) 1452–1455, [`1406.4088`].

[59] V. Lubicz, G. Martinelli, C. T. Sachrajda, F. Sanfilippo, S. Simula and N. Tantalo, *Finite-Volume QED Corrections to Decay Amplitudes in Lattice QCD*, *Phys. Rev.* **D95** (2017) 034504, [`1611.08497`].

[60] D. Giusti, V. Lubicz, C. Tarantino, G. Martinelli, S. Sanfilippo, S. Simula et al., *Leading isospin-breaking corrections to pion, kaon and charmed-meson masses with Twisted-Mass fermions*, *Phys. Rev.* **D95** (2017) 114504, [`1704.06561`].

[61] P. Boyle, V. Gülpers, J. Harrison, A. Jüttner, C. Lehner, A. Portelli et al., *Isospin breaking corrections to meson masses and the hadronic vacuum polarization: a comparative study*, `1706.05293`.

[62] E. Noether, *Invariante variationsprobleme*, *Nachrichten von der Gesellschaft der Wissenschaften zu Göttingen, Mathematisch-Physikalische Klasse* **1918** (1918) 235–257.

[63] J. C. Ward, *An identity in quantum electrodynamics*, *Phys. Rev.* **78** (Apr, 1950) 182–182.

[64] Y. Takahashi, *On the generalized ward identity*, *Il Nuovo Cimento (1955-1965)* **6** (Aug, 1957) 371–375.

[65] M. Luscher, *Advanced lattice QCD*, in *Probing the standard model of particle interactions. Proceedings, Summer School in Theoretical Physics, NATO Advanced Study Institute, 68th session, Les Houches, France, July 28-September 5, 1997. Pt. 1, 2*, pp. 229–280, 1998. `hep-lat/9802029`.

[66] F. Englert and R. Brout, *Broken symmetry and the mass of gauge vector mesons*, *Phys. Rev. Lett.* **13** (Aug, 1964) 321–323.

[67] P. W. Higgs, *Broken symmetries and the masses of gauge bosons*, *Phys. Rev. Lett.* **13** (Oct, 1964) 508–509.

[68] G. S. Guralnik, C. R. Hagen and T. W. B. Kibble, *Global conservation laws and massless particles*, *Phys. Rev. Lett.* **13** (Nov, 1964) 585–587.

[69] N. Cabibbo, *Unitary symmetry and leptonic decays*, *Phys. Rev. Lett.* **10** (Jun, 1963) 531–533.

[70] M. Kobayashi and T. Maskawa, *CP Violation in the Renormalizable Theory of Weak Interaction*, *Prog. Theor. Phys.* **49** (1973) 652–657.

[71] Super-Kamiokande Collaboration collaboration, Y. Fukuda, T. Hayakawa, E. Ichihara, K. Inoue, K. Ishihara, H. Ishino et al., *Evidence for oscillation of atmospheric neutrinos*, *Phys. Rev. Lett.* **81** (Aug, 1998) 1562–1567.

[72] SNO Collaboration collaboration, Q. R. Ahmad, R. C. Allen, T. C. Andersen, J. D. Anglin, G. Bühler, J. C. Barton et al., *Measurement of the rate of $\nu_e + d \to p + p + e^-$ interactions produced by ^8b solar neutrinos at the sudbury neutrino observatory*, *Phys. Rev. Lett.* **87** (Jul, 2001) 071301.

[73] SNO Collaboration collaboration, Q. R. Ahmad, R. C. Allen, T. C. Andersen, J. D.Anglin, J. C. Barton, E. W. Beier et al., *Direct evidence for neutrino flavor transformation from neutral-current interactions in the sudbury neutrino observatory*, *Phys. Rev. Lett.* **89** (Jun, 2002) 011301.

[74] B. Pontecorvo, *Inverse beta processes and nonconservation of lepton charge*, *Sov. Phys. JETP* **7** (1958) 172–173.

[75] Z. Maki, M. Nakagawa and S. Sakata, *Remarks on the unified model of elementary particles*, *Prog. Theor. Phys.* **28** (1962) 870–880.

[76] L.-L. Chau and W.-Y. Keung, *Comments on the parametrization of the kobayashi-maskawa matrix*, *Phys. Rev. Lett.* **53** (Nov, 1984) 1802–1805.

[77] G. Buchalla, A. J. Buras and M. E. Lautenbacher, *Weak decays beyond leading logarithms*, *Rev. Mod. Phys.* **68** (1996) 1125–1144, [`hep-ph/9512380`].

[78] A. J. Buras, *Weak Hamiltonian, CP violation and rare decays*, in *Probing the standard model of particle interactions. Proceedings, Summer School in Theoretical Physics, NATO Advanced Study Institute, 68th session, Les Houches, France, July 28-September 5, 1997. Pt. 1, 2*, pp. 281–539, 1998. `hep-ph/9806471`.

[79] A. J. Buras, M. Gorbahn, U. Haisch and U. Nierste, *Charm quark contribution to K+ —> pi+ nu anti-nu at next-to-next-to-leading order*, *JHEP* **0611** (2006) 002, [`hep-ph/0603079`].

[80] G. Ecker, *Chiral perturbation theory*, *Prog. Part. Nucl. Phys.* **35** (1995) 1–80, [`hep-ph/9501357`].

[81] S. Scherer, *Introduction to chiral perturbation theory*, *Adv. Nucl. Phys.* **27** (2003) 277, [hep-ph/0210398].

[82] M. Golterman, *Applications of chiral perturbation theory to lattice QCD*, in *Modern perspectives in lattice QCD: Quantum field theory and high performance computing. Proceedings, International School, 93rd Session, Les Houches, France, August 3-28, 2009*, pp. 423–515, 2009. 0912.4042.

[83] J. F. Nieves and P. B. Pal, *Generalized Fierz identities*, *Am. J. Phys.* **72** (2004) 1100–1108, [hep-ph/0306087].

[84] T. Inami and C. Lim, *Effects of Superheavy Quarks and Leptons in Low-Energy Weak Processes* $K_L \to \mu\bar{\mu}$, $K^+ \to \pi^+\nu\bar{\nu}$ *and* $K_0 \leftrightarrow \overline{K}_0$, *Prog. Theor. Phys.* **65** (1981) 297.

[85] S. L. Adler and W. A. Bardeen, *Absence of higher-order corrections in the anomalous axial-vector divergence equation*, *Phys. Rev.* **182** (Jun, 1969) 1517–1536.

[86] V. Cirigliano, G. Ecker, H. Neufeld and A. Pich, *Isospin breaking in* $K \to \pi\pi$ *decays*, *Eur. Phys. J.* (2004) 369–396.

[87] G. Buchalla, G. D'Ambrosio and G. Isidori, *Extracting short distance physics from K(L,S) —> pi0 e+ e- decays*, *Nucl. Phys.* **B672** (2003) 387–408, [hep-ph/0308008].

[88] A. J. Buras, M. E. Lautenbacher, M. Misiak and M. Munz, *Direct CP violation in K(L) —> pi0 e+ e- beyond leading logarithms*, *Nucl. Phys.* **B423** (1994) 349–383, [hep-ph/9402347].

[89] G. Buchalla and A. J. Buras, *The rare decays K —> pi neutrino anti-neutrino, B —> X neutrino anti-neutrino and B —> lepton+ lepton: An Update*, *Nucl.Phys.* **B548** (1999) 309–327, [hep-ph/9901288].

[90] A. Buras, M. Gorbahn, U. Haisch and U. Nierste, *The Rare decay K+ —> pi+ nu anti-nu at the next-to-next-to-leading order in QCD*, *Phys.Rev.Lett.* **95** (2005) 261805, [hep-ph/0508165].

[91] J. Brod, M. Gorbahn and E. Stamou, *Two-Loop Electroweak Corrections for the* $K\!-\!\!>\!\pi\nu\bar{nu}$ *Decays*, *Phys. Rev.* **D83** (2011) 034030, [1009.0947].

[92] G. Isidori, F. Mescia and C. Smith, *Light-quark loops in K —> pi nu anti-nu*, *Nucl. Phys.* **B718** (2005) 319–338, [hep-ph/0503107].

[93] T. DeGrand and C. E. Detar, *Lattice methods for quantum chromodynamics*. 2006.

[94] C. Gattringer and C. B. Lang, *Quantum chromodynamics on the lattice*, *Lect. Notes Phys.* **788** (2010) 1–343.

[95] K. G. Wilson, *Confinement of Quarks*, *Phys. Rev.* **D10** (1974) 2445–2459.

[96] Y. Iwasaki, *Renormalization Group Analysis of Lattice Theories and Improved Lattice Action. II. Four-dimensional non-Abelian SU(N) gauge model*, `1111.7054`.

[97] Y. Iwasaki and T. Yoshie, *Renormalization Group Improved Action for SU(3) Lattice Gauge Theory and the String Tension*, *Phys. Lett.* **143B** (1984) 449–452.

[98] T. Takaishi, *Heavy quark potential and effective actions on blocked configurations*, *Phys. Rev.* **D54** (1996) 1050–1053.

[99] QCD-TARO collaboration, P. de Forcrand, M. Garcia Perez, T. Hashimoto, S. Hioki, H. Matsufuru, O. Miyamura et al., *Renormalization group flow of SU(3) lattice gauge theory: Numerical studies in a two coupling space*, *Nucl. Phys.* **B577** (2000) 263–278, [`hep-lat/9911033`].

[100] H. B. Nielsen and M. Ninomiya, *No Go Theorem for Regularizing Chiral Fermions*, *Phys. Lett.* **B105** (1981) 219.

[101] P. H. Ginsparg and K. G. Wilson, *A Remnant of Chiral Symmetry on the Lattice*, *Phys. Rev.* **D25** (1982) 2649.

[102] S. Capitani, *Lattice perturbation theory*, *Phys. Rept.* **382** (2003) 113–302, [`hep-lat/0211036`].

[103] D. B. Kaplan, *A Method for simulating chiral fermions on the lattice*, *Phys. Lett.* **B288** (1992) 342–347, [`hep-lat/9206013`].

[104] Y. Shamir, *Anomalies and chiral defects fermions*, *Nucl. Phys.* **B417** (1994) 167–180, [`hep-lat/9310006`].

[105] R. C. Brower, H. Neff and K. Orginos, *Mobius fermions: Improved domain wall chiral fermions*, *Nucl. Phys. Proc. Suppl.* **140** (2005) 686–688, [`hep-lat/0409118`].

[106] P. A. Boyle, *Conserved currents for Mobius Domain Wall Fermions*, `1411.5728`.

[107] M. Bochicchio, L. Maiani, G. Martinelli, G. C. Rossi and M. Testa, *Chiral Symmetry on the Lattice with Wilson Fermions*, *Nucl. Phys.* **B262** (1985) 331.

[108] S. Duane, A. Kennedy, B. J. Pendleton and D. Roweth, *Hybrid monte carlo*, *Physics Letters B* **195** (1987) 216 – 222.

[109] G. Martinelli and C. T. Sachrajda, *A Lattice Study of Nucleon Structure*, *Nucl. Phys.* **B316** (1989) 355–372.

[110] S. Bernardson, P. McCarty and C. Thron, *Monte Carlo methods for estimating linear combinations of inverse matrix entries in lattice QCD*, *Comput. Phys. Commun.* **78** (1994) 256–264.

[111] S.-J. Dong and K.-F. Liu, *Stochastic estimation with Z_2 noise*, *Phys. Lett.* **B328** (1994) 130–136, [`hep-lat/9308015`].

[112] UKQCD collaboration, M. Foster and C. Michael, *Quark mass dependence of hadron masses from lattice QCD*, *Phys. Rev.* **D59** (1999) 074503, [`hep-lat/9810021`].

[113] L. Giusti, M. L. Paciello, C. Parrinello, S. Petrarca and B. Taglienti, *Problems on lattice gauge fixing*, *Int. J. Mod. Phys.* **A16** (2001) 3487–3534, [`hep-lat/0104012`].

[114] C. T. Sachrajda and G. Villadoro, *Twisted boundary conditions in lattice simulations*, *Phys. Lett.* **B609** (2005) 73–85, [`hep-lat/0411033`].

[115] Z. Bai, N. Christ, T. Izubuchi, C. Sachrajda, A. Soni et al., *$K_L - K_S$ mass difference from lattice QCD*, *Phys. Rev. Lett.* **113** (2014) 112003, [`1406.0916`].

[116] M. K. Gaillard and B. W. Lee, *Delta I = 1/2 Rule for Nonleptonic Decays in Asymptotically Free Field Theories*, *Phys. Rev. Lett.* **33** (1974) 108.

[117] G. Altarelli and L. Maiani, *Octet Enhancement of Nonleptonic Weak Interactions in Asymptotically Free Gauge Theories*, *Phys. Lett.* **52B** (1974) 351–354.

[118] RBC, UKQCD collaboration, P. A. Boyle et al., *Emerging understanding of the $\Delta I = 1/2$ Rule from Lattice QCD*, *Phys. Rev. Lett.* **110** (2013) 152001, [`1212.1474`].

[119] M. T. Hansen and S. R. Sharpe, *Relativistic, model-independent, three-particle quantization condition*, *Phys. Rev.* **D90** (2014) 116003, [`1408.5933`].

[120] M. T. Hansen and S. R. Sharpe, *Expressing the three-particle finite-volume spectrum in terms of the three-to-three scattering amplitude*, *Phys. Rev.* **D92** (2015) 114509, [`1504.04248`].

[121] L. Lellouch and M. Luscher, *Weak transition matrix elements from finite volume correlation functions*, *Commun. Math. Phys.* **219** (2001) 31–44, [`hep-lat/0003023`].

[122] N. H. Christ, G. Martinelli and C. T. Sachrajda, *Finite-volume effects in the evaluation of the K_L - K_S mass difference*, *PoS* **LATTICE2013** (2014) 399, [`1401.1362`].

[123] N. H. Christ, X. Feng, G. Martinelli and C. T. Sachrajda, *Effects of finite volume on the K_L-K_S mass difference*, *Phys. Rev.* **D91** (2015) 114510, [`1504.01170`].

[124] C. h. Kim, C. T. Sachrajda and S. R. Sharpe, *Finite-volume effects for two-hadron states in moving frames*, *Nucl. Phys.* **B727** (2005) 218–243, [`hep-lat/0507006`].

[125] M. T. Hansen and S. R. Sharpe, *Multiple-channel generalization of Lellouch-Luscher formula*, *Phys. Rev.* **D86** (2012) 016007, [`1204.0826`].

[126] G. Martinelli, C. Pittori, C. T. Sachrajda, M. Testa and A. Vladikas, *A General method for nonperturbative renormalization of lattice operators*, *Nucl. Phys.* **B445** (1995) 81–108, [`hep-lat/9411010`].

[127] Y. Aoki et al., *Non-perturbative renormalization of quark bilinear operators and B(K) using domain wall fermions*, *Phys. Rev.* **D78** (2008) 054510, [`0712.1061`].

[128] C. Sturm, Y. Aoki, N. Christ, T. Izubuchi, C. Sachrajda et al., *Renormalization of quark bilinear operators in a momentum-subtraction scheme with a nonexceptional subtraction point*, *Phys. Rev.* **D80** (2009) 014501, [`0901.2599`].

[129] C. Lehner and C. Sturm, *Matching factors for $\Delta S = 1$ four-quark operators in RI/SMOM schemes*, *Phys. Rev.* **D84** (2011) 014001, [`1104.4948`].

[130] RBC-UKQCD collaboration, C. Allton et al., *Physical Results from 2+1 Flavor Domain Wall QCD and SU(2) Chiral Perturbation Theory*, *Phys. Rev.* **D78** (2008) 114509, [`0804.0473`].

[131] RBC-UKQCD collaboration, Y. Aoki et al., *Continuum Limit Physics from 2+1 Flavor Domain Wall QCD*, *Phys. Rev.* **D83** (2011) 074508, [`1011.0892`].

[132] RBC-UKQCD collaboration, T. Blum et al., *Domain wall QCD with physical quark masses*, *Phys. Rev.* **D93** (2016) 074505, [`1411.7017`].

[133] M. Della Morte and A. Juttner, *Quark disconnected diagrams in chiral perturbation theory*, *JHEP* **11** (2010) 154, [`1009.3783`].

[134] P. A. Boyle, *Hierarchically deflated conjugate gradient*, `1402.2585`.

[135] T. Blum, P. Boyle, N. Christ, N. Garron, E. Goode et al., *K to $\pi\pi$ Decay amplitudes from Lattice QCD*, *Phys. Rev.* **D84** (2011) 114503, [`1106.2714`].

[136] T. Blum et al., *$K \to \pi\pi$ $\Delta I = 3/2$ decay amplitude in the continuum limit*, *Phys. Rev.* **D91** (2015) 074502, [`1502.00263`].

[137] P. Boyle et al., “Grid.” `https://github.com/paboyle/Grid`, 2017.

[138] T. Blum, T. Izubuchi and E. Shintani, *New class of variance-reduction techniques using lattice symmetries*, *Phys. Rev.* **D88** (2013) 094503, [`1208.4349`].

[139] M. Luscher, *Deflation acceleration of lattice QCD simulations*, *JHEP* **12** (2007) 011, [`0710.5417`].

[140] M. Luscher, *Local coherence and deflation of the low quark modes in lattice QCD*, *JHEP* **07** (2007) 081, [`0706.2298`].

[141] C. Aubin, T. Blum, M. Golterman and S. Peris, *Hadronic vacuum polarization with twisted boundary conditions*, *Phys. Rev.* **D88** (2013) 074505, [`1307.4701`].

[142] Y. Kikukawa and K. Usui, *Reflection Positivity of Free Overlap Fermions*, *Phys. Rev.* **D82** (2010) 114503, [`1005.3751`].

[143] C. Lanczos, *An iteration method for the solution of the eigenvalue problem of linear differential and integral operators*, *J. Res. Natl. Bur. Stand. B* **45** (1950) 255–282.

[144] G. S. Bali, S. Collins and A. Schafer, *Effective noise reduction techniques for disconnected loops in Lattice QCD*, *Comput. Phys. Commun.* **181** (2010) 1570–1583, [`0910.3970`].

[145] J. Foley, K. Jimmy Juge, A. O'Cais, M. Peardon, S. M. Ryan and J.-I. Skullerud, *Practical all-to-all propagators for lattice QCD*, *Comput. Phys. Commun.* **172** (2005) 145–162, [`hep-lat/0505023`].